THE UNIVERSITY *of* EDINBURGH

Cylindrical Linear Water Waves and their Application to the Wave-body Problem

James Cameron McNatt

Doctor of Philosophy

The University of Edinburgh

2015

For my Dad

Abstract

The interaction between water waves and a floating or fixed body is bi-directional: wave forces act on and cause motion in the body, and the body alters the wave field. The impact of the body on its wave field is important to understand because: 1) it may have positive or negative consequences on the natural or built environment; 2) multiple bodies in proximity interact via the waves that are scattered and radiated by them; and 3) in ocean wave energy conversion, by conservation of energy, as a device absorbs energy, so too must the energy be removed from the wave field.

Herein, the cylindrical solutions to the linear wave boundary-value problem are used to analyze the floating body wave field. These solutions describe small-amplitude, harmonic, potential-flow waves in the form of a Fourier summation of incoming and outgoing, partial, cylindrical, wave components. For a given geometry and mode of motion, the scattered or radiated waves are characterized by a particular set of complex cylindrical coefficients.

A novel method is developed for finding the cylindrical coefficients of a scattered or radiated wave field by making measurements, either computationally or experimentally, over a circular-cylindrical surface that circumscribes the body and taking a Fourier transform as a function of spatial direction. To isolate evanescent modes, measurements are made on the free-surface and as a function of depth. The technique is demonstrated computationally with the boundary-element method software, WAMIT. The resulting analytical wave fields are compared with those computed directly by WAMIT and the match is found to be within 0.1%.

A similar measurement and comparisons are made with experimental results. Because of the difficulty in making depth-dependent measurements, only free-surface measurements were made with a circular wave gauge array, where the gauges were positioned far from the body in order to neglect evanescent modes. The experimental results are also very good. However, both high-order harmonics and wave reflections led to difficulties.

To compute efficiently the wave interactions between multiple bodies, a well-known multiple-scattering theory is employed, in which waves that are scattered and radiated by one body are considered incident to another body, which in turn radiates and scatters waves, sending energy back to the first. Wave fields are given by their cylindrical representations and unknown scattered wave amplitudes are formulated into a linear system to solve the problem. Critical to the approach is the characterization of, for each unique geometry, the cylindrical forces, the radiated wave coefficients, and the scattered waves in the form of the diffraction transfer matrix.

The method developed herein for determining cylindrical coefficients is extended to

new methods for finding the quantities necessary to solve the interaction problem. The approach is demonstrated computationally with WAMIT for a simple cylinder and a more complex wave energy converter (WEC). Multiple-scattering computations are verified against direct computations from WAMIT and are performed for spectral seas and a very large array of 101 WECs. The multiple-scattering computation is 1,000-10,000 times faster than a direct computation because each body is represented by 10s of wave coefficients, rather than 100s to 1,000s of panels.

A new expression for wave energy absorption using cylindrical coefficients is derived, leading to a formulation of wave energy absorption efficiency, which is extended to a nondimensional parameter that relates to efficiency, capture width and gain. Cylindrical wave energy absorption analysis allows classical results of heaving and surging point absorbers to be easily reproduced and enables interesting computations of a WEC in three-dimensions. A Bristol Cylinder type WEC is examined and it is found that its performance can be improved by flaring its ends to reduce "end effects". Finally, a computation of 100% wave absorption is demonstrated using a generalized incident wave.

Cylindrical representations of linear water waves are shown to be effective for the computations of wave-body wave fields, multi-body interactions, and wave power absorption, and novel methods are presented for determining cylindrical quantities. One of the approach's greatest attributes is that once the cylindrical coefficients are found, complex representations of waves in three dimensions are stored in vectors and matrices and are manipulated with linear algebra. Further research in cylindrical water waves will likely yield useful applications such as: efficient computations of bodies interacting with short-crested seas, and continued progress in the understanding of wave energy absorption efficiency.

Acknowledgements

I could not have completed this PhD without the material, intellectual, moral and emotional support of so many teachers, colleagues, friends, and family. First, I am extremely grateful to The University of Edinburgh for providing the financial means for me to pursue my PhD through the Principal's Career Development and the Edinburgh Global Research Scholarships. I would like to thank Henry Jeffrey for mentoring me in the OpenORE project, James Sinfield and Steve Earl who helped me in the search for funding, and of course, the INORE community and committee for taking it on. In the design and construction of my experiments, I would like to thank the French exchange students, Jonathan, Matthieu, and Cyril for your month of unpaid labor. Thank you to Steve Gourlay and Kevin in the workshop who built the components. Thank you to Jean-Baptiste Richon for your help with the wave tank. And a huge thank you to Greg Payne for your expert advice in the model design. Instrumental to a thesis are one's supervisors. Venki Venugopal and David Forehand, thank you so much. Venki, you supported me even before my PhD began in my applications, and throughout you provided astute guidance. David, having you nearby was a huge benefit; your support, feedback, and friendship meant a lot.

I am so grateful for all the friends I have made through my life as a PhD student, those within the University, those in INORE, and those outside of school. I will remember fondly all of you and the adventures we had together. I could not have done this PhD without the support of my family. Brecht, Sally, Elizabeth, and Croom, thank you for letting me drag Tess across the ocean. Nory and Peter, I cannot thank you enough for the emotional, financial, and family support you have given us throughout my time as a student. Marisa and Aaron, it has been great being able to talk about my work with you, and Marisa I am happy we had our own marine-energy adventure to the far-reaches of Scotland. Mom, I know it has been hard having your grandchildren so far away, but I am so glad you visited us and were around for important events. Your love and support has meant the world to me. Dad, I know you would be proud, and it was your love and encouragement throughout my life that enabled me to even start such an endeavor. I miss and love you everyday.

Stuart and Eshlyn, I am not sure whether you have helped or hindered in my PhD (wink). I am fortunate to have raised two wonderful children while I had the freedom of school. Tess, words cannot capture what you have meant to me, especially over the last three years. You have been brave to take on starting and raising a family on little means in a new part of the world. It has not always been easy, but it has been amazing. I love you all so much.

Declaration

I declare that this thesis was composed by myself, that the work contained herein is my own except where explicitly stated otherwise in the text, and that this work has not been submitted for any other degree or professional qualification except as specified.

James Cameron McNatt

Contents

Figures and Tables

Figures

Tables

Nomenclature

Abbreviations

2D	Two-dimensions or two-dimensional
3D	Three-dimensions or three-dimensional
BC	Boundary condition
BEM	Boundary-element method
BVP	Boundary-value problem
CG	Center of gravity
DOF	Degree-of-freedom
PTO	Power take off
WEC	Wave energy converter

Mathematical Symbols

*	Complex conjugate
†	Complex conjugate transpose
$H_m^{(1)}$	Hankel function of the first kind of order m
$H_m^{(2)}$	Hankel function of the second kind of order m
I_m	Modified bessel function of the first kind of order m
J_m	Bessel function of the first kind of order m
K_m	Modified bessel function of the second kind of order m
Y_m	Bessel function of the second kind of order m

Constants

i	Imaginary 1
g	Gravitational constant

Coordinates

γ	Orientation angle of body or body coordinates
$\boldsymbol{x}$	Position vector
t	Time
$\{r, \theta, z\}$	Cylindrical coordinates
$\{x, y, z\}$	Cartesian coordinates (3D)
$\{x, z\}$	Cartesian coordinates (2D)
$\left\{\hat{\boldsymbol{i}}, \hat{\boldsymbol{j}}, \hat{\boldsymbol{k}}\right\}$	Unit vectors in Cartesian coordinates

Nondimensional Quantities

$\bar{a}$	Nodimensional variable
ϵ	Wave slope
μ	Size of body motions relative to wavelength

Wave Symbols

β Plane wave direction

λ Wavelength

$\mathcal{E}_f^P$ Wave energy flux (per meter crestwidth of a plane wave)

ω Wave frequency (radial)

ρ Fluid density

ε Wave phase

a Wave amplitude

a_m Progressive incident wave amplitude (m^{th} circular mode)

b_m Progressive wave amplitude due to body (m^{th} circular mode)

B_n Evanescent wave amplitude (n^{th} evanescent mode)

B_{mn} Evanescent wave amplitude (m^{th} circular mode, n^{th} evanescent mode)

c Phase velocity

c_g Group velocity

E Wave energy density (per area)

h Fluid depth

k Wave number

k_n Evanescent wave number

$\mathbf{B}^R$ Matrix of radiated wave coefficients

$\mathbf{D}$ Diffraction transfer matrix

$\mathbf{G}$ Force transfer matrix

$\boldsymbol{\Psi}$ Vector of wave basis functions

$\boldsymbol{a}$ Vector of progressive incident wave amplitudes

$\boldsymbol{b}$ Vector of progressive body wave amplitudes

ζ Free surface elevation (time dependent)

η Free surface elevation (time independent)

$p^{(t)}$ Fluid pressure (time dependent)

p Fluid pressure (time independent)

$\boldsymbol{U}$ Fluid velocity (time dependent)

$\boldsymbol{u}$ Fluid velocity (time independent)

Φ Velocity potential (time dependent)

ϕ Velocity potential (time independent)

$\mathcal{F}(\theta)$ Kochin function

σ Source strength

$f(z)$ Depth dependence function for progressive waves

$f_n(z)$ Depth dependence function for the n^{th} evanescent wave

$G(\boldsymbol{x}, \boldsymbol{X})$ Green's function for field point $\boldsymbol{x}$ due to a source at location $\boldsymbol{X}$

Body Symbols

$\mathcal{V}_b$ Body volume

ρ_b Density of body

m	Body mass
N	Number of DOF or in Chapter 6, number of bodies in array
Q_i	Number of DOF of body i
S_b	Body boundary
S_b^C	Submerged body surface with closing surface at $z = 0$
Q	Total number of DOF of array
$\boldsymbol{\chi}$	Body surface position (time dependent)
$\boldsymbol{V}$	Body surface velocity (time dependent)
$\boldsymbol{v}$	Body surface velocity (time independent)
$\boldsymbol{n}$	Surface normal vector
$\boldsymbol{n}_i$	Generalized motion normal (for motion i)
$\boldsymbol{n}_\xi$	Generalized motion normal (for motion ξ)
ξ	Body motion amplitude
ξ_i	Body motion amplitude in DOF i
$\boldsymbol{\mathcal{A}}$	Added mass matrix ($N \times N$)
$\boldsymbol{\mathcal{B}}$	Hydrodynamic damping matrix ($N \times N$)
$\boldsymbol{\xi}$	Body motions vector ($N \times 1$)
$\boldsymbol{C}$	Hydrostatic force matrix ($N \times N$)
$\boldsymbol{D}$	Mechanical damping matrix ($N \times N$)
$\boldsymbol{f}$	Force vector ($N \times 1$)
$\boldsymbol{K}$	Mechanical stiffness matrix ($N \times N$)
$\boldsymbol{M}$	Body mass-interia matrix ($N \times N$)
CW	Capture width
P	Power

Superscripts

^{A}	Ambient incident wave
^{D}	Diffracted
^{I}	Incident
^{P}	Plane wave
^{R}	Radiated
^{S}	Scattered
^{T}	Total (both submerged and dry) body surface or volume
$^{(t)}$	Time dependent
^{HD}	Hydrodynamic
^{HS}	Hydrostatic
^{ME}	Mechanical

Subscripts

γ	Of a body rotated by γ
c	Over a circular-cylindrical surface

h	Horizontal coordinates
i	DOF i or in Chapter 6, body i in the array
j	DOF j or in Chapter 6, body j in the array
m	Circular mode m
n	Evanescent mode n
q_i	DOF q of body i
z	Vertical coordinate
cg	Center of gravity

Chapter 1

Introduction

A body floating in a fluid interacts with and alters its environment. It is a bi-directional interaction: fluid forces act on and cause the body to move and the body changes the flow of the fluid. The physics of the fluid-structure interaction can be divided into a variety of categories at various temporal and spatial scales: pressure forces, viscous stresses, compressible effects, turbulence, steady flows, unsteady flows, oscillatory interfacial waves, and so on.

This thesis focuses on one category: inviscid, incompressible surface gravity water waves and their interaction with floating bodies. Further simplifications are made by assuming linear wave theory; that is, the wave heights and motions of bodies are small compared to the wave length, and waves and motions are time harmonic. While these assumptions and the fluid physics may seem limiting, for certain problems in ocean engineering, particularly for wave energy conversion, a linear-wave-theory computation is fast and reasonable approach to determine the dominant dynamics and kinematics. Furthermore, the simplifications of the physics do not necessarily mean that the mathematics or the resulting phenomena are simple; in fact, linear wave theory can yield complex problems and intriguing results.

The linear wave approach taken herein is the analysis of the problem using cylindrical spatial coordinates, $\{r, \theta, z\}$, which results in a series of circular waves of various orders that can be superimposed to create complex wave fields. The application of cylindrical coordinates to linear wave theory is not new. However, historically, they have been used almost solely to analyze axisymmetric geometries: circular lakes, cylindrical piles, etc. While in reality, the cylindrical solutions to the linear wave boundary-value problem (BVP) are useful general solutions for any finite sized geometry in three dimensions (3D).

The cylindrical solutions are in contrast to the ubiquitous Cartesian coordinate, $\{x, y, z\}$, solution: the long-crested plane wave. A plane wave is a solution to the BVP in 3D, but it can be considered a two-dimensional (2D) solution extended along a third orthogonal axis. Figure 1.1 shows a 2D wave, a 3D plane wave, and a plane wave in the FloWave wave tank (FloWave, 2015). Real water waves do not look like plane waves (except in

(a) 2D plane wave

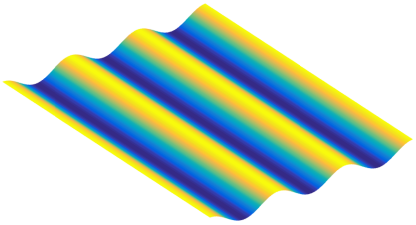

(b) 3D long-crested plane wave

(c) Plane waves in the FloWave wave tank. (FloWave, 2015)

Figure 1.1: The figures show computational 2D and 3D plane waves, and a plane wave in a wave tank.

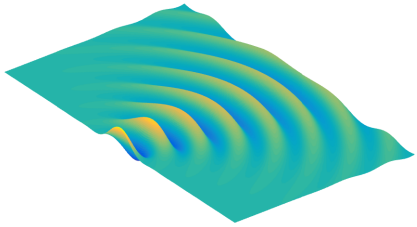

(a) 3D computational curved wave

(b) Ripples or short-crested waves (Unsplash, 2015)

(c) The circular waves created by a drop splashing into water (Bykst, 2015)

(d) Curved waves in a wave-body interaction from the experiments conducted in this thesis. See Chapter 5.

Figure 1.2: The figures show a computational and various real curved waves.

a wave tank); real waves have curved crests. Figure 1.2 shows a computational curved wave and three real curved waves. 1.2-b is a photograph of ripples, which is conceptually the same as short-crested seas; 1.2-c is the circular splash of a water drop; and 1.2-d is a photograph of a wave-body interaction from the experiments conducted in this thesis (see Chapter 5).

The cylindrical solutions are an efficient way to represent curved waves. In cylindrical coordinates, the waves radiated or scattered by a body can be represented accurately in the near field by the product of a finite number of cylindrical basis functions and coefficients. Likewise, plane waves can be used as a basis function to form curved waves, for example in the plane-wave formulation of a short-crested sea or with the use of a Kochin function, which is a continuous function in θ, that, with a plane-wave-like function in r, describes waves produced by a body, but is only valid in the far field.

One may think of the cylindrical-coefficient representation of the directional wave field as a sort of "frequency domain" description. That is, plane wave theory describes a directional wave with a continuous function of direction, while cylindrical wave theory uses a set of discrete values that are the amplitudes and phases of the directional function decomposed into sinusoidal components.

Why might one care about the waves that are radiated or scattered by the body? Typically, engineers and scientists are concerned about the effects of waves or wave forces *on* the body, rather than vice versa. However, these two relationships are obviously coupled. For example, the famous Haskind relation says that the wave forces on the body in a given degree-of-freedom (DOF) can be computed from the waves radiated by motion in that DOF (Newman, 1962). Recent work has shown that if one can (nearly) eliminate the scattered waves in a process known as cloaking, the body will experience no second-order drift force (see Newman (2014) and Section 2.4.5).

In the process of wave energy conversion, by the conservation of energy, as a wave energy converter (WEC) absorbs power, so too must energy be removed from the wave field. In linear wave theory, this power absorption occurs due to the destructive interference between the ambient incident waves and waves generated by the body.

One may also want to know the impact on the built or natural environment, whether it is positive or negative, of man-made structures such as breakwaters or wave farms. Linear wave theory can be used to determine the directional near-field wave field around such structures, which could be fed into other wave models such as phase-averaged models to propagate the effects over realistic bathymetry.

Arrays of floating or fixed bodies interact via waves that are scattered and radiated by each body. That is, the waves that are scattered by body one become incident waves on body two, which scatters them and sends the waves back to body one, and so on.

These types of interactions are important in the engineering analysis of man-made very large floating structures, in understanding the environmental progression of ice floe formation and breakup in the marginal ice zone, and in the power performance of wave farms composed of many WECs.

Array interactions is the one area where, historically, cylindrical waves have frequently been applied. Because using the cylindrical solution, the wave field of a floating body can be represented by finite length vectors of coefficients, once these coefficients have been determined for a given geometry, the array interaction problem can be solved with linear algebra. The multiple scattering theory developed by Kagemoto and Yue (1986) is extremely powerful. However, it has been applied mostly to cylindrical geometries. This is likely the result of several factors: 1) Kagemoto and Yue (1986) only demonstrated the computation with axisymmetric geometries and there may have been a misconception that it only applied to axisymmetric geometries; 2) the paper that extended their theory nicely to arbitrary geometries (Goo and Yoshida, 1990) is a not-well-known conference paper and required a custom boundary-element method code; and 3) perhaps there has not really been the need: many man-made structures are made up of, or at least can be approximated by, arrays of cylinders. Only recently has the computation of farms of WECs with non-cylindrical shapes become important.

Furthermore, the cylindrical solutions of the linear wave BVP are not generally taught to ocean engineers and scientists and so are used very little in practical applications. They are mathematically and conceptually more complicated than plane waves. In most cases, plane waves can be used to solve a given curved wave problem. For example, multiple plane waves traveling in different directions can represent a short-crested sea. Furthermore, a plane wave is a representation of a sea state where all of the energy is coherent and focused in one direction; mathematically speaking, there is an infinite amount of power in each wave crest (see Chapter 7). While in short-crested seas, there is a finite amount of power in each crest. In a sense, a long-crested plane wave is the worst case scenario for wave forces on an offshore structure, and so using plane waves in engineering analyses provides a safety factor.

However, just because the cylindrical solutions are not often used in practical applications, does not mean they do not have practical applications. As has been mentioned above, they can compactly and accurately represent the wave field of finite sized bodies; they are the only practical means to efficiently compute the wave interactions in large arrays of bodies; and as shall be discussed in Chapter 7, they are useful for understanding the power absorption of WECs in 3D.

1.1 Aims and objectives

The aim of this work is to develop practical methods for finding and applying the coefficients of the cylindrical solutions to the linear wave field. The cylindrical wave applications addressed herein are the analytical representation of floating body wave fields, the computation of multi-body wave interactions, and assessment of the performance of WECs.

A novel method is introduced for finding cylindrical coefficients of the scattered and radiated wave fields of a floating body, and is validated computationally and experimentally. The method is extended to find the diffraction transfer matrix, which is a linear operator of cylindrical coefficients necessary to solve the interaction problem. A new operator, the force transfer matrix, is presented, which enables the efficient computation of forces due to cylindrical incident waves. With the diffraction transfer matrix and the force transfer matrix, multi-body interactions can be performed, which are on the order of 1,000-10,000 times faster than the often-used direct method. Finally, a new approach for finding the hydrodynamic power and efficiency of a WEC in terms of cylindrical coefficients is developed.

In some respects, linear wave theory appears to be well established, and modern research tends to focus on nonlinear wave-body interactions. However, there are still advances to be made in linear wave theory with the cylindrical solutions; some of which are discussed throughout the thesis. In particular, the cylindrical wave energy analysis of 3D bodies in Chapter 7 is presented for the first time, and aids significantly in the understanding and design of WECs. Further research on the incident form of cylindrical waves could result in more efficient body and array computations in short-crested seas and a more general expression for hydrodynamic wave energy absorption efficiency.

1.2 Outline

An outline of the thesis is as follows:

- Chapter 2 reviews the literature on 1) the cylindrical solutions to the linear wave BVP, 2) multi-body interaction theory, and 3) the applications of the wave field of floating bodies.
- Chapter 3 provides necessary background theory, including the derivation of the solutions to the linear wave BVP in cylindrical coordinates.
- Chapter 4 presents a new method for finding the cylindrical coefficients for an arbitrary body using numerical or experimental measurements of the wave field over a circular-cylindrical surface that circumscribes the body. The method is demonstrated computationally.

- Chapter 5 validates the cylindrical surface method using experimental results.
- Chapter 6 introduces a new method for finding the diffraction transfer matrix based on the cylindrical surface method. Interaction computations are then demonstrated.
- Chapter 7, the final chapter of content, supplies a new formulation for wave power absorption based on a body's cylindrical wave coefficients and applies it to well-known and new problems. The concept of wave energy absorption efficiency is discussed as it relates to the cylindrical coefficients.
- Chapter 8 summarizes the work presented herein, providing concluding remarks and discusses potential future research.

1.3 Published papers

The following papers have been published from the research conducted in this thesis:

J. C. McNatt, V. Venugopal, and D. Forehand. The cylindrical wave field of wave energy converters. *International Journal of Marine Energy*, 3-4:e26–e39, December 2013a.

J. C. McNatt, V. Venugopal, and D. Forehand. The Cylindrical Wave Field of Wave Energy Converters. In *Proc. of the 10th European Wave and Tidal Energy Conf., Aalborg, Denmark*, Aalborg, Denmark, 2013b.

J. C. McNatt, V. Venugopal, and D. Forehand. A novel method for deriving the diffraction transfer matrix and its application to multi-body interactions in water waves. *Ocean Engineering*, 94:173–185, January 2015a.

J. C. McNatt, V. Venugopal, D. Forehand, and G. S. Payne. Experimental Analysis of Cylindrical Wave Fields. In *Proc. of the 11th European Wave and Tidal Energy Conf., Nantes, France*, 2015b.

Chapter 2

Literature Review

2.1 Introduction

The thesis focuses on the wave field around floating bodies, particularly with respect to solutions in cylindrical coordinates of the linear wave boundary-value problem (BVP), the wave interactions of multiple bodies, and wave energy absorption. The literature review reflects this; it begins with a review of general applications of the cylindrical solutions to the boundary-value problem (BVP). It then proceeds to a particular application of the floating body wave field: interactions between multiple bodies in proximity. Next, interesting features of the wave field are briefly discussed, and applications of the floating body wave field for wave energy absorption are examined. There is of course some overlap between the categories, and to the extent possible work is fitted into its most relevant section.

Equations are presented throughout the Literature Review, and to aid in the flow of the reading, not all nomenclature is described in this chapter. However, the nomenclature here is consistent with the rest of the thesis (not the documents it references), and so can be found in the Nomenclature Section.

2.2 Cylindrical solutions to the linear wave boundary-value problem

The cylindrical solutions to the linear wave BVP are generally found in the computation of the Green's function or for wave fields with cylindrical boundaries.

Lamb (1932), Chapter 8, considers modes of a circular basin of shallow water, and shows that the modes of the wave elevation are given by:

$$\zeta\left(r,\theta,t\right)=a_m J_m\left(kr\right)\left\{\begin{array}{c}\cos m\theta\\ \sin m\theta\end{array}\right\}\cos\left(\omega t+\epsilon_m\right) \tag{2.1}$$

where in this case, a_m and ϵ_m are real-valued. The boundary of the circular basin at $r = r_0$ corresponds to the boundary condition, $J'_m(k_n r_0) = 0$, which defines a set of roots, k_n. The most general case is then

$$\zeta = \sum_m \sum_n \left(a_m^c \cos m\theta \cos\left(\omega t + \epsilon^c\right) + a_m^s \sin m\theta \cos\left(\omega t + \epsilon^s\right)\right) J_m(k_n r) \tag{2.2}$$

Lamb (1932) shows nice contour diagrams of surface elevation of a circular body of water for $m = 0, 1$, as well as equations for surface elevation due to forcing, for example by tides. Lamb also presents another result for a circular boundary: by adding the two modes, $\cos m\theta$ and $\sin m\theta$, with different phases, $\epsilon^c = \epsilon^s - \frac{\pi}{2}$, one can create a wave that travels in a circle around the origin.[1]

In a textbook on partial differential equations, Sommerfeld (1949) shows how the integral form of the Bessel functions is derived from the wave equation by comparing the solution as an integral over plane waves to the solution in cylindrical coordinates. The time-independent formulations of the wave elevation are:

$$\eta = \int_\alpha^\gamma a(\beta)\, e^{\mathrm{i}kr\cos(\theta-\beta)} d\beta \qquad \text{plane} \tag{2.3a}$$

$$\eta = Z_m(kr)\, e^{\mathrm{i}m\theta} \qquad \text{cylindrical} \tag{2.3b}$$

where $Z_m(kr)$ is a yet-to-be-known function of the radial direction alone. Setting $a(\beta) = a_m e^{\mathrm{i}m\beta}$, where a_m is independent of direction, β, and making the substitutions $\beta = w + \theta$, $w_0 = \alpha - \theta$, $w_1 = \gamma - \theta$ leads to the integral

$$\eta = a_m \left\{ \int_{w_0}^{w_1} e^{\mathrm{i}kr\cos w} e^{\mathrm{i}mw} dw \right\} \cdot e^{\mathrm{i}m\theta} \tag{2.4}$$

If the dependency on θ of the integral inside the braces can be removed, it is clearly the function $Z_m(kr)$. This is done by taking the limits of integration to infinity in the complex plane. Different choices for limits and paths of integration, some of which were devised by Sommerfeld, result in the various types of Bessel and Hankel functions.

Another useful textbook is Methods of Theoretical Physics, Morse and Feshbach (1953), which develops in detail a variety of Green's functions and considers the wave equation in cylindrical coordinates, solving analytically a number of problems with cylindrical geometries.

In a seminal work, John (1950) approaches the linear wave-body BVP in a general

1. Probably the most common place to see the waves that Lamb describes, both the sloshing and rotating modes, is in your coffee cup as you walk down the hall in the morning.

sense. John puts forward a Green's function that is a summation of the 0^{th} order Hankel function to account for progressive waves and the 0^{th} order modified Bessel function of the second kind for evanescent waves. The work is probably best known for its consideration of the Sommerfeld radiation condition for outgoing waves, showing that there are unique solutions for bodies where the free surface lies above no portion of the geometry. These unique solutions emit only outgoing radiated and scattered waves. However, John is not able to show that there are unique solutions for arbitrary geometries, such as the seemingly simple case of a fully submerged body. In fact, later work shows that certain geometries do not necessarily have unique solutions, and can produce waves that propagate towards the origin. These may lead to trapped waves or wave cloaking, which shall be discussed briefly in Section 2.4.

Highly relevant to this thesis is the analysis in Section 5 of John (1950), which addresses the regions of the wave field described by "simple waves of order 0." The regions are bounded in the vertical direction by the free surface and a flat bottom, and the waves have a depth dependence of $f(z) = \cosh k(z+h)$. For these regions, the wave elevation is given by John's equation 5.12 as:

$$\eta = \sum_{m=-\infty}^{\infty} a_m J_m(kr)\, e^{\mathrm{i}m\theta} + \sum_{m=-\infty}^{\infty} b_m H_m^{(2)}(kr)\, e^{\mathrm{i}m\theta} \tag{2.5}$$

where the summation is over partial cylindrical waves. The first series represents incident waves, or as John terms primary waves, and the second summation are waves due to the body, secondary waves. John gives relationships between the coefficients, b_m, and the far-field analytical function of the body's waves, $\mathcal{F}(\theta)$, also known as the Kochin function. The incident waves are considered to have a general plane wave form with a directional amplitude function, $a(\beta)$, discussed by Sommerfeld. John shows that $a(\beta)$ does not have to be analytic, while $\mathcal{F}(\theta)$ does. John gives an expression for energy flux for the wave defined above through a circular-cylindrical boundary, which shall be discussed in section 2.5. A relationship between the "domain of regularity" of the body's waves and the coefficients, b_m is described; that is, the maximum radial extent of the body that generates the waves is directly related to the magnitude of its highest coefficient.

Havelock (1940) uses a continuous distribution of sources that were developed by Lamb (1923), defined by the 0^{th} order Hankel function, to represent the scattered waves due to a "ship" with vertical sides extending to an infinite depth. Havelock then considers the case of a vertical circular cylinder of infinite depth and formulates the complete solution as a summation over Bessel functions representing the incident plane waves and Hankel function modified by complex coefficients for the scattered waves. Due to the boundary condition on the cylinder, $\frac{\partial \phi^I}{\partial r} = -\frac{\partial \phi^S}{\partial r}$, it is straightforward to work out

the values of the coefficients of the scattered waves. Havelock goes on to find the linear pressure force, which depends only on the Bessel function of order $m = 1$, as well as the quadratic pressure force, which is also known as the second-order drift force.

From an era prior to widely available computational resources, The Mathematical Tables Project and The MIT Underwater Sound Laboratory (1946) gives a set of tables of the amplitude and phase of waves scattered and radiated by a cylinder for various orders, m, and various cylinder radii.

MacCamy and Fuchs (1954) extend the theory of Havelock (1940) to the case of a circular-cylindrical pile extending to the bottom in finite depth and compute the linear surge force, and both the linear and second-order moment on the pile about its base. Miles and Gilbert (1968) consider the case of a floating circular-cylindrical dock by separating the fluid domain into two regions, one under the dock, and one outside it where John's (1950) "simple waves of order 0" exist. They match the interior and exterior regions with a variational formulation, and compute forces on the dock as well as the directional scattered wave energy. Garrett (1971) solves the same floating circular dock problem with a simpler approach to find the excitation forces, and notes that Miles and Gilbert's (1968) work contains errors. Yeung (1981) develops analytical formulations for the heave, surge, and roll added mass and damping of a truncated circular cylinder.

To solve for axisymmetric bodies, Black (1975) expands John's (1950) Green's function into a Fourier series of Bessel functions (i.e. partial cylindrical waves), and shows that even though an infinite number of equations is generated, one for each angular mode, the heave and surge forces can be computed with only two equations, based on the 0^{th} and 1^{st} angular modes. Black makes the claim that the resulting Green's function does not contain a singularity, which Fenton (1978) shows to be incorrect. Fenton (1978) uses the same method as Black, but includes a numerical technique to remove the singularities and greatly accelerate the computation.

Davis (1976) applies the cylindrical solutions to evaluate the relationship between the scattered and radiated wave fields. For this, Davis separates the Bessel functions for incident waves into incoming and outgoing waves represented by Hankel functions. For axisymmetric bodies, Davis finds relationships equivalent to Newman's (1975) for two-dimensions (2D).

Hunt and Baddour (1981) develop a solution to the second-order diffraction force on a vertical circular cylinder using cylindrical coordinates and a linear incident plane wave. Because they take the incident wave to be linear and to satisfy the condition that the net energy flux of the diffracted system is zero, they construct the second order solution out of a combination of incoming and outgoing waves (Hankel functions of

the first and second kind respectively) whose net outgoing energy contribution is zero. By accounting for second-order diffraction forces, they find that the total force on the cylinder is increased by 14% compared to linear theory alone for some frequencies.

Newman (1996) also considers the second-order diffraction force on a circular cylinder using cylindrical solutions. Newman's work contains a review of related second-order work up to that point. Newman separates nicely different components of the second-order force: the second order forces due to a linear incident wave (as in Hunt and Baddour (1981)) and the forces due to a second order potential. The solution due of the second-order potential is complicated and involves Weber transforms. By considering the second-order incident potential, a second-order outgoing wave is allowed which is analogous to the first-order outgoing wave.

In order to assess the effects of ice floes on the ocean wave field, Meylan and Squire (1996) consider a single ice floe as a flexible circular flat plate with zero draft. The BVP then includes the fluid conditions as well as the governing equations of the flexible plate. To evaluate the problem, they consider two solutions. In the first, they capitalize on the cylindrical geometry by using the cylindrical eigenfunctions of a circular plate, and an infinite depth Green's function developed by Buchner (1993), which includes Bessel functions as well as a Struve function. The second is a computationally slower but more general solution, which uses a Green's function that satisfied the conditions of the flexible plate. Results for plates of various diameters and thickness are presented including figures showing the flexing of the plates, the waves generated by the plates, and polar plots of the scattered and radiated wave energy (See Figure 2.1). Meylan (2002) extends the zero draft flexible flat plate method to arbitrary geometries, for which a finite element method is used to solve for the flex modes and the entire wave body system is considered as the linear superposition of the diffraction and flexural mode effects.

As stated in Meylan and Squire (1996) and Meylan (2002), their work has the end goal of modelling large arrays of ice floes in the so-called Marginal Ice Zone. The modelling of the wave interactions between multiple floating bodies is an area where the cylindrical solutions to the linear wave BVP have been well adapted. These multi-body interaction approaches are discussed in the next section.

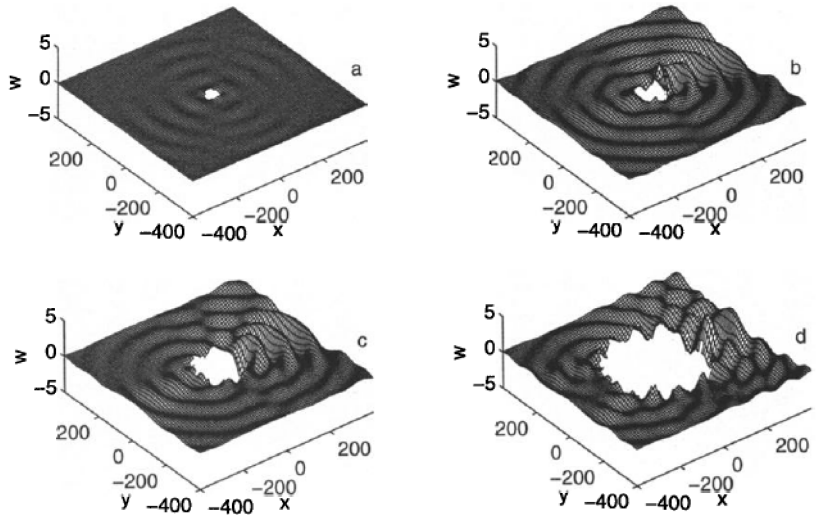

Figure 2.1: The figures from Meylan and Squire (1996) show wave patterns due to a flexible circular disk that represents a 1 m thick ice floe with diameters of: a) 50 m, b) 100 m, c) 200 m and d) 400 m. The incident wavelength is 100 m.

2.3 Multi-body wave interactions

Several scientific and engineering applications require an efficient means of computing the wave interactions between large arrays of floating bodies. In the Marginal Ice Zone near the Earth's poles, bi-directional interactions between ice floes and ocean waves take place - waves break up ice floes into smaller pieces and move them through the field, in some cases bunching them together to form new floes, and the ice floes redistribute waves through scattering and radiation and their elastic body motions dampen wave energy (e.g. Squire *et al.* (1995); Squire (2007)). An ocean engineering application is design of Very Large Floating Structures (VLFS) for expanding human usable space into the sea (e.g. Watanabe *et al.* (2004); Wang and Tay (2011); Kashiwagi (2000b)). The semi-submersible type VLFS consists of a large number of legs amongst which multi-body wave interactions are significant. This thesis examines ocean devices that absorb wave energy. To be cost effective, WECs must be placed in close proximity in farms in order to share infrastructure such as mooring points and electrical connections. In wave farms, multi-body wave interactions may have a significant impact on the power performance (e.g. Folley *et al.* (2012); Babarit (2013)).

There are a variety of techniques for computing or approximating the wave effects and interactions of large arrays of devices. In the field of wave energy, Budal (1977) was the first to consider the problem of a wave farm. Budal used the point-absorber theory, in which bodies are assumed small enough to neglect scattering, and so the only means of interaction is wave radiation. Garnaud and Mei (2010) divide the problem

into various scales, and for very large fields of bodies develop an analytical form to evaluate wave energy absorption and the effect of Bragg scattering. In channels, Linton and Evans (1992) and Linton and McIver (1996) apply the method of multipoles to solve the cylinder and channel boundary conditions. To model the scattering of waves by ice floes, Masson and Leblond (1989) develop a spectral transfer function based on linear wave theory. The direct panel method is also common, in which all the bodies in the array are represented by panels, and Green's theorem is applied to all body boundaries simultaneously to solve the problem. This is done for example by Borgarino *et al.* (2012a) to solve for 25 WECs using a fast multipole algorithm in the Green's function (Borgarino *et al.*, 2012b).

McIver (2002) gives a survey of the literature on the interaction of water waves in arrays until 2002, including various important phenomena. Martin (2006) is an excellent resource for the study of the scattering of waves by arrays and considers the problem for water waves as well as sound and electromagnetic waves.

Given the extent of the literature on multi-body wave interactions, the remainder of this section will focus on the multiple scattering approach of Kagemoto and Yue (1986), including the theory leading up to it, and significant developments in the theory following it.

One of the first approaches to the problem of wave scattering by many bodies is to consider the bodies as "weak scatterers" so that only the scattering of the incident wave is considered. Twersky (1952) develops the idea of "multiple scattering," in the context acoustics or electromagnetic waves in 2D. In Twersky's hierarchical theory, in the first order problem the incident wave is scattered, then in the subsequent problem, the waves scattered in the previous problem are scattered by the bodies, and so on. The problem can be solved to an infinite number of scatterings. Incident and scattered waves are given in a cylindrical Bessel and Hankel function form about each body's own coordinate system. The scattered waves of one body in its own coordinates are translated to the coordinates of another body by means of Graf's addition theorem for Bessel functions. The problem only considers circular geometries where the scattered coefficients could be computed in a straight-forward manner.

Ohkusu (1974) considers multiple scattering in the hierarchical manner of Twersky (1952) for the case of three circular-cylindrical floating docks. Ohkusu's interaction computations include evanescent waves and the propagating and evanescent scattered waves on a single cylinder are computed following the solution of Garrett (1971).

Spring and Monkmeyer (1974) develop a matrix method to evaluate the multiple scattering of bottom mounted vertical circular cylinders in water waves using cylindrical waves. The entire BVP is set up as a system of equations based on the boundary con-

ditions of the cylinders where the unknowns are the scattered wave amplitudes of each cylinder. Their method offers considerable advantage compared to Twersky's (1952) hierarchical method in that, the scattering amplitudes are solved exactly, while the same values would only be reached in the limit of scattering steps for the hierarchical method. Compared to Ohkusu (1974), evanescent wave are neglected because the geometries are bottom mounted cylinders. If the summation of the scattered coefficients is truncated, taken from $-M$ to M , and N is the number of bodies, then the number of unknowns is $N\,(N-1)\,(2M+1)$.

Simon (1982) also develops a matrix method for computing multiple scattering, particularly to examine the problem of wave energy absorption in a wave farm. The chief assumption is that the curved scattered waves of bodies in the array can be represented as locally plane waves at other bodies, where the amplitude of that plane wave is given by the 0^{th} order Bessel function of the curved wave. Another significant assumption is that all bodies are axisymmetric, so that directional dependence in the relationship of one body to another is removed. Simon's method is conceptually similar to that of Spring and Monkmeyer (1974) in that multiple unknown amplitudes are solved for simultaneously, but it reduces the number of unknowns considerably. For every pair of bodies, there are two unknowns which represent the amplitude of the scattered wave at each body due to the other body. The number of unknowns is $N\,(N-1)$.

McIver and Evans (1984) improve upon the plane wave approximation by adding an additional correction term based on an asymptotic form of the Hankel function for large arguments. They compare the computation with the correction to the original plane wave method as well as the exact method of Spring and Monkmeyer (1974). The method adds one more unknown at each body to Simon's (1982) method, making the total number of unknowns: $2N\,(N-1)$.

The multiple scattering method applied in this thesis is the very powerful method of Kagemoto and Yue (1986), which is exact within the limits of linear wave theory for finite water depth, accounts for propagating and evanescent modes, is solved with a system of equations, and can be applied to arbitrary geometries. The principal difference between the methods of Spring and Monkmeyer (1974) and Kagemoto and Yue (1986), is that in the interaction computation, Kagemoto and Yue's (1986) method does not solve the BVP problem per se, instead the scattering behaviour of each geometry is precomputed and represented by the so-called "diffraction transfer matrix". The diffraction transfer matrix is a linear operator that transforms a vector of incident cylindrical wave amplitudes, including incident evanescent waves into a vector of outgoing wave amplitudes, including evanescent modes. It is essentially found (prior to the interaction theory computation) by solving the linear wave BVP for each partial incident wave mode and finding the scattered wave coefficients. Because the BVP is not solved com-

pletely in the interaction theory (the diffraction transfer matrix being pre-computed), for L evanescent modes, the number of unknowns is: $N\,(L+1)\,(2M+1)$. Neglecting the evanescent modes for comparison with Spring and Monkmeyer (1974) and the plane wave method, the number of unknowns is: $N\,(2M+1)$.

Clearly a significant requirement of the theory of Kagemoto and Yue (1986) is to compute the diffraction transfer matrix. Kagemoto and Yue (1986) give an example of how to find the diffraction transfer matrix for an axisymmetric body and perform the computation with a hybrid element method. They give interaction results for pairs of cylinders, an array of four floating truncated cylinders and an array of 33 composite truncated cylinders. However, a method for finding the diffraction transfer matrix for an arbitrary geometry is not discussed.

Goo and Yoshida (1990) develop a notable method for computing the diffraction transfer matrix for an arbitrary geometry using a boundary-element method (BEM) and the Fourier series Green's function developed by Fenton (1978) and Black (1975). The essence of the method is that integral of the product of the body source strength distributions and cylindrical eigenfunctions can be used to isolate and find each outgoing cylindrical body wave amplitude. The terms of the diffraction transfer are found by solving for various incident cylindrical partial waves. The method is described in detail in Section 3.5.2.

Linton and Evans (1990) consider the bottom-mounted circular cylinder array of Spring and Monkmeyer (1974) and use an algebraic manipulation to greatly simplify the scattering problem. In their resulting system of equations, the number of unknowns is $N\,(2M+1)$. They compute first order forces and second order drift forces, and compare their results to the approximate method of McIver and Evans (1984).

Kagemoto (1992) considers the problem of how to minimize the total force on a large floating platform supported by multiple floating bodies using Kagemoto and Yue (1986). In the first case, he sets the partial derivatives of the total force equation with respect to each body's position to zero, but notes that as there is no means of applying constraints (to prevent the bodies from overlapping for example), which typically leads to trivial solutions. To include constraints, Kagemoto develops a nonlinear "force" function that includes the bodies' positions, which Kagemoto tries to minimize with a nonlinear search. Kagemoto and Yue (1993) also consider the problem of minimization, and reduce the problem of a very large number of floating bodies to a solution for an interior region, which is assumed infinite, that is matched to exterior regions with finite numbers of bodies.

In the context of wave energy, Mavrakos and McIver (1997) compare results for five cylindrical WECs operating under optimal motions using the multiple scattering method

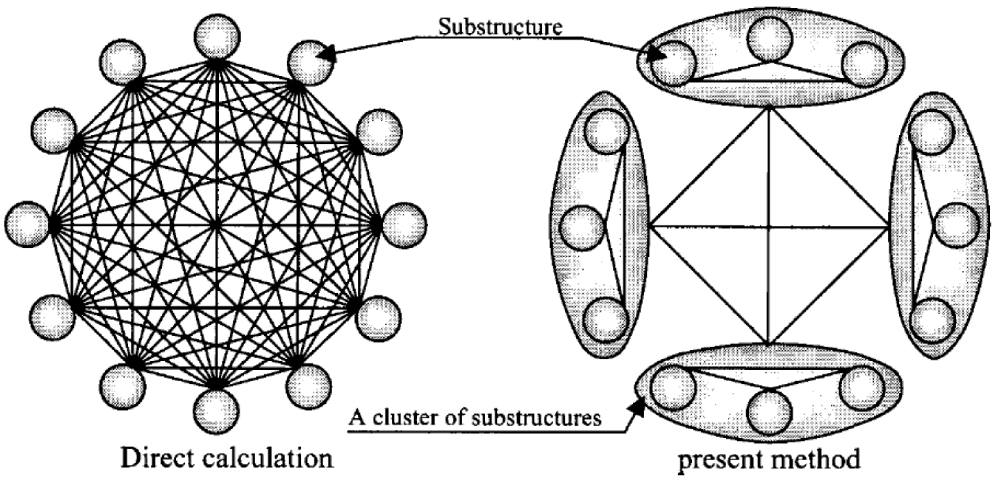

Figure 2.2: Diagram of the hierarchical interaction theory from Murai *et al.* (1999). Instead of directly computing the interactions between all bodies, the interactions within subgroups are computed to represent fictitious bodies and the interactions between the fictitious bodies are then computed to solve the entire problem.

of Ohkusu (1974), the plane wave method with a correction term (McIver and Evans, 1984) and the point absorber method (Budal, 1977).

For a VLFS, Kagemoto *et al.* (1998) use the interaction theory of Kagemoto and Yue (1986) with a plate model of the structure. Structural deformation is modelled by allowing each component sturcture-leg member to move, but with mechanical forces from adjacent members. They compare computational results to results from an experimental model, which consisted of 100 rectangular legs.

Yilmaz (1998) and Yilmaz and Incecik (1998) apply the analytical solutions of Garrett (1971) for a single truncated floating cylinder operating in heave to the interaction problem. They extend Garrett's (1971) method to include the effects of incident evanescent waves in the diffraction transfer matrix. Kagemoto and Yue's (1986) interaction theory is then used to compute simple arrays of cylinders. The results are checked against other numerical methods. Yilmaz *et al.* (2001) apply the method to four truncated cylinders and compared the results to experiments.

Murai *et al.* (1999) and Kashiwagi (2000a) develop a hierarchical interaction theory based on Kagemoto and Yue (1986) in which a large array of bodies is subdivided into smaller groups (see figure 2.2); the interactions at the group level are computed to form fictitious bodies, and the interactions between the fictitious bodies are computed to solve for the entire array. The diffraction transfer matrix of a fictitious body is found by use of an addition theorem that transforms the scattered wave amplitudes of each

body to amplitudes of the coordinates of the fictitious body.

Malenica (1999) extends Linton and Evans's (1990) method to second-order to compute forces and wave elevations on bottom mounted cylinders.

Chakrabarti (2000) uses the method of Goo and Yoshida (1990) as well as a semi-analytical method to compute the diffraction transfer matrix for cylinders and compares the values of the diffraction transfer matrix coefficients and forces on single cylinders and cylinder arrays.

Kashiwagi and Ohwatari (2002) presents spatially dense experimental measurements of the wave field (wave gauge measurements at 305 positions) around an array of four cylinders. They find that the experimental results agree quite well with linear theory, but the second-order effects are not in good agreement with the second order theory of Malenica (1999). Kagemoto *et al.* (2002) gives experimental results of the wave elevation in the vicinity of a long array of 50 cylinders, near frequencies of trapped modes, and finds that it is necessary to include viscous dissipation to the computational model of the cylinders to match the experimental results.

Peter and Meylan (2004a) extends Kagemoto and Yue's (1986) interaction theory to infinite water depth using an infinite depth Green's function, also developed by those authors in Peter and Meylan (2004b). They demonstrate how the diffraction transfer matrix is modified due to a rotation of a body. The method is then applied to ice floes modelled as thin plates. Peter *et al.* (2006) adds more information to the theory of Kagemoto and Yue (1986) including an effective method for computing the addition-theory transformation matrix, which depends on Bessel functions of very high orders, and a method for computing the far-field reflected and transmitted wave.

Siddorn and Eatock Taylor (2008) use Kagemoto and Yue's (1986) method with analytical solutions similar to Yeung (1981) for truncated circular cylinders operating in heave, sway and roll.

The application of interaction theory in the treatment very closely spaced bodies requires careful consideration. Graf's addition theorem imposes a restriction that the origin of body one must be outside the radius of a circle circumscribing body two. Furthermore, the solutions for body two are only valid outside of its circumscribed radius, which imposes a more strict limitation: no part of body one should be inside the circumscribed circle of body two. However, Kashiwagi (2008) challenges this requirement and considers an array of four rectangular bodies, which violates the second rule. Kashiwagi finds that the surge force was accurate because inaccuracies tend to cancel in matched pairs on the neighbouring bodies, but the heave force does not have this benefit and is not accurate. Kagemoto *et al.* (2010) considers this situation in more detail by dividing it into two questions, to use interaction theory: 1) does it matter if

there is water between the bodies? and 2) can the bodies violate the spacing requirement and still be computed accurately? They conclude that the answer to 1 is yes, because the behaviour of the fluid naturally converges to the case of a unified body as the bodies become close together. Like, Kashiwagi (2008), they decide that the answer to 2 is no, but is some cases, particularly for bodies with low ratios of length to width, reasonable results can be obtained.

To compute the performance of a wave farm, Child and Venugopal (2010) and Child (2011) apply the method of Yilmaz and Incecik (1998) and Yilmaz (1998) on an array of five truncated cylinders operating in heave. Because of the speed of the computation, they are able to use a genetic algorithm to search for optimal configurations. Child and Venugopal (2010) only consider regular waves, but Child (2011) also considers the more realistic case of spectral seas. Also devised is a heuristic method for designing the layout of wave farms: the "parabolic intersection method," in which WECs are placed on the anti-nodes of partial standing waves formed by the scattering or radiation of other cylinders. In the horizontal plane, these anti-nodes take on a parabolic shape.

Also to evaluate wave farms, Singh and Babarit (2014) revisit the plane wave method. In their work, the amplitudes of incident plane waves on body one due to other bodies are given by the potential due to the scattering of the other bodies at the location of body one. The system is solved iteratively until it converges on a solution. The potential for unit amplitude scattering is computed by means of a BEM allowing for arbitrary geometries to be employed.

The interactions between multiple bodies is not the only application of the floating body wave field. In the next two sections other applications and phenomena are considered.

2.4 The wave field of floating bodies

To analyze the effects of waves on a floating body, one may integrate the fluid forces over its wetted surface. However, a deeper understanding of the wave body interaction can be gained by examining the wave field as well. In this section, a brief review is given of three important linear wave field mathematical concepts, namely the Kochin function, the Haskind relation, and the relationship between scattered and radiated waves, and a description is given of two interesting wave phenomena, wave trapping, and wave cloaking. Wave energy absorption shall be discussed in section 2.5.

2.4.1 The Kochin function

In the far-field, there exists an asymptotic plane-wave-like formulation in separated polar coordinates of the scattered wave or any radiated wave:

$$\eta^{S,R} = \frac{e^{\mathrm{i}\frac{\pi}{4}}}{\sqrt{2\pi}} \frac{1}{\sqrt{kr}} e^{\mathrm{i}kr} \mathcal{F}^{S,R}(\theta) + O\left(r^{-3/2}\right) \tag{2.6}$$

where $\mathcal{F}^{S,R}(\theta)$ is a complex function of the angular direction around the body and is commonly known as the Kochin function (c.f. Wehausen (1971)). The Kochin function is analytic, and can be directly related to the cylindrical coefficients of the scattered or radiated wave field (John, 1950). It can be used to compute wave forces on a body, as shall be discussed in the next section, as well as wave power absorbed by a body, which shall be discussed in section 2.5, and it has been suggested as a means of coupling wave body models with other wave models (Babarit *et al.*, 2013).

2.4.2 The Haskind relation

The Haskind relation, made famous by Newman (1962), says that the excitation force in a given degree of freedom due to an incident wave can be found without solving the diffraction problem, but instead by only knowing the wave radiation characteristics (i.e. the Kochin function) of motion in the absence of incident waves. This is shown by Newman (1962) with an application of Green's theorem using the scattered wave potential and the radiated wave potential in the mode of interest. It means that in practice, computational time can be saved by only solving the radiation problems, and finding the excitation force via the Haskind relation.

2.4.3 Scattered and radiated wave relationships

Like with the Haskind relation, Green's theorem can be used to find various relationships between different wave fields: the scattered and the radiated, two scattered, or two radiated. Newman (1975) devises relationships in 2D for the forward and backward radiated waves and the reflected and transmitted scattered waves. Newman (1976) considers the same problem in three-dimensions (3D) using Kochin functions. Newman's results are reviewed by Mei *et al.* (2005), Chapter 8. As discussed in section 2.2, Davis (1976) shows similar results using the cylindrical wave field of an axisymmetric body.

A few results from these relationships shall be given from Mei *et al.* (2005). The relationship between two radiation problems can give the added mass or damping coefficient, shows that the added mass and damping matrices must be symmetric, and that all radiated power must be positive. Considering two diffraction problems, in 2D, it can be shown that the transmission coefficient is independent of wave direction,

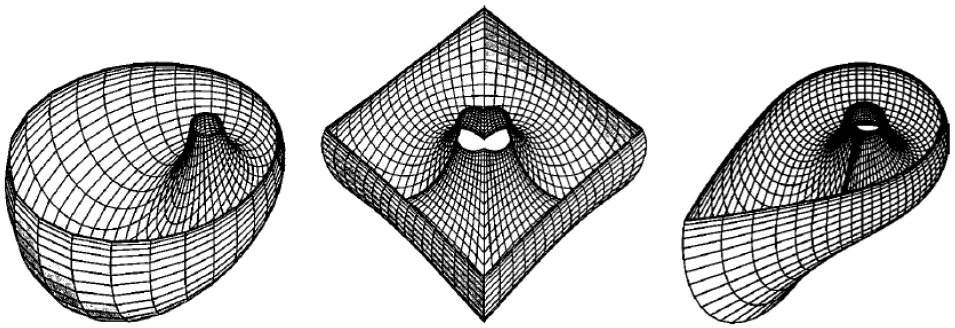

Figure 2.3: From McIver and Newman (2003), examples of asymmetric structures in which trapped wave modes occur

even if the body is asymmetric, and in three dimensions, the magnitude of the total scattered energy can be directly related to the amplitude of the scattered wave in the same direction as the incident. Consideration of a scattered wave and a radiated wave, gives the Haskind relation as well as the result in two or three dimensions, that for symmetric bodies the phase angle of the surge and pitch radiated waves must be the same or 180 degrees out of phase. This means that if the amplitudes of the waves are the same, a body can move simultaneously in surge and pitch without generating any waves. This phenomenon is referred to by Pizer (1993) as a "wave free" mode, and is incapable of absorbing energy.

2.4.4 Wave trapping

John (1950) was unable to show mathematically uniqueness for an arbitrary geometry in the water wave problem with the Sommerfeld radiation condition. What this means physically is that for some geometries, body waves may radiate towards the origin, or both towards and away. In the frequency domain problem, waves exist over an infinite time span, and so waves that propagate away from the body contain an infinite amount of energy. Trapped modes, on the other hand, contain a finite amount of energy. Because they cannot carry energy away from the body, under forced conditions, trapped modes can lead to high resonant wave peaks at certain field locations, which may cause practical engineering problems.

Trapped modes can occur on beaches with very small slopes, on bodies in a canal (Ursell, 1951, 1987), in arrays of vertical cylinders (Evans and Porter, 1997a,b), or bodies with an internal "moon pool" (McIver and Newman, 2003). A selection of these bodies is shown in Figure 2.3. McIver (2005) gives a detailed explanation of the trapping problem and shows that for floating bodies the scattered wave trapping, radiated wave trapping, and the body resonance occur at different frequencies, which mitigates the effect of resonant wave peaks due to trapping in a moving body.

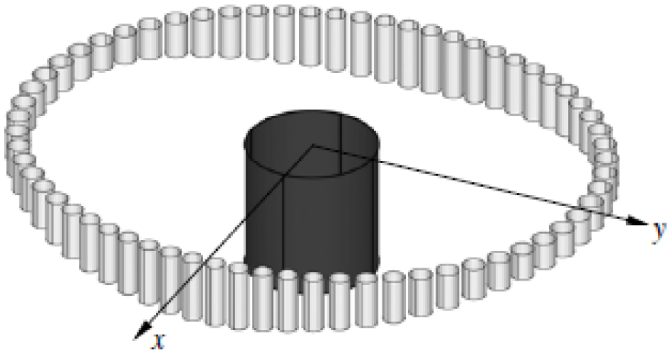

Figure 2.4: From Newman (2014), a particular arrangement of cylinders that can produce an almost completely cloaked body at a given frequency

2.4.5 Wave cloaking

Cloaking is a fascinating phenomenon where the physics of waves is used to make an object invisible to an observer in the far field. In optics, waves can be refracted around a structure to make it nearly (although not completely) invisible (Leonhardt, 2006). In water waves, a body is surrounded by another structure, so that in the region outside of the bodies, the diffracted wave field, looks like the incident.

Cloaking can be accomplished by a selection of particular bathymetry (Porter and Newman, 2014) or by surrounding a central body with other bodies (Newman, 2014) - see Figure 2.4. Besides being a curiosity, cloaking could have a practical application in that a cloaked floating body would not experience a second-order drift force (Newman, 2014). For a given geometric arrangement, cloaking only occurs at a single frequency, however near-cloaking and the effect on forces is more broad-banded. Newman (2014) points out that because the incident wave is the same in both the front and the back of the structure, if time were reversed, the body would be cloaked from the other direction as well. From this, he deduced that cloaked bodies must have fore and aft symmetry in plane waves. McIver (2014) studies the problem in detail and shows that bodies which have unique solutions of outgoing waves as given by John (1950) could not experience cloaking, and so, like wave trapping, cloaking is related to non-uniqueness.

In this section, various facets of the wave field around floating bodies were considered. In the next section, a particular aspect shall be considered in more detail: wave energy absorption.

2.5 Waves and wave energy absorption

> The physical law of conservation of energy requires that the energy-extracting device must interact with the waves such as to reduce the amount of wave energy that is otherwise present in the sea. (Falnes, 2007)

Budal and Falnes (1975), in the early seminal work on wave energy, note on their WEC:

> Thereby, in a very efficient way, a secondary, ring-shaped, outgoing wave is generated, which interferes with the incoming wave in such a way that the resulting transmitted wave carries with it less energy that the incoming wave does.

To absorb wave energy, a WEC alters the wave field in a manner that follows a particular pattern. The wave energy absorbed by a WEC can be measured from the wave field itself, and it seems that an improved understanding of the WEC wave field can aid in the design of more effective devices. The following section discusses literature where the wave field is used to understand or compute wave energy absorption.

In 2D, the effect of energy absorption in linear wave theory can be understood as the destructive interference of the incident and scattered waves with the body's radiated waves. There is a finite amount of incident wave energy, which can be either absorbed completely or fractionally, giving a clear-cut measure for wave power absorption efficiency. In early works, both Mei (1976) and Evans (1976) compute the efficiencies of wave absorption from the waves, and demonstrate 100% energy absorption. Ogilvie (1963) shows that a fully submerged horizontal circular cylinder moving in surge and heave can generate a wave that propagates in only one direction. Evans (1976) uses this effect to design a WEC in 2D, known as the "Bristol Cylinder," where the unidirectional radiated wave cancels the incident wave and absorbs 100% of the incoming energy. In Salter (1974), the famous "Duck" is described, which being asymmetric, can radiate a wave in one direction, and was found experimentally to have an efficiency of 80% for 2D.

In 3D, the means of wave energy absorption is the same: that is, the radiated waves destructively interfere with the incident and scattered waves. However, radiated and scattered waves are directionally dependent and decay with radial distance, while the incident wave is usually a long-crested plane wave which is unidirectional and spatially uniform in magnitude. Furthermore, bodies are finite-sized and the wave field is infinitely large. All of which makes understanding energy absorption in 3D conceptually more challenging. Indeed, the efficiency of wave energy absorption in three dimensions is not really defined.

A common means of characterizing the wave energy absorption through the wave field in 3D is the capture width (CW) or relative capture width (RCW). The CW is a measure of power absorption with units of length, and is the ratio of the power absorbed by the

device to wave power per crest-width of a long-crested plane wave. Budal and Falnes (1975) are the first to describe wave power absorption using capture width, though they call it the "absorption length." The RCW is the CW normalized by the width of the body, and it is first used by Evans (1976) who calls it the "absorption length ratio".

Although it may appear to be, the RCW is not a measure of efficiency. It can obtain values greater than 1 (Evans, 1976), which if it were an efficiency would indicate greater than 100% energy absorption, which does not make physical sense. That the RCW can achieve values greater than 1 arises from the ability of a WEC to pull wave energy in from surrounding areas. This occurs because waves diffract and move latterly from areas of higher energy to those of lower, in particular to the sink created by a WEC. This is the same process that allows a radio antenna consisting of a thin metal rod to absorb a finite amount of electromagnetic power. Antennas are often specified by their effective aperture or area (Stutzman and Thiele, 1998), a measure analogous to the CW of a WEC.

Several authors compute power absorbed by a WEC through its wave field in 3D based on the Kochin Function. Using the Haskind relation, Evans (1980) defines a relationship for optimal CW based on the angular dependence of the WEC's radiated waves:

$$CW_{max} = \frac{\lambda \left|\mathcal{F}\left(\beta\right)\right|^2}{\int_{-\pi}^{\pi} \left|\mathcal{F}\left(\theta\right)\right|^2 d\theta} \tag{2.7}$$

where $\mathcal{F}\left(\theta\right)$ is the Kochin function of the total radiated wave. The numerator represents the total amount of energy propagating in the direction, β, of the incident wave and the denominator represents the integral of the radiated energy over all directions. The CW is proportional to λ, the wavelength. To increase the CW, one wants to increases the numerator and/or reduce the denominator. As Evans (1980) states: "it is clear that a good wave absorber is a body which has the ability when making waves, to concentrate the wave energy along a narrow sector rather than distribute the energy evenly over all angles. The ideal body would be such that $\mathcal{F}\left(\theta\right) = \delta\left(\theta - \beta\right)$ which gives an infinite capture width." It appears that the optimal absorption of an incident plane wave, which, mathematically, has an infinite amount of power, is to absorb all of the power.

Newman (1976) uses Green's theorem and the Kochin function to derive a variety of relationships between radiated and scattered waves, in particular, he gives power absorption in terms of the Kochin functions for the total radiated and scattered wave field as well as for the radiated wave alone. Farley (2012) considers in more detail Newman's expression that uses both the scattered and radiated waves, which Farley calls the "generated wave". Farley says: "The waves emitted by the WEC inevitably propagate away from it. Therefore, they can only interfere usefully with some part of the original wave which is also propagating away from the WEC." Here, Farley is

referring to is a destructive interference or wave cancellation process. Farley points out that Newman's other expression (used extensively in Newman (1979)), shows that the radiated wave that propagates in the opposite direction of the incident is critical to absorbing power, which seems to contradict Farley's assessment. The expressions for capture width given by Farley and Newman are:

$$CW = -\lambda \left(2\mathrm{Re}\left\{ \mathcal{F}\left(\beta\right) \right\} + \int_{-\pi}^{\pi} \left| \mathcal{F}\left(\theta\right) \right|^2 d\theta \right) \qquad \text{Farley} \quad (2.8a)$$

$$CW = -\lambda \left(2\mathrm{Re}\left\{ \sum_i \zeta_i \mathcal{F}_i^{R*}\left(\beta - \pi\right) \right\} + \int_{-\pi}^{\pi} \left| \sum_i \zeta_i \mathcal{F}_i^{R}\left(\theta\right) \right|^2 d\theta \right) \qquad \text{Newman} \quad (2.8b)$$

where $\mathrm{Re}\left\{ \mathcal{F}\left(\beta\right) \right\}$ in Farley's expression indicates the portion of the total radiated and scattered wave traveling in the direction of the incident plane wave, and $\mathrm{Re}\left\{ \sum_i \zeta_i \mathcal{F}_i^{R*}\left(\beta - \pi\right) \right\}$ in Newman's expression is the total radiated wave due to all modes of motion travelling in the opposite direction of the incident plane wave, and * denotes the complex conjugate. These expressions are slightly different than those given in the original papers, because they are formed with the definition of the Kochin function given in this thesis (Eq. 3.93). In order to make the capture width positive and maximize it, the first term in each expression must be negative and large, as the integral term in each equation must be positive. The expression given by Evans (1980) can be obtained from Farley's expression, by taking $\mathcal{F}\left(\theta\right) = A\hat{\mathcal{F}}\left(\theta\right)$, where A is a complex amplitude and $\hat{\mathcal{F}}$ is the Kochin function per amplitude. The capture width is maximized and equals Evan's CW_{max} when $A = -\hat{\mathcal{F}}^*\left(\beta\right) / \int_{-\pi}^{\pi} \left| \hat{\mathcal{F}}\left(\theta\right) \right|^2 d\theta$.

Mei *et al.* (2005) in Chapter 8 gives an excellent summary of Newman's (1976) results including the two expressions for wave power absorption shown above. However, they do not attempt to address the difference between the two. They go on to present a dimensionless parameter: $k \cdot CW$, where k is the wave number, and they suggest that it "is clearly a measure of efficiency." Mei *et al.* (2005) also discusses power absorption through the interaction of the outgoing portion of the radiated wave with the outgoing ("diverging") portion of the incident wave in terms of the far-field form of cylindrical partial waves. They show that this relationship can be used to compute the heaving and surging point absorber capture widths, and that for a large body, such as a floating raft: "Heuristically, the radiated waves should be made to cancel the diverging part of as many partial wave modes in the incident wave as possible."

In the first work on WEC arrays, Budal (1977) uses the combined far-field radiation patterns of all devices, and an application of Green's theorem to compute the power performance, which results in an equation very similar to those of Farley (2012) and Newman (1976). All of these works use the far-field form of the cylindrical representation

of the WEC wave field to compute wave energy absorption, and result in complimentary equations.

Other works apply or examine the wave field of WECs, although not necessarily to compute energy absorption. Folley and Whittaker (2009) produce polar plots of the total radiated wave field for four different wave energy converter array arrangements. The plots show the focusing effect mentioned by Evans (1980), and are not surprisingly similar to polar plots produced for the analysis of radio antennas (Stutzman and Thiele, 1998). McNatt (2012) examines the wave field generally and gives an expression for the power through a circle on the free-surface of the wave field in terms of pressure and velocity, and then computes power though the wave field for WECs using results from the BEM, WAMIT (WAMIT, 2012). In order to give a generic assessment of generalized shapes and consider motion amplitude limitations due to volume, Stansell and Pizer (2013) compute power from the wave field by means of the velocity potential. They demonstrate that a line of heaving elements can focus the wave to increase power absorption.

Very little work has been done on wave energy absorption using the full cylindrical linear wave solutions (i.e. not just the far-field solutions.) As discussed in Section 2.2, John (1950) gives an expression for power through the wave field directly in terms of the coefficients of the incident wave and those of the outgoing scattered and radiated waves. John derives this by first noting that the power through the wave field can be computed on a circular control surface, independent of its radius, and then by considering the far-field form. John's expression for power is:

$$\mathcal{F} = \frac{\rho\omega}{C_0} \sum_{m=-\infty}^{\infty} \left(b_m b_m^* + \frac{1}{2} a_m b_m^* + \frac{1}{2} a_m^* b_m \right) \tag{2.9}$$

where, C_0 is a constant, a_m are the coefficients of the incident waves, b_m are the coefficients of the scattered and radiated waves. John (1950) does not attempt to compute wave energy absorption by a WEC, but John uses the result to show that the radiated wave alone emits power and that the incident wave alone has zero net energy flux.

Wypych *et al.* (2012) and Wypych (2012) apply cylindrical solutions to the understanding of wave energy absorption for heaving and surging point absorber-type WECs. They take the 0^{th} order cylindrical partial wave to be the wave generated by a heaving point absorber, and the 1^{st} order cylindrical wave to be the wave generated by a surging point absorber (see Figure 2.5), and compute the optimal capture widths given originally by Evans (1976) for heaving and surging point absorbers interacting with long-crested plane waves as $CW = \frac{\lambda}{2\pi}$ and $CW = \frac{\lambda}{\pi}$ respectively. They also present results from experiments that show that the waves around a heaving and surging sphere were

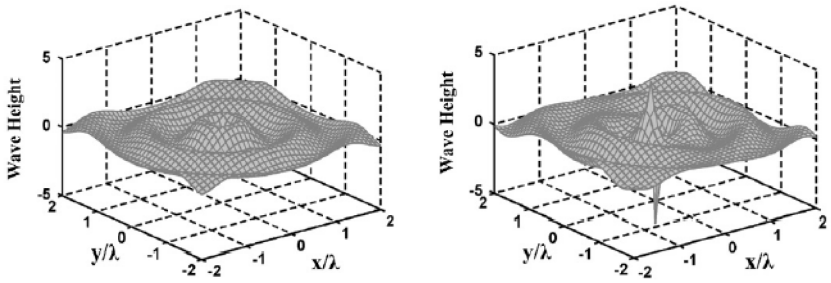

Figure 2.5: From Wypych *et al.* (2012), 0^{th} and 1^{st} order cylindrical waves used to compute wave power absorption by heaving and surging point-absorber type WECs.

primarily cylindrical heaving and surging waves respectively, with the biggest differences being higher-order effects at twice the harmonic frequency.

2.6 Summary

In summary, cylindrical solutions to the linear wave BVP are not new, but for single body computations have been mostly used to compute cylindrical shapes. Because the waves radiated and scattered by a body in 3D are essentially circular, a very powerful application of cylindrical waves is in finding the interaction between many floating bodies. Again, almost all studies used cylindrical shapes. Interesting phenomena of the wave field of floating bodies have been shown and the wave field can be used to compute quantities of interest, in particular wave energy absorption. However, for the most part, wave energy absorption computed from the wave field has been computed with the far-field wave.

There are gaps in the body of knowledge with regards to the application of the cylindrical solutions to bodies with arbitrary shapes. Very little has been done to compute the wave field of and evaluate the multiple scattering between non-cylindrical geometries. Furthermore, there is no universally applicable method (i.e. applicable to any numerical or experimental setup. Goo and Yoshida's (1990) method requires the use of a BEM) for finding the cylindrical coefficients and diffraction transfer matrix for an arbitrary floating body. Finally, there has been only limited application of the cylindrical solutions to the problem of wave energy absorption.

Chapter 3

Theory

3.1 Introduction

This chapter lays the groundwork for the new theory developed later in the thesis, of which, the most important background material is the solution to the linear wave-body boundary value problem (BVP) in cylindrical coordinates. In Section 3.2, the general harmonic linear wave-body BVP is formulated from Euler's equations. In Section 3.3, the solutions to the BVP are given in two-dimensions (2D), and in Section 3.4 the solutions are given in three-dimensions (3D) both as a plane wave, and in terms of the eigensolutions in cylindrical coordinates. In Section 3.5, solutions using Green's theorem and Green's functions are discussed. Finally, in Section 3.6, quantities derived from the solutions, such as forces, motions, and power absorption are shown.

An aspect of this theory that differentiates it somewhat from others is that it focuses on *generalized motions* of the body surface rather than solely the standard 6 degree-of-freedom (DOF) rigid body motions. The generalized motions are defined by a vector that describes a displacement of the body surface as a function of space and time. These displacements may be the 6 DOF rigid body motions, which is well addressed by Newman (1977) and Mei *et al.* (2005); they could be motions due to a flexing plate (e.g. Meylan (2002)); or they could be defined as a generalized mode of motion (e.g. Newman (1979) or Newman (1994)). The focus on generalized motions primarily affects the formulation of linearity (Section 3.2.4), the hydrostatic matrix (Section 3.6.2), and the mass matrix (Section 3.6.3).

The chapter was written with the aid of Morse and Feshbach (1953), Newman (1977), Dean and Dalrymple (1991), Mei *et al.* (2005) and Munson *et al.* (2009).

3.2 The linear wave-body boundary-value problem

The linear wave-body BVP is one of the simplest formulations for computing the effects of waves on a body and the effects of the body on the wave field. Nevertheless, it provides meaningful results when the conditions of the assumptions are met, and its solutions can be complex and enlightening.

The primary assumptions of the linear wave-body BVP are:

1. The fluid is incompressible.
2. The fluid is inviscid.
3. The flow is irrotational.
4. Surface tension is negligible.
5. Fluid pressure is taken as gauge pressure relative to constant air pressure above the free surface.
6. In the area of interest, the sea floor is flat or is so deep that it can be considered infinite.
7. The amplitudes of the free-surface waves are small compared to the wavelengths and water depth.
8. Over the relevant time scale, body motions are small compared to the wavelengths.
9. Waves and body motions are harmonic and have existed for all time, which means that the amplitudes of waves, body motions, forces and so on are complex valued.

The assumptions can be nearly met by bodies floating in a wave tank or in the ocean, and the linear wave-body BVP is a good first approach to evaluating many ocean engineering problems.

3.2.1 Incompressible, inviscid, irrotational fluid

The governing equations for an incompressible and inviscid fluid are Euler's equations:

$$\nabla \cdot \boldsymbol{U} = 0 \qquad \text{Mass} \tag{3.1a}$$

$$\left(\frac{\partial}{\partial t} + \boldsymbol{U} \cdot \nabla\right) \boldsymbol{U} = -\nabla \left(\frac{p^{(t)}}{\rho} + gz\right) \qquad \text{Momentum} \tag{3.1b}$$

where $\boldsymbol{U}(\boldsymbol{x}, t)$ is the time-dependent fluid velocity vector, $\boldsymbol{x}$ is the position vector, and t is time; ρ is the fluid density; $p^{(t)}(\boldsymbol{x}, t)$ is the time-dependent fluid pressure; g is the gravitational constant; z is the vertical position.

Take the flow to be irrotational: $\nabla \times \boldsymbol{U} \equiv 0$. A vector field that is irrotational can be written as the gradient of a scalar function:

$$\boldsymbol{U} = \nabla\Phi \tag{3.2}$$

where $\Phi(\boldsymbol{x}, t)$ is the velocity potential as a function of space and time.

The mass equation can be rewritten as Laplace's equation:

$$\nabla^2\Phi = 0 \tag{3.3}$$

which is sufficient to govern the motion of the fluid in the domain.

Considering the momentum equation, by the vector identity:

$$(\boldsymbol{U}\cdot\nabla)\,\boldsymbol{U} = \frac{1}{2}\nabla(\boldsymbol{U}\cdot\boldsymbol{U}) - \boldsymbol{U}\times(\nabla\times\boldsymbol{U}) \tag{3.4}$$

Because $\nabla\times\boldsymbol{U} = 0$, Eq. 3.1b becomes:

$$\frac{\partial\boldsymbol{U}}{\partial t} + \frac{1}{2}\nabla|\boldsymbol{U}|^2 + \nabla\left(\frac{p^{(t)}}{\rho} + gz\right) = 0 \tag{3.5}$$

Substituting in the velocity potential (Eq. 3.2) one gets:

$$\nabla\left(\frac{\partial\Phi}{\partial t} + \frac{1}{2}|\nabla\Phi|^2 + \frac{p^{(t)}}{\rho} + gz\right) = 0 \tag{3.6}$$

which can be integrated to be:

$$\frac{\partial\Phi}{\partial t} + \frac{1}{2}|\nabla\Phi|^2 + \frac{p^{(t)}}{\rho} + gz = C(t) \tag{3.7}$$

where $C(t)$ is a time-dependent constant. This is the unsteady Bernoulli equation and it describes the forces due to the inviscid fluid.

3.2.2 The boundaries

The BVP is shown in 2D and 3D in Fig. 3.1. In both 2D and 3D, the boundaries and the boundary conditions (BCs) are essentially the same. In both, the vertical coordinate is z, and the horizontal coordinate, which in 2D is x, and in 3D is $\{x, y\}$ or $\{r, \theta\}$, shall be represented by the vector notation $\boldsymbol{x}_h$.

The boundaries are:

1. On the top - a moving free surface at $z = \zeta$, where $\zeta(\boldsymbol{x}_h, t)$ is the free surface (or wave) elevation as a function of the horizontal coordinates and time. The calm water free surface (i.e. in the absence of waves) is located at $z = 0$.

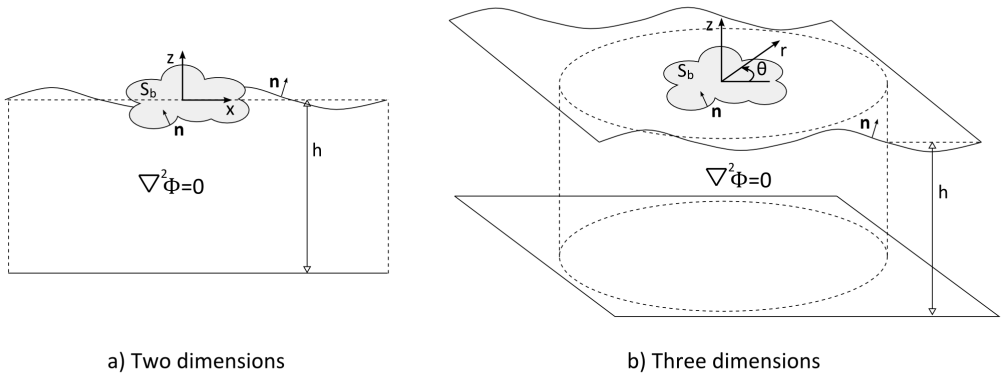

Figure 3.1: Diagram of the linear wave-body BVP in 2D and 3D

2. On the bottom - a flat bottom at $z = -h$, or infinite depth.
3. Lateral boundaries on the sides.
4. Solid moving boundaries on the surfaces of any bodies present.

The BC on all solid boundaries including the free surface, the bottom, and any bodies is the no penetration condition - the fluid cannot move through the boundary. The normal, $\boldsymbol{n}$, on the boundary points out of the fluid.

The free surface can be described by a function:

$$F_\zeta(\boldsymbol{x}, t) = z - \zeta = 0 \tag{3.8}$$

where the kinematic condition for a surface of the form of Eq. 3.8 is:

$$\left(\frac{\partial}{\partial t} + \boldsymbol{U} \cdot \nabla\right) F = 0 \tag{3.9}$$

Substituting in Eq. 3.8, results in the kinematic free-surface BC:

$$\left(\frac{\partial}{\partial t} + \boldsymbol{U}_h \cdot \nabla_h\right) \zeta = \frac{\partial \Phi}{\partial z} \qquad \text{on } z = \zeta \tag{3.10}$$

where $\boldsymbol{U}_h$ is the velocity in horizontal coordinates, and ∇_h is the horizontal gradient operator.

Above the free surface, one assumes a constant pressure of 0. Here, the effect of surface tension is also neglected. Using the Bernoulli equation (3.7), at $z = \zeta$, with $C(t) = 0$, one gets the dynamic free-surface BC:

$$\frac{\partial \Phi}{\partial t} + \frac{1}{2} |\nabla \Phi|^2 + g\zeta = 0 \qquad \text{on } z = \zeta \tag{3.11}$$

At the bottom boundary, the no penetration condition means that:

$$\frac{\partial \Phi}{\partial n} = 0 \qquad \text{on } z = -h \tag{3.12}$$

or for infinite depth:

$$\Phi \to 0 \qquad \text{as } z \to -\infty \tag{3.13}$$

The lateral BC is not necessary for harmonic waves when no body is present. When there is a body present, its radiated and scattered waves are governed by the Sommerfeld radiation condition, which shall be discussed in Section 3.2.4.

The simplest form of the linear wave BVP is the case of no body, for which, obviously, the body BC does not exist. However, when there is a body present, the BC is: on the surface of the body, the velocity of the fluid in the direction of the body normal is equal to the normal velocity of the body surface:

$$\frac{\partial \Phi}{\partial n} = \boldsymbol{V} \cdot \boldsymbol{n} \qquad \text{on } S_b^{(t)} \tag{3.14}$$

where $\boldsymbol{V}(\boldsymbol{x}, t)$ is the velocity of the body surface, $\boldsymbol{n}$ is the body surface unit normal, and $S_b^{(t)}$ is the location of the body boundary; all are functions of space and time.

This section has described the general time-dependent, nonlinear formulation for a body in an incompressible, inviscid, irrotational fluid. The governing equation, Laplace's equation, is a linear elliptic partial differential equation. However, the boundaries, in particular the free-surface and the body boundary, have nonlinear terms. In the next sections, by making additional assumptions, the problem shall be made linear.

3.2.3 Linear wave BVP (no body)

First, consider the BVP in the absence of bodies. One needs to know the appropriate conditions for which the problem can be made linear. To do so, form the nondimensional variables, indicated by an over bar:

$$\Phi = \frac{|a|\,\omega\lambda}{2\pi}\bar{\Phi} \tag{3.15a}$$

$$\boldsymbol{x}, h = \frac{\lambda}{2\pi}\bar{\boldsymbol{x}}, \frac{\lambda}{2\pi}\bar{h} \tag{3.15b}$$

$$t = \frac{1}{\omega}\bar{t} \tag{3.15c}$$

$$\zeta = |a|\,\bar{\zeta} \tag{3.15d}$$

where $|a|$, λ, and ω, characterize the wave amplitude ($|a|$ is used because a is complex valued), wavelength, and circular wave frequency respectively. Define the nondimensional wave slope as:

$$\epsilon = \frac{2\pi\,|a|}{\lambda} \tag{3.16}$$

In nondimensional variables, the BVP can be written as (showing only the finite depth form):

$$\bar{\nabla}^2\bar{\Phi} = 0, \qquad -\bar{h} < \bar{z} < \epsilon\bar{\zeta} \tag{3.17a}$$

$$\frac{\partial\bar{\Phi}}{\partial\bar{n}} = 0, \qquad \bar{z} = -\bar{h} \tag{3.17b}$$

$$\frac{\partial\bar{\zeta}}{\partial\bar{t}} + \epsilon\bar{\boldsymbol{U}}_h \cdot \bar{\nabla}_h\bar{\zeta} = \frac{\partial\bar{\Phi}}{\partial\bar{z}}, \qquad \bar{z} = \epsilon\bar{\zeta} \tag{3.17c}$$

$$\frac{\partial\bar{\Phi}}{\partial\bar{t}} + \epsilon\frac{1}{2}\left|\nabla\bar{\Phi}\right|^2 + \frac{2\pi}{\omega^2\lambda}g\bar{\zeta} = 0, \qquad \bar{z} = \epsilon\bar{\zeta} \tag{3.17d}$$

The wave slope is clearly an important parameter for characterizing the BVP. The nondimensional terms are all $O(1)$. For small wave slope, $2\pi a/\lambda \ll 1$, the terms that are modified by ϵ can be neglected. Furthermore, as the free surface is modified by ϵ, it can be expanded about its mean position of $\bar{z} = 0$.

By assuming small wave slope, all nonlinear terms disappear. Switching back to dimensional coordinates, the time-dependent linear wave BVP in the absence of floating bodies is:

$$\nabla^2 \Phi = 0, \qquad -h < z < 0 \tag{3.18a}$$

$$\frac{\partial \Phi}{\partial n} = 0, \qquad z = -h \tag{3.18b}$$

$$\frac{\partial \zeta}{\partial t} = \frac{\partial \Phi}{\partial z}, \qquad z = 0 \tag{3.18c}$$

$$\frac{\partial \Phi}{\partial t} + g\zeta = 0 \qquad z = 0 \tag{3.18d}$$

The final assumption is that the waves have existed forever and have a harmonic time-dependence, $e^{\mathrm{i}\omega t}$, where $\mathrm{i} = \sqrt{-1}$. The time dependent quantities can be written as the real part of products of a complex time-independent quantity and the time dependence:

$$\Phi(\boldsymbol{x}, t) = \mathrm{Re}\left\{\phi(\boldsymbol{x})\, e^{\mathrm{i}\omega t}\right\} \tag{3.19a}$$

$$\boldsymbol{U}(\boldsymbol{x}, t) = \mathrm{Re}\left\{\boldsymbol{u}(\boldsymbol{x})\, e^{\mathrm{i}\omega t}\right\} \tag{3.19b}$$

$$\zeta(\boldsymbol{x}_h, t) = \mathrm{Re}\left\{\eta(\boldsymbol{x}_h)\, e^{\mathrm{i}\omega t}\right\} \tag{3.19c}$$

$$p^{(t)} = \mathrm{Re}\left\{p(\boldsymbol{x})\, e^{\mathrm{i}\omega t}\right\} \tag{3.19d}$$

Finally, in terms of the time-independent quantities, the linear wave BVP in the absence of bodies is:

$$\nabla^2 \phi = 0, \qquad -h < z < 0 \tag{3.20a}$$

$$\frac{\partial \phi}{\partial n} = 0, \qquad z = -h \tag{3.20b}$$

$$\mathrm{i}\omega\eta - \frac{\partial \phi}{\partial z} = 0, \qquad z = 0 \tag{3.20c}$$

$$\mathrm{i}\omega\phi + g\eta = 0, \qquad z = 0 \tag{3.20d}$$

3.2.4 Linear wave-body BVP

The wave-body BVP is the same as for the case of no body, except with the additional boundary of the body, $S_b^{(t)}$, on which the BC is given by Eq. 3.14.

The analysis of the body BC can be aided by introducing a function to describe the body surface:

$$F_b(\boldsymbol{x}, t) = z - \psi_b^{(t)}(\boldsymbol{x}_h, t) = 0 \tag{3.21}$$

where, $\psi_b^{(t)}$ is a function of the horizontal coordinates, $\boldsymbol{x}_h$, and time, t.

Applying the kinematic condition for a surface, Eq. 3.9, one obtains:

$$\frac{\partial \psi_b^{(t)}}{\partial t} + \boldsymbol{V}_h \cdot \nabla_h \psi_b^{(t)} = V_z, \qquad z = \psi_b^{(t)} \tag{3.22}$$

where $\boldsymbol{V}_h$ and V_z are the horizontal and vertical velocities of the body surface respectively.

The body size and body motions can be characterized by a magnitude, $|\xi|$, which is proportional to the magnitude of the movement of the body surface. Forming nondimensional variables for the body:

$$\psi_b^{(t)} = |\xi|\, \bar{\psi}_b^{(t)} \tag{3.23a}$$

$$\boldsymbol{V} = |\xi|\, \omega \bar{\boldsymbol{V}} \tag{3.23b}$$

Define a nondimensional parameter that represents the magnitude of the body motions relative to the wavelength:

$$\mu = \frac{2\pi\, |\xi|}{\lambda} \tag{3.24}$$

The body BC in nondimensional variables is:

$$\frac{\partial \bar{\psi}_b^{(t)}}{\partial \bar{t}} + \mu \bar{\boldsymbol{V}}_h \cdot \bar{\nabla}_h \bar{\psi}_b^{(t)} = \bar{V}_z, \qquad \bar{z} = \mu \bar{\psi}_b^{(t)} \tag{3.25}$$

Here, the nonlinear term and the location of the boundary are proportional to μ.

The effect on the location of the boundary can be better understood by rewriting the BC as the function:

$$\bar{f} = \frac{\partial \bar{\psi}_b^{(t)}}{\partial \bar{t}} + \mu \bar{\boldsymbol{V}}_h \cdot \bar{\nabla}_h \bar{\psi}_b^{(t)} - \bar{V}_z = 0 \tag{3.26}$$

which can be expanded as a Taylor series about a mean body position:

$$\bar{f} = \bar{f}\big|_{z=\mu\bar{\psi}_b^{(0)}} + \mu \Delta \bar{z}\, \frac{\partial \bar{f}}{\partial \bar{z}}\bigg|_{z=\mu\bar{\psi}_b^{(0)}} + O\left(\mu^2\right) \tag{3.27}$$

where $z = \mu\bar{\psi}_b^{(0)}$ is a quasi-fixed position of the body surface at a time, $t = t_0$. In the expansion, all higher-order terms are modified by μ and can be neglected. So for small

body motions, only the quasi-fixed boundary needs to be considered.

In dimensional variables, the linear BC is:

$$\frac{\partial \psi_b^{(t)}}{\partial t} = V_z, \qquad z = \psi_b^{(0)} \tag{3.28}$$

Switching back to a form of the body BC similar to Eq. 3.14, the linear body BC, which holds for small body motions as compared to the wavelength is:

$$\frac{\partial \Phi}{\partial n} = \boldsymbol{V} \cdot \boldsymbol{n} \qquad \text{on } S_b \tag{3.29}$$

where S_b is the instantaneous body boundary position at $t = t_0$.

As the advective term is dropped by the linearization, the body velocity is then approximated by a time derivative:

$$\boldsymbol{V} = \frac{\partial \boldsymbol{\chi}}{\partial t} \tag{3.30}$$

where $\boldsymbol{\chi}$ is the position of the body surface and is a function of space and time.

If time were discritized, at each time-step the linear wave BVP could be solved for linear BCs given by Eqs. 3.18 and 3.29 at the body's instantaneous position as long as the motion of the body surface in each time step was small compared to the wavelength. For such an initial value problem, the body BC (Eq. 3.29) along with an initial condition are sufficient to solve the BVP (Noblesse and Yang, 2007).

Here, it is also worth considering the pressure on the surface of the body to determine whether the quadratic velocity term can be neglected. The pressure on the body surface as given by Bernoulli's equation (Eq. 3.7) is:

$$\frac{p^{(t)}}{\rho} = -\frac{\partial \Phi}{\partial t} - \frac{1}{2} \left| \nabla \Phi \right|^2 - gz \qquad \text{on } S_b^{(t)} \tag{3.31}$$

The velocity on the body surface can be formulated in orthogonal coordinates of the body normal vector and vectors tangential to the body:

$$\nabla \Phi = \{U_n, \boldsymbol{U}_\tau\} \tag{3.32}$$

where $U_n = \boldsymbol{U} \cdot \boldsymbol{n}$ is the normal velocity and $\boldsymbol{U}_\tau$ is the tangential velocity vector. By

the body BC, $U_n = \boldsymbol{V} \cdot \boldsymbol{n}$. Also, $\boldsymbol{U}_\tau = \nabla_\tau \Phi$, where ∇_τ is the gradient in the direction of the tangential coordinates. The quadratic velocity term can be written as:

$$\frac{1}{2} |\nabla \Phi|^2 = \frac{1}{2} |\nabla_\tau \Phi|^2 + \frac{1}{2} (\boldsymbol{V} \cdot \boldsymbol{n})^2 \tag{3.33}$$

Rewriting the pressure with the substitution of the normal-tangential velocity term and nondimensional variables, one gets:

$$\frac{2\pi}{|a|\,\omega^2 \lambda} \frac{p^{(t)}}{\rho} = -\frac{\partial \bar{\Phi}}{\partial \bar{t}} - \frac{1}{2} \epsilon |\nabla_\tau \Phi|^2 - \frac{1}{2} \frac{|\xi|}{|a|} \mu \left(\bar{\boldsymbol{V}} \cdot \boldsymbol{n} \right)^2 - \frac{g}{|a|\,\omega^2} \bar{z} \qquad \text{on } S_b^{(t)} \tag{3.34}$$

The tangential velocities are proportional to ϵ and the normal velocity is proportional to μ.

Under the assumptions that compared to the wavelength, both the wave amplitude and body motions are small, it is appropriate to neglect the quadratic terms. The dynamic pressure, which is the pressure proportional to Φ, on the body is:

$$p^{(t)} = -\rho \frac{\partial \Phi}{\partial t} \qquad \text{on } S_b \tag{3.35}$$

on the instantaneous surface of the body.

As was done in the BVP in the absence of a body, one assumes harmonic motions. The body position can be written as the product of a time independent quantity and a time dependence:

$$\boldsymbol{\chi}(\boldsymbol{x}, t) = \mathrm{Re}\left\{ \xi \boldsymbol{n}_\xi(\boldsymbol{x})\, e^{\mathrm{i}\omega t} \right\} \tag{3.36a}$$

$$\boldsymbol{V}(\boldsymbol{x}, t) = \mathrm{Re}\left\{ \boldsymbol{v}(\boldsymbol{x})\, e^{\mathrm{i}\omega t} \right\} \tag{3.36b}$$

where ξ is a complex amplitude of motion and $\boldsymbol{n}_\xi(\boldsymbol{x})$ is the *generalized motion* normal. $\boldsymbol{n}_\xi$ is a complex function of space and defines the direction of the body motions due a unit-amplitude motion, $\xi = 1$. Also: $\boldsymbol{v} = \mathrm{i}\omega \xi \boldsymbol{n}_\xi$.

In time-independent quantities, the body BC is:

$$\frac{\partial \phi}{\partial n} = \boldsymbol{v} \cdot \boldsymbol{n} \qquad \text{on } S_b \tag{3.37}$$

Under linear assumptions, a very useful decomposition can be performed. The velocity

potential can be formed as the sum of three velocity potentials, the incident, ϕ^I, the scattered, ϕ^S, and the radiated, ϕ^R:

$$\phi = \phi^I + \phi^S + \phi^R \tag{3.38}$$

The incident velocity potential is the velocity potential that exists in the absence of a body, and can be found by solving the BVP given in Section 3.2.3.

The sum of the incident and the scattered forms the diffracted velocity potential:

$$\phi^D = \phi^I + \phi^S \tag{3.39}$$

The diffracted velocity potential is defined as the velocity potential that satisfies the wave-body BVP for the body held fixed, $\boldsymbol{v} = 0$. For the diffraction problem the body BC is:

$$\frac{\partial \phi^I}{\partial n} = -\frac{\partial \phi^S}{\partial n} \qquad \text{on } S_b \tag{3.40}$$

Substituting the decomposition of the velocity potential, Eq. 3.38, into the body BC, Eq. 3.37, and using the relationship given by Eq. 3.40, one gets the radiated wave BC:

$$\frac{\partial \phi^R}{\partial n} = \boldsymbol{v} \cdot \boldsymbol{n} \qquad \text{on } S_b \tag{3.41}$$

The radiated wave velocity potential satisfies the BC for the body making small motions about its mean position. Because it is solved on a fixed body position, (i.e. it is linear), the body velocity can be written as the sum of velocities due to different independent DOF. Furthermore, for each DOF the velocity can be written as the product of a complex magnitude and the generalized normal vector:

$$\boldsymbol{v}(\boldsymbol{x}) = \mathrm{i}\omega \sum_{i=1}^{N} \xi_i \boldsymbol{n}_i(\boldsymbol{x}) \tag{3.42}$$

where N is the number of DOF, ξ_i is a complex amplitude of generalized motion i. The normal, $\boldsymbol{n}_i$, is the generalized motion normal function; it is the same as $\boldsymbol{n}_\xi$ except that it is for a particular motion in DOF i.

As addressed in the introduction of this chapter, the generalized motions are arbitrary functions. However, in order to help explain the concept, here the specific generalized normal vectors of the standard 6 DOF rigid body motions shall be given:

$$\boldsymbol{n}_1 = \hat{\boldsymbol{i}} \qquad \text{Surge} \tag{3.43a}$$

$$\boldsymbol{n}_2 = \hat{\boldsymbol{j}} \qquad \text{Sway} \tag{3.43b}$$

$$\boldsymbol{n}_3 = \hat{\boldsymbol{k}} \qquad \text{Heave} \tag{3.43c}$$

$$\boldsymbol{n}_4 = -z\hat{\boldsymbol{j}} + y\hat{\boldsymbol{k}} \qquad \text{Roll} \tag{3.43d}$$

$$\boldsymbol{n}_5 = z\hat{\boldsymbol{i}} - x\hat{\boldsymbol{k}} \qquad \text{Pitch} \tag{3.43e}$$

$$\boldsymbol{n}_6 = -y\hat{\boldsymbol{i}} + x\hat{\boldsymbol{j}} \qquad \text{Yaw} \tag{3.43f}$$

where, $\left\{\hat{\boldsymbol{i}}, \hat{\boldsymbol{j}}, \hat{\boldsymbol{k}}\right\}$ are the unit vectors in the Cartesian coordinate system. Here roll, pitch, and yaw are defined as being about the origin. Although $\boldsymbol{n}_i$ is not necessarily a normal of unit magnitude (it may be in some cases, such as the 6 DOF translational motions), it represents motion due to a unit amplitude $\xi_i = 1$.

The radiation potential can also be decomposed into velocity potentials due to each mode of motion of the body:

$$\phi^R = \sum_{i=1}^{N} \xi_i \phi_i^R \tag{3.44}$$

Here it should be noted, that ϕ_i^R does not have units of velocity potential but is rather a velocity potential per amplitude.

Finally for each mode of motion, there exists an independent BVP governed by the boundary condition:

$$\frac{\partial \phi_i^R}{\partial n} = \mathrm{i}\omega \boldsymbol{n}_i \cdot \boldsymbol{n} \qquad \text{on } S_b \tag{3.45}$$

The radiated and scattered waves also require another condition, which is an intuitive one, that states that their waves must radiate away from the body and disappear at infinity. At a sufficiently far distance, one sees only the incident wave. This is known as the Sommerfeld radiation condition and has slightly different forms for two and three dimensions:

$$\lim_{kx \to \pm\infty} \left(\frac{\partial}{\partial x} \pm \mathrm{i}k \right) \left(\phi^{S,R} - \phi^I \right) = 0 \qquad \text{2D} \tag{3.46a}$$

$$\lim_{kr \to \infty} \sqrt{kr} \left(\frac{\partial}{\partial r} + \mathrm{i}k \right) \left(\phi^{S,R} - \phi^I \right) = 0 \qquad \text{3D} \tag{3.46b}$$

where r is the radial coordinate.

Finally, the velocity potential of the linear wave-body BVP is:

$$\phi = \phi^I + \phi^S + \sum_{i=1}^{N} \xi_i \phi_i^R \tag{3.47}$$

and the wave-body BVP is:

$$\nabla^2 \phi = 0, \qquad -h < z < 0 \tag{3.48a}$$

$$\frac{\partial \phi}{\partial n} = 0, \qquad z = -h \tag{3.48b}$$

$$\mathrm{i}\omega\eta - \frac{\partial \phi}{\partial z} = 0, \qquad z = 0 \tag{3.48c}$$

$$\mathrm{i}\omega\phi + g\eta = 0, \qquad z = 0 \tag{3.48d}$$

$$\frac{\partial \phi^I}{\partial n} = -\frac{\partial \phi^S}{\partial n} \qquad \text{on } S_b \tag{3.48e}$$

$$\frac{\partial \phi_i^R}{\partial n} = \mathrm{i}\omega \boldsymbol{n}_i \cdot \boldsymbol{n} \qquad \text{on } S_b \tag{3.48f}$$

$$\sqrt{kr}\left(\frac{\partial}{\partial r} + \mathrm{i}k\right)\left(\phi^{S,R} - \phi^I\right) = 0 \qquad kr \to \infty \tag{3.48g}$$

where when no superscript on ϕ is used, the condition applies to all velocity potentials, and only the flat bottom and 3D radiation conditions are given.

3.3 Solutions to the BVP in two dimensions

In this section, general solutions to the linear wave-body BVP in 2D are given. They are general in that they do not directly satisfy the body BC for a particular body and are given with unknown complex coefficients. These are sometimes called eigensolutions or eigenfunctions. Solutions that satisfy the body BC will be discussed in Section 3.5.

Consider the solutions to Eqs. 3.48 in 2D - see Figure 3.1. The BVP can be solved by a separation of variables:

$$\phi(x, z) = X(x)\, Z(z) \tag{3.49}$$

Substituting this into Laplace's equation:

$$\frac{1}{X}\frac{d^2 X}{dx^2} + \frac{1}{Z}\frac{d^2 Z}{dz^2} = 0 \tag{3.50}$$

Because of the separation of variables, Eq. 3.50 can be written as two second order differential equations:

$$\frac{d^2X}{dx^2} + \kappa^2 X = 0 \tag{3.51a}$$

$$\frac{d^2Z}{dz^2} - \kappa^2 Z = 0 \tag{3.51b}$$

where κ^2 is some unknown constant. If $\kappa^2 > 0$, take $\kappa = k$, where k is real, and the general solutions are of the form:

$$X(x) = C_1 e^{\mathrm{i}kx} + C_2 e^{-\mathrm{i}kx} \tag{3.52a}$$

$$Z(z) = C_3 e^{kz} + C_4 e^{-kz} \tag{3.52b}$$

where, C_1, C_2, C_3, and C_4 are unknown complex coefficients.

The equation for X represents waves that travel to the left (negative x direction), for which take $C_1 = a^{(-)}$ or to the right (positive x direction), $C_2 = a^{(+)}$. It is not uncommon to refer to these waves as left running and right running respectively, and the real portion of the wave is:

$$\mathrm{Re}\left\{a^{(-)} e^{\mathrm{i}kx} e^{\mathrm{i}\omega t}\right\} = \left|a^{(-)}\right| \cos\left(kx + \omega t + \varepsilon^{(-)}\right) \qquad \text{left running} \tag{3.53a}$$

$$\mathrm{Re}\left\{a^{(+)} e^{-\mathrm{i}kx} e^{\mathrm{i}\omega t}\right\} = \left|a^{(+)}\right| \cos\left(kx - \omega t - \varepsilon^{(+)}\right) \qquad \text{right running} \tag{3.53b}$$

where $\left|a^{(-)}\right|$, $\left|a^{(+)}\right|$ are the magnitudes and $\varepsilon^{(-)}$, $\varepsilon^{(+)}$ are the phases of the left-running and right-running waves respectively. These are known as progressive waves and can be combined to produce various complete and partial standing waves.

k is a spatial frequency or wave number. The wave number is related to the wavelength by:

$$k = \frac{2\pi}{\lambda} \tag{3.54}$$

Considering the equation for Z and the bottom BC (Eq. 3.48b) leads to: $C_3 = C_4 e^{2kh}$, which when substituted back into the equation for Z results in a dependency with a single coefficient:

$$Z(z) = C_5 \cosh k(z+h) \tag{3.55}$$

where $C_5 = 2C_4 e^{kh}$. In the case of infinite depth, $Z \to 0$, as $z \to -\infty$. The only valid solution is:

$$Z(z) = C_3 e^{kz} \tag{3.56}$$

By the dynamic free surface BC (Eq. 3.48d):

$$\eta = -\mathrm{i}\frac{\omega}{g}\,\phi|_{z=0} \tag{3.57}$$

One would like the free surface elevation to be of the form of Eq. 3.53:

$$\eta = a^{(-)} e^{\mathrm{i}kx} + a^{(+)} e^{-\mathrm{i}kx} \tag{3.58}$$

which means the depth dependence should be unity at $z = 0$, and so the depth coefficients are: $C_5 = \frac{1}{\cosh kh}$ for finite depth and $C_3 = 1$ for infinite depth. Finally the depth dependence is:

$$f(z) = \begin{cases} \frac{\cosh k(z+h)}{\cosh kh}, & \text{finite depth} \\ e^{kz}, & \text{infinite depth} \end{cases} \tag{3.59}$$

where the notation $f(z)$ shall be used to indicate the progressive wave depth dependence function throughout the document.

Combining equations 3.57, 3.58, and 3.59, one gets the velocity potential for progressive waves:

$$\phi = \mathrm{i}\frac{g}{\omega} f(z) \left(a^{(-)} e^{\mathrm{i}kx} + a^{(+)} e^{-\mathrm{i}kx} \right) \tag{3.60}$$

The kinematic (Eq. 3.48c) and dynamic free surface (Eq. 3.48d) conditions can be combined as:

$$\omega^2 \phi - g\frac{\partial \phi}{\partial z} = 0 \tag{3.61}$$

Making the substitution of the depth dependence (Eq. 3.59), leads to the dispersion relation, which relates the wave number to the frequency and depth:

$$\omega^2 = \begin{cases} gk \tanh kh, & \text{finite depth} \\ gk, & \text{infinite depth} \end{cases} \tag{3.62}$$

Returning to Eqs. 3.51, when $\kappa^2 = 0$, leads to solutions: $X(x) = C_1 x + C_2$ and $Z(z) = C_3 z + C_4$, which represent uniform flows, not waves, and shall not be considered here.

When $\kappa^2 < 0$, for finite depth, one can set $\kappa = \mathrm{i}k_n$ which leads to:

$$X(x) = C_{n1} e^{k_n x} + C_{n2} e^{-k_n x} \tag{3.63a}$$

$$Z(z) = C_{n3} e^{\mathrm{i}k_n z} + C_{n4} e^{-\mathrm{i}k_n z} \tag{3.63b}$$

which are solutions that decay or grow exponentially in x, and are sinusoidal in z. Because of the exponential growth in x, the solutions are not valid in the absence of a body in the BVP. However, when a body is present, the singularity can essentially be hidden inside of its boundary and outside of the fluid domain.

For the solutions of Z in finite depth, following the same procedure as before, one gets the depth dependence:

$$f_n(z) = \cos k_n (z + h) \tag{3.64}$$

Here, normalizing the depth dependence to unity at $z = 0$ is not important because one cannot create a constant amplitude propagating wave. In fact, any amplitude that modifies the depth function will be defined by the body.

Applying the combined kinematic (Eq. 3.48c) and dynamic (Eq. 3.48d) free surface BCs, one gets another dispersion relation:

$$\omega^2 = -gk_n \tan k_n h \tag{3.65}$$

which has infinitely many roots, k_n. k_n are known as the evanescent wave numbers. Combining equations 3.63, 3.64, and 3.57, the velocity potential of finite depth evanescent waves is:

$$\phi = \mathrm{i}\frac{g}{\omega} \sum_{n=-\infty}^{\infty} \cos k_n (z + h) \left(B_n^{(-)} e^{k_n x} + B_n^{(+)} e^{-k_n x} \right) \tag{3.66}$$

where $B_n^{(-)}$ and $B_n^{(+)}$ are unknown coefficients.

For infinite depth, the solutions are not separable, and instead are an integral over a continuous distribution of coefficients. (e.g. Peter and Meylan (2004b,a))

$$\phi = \mathrm{i}\frac{g}{\omega}\int_0^\infty \left(\cos\kappa z + \frac{k}{\kappa}\sin\kappa z\right)\left(B^{(-)}(\kappa)\, e^{\kappa x} + B^{(+)}(\kappa)\, e^{-\kappa x}\right) d\kappa \tag{3.67}$$

Final, the general velocity potential for 2D waves is:

$$\begin{aligned}\phi =& \mathrm{i}\frac{g}{\omega} f(z)\left(a^{(-)}e^{\mathrm{i}kx} + a^{(+)}e^{-\mathrm{i}kx}\right) \\ &+ \mathrm{i}\frac{g}{\omega}\begin{cases}\sum_n \cos k_n (z+h)\left(B_n^{(-)}e^{k_n x} + B_n^{(+)}e^{-k_n x}\right) & \text{finite depth} \\ \int_0^\infty \left(\cos\kappa z + \frac{k}{\kappa}\sin\kappa z\right)\left(B^{(-)}(\kappa)\, e^{\kappa x} + B^{(+)}(\kappa)\, e^{-\kappa x}\right) d\kappa & \text{infinite depth}\end{cases}\end{aligned} \tag{3.68}$$

3.4 Solutions to the BVP in three dimensions

3.4.1 Solutions in Cartesian coordinates

In 3D, first consider the solution in Cartesian coordinates, $\{x, y, z\}$. Define another set of Cartesian coordinates: $\{x', y', z\}$, which is a rotation of the original coordinates by angle, β,:

$$x' = x\cos\beta + y\sin\beta \tag{3.69a}$$
$$y' = -x\sin\beta + y\cos\beta \tag{3.69b}$$

By a separation of variables in $\{x', y', z\}$:

$$\phi = X'(x')\, Y'(y')\, Z(z) \tag{3.70}$$

For which, a particular solution is $Y'(y') = 1$ and the 2D solution in $\{x', z\}$. This can written as a particular solution in the original coordinates $\{x, y, z\}$:

$$\phi^P = \mathrm{i}a\frac{g}{\omega} f(z)\, e^{-\mathrm{i}k(x\cos\beta + y\sin\beta)} \tag{3.71}$$

which is a long-crested plane wave of amplitude, a, traveling in the direction, β. Equation 3.71 is essentially a 2D solution that is extended along a third coordinate to form a 3D solution.

The cylindrical coordinates, $\{r, \theta, z\}$ are related to the Cartesian coordinates by:

$$x = r\cos\theta \tag{3.72a}$$

$$y = r\sin\theta \tag{3.72b}$$

and the plane wave can be written in cylindrical coordinates as:

$$\phi^P = \mathrm{i}a\frac{g}{\omega}f\left(z\right)e^{-\mathrm{i}kr\cos(\theta-\beta)} \tag{3.73}$$

Equation 3.73 is still a particular solution, but can be made into a general solution by considering the wave amplitude to be a function of direction, and integrating over direction:

$$\phi = \mathrm{i}\frac{g}{\omega}f\left(z\right)\int_{-\pi}^{\pi}a\left(\beta\right)e^{-\mathrm{i}kr\cos(\theta-\beta)}d\beta \tag{3.74}$$

3.4.2 Solutions in cylindrical coordinates

One can also consider the solutions to the linear wave BVP directly in cylindrical coordinates. In cylindrical coordinates, Laplace's equation, $\nabla^2\phi$, is:

$$\frac{1}{r}\frac{\partial}{\partial r}\left(r\frac{\partial\phi}{\partial r}\right)+\frac{1}{r^2}\frac{\partial^2\phi}{\partial\theta^2}+\frac{\partial^2\phi}{\partial z^2}=0 \tag{3.75}$$

The BVP can be solved directly with a separation of variables:

$$\phi = R\left(r\right)\Theta\left(\theta\right)Z\left(z\right) \tag{3.76}$$

which leads to:

$$\frac{1}{Z}\frac{d^2Z}{dz^2}=-\frac{1}{R}\frac{d^2R}{dr^2}-\frac{1}{r}\frac{1}{R}\frac{dR}{dr}-\frac{1}{r^2}\frac{1}{\Theta}\frac{d^2\Theta}{d\theta^2}=\kappa^2 \tag{3.77}$$

In Z, one can again form the second order differential equation: $\frac{d^2Z}{dz^2}-\kappa^2Z=0$, which leads to the same solutions in z as in the 2D BVP - see Eqs. 3.59, 3.62, 3.64, 3.65, and 3.67.

In the angular direction, Θ can be separated as:

$$\frac{1}{\Theta}\frac{d^2\Theta}{d\theta^2}=-\frac{r^2}{R}\frac{d^2R}{dr^2}-r\frac{1}{R}\frac{dR}{dr}-\kappa^2r^2=-m^2 \tag{3.78}$$

which results in the differential equation:

$$\frac{d^2\Theta}{d\theta^2} + m^2\Theta = 0 \tag{3.79}$$

The fluid must be continuous throughout the domain, that is, $\Theta(\pi) = \Theta(-\pi)$. Because they would result in exponential forms in θ, which cannot be continuous around the circle, solutions for $m^2 > 0$ are not valid. Similarly, for $m = 0$, only a constant solution is admissible and so is not considered.

Therefore, $m^2 < 0$, which results in the periodic solution. Furthermore, to ensure $\Theta(\pi) = \Theta(-\pi)$, m must be an integer, and so the solution is:

$$\Theta = C_m e^{\mathrm{i}m\theta} \qquad\qquad m = \{\ldots, -2, -1, 0, 1, 2, \ldots\}$$

where C_m are an unknown coefficients.

In r, one obtains the differential equation:

$$r^2\frac{d^2R}{dr^2} + r\frac{dR}{dr} + \left(\kappa^2 r^2 - m^2\right)R = 0 \tag{3.80}$$

This is well-known as Bessel's differential equation, which has the eigensolutions (Morse and Feshbach, 1953, Sec. 11.2):

$$R(r) = c_m^{(1)} J_m(kr) + c_m^{(2)} Y_m(kr), \qquad \kappa = k, \qquad \kappa^2 > 0 \tag{3.81a}$$

$$R(r) = C_{mn}^{(1)} I_m(k_n r) + C_{mn}^{(2)} K_m(k_n r), \qquad \kappa = \mathrm{i}k, \qquad \kappa^2 < 0 \tag{3.81b}$$

where $c_m^{(1)}$, $c_m^{(2)}$, $C_{mn}^{(1)}$, and $C_{mn}^{(2)}$ are complex coefficients; $J_m(kr)$ and $Y_m(kr)$ are the Bessel functions or order m of the first and second kind respectively; and $I_m(kr)$ and $K_m(kr)$ are the modified Bessel functions or order m of the first and second kind respectively. For more information on the formulations and derivations of the Bessel functions see Sommerfeld (1949).

The behaviour of each of these Bessel functions is important to the solutions of the BVP. Figure 3.2 shows the Bessel functions of order, $m = 0, 1$ in the left two plots, and $m = 7$ in the right plot. First, notice that only J_m are finite for all kr. Y_m and K_m go to infinity as $kr \to 0$, and I_m goes to infinity as $kr \to \infty$. K_m and I_m are exponential-like, while J_m and Y_m are sinusoidal-like, but decay in magnitude as the argument increases. $J_0(0) = 1$, while for $|m| \neq 0$, $J_m(0) = 0$. As $|m|$ gets larger, $J_m(kr)$ is nearly 0 for a larger range of values of kr near 0. In contrast, for larger $|m|$, and small arguments, $Y_m(kr)$ gets larger - see the plot of J_7, Y_7 in Fig. 3.2.

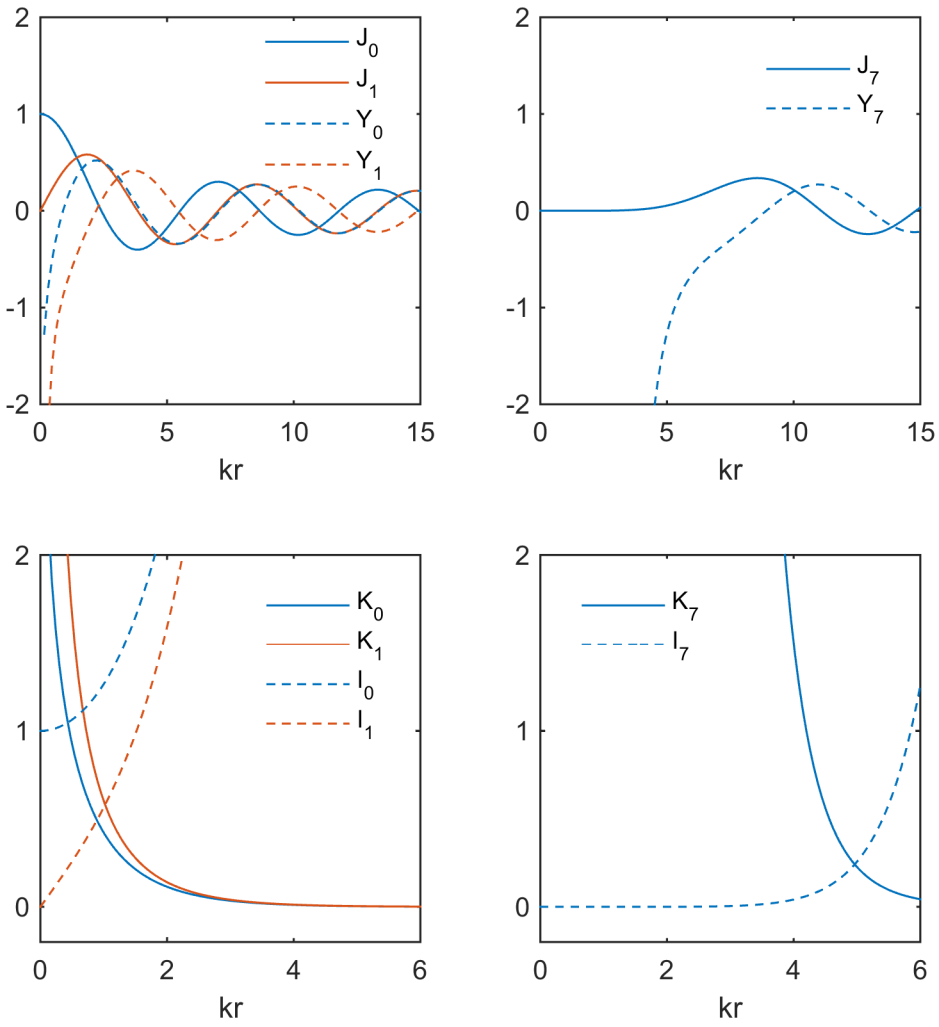

Figure 3.2: Plots of various Bessel functions of different orders for positive arguments.

The Bessel functions are often written as the complex Hankel functions:

$$H_m^{(1)}(kr) = J_m(kr) + \mathrm{i}Y_m(kr) \tag{3.82a}$$
$$H_m^{(2)}(kr) = J_m(kr) - \mathrm{i}Y_m(kr) \tag{3.82b}$$

Clearly, $H_m^{(1)} = H_m^{(2)*}$, where * indicates the complex conjugate. Using the Hankel functions, one can write equations for waves that are incoming to the origin (for $H_m^{(1)}$) and outgoing from the origin (for $H_m^{(2)}$):

$$\eta_m^{(i)} = c_m^{(i)} H_m^{(1)}(kr)\, e^{\mathrm{i}m\theta} \qquad \text{incoming} \tag{3.83a}$$
$$\eta_m^{(o)} = c_m^{(o)} H_m^{(2)}(kr)\, e^{\mathrm{i}m\theta} \qquad \text{outgoing} \tag{3.83b}$$

The outgoing waves are wave sources, where the wave essentially emerges from the imaginary portion of $H_m^{(2)}$, which is the singular Y_m Bessel function. Similarly, incoming waves are sinks, where the wave disappears into the Y_m Bessel function.

The waves in equation 3.83 represent single discrete cylindrical wave components of order m, which shall be referred to as cylindrical wave components or *partial cylindrical waves*.

A general solution can be formed as a summation over these components, which for progressive waves is:

$$\phi^{pr} = \mathrm{i}\frac{g}{\omega} f(z) \sum_{m=-\infty}^{\infty} \left(c_m^{(i)} H_m^{(1)}(kr) + c_m^{(o)} H_m^{(2)}(kr) \right) e^{\mathrm{i}m\theta} \tag{3.84}$$

and for evanescent waves is:

$$\phi^{ev} = \mathrm{i}\frac{g}{\omega} \sum_{n=-\infty}^{\infty} \cos k_n(z+h) \qquad \text{finite depth} \tag{3.85a}$$
$$\times \sum_{m=-\infty}^{\infty} \left(C_{mn}^{(1)} K_m(k_n r) + C_{mn}^{(2)} I_m(k_n r) \right) e^{\mathrm{i}m\theta} \tag{3.85b}$$
$$\phi^{ev} = \int_0^{\infty} \left(\cos \kappa z + \frac{k}{\kappa} \sin \kappa z \right)$$
$$\times \sum_{m=-\infty}^{\infty} \left(C_m^{(1)}(\kappa) K_m(\kappa r) + C_m^{(2)}(\kappa) I_m(\kappa r) \right) e^{\mathrm{i}m\theta} d\kappa \qquad \text{infinite depth} \tag{3.85c}$$

where $\phi = \phi^{pr} + \phi^{ev}$. The infinite depth evanescent solution comes from Peter and

Meylan (2004a,b). All of the terms in Eqs. 3.84 and 3.85 are potentially valid when bodies are present. As was the case for the 2D solution, the singularities can be hidden inside bodies and out of the fluid domain.

3.4.3 Incident waves

In the case where no bodies are present, all singularities must be removed from the equations for velocity potential, and so the only valid solution is the J_m Bessel function, which can be formed with the superposition of the two types of Hankel functions:

$$J_m(kr) = \frac{1}{2}\left(H_m^{(1)}(kr) + H_m^{(2)}(kr)\right) \tag{3.86}$$

For incident waves (i.e. in the absence of bodies) the general solution is:

$$\phi^I = \mathrm{i}\frac{g}{\omega} f(z) \sum_{m=-\infty}^{\infty} a_m J_m(kr)\, e^{\mathrm{i}m\theta} \tag{3.87}$$

From either the moment generating function (Tang, 2007) or from the integral representation of the Bessel function (Sommerfeld, 1949), one can derive the so-called Jacobi-Anger Expansion, which expresses a long-crested plane wave as a summation of cylindrical waves. In a convenient form, it is:

$$e^{-\mathrm{i}kr\cos(\theta-\beta)} = \sum_{m=-\infty}^{\infty} e^{-\mathrm{i}m\left(\beta+\frac{\pi}{2}\right)} J_m(kr)\, e^{\mathrm{i}m\theta} \tag{3.88}$$

By comparison of the polar form of the plane wave (Eq. 3.73), the general cylindrical form of the incident wave (3.87), and the Jacobi-Anger expansion, one sees that the cylindrical coefficients required to generate a plane wave are:

$$a_m^P = a e^{-\mathrm{i}m\left(\beta+\frac{\pi}{2}\right)} \tag{3.89}$$

and so an incident plane wave in cylindrical form is:

$$\phi^P = \mathrm{i}a\frac{g}{\omega} f(z) \sum_{m=-\infty}^{\infty} e^{-\mathrm{i}m\left(\beta+\frac{\pi}{2}\right)} J_m(kr)\, e^{\mathrm{i}m\theta} \tag{3.90}$$

3.4.4 Scattered and radiated waves

When bodies are present, by the radiation conditions (Eq. 3.48g), at a sufficiently large distance, the scattered and radiated waves must 1) travel away from the bodies and 2) must decay in amplitude as they travel away from the bodies. The first condition excludes incoming progressives waves of the form, $H_m^{(1)}$, so $c_m^{(i)} = 0$ for all m. The second condition excludes evanescent waves modified by I_m, which goes to infinity as its argument gets larger. Finally, the general solution for scattered and radiated waves for a region outside of bodies is:

$$\begin{aligned}\phi^{S,R} =& \mathrm{i}\frac{g}{\omega}\sum_{m=-\infty}^{\infty}\left(b_m^{S,R}\frac{\cosh k\left(z+h\right)}{\cosh kh}H_m^{(2)}\left(kr\right)\right. \\ &\left.+\sum_{n=-\infty}^{\infty}B_{mn}^{S,R}\cos k_n\left(z+h\right)K_m\left(k_nr\right)\right)e^{\mathrm{i}m\theta}\end{aligned} \tag{3.91}$$

Here, only the finite depth form is given. Due to the extra complexity of the infinite depth form, for the remainder of this thesis only the finite depth form will be considered. A quasi-infinite depth solution can be obtained from the finite depth form by taking a sufficiently large value for h.

In Section 3.4, general or eigenfunction solutions have been given for the linear wave-body BVP in cylindrical coordinates. These solutions can be used to solve analytically BVPs for cylindrical and axisymmetric geometries. For example, Miles and Gilbert (1968) and Garrett (1971) use the cylindrical solutions to solve for a floating circular-cylindrical dock. A particularly simple case is that of a fixed bottom-mounted circular-cylindrical pile, treated by Havelock (1940) for infinite depth and MacCamy and Fuchs (1954) for finite depth, which shall be given briefly in the next section.

John (1950) shows that the cylindrical solutions are valid for a region outside of a circular cylinder that circumscribes all of the bodies under consideration. This shall also be shown in a different way following Goo and Yoshida (1990) in Section 3.5.2, in which a way of finding the coefficients from a body using Green's function shall be shown. Green's theorem and Green's functions are capable of solving the linear wave-body BVP for arbitrary geometries and shall be discussed in Section 3.5.

3.4.5 Cylindrical pile solution

Take a fixed, bottom-mounted, circular-cylindrical pile of radius, $r = r_0$. The BC on the surface of the pile is $\frac{\partial \phi^I}{\partial r} = -\frac{\partial \phi^S}{\partial r}$, where the incident wave is given by Eq. 3.87, and the scattered wave is given by Eq. 3.91. By the body BC, the evanescent coefficients must be zero, and the m^{th} progressive scattered coefficient is:

$$b_m^S = -a_m \frac{\frac{d}{dr}\left(J_m\left(kr\right)\right)_{r=r_0}}{\frac{d}{dr}\left(H_m^{(2)}\left(kr\right)\right)_{r=r_0}} \tag{3.92}$$

3.4.6 Far-field solution

In the limit that $r \to \infty$, the cylindrical solution can be written in plane-wave-like form using an amplitude function of θ, $\mathcal{F}\left(\theta\right)$, which is commonly known as the Kochin function. As was discussed in Section 2.4, the Kochin function can be used to compute the excitation force on a body via the Haskind relation, and wave power absorption through the wave field.

Consider the cylindrical solution for radiated or scattered waves, Eq. 3.91. In the limit as $r \to \infty$, $H_m^{(2)} \to \sqrt{\frac{2}{\pi kr}} e^{-\mathrm{i}\left(kr - \frac{m\pi}{2} - \frac{\pi}{4}\right)}$ and $K_m\left(k_n r\right) \to 0$. In the far-field, the velocity potential due to a body can be written in a plane-wave-like form with separated variables as:

$$\phi^{S,R} \approx \sqrt{2\pi} e^{\mathrm{i}\frac{\pi}{4}} f\left(z\right) \frac{e^{-\mathrm{i}kr}}{\sqrt{kr}} \mathcal{F}^{S,R}\left(\theta\right) \tag{3.93}$$

By comparing 3.91 as $r \to \infty$, to Eq. 3.93, one sees that the Kochin function is a Fourier series of the cylindrical coefficients:

$$\mathcal{F}^{S,R}\left(\theta\right) = \frac{1}{\pi} \sum_{m=-\infty}^{\infty} e^{\mathrm{i}m\frac{\pi}{2}} b_m^{S,R} e^{\mathrm{i}m\theta} \tag{3.94}$$

3.4.7 On partial cylindrical waves

Although they shall be explored to a much greater extent throughout the rest of the thesis, here, a brief description shall be given of outgoing and incident partial cylindrical waves, and how they combine to form wave fields.

The progressive outgoing $m = 0$ partial wave (Eq. 3.83b) can be understood to represent an isotropic circular wave radiated by an axisymmetric body operating in heave (Wypych *et al.*, 2012). For such a body and motion, only the $m = 0$ coefficient in Eq. 3.91 would be non-zero. The Heave wave elevation is:

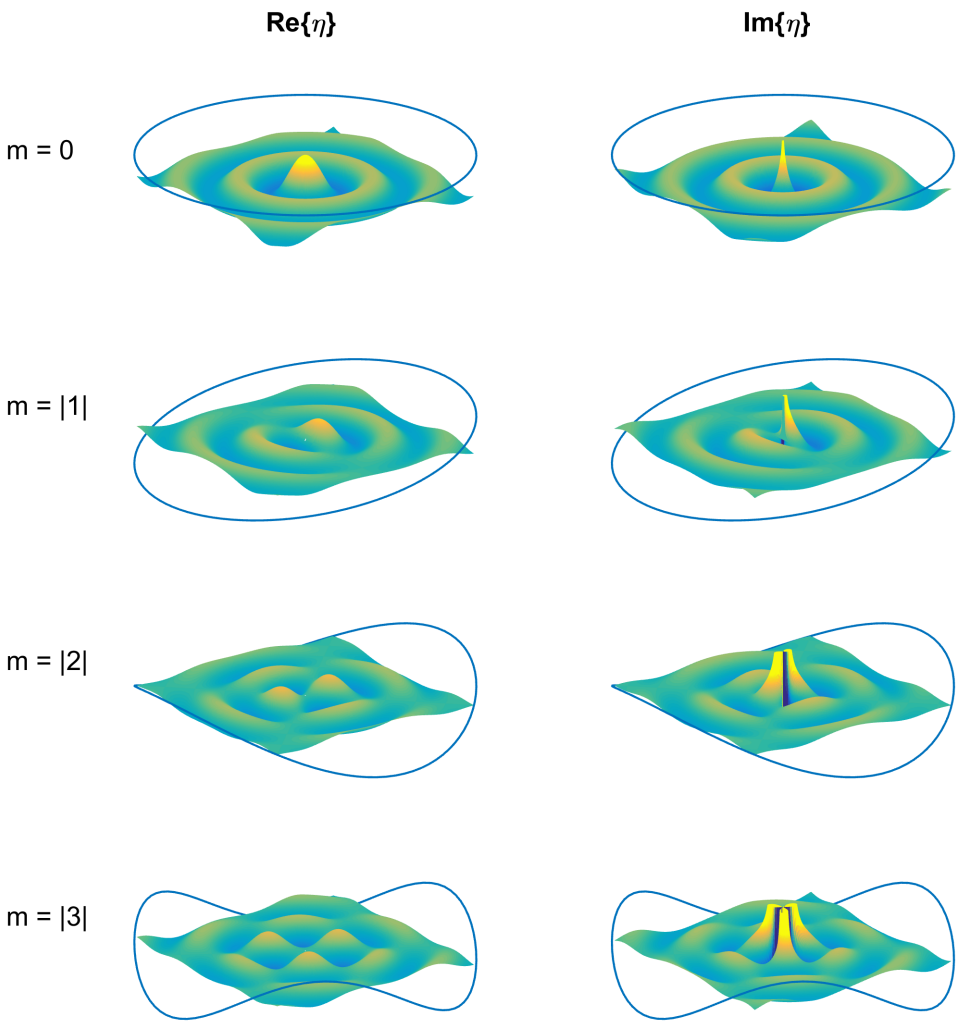

Figure 3.3: Real and imaginary portions of the the first four outgoing propagating cylindrical partial waves. See Eq. 3.83b.

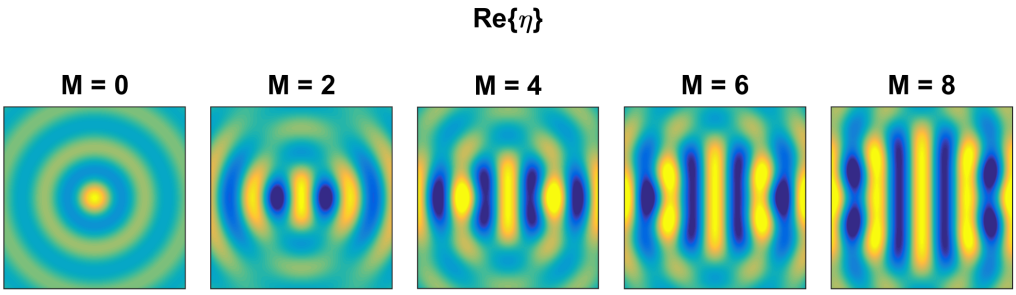

Figure 3.4: Real portion of an incident plane wave in cylindrical form (Eq. 3.90) for increasing truncation values, M.

$$\eta^H = b_0 H_0^{(2)}(kr) \tag{3.95}$$

Similarly, for an axisymmetric body moving in surge, only two partial waves at $m = -1$ and $m = 1$ are needed (Wypych *et al.*, 2012). Their coefficients are equal in magnitude but opposite in sign, so that one gets the surge wave elevation:

$$\begin{aligned} \eta^{Su} &= b_{-1} H_{-1}^{(2)}(kr)\, e^{-\mathrm{i}\theta} + b_1 H_1^{(2)}(kr)\, e^{\mathrm{i}\theta} \\ &= b^{Su} H_1^{(2)}(kr) \cos\theta \end{aligned}$$

where $b_{-1} = -b_1 = \frac{1}{2} b^{Su}$, and the relationships: $H_{-m}^{(2)} = (-1)^m H_m^{(2)}$, and $\frac{1}{2}\left(e^{-\mathrm{i}\theta} + e^{\mathrm{i}\theta}\right) = \cos\theta$ have been used.

At indices of $|m| > 1$, the individual partial waves do not obviously represent physical waves that could be created by a body moving in a single DOF. However, with the appropriate coefficients, the summation of partial waves can represent any linear scattered or radiated wave just as a Fourier series can represent any function.

Figure 3.3 shows the real and imaginary components of the first four individual outgoing progressive partial waves, where the $-m$ and m waves are combined to form a single wave. Also shown are nondimensional Kochin functions which indicate the relative magnitude of the wave as a function of direction. Note that the real portion of the wave, the J_m Bessel function, is finite at the origin, while the imaginary portion, Y_m, is singular at the origin.

It is worth considering how the cylindrical form of the incident wave forms a plane progressive wave (Eq. 3.90). Figure 3.4 shows the incident wave computed with its cylindrical representation for increasing truncation values, M. For a truncation value

M the summation in Eq. 3.90 is computed from $m = -M$ to M rather than from $m = -\infty$ to ∞. At $M = 0$, the pattern is isotropic in direction, but as M gets larger, the wave becomes more and more plane-wave-like in the region near the origin. Note that here, it is only worth considering even increments of M, because for a plane wave with $\beta = 0$, the odd m coefficients in Eq. 3.90 are zero.

3.5 Solutions with Green's functions

In this section, a well-known method for finding the solutions to the linear wave-body BVP of arbitrary bodies shall be shown. The solutions with Green's function are applied in what is known as a boundary-element method (BEM), which is the method used by WAMIT (WAMIT, 2012), the linear wave software employed throughout the thesis. A particularly relevant application of the solution to the BVP with Green's functions is method for finding the cylindrical coefficients developed by Goo and Yoshida (1990), which is presented in Section 3.5.2.

Consider two velocity potentials that each independently satisfy Laplace's equation, $\phi^{(1)}$ and $\phi^{(2)}$. Define a function $F = \phi^{(1)}\nabla\phi^{(2)} - \phi^{(2)}\nabla\phi^{(1)}$, and apply the divergence theorem over a volume, $\mathcal{V}$, enclosed by a surface, S:

$$\int\int_S \left(\phi^{(1)}\nabla\phi^{(2)} - \phi^{(2)}\nabla\phi^{(1)}\right)\cdot \boldsymbol{n} dS = \int\int\int_{\mathcal{V}} \nabla\left(\phi^{(1)}\nabla\phi^{(2)} - \phi^{(2)}\nabla\phi^{(1)}\right) d\mathcal{V} \quad (3.96a)$$

$$\int\int_S \left(\phi^{(1)}\frac{\partial\phi^{(2)}}{\partial n} - \phi^{(2)}\frac{\partial\phi^{(1)}}{\partial n}\right) dS = \int\int\int_{\mathcal{V}} \Big(\nabla\phi^{(1)}\cdot\nabla\phi^{(2)} + \phi^{(1)}\nabla^2\phi^{(2)} - \nabla\phi^{(1)}\cdot\nabla\phi^{(2)} - \phi^{(2)}\nabla^2\phi^{(1)}\Big) d\mathcal{V} \quad (3.96b)$$

On the right-hand side: $\nabla\phi^{(1)}\cdot\nabla\phi^{(2)} - \nabla\phi^{(1)}\cdot\nabla\phi^{(2)} = 0$, and because they satisfy Laplace's equation: $\phi^{(1)}\nabla^2\phi^{(2)} = \phi^{(2)}\nabla^2\phi^{(1)} = 0$, which results in:

$$\int\int_S \left(\phi^{(1)}\frac{\partial\phi^{(2)}}{\partial n} - \phi^{(2)}\frac{\partial\phi^{(1)}}{\partial n}\right) dS = 0 \quad (3.97)$$

This is known as Green's theorem.

Next consider a source function, $G(\boldsymbol{x}, \boldsymbol{X})$, where $\boldsymbol{x}$ is the field point and here $\boldsymbol{X}$ is the location of the source. G satisfies the free-surface BC, the bottom BC, and the radiation condition. In the fluid domain, G satisfies Laplace's equation everywhere except at the location of the source:

$$\nabla^2 G(\boldsymbol{x}, \boldsymbol{X}) = \begin{cases} 4\pi\delta(\boldsymbol{x} - \boldsymbol{X}), & \boldsymbol{X} \text{ in domain} \\ 2\pi\delta(\boldsymbol{x} - \boldsymbol{X}), & \boldsymbol{X} \text{ on } S,\ \boldsymbol{x}^+ \to \boldsymbol{X} \\ 0, & \boldsymbol{X} \text{ outside domain} \end{cases} \tag{3.98}$$

where $\boldsymbol{x}^+ \to \boldsymbol{X}$ means that the field point approaches the source from outside of the body.

Take an unknown velocity potential, ϕ, and a Green's function, and the enclosed surface to be the body surface, S_b, the free-surface, S_η, a vertical circular wall at some radius sufficient to satisfy the radiation condition, S_∞, and the bottom, S_h.

$$\int\int_{S_b+S_\eta+S_\infty+S_h} \left(G\frac{\partial\phi}{\partial n} - \phi\frac{\partial G}{\partial n} \right) dS = -\phi(\boldsymbol{x} \to \boldsymbol{X}) \nabla^2 G(\boldsymbol{x} \to \boldsymbol{X}, \boldsymbol{X}) \tag{3.99}$$

Since both ϕ and G satisfy the BC on S_η, S_∞, and S_h, it can be shown that by substitution of the BCs into Eq. 3.99, that $G\frac{\partial\phi}{\partial n} - \phi\frac{\partial G}{\partial n} = 0$ on these surfaces. If the source is located on the body, one obtains:

$$\int\int_{S_b} \left(G\frac{\partial\phi}{\partial n} - \phi\frac{\partial G}{\partial n} \right) dS = -2\pi\phi(\boldsymbol{x}) \tag{3.100}$$

which is an equation for the velocity potential on the body surface in terms of a distribution of sources (G with amplitude $\frac{\partial\phi}{\partial n}$) and dipoles ($\frac{\partial G}{\partial n}$ with amplitude ϕ) over the surface of the body.

To find solutions to the radiation and scattering problems, substitute body boundary conditions and the equation can be rewritten in terms of the unknown velocity potential on the left and the known BC on the right:

$$2\pi\phi^S - \int\int_{S_b} \phi^S \frac{\partial G}{\partial n} dS = \int\int_{S_b} G\frac{\partial\phi^I}{\partial n} dS \qquad \text{Scattered} \tag{3.101a}$$

$$2\pi\phi_i^R - \int\int_{S_b} \phi_i^R \frac{\partial G}{\partial n} dS = -\int\int_{S_b} G\boldsymbol{n}_i dS \qquad \text{Radiated} \tag{3.101b}$$

which are Fredholm integral equations of the second kind and can be used to find the unknown velocity potentials using panel methods or the so-called higher-order method (WAMIT, 2012).

3.5.1 Green's source solution

One could also consider the BVP for the region *inside* the body, that is, enclosed by the body surface on the outside and a free-surface or a closed surface at $z = 0$. Call the potential that satisfies this interior problem, ϕ'. In the interior region, the Green's function is:

$$\nabla^2 G = \begin{cases} 0, & \boldsymbol{X} \text{ in domain (outside body)} \\ -2\pi\delta\left(\boldsymbol{x} - \boldsymbol{X}\right), & \boldsymbol{X} \text{ on } S,\ \boldsymbol{x}^- \to \boldsymbol{X} \\ -4\pi\delta\left(\boldsymbol{x} - \boldsymbol{X}\right), & \boldsymbol{X} \text{ in body} \end{cases} \tag{3.102}$$

On points on the body approached from outside the body:

$$\int\int_{S_b} \left(G\frac{\partial \phi'}{\partial n} - \phi' \frac{\partial G}{\partial n} \right) dS = 2\pi\phi'\left(\boldsymbol{x}\right) \tag{3.103}$$

Subtracting Eq. 3.103 from Eq. 3.100, one obtains:

$$-2\pi\left(\phi + \phi'\right) = \int\int_{S_b} \left(G\left(\frac{\partial \phi}{\partial n} - \frac{\partial \phi'}{\partial n} \right) - \left(\phi - \phi'\right) \frac{\partial G}{\partial n} \right) dS \tag{3.104}$$

If a condition on the body, $\phi = \phi'$, is imposed, the second term disappears and one obtains an expression for the velocity potential in terms of a distribution of sources alone:

$$\phi = \int\int_{S_b} \sigma\left(\boldsymbol{x}\right) G\left(\boldsymbol{x}, \boldsymbol{X}\right) dS \tag{3.105}$$

where σ is the distribution of source strengths, and is equal to: $\sigma = -\frac{1}{4\pi}\left(\frac{\partial \phi}{\partial n} - \frac{\partial \phi'}{\partial n} \right)$.

Now take the normal derivative, $\frac{\partial}{\partial N}$, of Eq. 3.104 with respect to the coordinates of the Green's function, $\boldsymbol{X}$ (Delhommeau, 1987, Annexe 2):

$$\left(\frac{\partial \phi}{\partial n} - \frac{1}{2}\left(\frac{\partial \phi}{\partial n} - \frac{\partial \phi'}{\partial n} \right) \right) = -\frac{1}{4\pi} \int\int_{S_b} \left(\frac{\partial G}{\partial N}\left(\frac{\partial \phi}{\partial n} - \frac{\partial \phi'}{\partial n} \right) - \left(\phi - \phi'\right) \frac{\partial^2 G}{\partial N \partial n} \right) dS \tag{3.106}$$

where on the left-hand side, $\frac{\partial}{\partial N} = \frac{\partial}{\partial n}$ because ϕ and ϕ' are the velocity potentials at the locations of the Green's functions. However on the right-hand side, $\frac{\partial \phi}{\partial N} = 0$ and $\frac{\partial \phi'}{\partial N} = 0$, because they are not functions of $\boldsymbol{X}$. Furthermore, the following manipulations are made on the left-hand side: $\frac{1}{2}\frac{\partial \phi}{\partial n} = \frac{\partial \phi}{\partial n} - \frac{1}{2}\frac{\partial \phi}{\partial n}$, and $\frac{\partial \phi'}{\partial n} = -\left(-\frac{\partial \phi'}{\partial n} \right)$.

Again taking $\phi = \phi'$ and $\sigma = -\frac{1}{4\pi}\left(\frac{\partial \phi}{\partial n} - \frac{\partial \phi'}{\partial n} \right)$, and applying either the diffracted or the

radiated BCs, from Eq. 3.106, one obtains another set of Fredholm integral equations, which can be solved for the scattered and radiated problems in terms of the source strengths:

$$2\pi\sigma^{S,R} - \int\int_{S_b} \sigma^{S,R} \frac{\partial G}{\partial N} dS = \begin{cases} \frac{\partial \phi^I}{\partial n} & \text{Scattered} \\ -\boldsymbol{n}_i & \text{Radiated} \end{cases} \tag{3.107}$$

For more on the source solution, see Mei *et al.* (2005), Chapter 8.

3.5.2 Cylindrical coefficients with Green's functions

The following is a method formulated by Goo and Yoshida (1990), which uses Green's theorem and Green's functions to find the cylindrical progressive and evanescent coefficients for an arbitrary body.

Taking $\boldsymbol{x} = \{r, \theta, z\}$ and $\boldsymbol{X} = \{R, \Theta, Z\}$, the cylindrical Green's function developed by Fenton (1978) is:

$$\begin{aligned} G(r,\theta,z;R,\theta,Z) =& \frac{\mathrm{i}}{2} C_0 \cosh k(z+h) \cosh k(Z+h) \\ & \times \sum_{m=-\infty}^{\infty} \left\{ \begin{array}{l} H_m^{(2)}(kr) J_m(kR) \\ H_m^{(2)}(kR) J_m(kr) \end{array} \right\} e^{\mathrm{i}m(\theta-\Theta)} \\ & - \frac{1}{\pi} \sum_{n=1}^{\infty} C_n \cos k_n(z+h) \cos k_n(Z+h) \\ & \times \sum_{m=-\infty}^{\infty} \left\{ \begin{array}{l} K_m(k_n r) I_m(k_n R) \\ K_m(k_n R) I_m(k_n r) \end{array} \right\} e^{\mathrm{i}m(\theta-\Theta)} \end{aligned} \tag{3.108}$$

where:

$$C_0 = \frac{K^2 - k^2}{(k^2 - K^2)h + K} \tag{3.109a}$$

$$C_n = \frac{k_n^2 + K^2}{(k_n^2 + K^2)h - K} \tag{3.109b}$$

$$K = \frac{\omega^2}{g} \tag{3.109c}$$

In the Green's function, the upper term in the braces is used when $r \geq R$ and the lower term when $r < R$.

For the region outside of a circular cylinder that circumscribes the body or bodies, $r > R$, the upper term is used. When Fenton's Green's function (Eq. 3.108) is substituted

into the source formulation for the velocity potential (Eq. 3.105) one obtains the cylindrical formulation for the radiated and scattered waves (Eq. 3.91), where the progressive and evanescent cylindrical coefficients are given by:

$$b_m^{S,R} = \frac{1}{2}\frac{\omega}{g} C_0 \cosh kh \times \int\int_{S_b} \sigma^{S,R}(R,\Theta,Z) \cosh k(Z+h) J_m(kR) e^{-\mathrm{i}m\Theta} dS \tag{3.110a}$$

$$B_{mn}^{S,R} = \frac{\mathrm{i}}{\pi}\frac{\omega}{g} C_n \times \int\int_{S_b} \sigma^{S,R}(R,\Theta,Z) \cos k_n(Z+h) I_m(k_n R) e^{-\mathrm{i}m\Theta} dS \tag{3.110b}$$

Once the source strength distribution is found (and it need not be found with Fenton's Green's function), the progressive and evanescent cylindrical coefficients can be determined for an arbitrary body.

3.6 Derived quantities

Velocity potential is used to derive other quantities: fluid velocity, fluid pressure, and surface elevation, as well as the forces on or power absorbed by floating bodies.

The fluid quantities derived from the velocity potential are:

$$\boldsymbol{u} = \nabla\phi \qquad \text{velocity} \tag{3.111a}$$

$$p = -\mathrm{i}\omega\rho\phi \qquad \text{dynamic pressure} \tag{3.111b}$$

$$\eta = -\mathrm{i}\frac{\omega}{g}\,\phi|_{z=0} \qquad \text{surface elevation} \tag{3.111c}$$

3.6.1 Hydrodynamic forces on the body

Often, rather than pressure at a location on the body surface, one wants to know the total force, which is the pressure integrated over the surface. In the linearized problem, the pressure is divided into three quantities and thus three forces: the hydrostatic force, the excitation (or diffraction) force, and the radiation force. The hydrostatic force shall be considered in the next section. The hydrodynamic forces are those due to fluid motions due to the incident wave and body motions.

The excitation force is the integral of the pressure due to the diffraction potential over the mean body surface in the direction the normal of a given DOF. f_i^D is the excitation

force on mode of motion i, and is found as:

$$f_i^D = -\mathrm{i}\omega\rho \int\int_{S_b} \left(\phi^I + \phi^S\right) \boldsymbol{n}_i \cdot \boldsymbol{n} dS \tag{3.112}$$

The radiation force is the integral of the pressure due to particular mode of motion on itself or on another mode of motion. f_{ij}^R is the radiation force on mode i due to motion j, and is found as:

$$f_{ij}^R = -\rho \int\int_{S_b} \frac{\partial \phi_i^R}{\partial n} \xi_j \phi_j^R dS \tag{3.113}$$

where the radiation BC, $\frac{\partial \phi_i^R}{\partial n} = \mathrm{i}\omega \boldsymbol{n}_i \cdot \boldsymbol{n}$, has been used. The radiation force is often split into real and imaginary parts as:

$$-\rho \int\int_{S_b} \frac{\partial \phi_i^R}{\partial n} \xi_j \phi_j^R dS = \omega^2 \mathcal{A}_{ij} \xi_j - \mathrm{i}\omega \mathcal{B}_{ij} \xi_j \tag{3.114}$$

where $\mathcal{A}_{ij}$ and $\mathcal{B}_{ij}$ are real-valued quantities known as the added mass and hydrodynamic damping respectively. The terminology added mass and damping arises because in the equations of motion, $\mathcal{A}_{ij}$ appears like a virtual mass quantity added to the acceleration term, and $\mathcal{B}_{ij}$ appears like a quantity applied to the velocity term like a linear damping.

The sum of the excitation force and the radiation forces constitutes the hydrodynamic body forces, which can be written in vector and matrix form as:

$$\boldsymbol{f}^{HD} = \boldsymbol{f}^D + \omega^2 \boldsymbol{\mathcal{A}} \boldsymbol{\xi} - \mathrm{i}\omega \boldsymbol{\mathcal{B}} \boldsymbol{\xi} \tag{3.115}$$

where $\boldsymbol{f}^D$ is an $N \times 1$ vector whose components are given by Eq. 3.112, $\boldsymbol{\mathcal{A}}$ and $\boldsymbol{\mathcal{B}}$ are the $N \times N$ added mass and damping matrices, whose components are given by 3.114, and $\boldsymbol{\xi}$ is an $N \times 1$ vector of the body motion amplitudes.

All hydrodynamic quantities are frequency dependent and the excitation force is also dependent on the incident wave, which for the case of incident plane waves means it is a function of the incident direction.

3.6.2 Hydrostatic forces on the body

The purely hydrostatic force is the integral of the hydrostatic pressure (the $-gz$ term in Bernoulli's equation, Eq. 3.7) over the body surface. However, in the context of linear wave theory, it is natural to combine the hydrostatic force with the forces on the body due to gravity, which results in a linear spring force that is proportional to body position. For a rigid body with the standard 6 DOF, this formulation is well understood and is addressed by, for example, Newman (1977). For generalized modes of motion, the formulation is less well-known and is given here.

The purely hydrostatic force in DOF i is:

$$f_i^{HS-p} = -\rho g \int \int_{S_b^{(t)}} z \boldsymbol{n}_i \cdot \boldsymbol{n} dS \tag{3.116}$$

The integral is over the instantaneous body surface, $S_b^{(t)}$, (not the mean S_b). The force acts in the $+\hat{\boldsymbol{k}}$ direction, where the negative sign is because to $z \leq 0$.

The gravitational force in DOF i is the integral over the total body volume (both the submerged and dry) of the product of the body density and the component of $\boldsymbol{n}_i$ in the direction of the gravitational force:

$$f_i^G = -g \int \int \int_{\mathcal{V}_b^{T(t)}} \rho_b(\boldsymbol{x}) \boldsymbol{n}_i \cdot \hat{\boldsymbol{k}} d\mathcal{V} \tag{3.117}$$

where $\mathcal{V}_b^{T(t)}$ is the total body volume as a function of time, and $\rho_b(\boldsymbol{x})$ is in general a function of space. For the generalized motion heave, as one would expect, the gravitational force is the weight: $f_3^G = -mg$, where m is the mass.

The sum of these forces forms what is generally consider to be the hydrostatic force in the linear wave problem:

$$f_i^{HS} = f_i^{HS-p} + f_i^G \tag{3.118}$$

For linear harmonic motion, the instantaneous body surface and volume are equal to the mean locations of the body surface and volume plus small changes due to motions in each DOF:

$$S_b^{(t)} = S_b + \sum_{j=1}^{N} \xi_j \delta S_j \tag{3.119a}$$

$$\mathcal{V}_b^{T(t)} = \mathcal{V}_b^T + \sum_{j=1}^{N} \xi_j \delta \mathcal{V}_j^T \tag{3.119b}$$

where δS_j is the small closed surface between S_b and the new position of the surface including the connecting surface at $z = 0$; $\delta \mathcal{V}_j^T$ is the delta volume enclosed by the differences in the surface over the total volume. The total hydrostatic force is then the sum of the forces on the mean position and the sum of the forces due to small changes in position:

$$\begin{aligned} f_i^{HS} = &- \rho g \int\int_{S_b} z \boldsymbol{n}_i \cdot \boldsymbol{n} dS - g \int\int\int_{\mathcal{V}_b^T} \rho_b \boldsymbol{n}_i \cdot \hat{\boldsymbol{k}} d\mathcal{V} \\ &- \sum_{j=1}^{N} \left(\rho g \int\int_{\xi_j \delta S_j} z \boldsymbol{n}_i \boldsymbol{n} dS + g \int\int\int_{\xi_j \delta \mathcal{V}_j^T} \rho_b \boldsymbol{n}_i \cdot \hat{\boldsymbol{k}} d\mathcal{V} \right) \end{aligned} \tag{3.120}$$

By definition, a body floats statically at its mean position, which means that there must be a balance of hydrostatic forces with the gravitational forces, and so the sum of the first two terms on the right-hand side is zero:

$$- \rho g \int\int_{S_b} z \boldsymbol{n}_i \cdot \boldsymbol{n} dS - g \int\int\int_{\mathcal{V}_b^T} \rho_b \boldsymbol{n}_i \cdot \hat{\boldsymbol{k}} d\mathcal{V} = 0 \tag{3.121}$$

Following the method used by Newman (1994), the first term inside the parentheses of Eq. 3.120 (the purely hydrostatic portion) can be rewritten as a volume integral over the small volume, $\delta \mathcal{V}_i$, using the divergence theorem:

$$\rho g \int\int_{\xi_j \delta S_j} z \boldsymbol{n}_i \boldsymbol{n} dS = \rho g \int\int\int_{\xi_j \delta \mathcal{V}_j} \nabla \cdot (z \boldsymbol{n}_i) \, d\mathcal{V} \tag{3.122}$$

where here the small volume, $\delta \mathcal{V}_i$, is just the submerged portion (i.e. below $z = 0$), and so:

$$f_i^{HS} = -g \sum_{j=1}^{N} \left(\rho \int\int\int_{\xi_j \delta \mathcal{V}_j} \nabla \cdot (z \boldsymbol{n}_i) \, d\mathcal{V} + \int\int\int_{\xi_j \delta \mathcal{V}_j^T} \rho_b \boldsymbol{n}_i \cdot \hat{\boldsymbol{k}} d\mathcal{V} \right) \tag{3.123}$$

The divergence can be rewritten as:

$$\nabla \cdot (z\boldsymbol{n}_i) = \left(\boldsymbol{n}_i \cdot \hat{\boldsymbol{k}} + z\nabla \cdot \boldsymbol{n}_i\right) \tag{3.124}$$

For small transformations, $\xi_j \delta \mathcal{V}_j$ is thin, and the delta volume can be approximated by the product of the mean body surface and the translation of the normal from the surface, which results in integrals over the mean body surfaces:

$$f_i^{HS} = -g \sum_{j=1}^{N} \xi_j \left(\rho \int\int_{S_b} \left(\boldsymbol{n}_i \cdot \hat{\boldsymbol{k}} + z\nabla \cdot \boldsymbol{n}_i\right) \boldsymbol{n}_j \cdot \boldsymbol{n} dS + \int\int_{S_b^T} \left(\rho_b \boldsymbol{n}_i \cdot \hat{\boldsymbol{k}}\right) \boldsymbol{n}_j \cdot \boldsymbol{n} dS \right) \tag{3.125}$$

where S_b^T is the total (submerged and dry) mean body surface. Eq. 3.125 says that the hydrostatic force in DOF i is the sum of forces due to changes in the surface by motions in all DOFs.

Finally, the hydrostatic force can be written as the product of vector of body motion amplitudes, $\boldsymbol{\xi}$, and a hydrostatic matrix, $\boldsymbol{C}$:

$$\boldsymbol{f}^{HS} = -\boldsymbol{C}\boldsymbol{\xi} \tag{3.126}$$

where the ij^{th} component is:

$$C_{ij} = \rho g \int\int_{S_b} \left(\boldsymbol{n}_i \cdot \hat{\boldsymbol{k}} + z\nabla \cdot \boldsymbol{n}_i\right) \boldsymbol{n}_j \cdot \boldsymbol{n} dS + g \int\int_{S_b^T} \left(\rho_b \boldsymbol{n}_i \cdot \hat{\boldsymbol{k}}\right) \boldsymbol{n}_j \cdot \boldsymbol{n} dS \tag{3.127}$$

When the divergence of the motion vector is not zero, $\nabla \cdot \boldsymbol{n}_i \neq 0$, it represents a sort of expanding or contracting, like the stretching of a membrane. One can imagine how an expanding or contracting volume would effect the buoyancy. For rigid body motions and other simple translational or rotational motions: $\nabla \cdot \boldsymbol{n}_i = 0$. It is also not unreasonable to assume the body has a constant density over its surface, that is $\rho_b(\boldsymbol{x}) = \rho_b$ on S_b^T and so:

$$C_{ij} = \rho g \int\int_{S_b} \left(\boldsymbol{n}_i \cdot \hat{\boldsymbol{k}}\right) \boldsymbol{n}_j \cdot \boldsymbol{n} dS + \rho_b g \int\int_{S_b^T} \left(\boldsymbol{n}_i \cdot \hat{\boldsymbol{k}}\right) \boldsymbol{n}_j \cdot \boldsymbol{n} dS, \quad \nabla \cdot \boldsymbol{n}_i = 0 \tag{3.128}$$

which results in two identical integrals but over two different surfaces: the submerged body surface, S_b, and the total body surface, S_b^T, modified by the fluid density, ρ, and the body's surface density, ρ_b, respectively.

3.6.3 Equations of motion

For linear time-harmonic forces applied to a body, the body motions will also be time harmonic. In this section, the linear time-harmonic equations of motion shall be given.

For a system with N DOF, it is convenient to write the equations of motions in matrix form:

$$-\omega^2 \boldsymbol{M}\boldsymbol{\xi} = \boldsymbol{f}^{ME} + \boldsymbol{f}^{HD} + \boldsymbol{f}^{HS} \tag{3.129}$$

where the left-hand side is the inertial term and the right-hand side is the sum of all forces on the body. $-\omega^2\boldsymbol{\xi}$ is the vector of accelerations in each DOF; $\boldsymbol{M}$ is the $N \times N$ mass-inertia matrix; $\boldsymbol{f}^{ME}$ is an $N \times 1$ vector of the total mechanical forces; $\boldsymbol{f}^{HD}$ is the hydrodynamic force vector given by Eq. 3.115, and $\boldsymbol{f}^{HS}$ is the hydrostatic force vector given by Eq. 3.126.

The mass matrix represents the resistance to or induction of movement in DOF i due to motion in DOF j. It is proportional to the density of the body as a function of space, $\rho_b(\boldsymbol{x})$, For generalized modes of motion, the ij^{th} term of the mass matrix is:

$$M_{ij} = \int\int\int_{\mathcal{V}_b^T} \rho_b(\boldsymbol{x})\, \boldsymbol{n}_i \cdot \boldsymbol{n}_j d\mathcal{V} \tag{3.130}$$

where the integral is performed over the total mean body volume. For more information, see Newman (1994) or Newman (1997).

The mechanical forces can be decomposed into linear forces proportional to the displacement and velocity of the body motions:

$$\boldsymbol{f}_{mech} = -\mathrm{i}\omega\boldsymbol{D}\boldsymbol{\xi} - \boldsymbol{K}\boldsymbol{\xi} \tag{3.131}$$

where $\mathrm{i}\omega\boldsymbol{\xi}$ is a vector of body velocities; $\boldsymbol{D}$ is an $N \times N$ mechanical damping matrix; and $\boldsymbol{K}$ is an $N \times N$ stiffness matrix.

The hydrodynamic and hydrostatic forces are given by Eqs. 3.115 and 3.126, respectively.

Finally, the linear harmonic equations of motion are:

$$\left(-\omega^2\left(\boldsymbol{M} + \boldsymbol{\mathcal{A}}\right) + \mathrm{i}\omega\left(\boldsymbol{D} + \boldsymbol{\mathcal{B}}\right) + \boldsymbol{K} + \boldsymbol{C}\right)\boldsymbol{\xi} = \boldsymbol{f}^D \tag{3.132}$$

which can be solved to find the amplitudes of the body motions, $\boldsymbol{\xi}$.

3.6.4 Wave and device power

For a wave energy converter (WEC), one wants to know how much power it will produce, which in linear wave theory is the same as the power it absorbs from the wave field. The instantaneous input power, $P^{(t)}$, to the device is the integral of the product of the instantaneous hydrodynamic pressure and the body velocity over the body's surface:

$$P^{(t)} = \sum_{i=1}^{N} \int \int_{S_b} \mathrm{Re}\left\{p^{HD} e^{\mathrm{i}\omega t}\right\} \mathrm{Re}\left\{\mathrm{i}\omega \xi_i e^{\mathrm{i}\omega t}\right\} \boldsymbol{n}_i \cdot \boldsymbol{n} dS \tag{3.133}$$

For linear harmonic motion, one considers the time-average power over a wave cycle, P, which is equal to:

$$P = \sum_{i=1}^{N} \int \int_{S_b} \mathrm{Re}\left\{\mathrm{i}\omega p^{HD*} \xi_i\right\} \boldsymbol{n}_i \cdot \boldsymbol{n} dS \tag{3.134}$$

The hydrodynamic pressure is is the sum of the radiated and diffracted pressures:

$$p^{HD} = -\mathrm{i}\omega\rho \left(\phi^I + \phi^S + \sum_{j=1}^{N} \xi_j \phi_j^R\right) \tag{3.135}$$

which when substituted into Eq. 3.134 for power and using the relationships for the excitation force (Eq. 3.112) and added mass and damping (Eq. 3.114) results in the following expression for time-averaged power in terms of the hydrodynamic quantities:

$$P = \frac{1}{2}\mathrm{Re}\left\{\mathrm{i}\omega \boldsymbol{f}^{D\dagger} \boldsymbol{\xi}\right\} - \frac{1}{2}\omega^2 \boldsymbol{\xi}^\dagger \boldsymbol{\mathcal{B}} \boldsymbol{\xi} \tag{3.136}$$

where † indicates the complex conjugate transpose. The $\frac{1}{2}\mathrm{Re}\left\{\mathrm{i}\omega \boldsymbol{f}^{D\dagger} \boldsymbol{\xi}\right\}$ term represents power that is absorbed by the body, and $-\frac{1}{2}\omega^2 \boldsymbol{\xi}^\dagger \boldsymbol{\mathcal{B}} \boldsymbol{\xi}$ is the power that is radiated back into the wave field by the body motions.

If the equations of motion (Eq. 3.132) are substituted in for the excitation force in the Eq. 3.136, and one assumes that $\boldsymbol{D}$ and $\boldsymbol{K}$ are symmetric, then the power is given in terms of the linear mechanical damping:

$$P = \frac{1}{2}\omega^2 \boldsymbol{\xi}^\dagger \boldsymbol{D} \boldsymbol{\xi} \tag{3.137}$$

This is a statement of the conservation of energy: the power absorbed by the body from the fluid acting over its moving surface is equal to the power that is dissipated mechanically.

A commonly used measure of wave power is the wave energy flux of a long-crested

plane-wave per meter of its crest-width (For brevity, the derivation shall not be given here, but can be found in, for example, Dean and Dalrymple (1991).):

$$\mathcal{E}_f^P = \frac{1}{2}\rho g a^2 c_g \tag{3.138}$$

where the quantity $\frac{1}{2}\rho g a^2$ is the wave energy density (wave energy per unit area):

$$E = \frac{1}{2}\rho g a^2 \tag{3.139}$$

and c_g is the speed at which the energy travels, also known as the group velocity:

$$c_g = \frac{1}{2}\left(1 + \frac{2kh}{\sinh 2kh}\right) c \tag{3.140}$$

where

$$c = \frac{k}{\omega} \tag{3.141}$$

and is the wave phase velocity.

As was discussed in Section 3.4, the plane wave solution is really a 2D solution. Similarly, the measure $\mathcal{E}_f^P$ is essentially a 2D measure of energy flux. Nevertheless, it is frequently used to formulate a measure of the power absorbed by a body known as the capture width:

$$CW = \frac{P}{\mathcal{E}_f^P} \tag{3.142}$$

The terminology width is used because CW has units of length and in a sense it represents the amount of power absorbed from a long-crested plane wave measured as if removing power from a section of the wave along its crest.

3.7 Summary

In this chapter, the linear theory of wave-body interactions was derived from Euler's equations. Of particular importance are the solutions to the linear wave-body BVP in cylindrical coordinates, where the method of Goo and Yoshida (1990) was shown for deriving the cylindrical coefficients of an arbitrary body. Finally, the derivation of the fluid forces, the equations of motion and the power absorption by a body were shown. This should serve as an adequate foundation upon which to build the rest of the thesis.

Chapter 4

Cylindrical Surface Method: Computation

4.1 Introduction

For a particular body defined by its geometry and modes of motions, particular cylindrical solutions to the linear wave-body boundary-value problem (BVP) can be found, which are the sets of cylindrical coefficients (or amplitudes) for both the progressive and evanescent modes that describe its scattered and radiated waves.

As was discussed in Section 3.5.2, the coefficients can be found using the cylindrical Green's function following the method of Goo and Yoshida (1990). However, to date, there is no off-the-shelf software available that implements this method, which means that one would need to modify an existing code or write a new boundary-element method (BEM) code from scratch. Furthermore, Goo and Yoshida (1990) is only applicable to the integral method for solving the linear wave BVP, and cannot be applied to other wave-body computations or experiments.

In this chapter, a new method for finding the progressive and evanescent cylindrical coefficients is presented. The coefficients are computed by making measurements of the wave field over a circular-cylindrical surface that circumscribes the body, and then applying a Fourier transform and integrating over depth using the orthogonality of the depth dependence. The approach is general in that it can be applied to the results from any numerical code or experiments as long as linearity is given or assumed.

The method is applied computationally using the commercial BEM WAMIT (WAMIT, 2012) to find the scattered and radiated wave field coefficients of four types of wave energy converters (WECs): a heaving point-absorber, a surging point-absorber, a terminator, and an attenuator, with three different geometries. The resulting analytical, cylindrical representations of the wave field are plotted and compared to wave fields computed completely by WAMIT.

The contents of this chapter was published in McNatt *et al.* (2013b) and republished with permission in McNatt *et al.* (2013a).

4.2 Cylindrical surface method

The cylindrical solution for the scattered or radiated wave fields of any body in finite depth is (Eq. 3.91):

$$\begin{aligned}\phi^{S,R} =& \mathrm{i}\frac{g}{\omega}\sum_{m=-\infty}^{\infty}\left(b_m^{S,R}\frac{\cosh k\left(z+h\right)}{\cosh kh}H_m^{(2)}\left(kr\right)\right.\\ &\left.+\sum_{n=-\infty}^{\infty}B_{mn}^{S,R}\cos k_n\left(z+h\right)K_m\left(k_nr\right)\right)e^{\mathrm{i}m\theta}\end{aligned} \tag{4.1}$$

Take the scattered or radiated wave field to be known over a circular-cylindrical surface that circumscribes the body at a radius, $r = r_0$ which extends from the bottom to $z = 0$:

$$\phi_c^{S,R} = \phi^{S,R}\left(r = r_0, \theta, z\right) \tag{4.2}$$

One may compute this surface directly as the velocity potential using a numerical method, or as pressure or velocity, where the velocity potential can be found through the relationships given by Eqs. 3.111.

The m^{th} progressive and evanescent cylindrical terms can be isolated by taking the Fourier transform in the angular direction of the known wave field:

$$\begin{aligned}b_m^{S,R}\frac{\cosh k\left(z+h\right)}{\cosh kh}H_m^{(2)}\left(kr_0\right)+\sum_{n=-\infty}^{\infty}B_{mn}^{S,R}\cos k_n\left(z+h\right)K_m\left(k_nr_0\right)&\\ =-\frac{\mathrm{i}}{2\pi}\frac{\omega}{g}\int_0^{2\pi}\phi_c^{S,R}e^{-\mathrm{i}m\theta}d\theta&\end{aligned} \tag{4.3}$$

By integration over depth and substitution of the progressive (Eq. 3.62) and evanescent (Eq. 3.65) dispersion relations, one may show the orthogonality of the depth dependence:

$$\int_{-h}^{0}\cosh k\left(h+z\right)\cos k_n\left(h+z\right)dz = 0 \tag{4.4a}$$

$$\int_{-h}^{0}\cos k_l\left(h+z\right)\cos k_n\left(h+z\right)dz = 0, \qquad l \neq n \tag{4.4b}$$

which can be used to isolate the progressive and evanescent coefficients from one another:

$$-\frac{\mathrm{i}}{2\pi}\frac{\omega}{g}\int_{-h}^{0}\int_{0}^{2\pi}\phi_c^{S,R}e^{-\mathrm{i}m\theta}\cosh k\left(h+z\right)d\theta dz$$
$$=\frac{h}{2\cosh kh}\left(1+\frac{\sinh 2kh}{2kh}\right)b_m^{S,R}H_m^{(2)}\left(kr_0\right) \quad \text{Progressive} \tag{4.5a}$$

$$-\frac{\mathrm{i}}{2\pi}\frac{\omega}{g}\int_{-h}^{0}\int_{0}^{2\pi}\phi_c^{S,R}e^{-\mathrm{i}m\theta}\cos k_n\left(h+z\right)d\theta dz$$
$$=\frac{h}{2}\left(1+\frac{\sin 2k_nh}{k_nh}\right)B_{mn}^{S,R}K_m\left(k_nr_0\right) \quad \text{Evanescent} \tag{4.5b}$$

so that finally, the progressive and evanescent coefficients for a particular scattered or radiated wave field are found as:

$$b_m^{S,R} = -\frac{\mathrm{i}}{2\pi}\frac{\omega}{g}\frac{2\cosh kh}{h\left(1+\frac{\sinh 2kh}{2kh}\right)}\frac{1}{H_m^{(2)}\left(kr_0\right)}$$
$$\times\int_{-h}^{0}\int_{0}^{2\pi}\phi_c^{S,R}e^{-\mathrm{i}m\theta}\cosh k\left(h+z\right)d\theta dz \quad \text{Progressive} \tag{4.6a}$$

$$B_{mn}^{S,R} = -\frac{\mathrm{i}}{2\pi}\frac{\omega}{g}\frac{2}{h\left(1+\frac{\sin 2k_nh}{k_nh}\right)}\frac{1}{K_m\left(k_nr_0\right)}$$
$$\times\int_{-h}^{0}\int_{0}^{2\pi}\phi_c^{S,R}e^{-\mathrm{i}m\theta}\cos k_n\left(h+z\right)d\theta dz \quad \text{Evanescent} \tag{4.6b}$$

4.3 Computational study

In this chapter, for a given geometry, the cylindrical coefficients of the scattered wave field (b_m^S and B_{mn}^S) and each radiated wave field ($b_{m,i}^R$ and $B_{mn,i}^R$, where the comma in the subscript separates the coefficient indices, mn, from the degree-of-freedom (DOF) index, i) are found by computing the circular-cylindrical section of the wave field with WAMIT and following the cylindrical surface method described in the previous section. The coefficients are then applied to compute the analytical cylindrical wave fields via Eq. 4.1, which are compared to a wave field computed completely with WAMIT.

It is important to point out a few aspects of the cylindrical representation of the wave field. Firstly, the cylindrical solutions are only valid in the region outside the circumscribing cylinder, and as such cannot be used directly to compute wave forces on the body and one should not expect accuracy of the cylindrical wave field inside the cylinder. Finally, in addition to being functions of the geometry, the cylindrical

coefficients are also functions of the wave period and water depth, and the scattered coefficients are functions of the incident wave direction. The cylindrical solutions have often been used with respect to axisymmetric devices, for which wave direction can be factored out of the coefficients, but for a general geometry, wave direction must be included.

WAMIT returns dynamic pressure at field points instead of velocity potential, where $p = -\mathrm{i}\omega\rho\phi$. WAMIT outputs the diffracted wave field, and so the scattered wave field is formed by subtracting the incident plane wave potential (Eq. 3.73) from the diffraction potential computed by WAMIT.

The circular-cylindrical surface is computed as a grid of $N\theta \times Nz$ discrete points where $N\theta$ is the number of angular directions and Nz is the number of depths measured. The distance r_0 is taken to be just slightly larger than the radius of a circle that circumscribes the geometry. The Fourier transform is performed with an FFT and the depth integration is performed using the trapezoidal method.

The summation in Eq. 4.1 is infinite in both m and n, which in practice must be truncated. As discussed in Section 3.4.7, heaving and surging radiated waves can be accurately produced from only either one or two partial waves respectively. Even for more complex waves, the magnitudes of the coefficients tend to zero as $|m|$ and n increase, which shall be discussed more in Chapter 7. Truncation values of M and N are used, where the m summation goes from $-M$ to M and the n summation goes from 1 to N. A cylindrical wave field is represented by the sum of $(2M+1) \times (N+1)$ partial cylindrical waves.

4.3.1 Far-field approximation

It is also of interest to examine the range of accuracy of the far-field solution, particularly near the body. For convenience, the far-field solution (Eq. 3.93) is repeated here:

$$\phi^{S,R} \approx \sqrt{2\pi} e^{\mathrm{i}\frac{\pi}{4}} f(z) \frac{e^{-\mathrm{i}kr}}{\sqrt{kr}} \mathcal{F}^{S,R}(\theta) \tag{4.7}$$

where the Kochin function, $\mathcal{F}(\theta)$, is computed directly from the progressive cylindrical coefficients (Eq. 3.94):

$$\mathcal{F}^{S,R}(\theta) = \frac{1}{\pi} \sum_{m=-\infty}^{\infty} e^{\mathrm{i}m\frac{\pi}{2}} b_m^{S,R} e^{\mathrm{i}m\theta} \tag{4.8}$$

In the results section, in addition to the cylindrical wave fields, the far-field wave fields are compared for accuracy to the WAMIT wave fields.

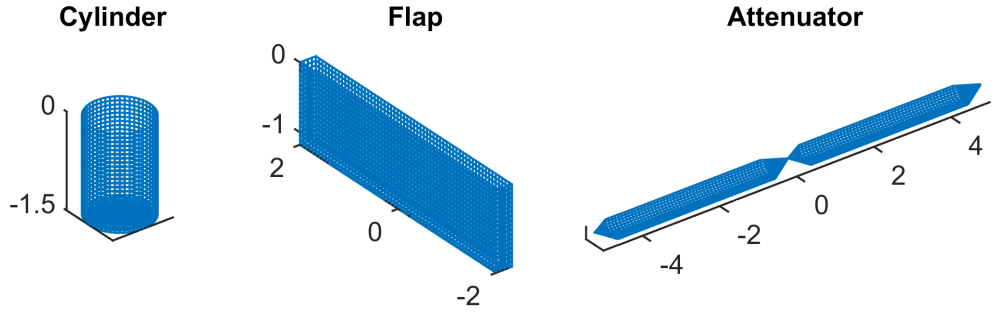

Figure 4.1: The geometries used in this study, which are shown as the panel mesh used in the low-order WAMIT computations. The axes are non-dimensionalized by the cylinder diameter, d.

	Parameters	Volume ($= \frac{3\pi}{8}$)	Motions	
Cylinder	$d = 1$	$\frac{\pi}{4} d^2 c_c$	Heave	$\boldsymbol{n}_3 = \hat{\boldsymbol{k}}$
	$c_c = 1$		Surge	$\boldsymbol{n}_1 = \hat{\boldsymbol{i}}$
Flap	$d_f = 4$	$d_f l_f c_f$	Pitch	$\boldsymbol{n}_5 = (z + c_f)\,\hat{\boldsymbol{i}} - x\hat{\boldsymbol{k}}$
	$l_f = \frac{1}{4}$			
	$c_f = \frac{3\pi}{8}$			
Attenuator	$d_a = \frac{3}{\sqrt{26}}$	$\frac{13}{120}\pi d_a^2 l_a$	Heave	$\boldsymbol{n}_3 = \hat{\boldsymbol{k}}$
	$l_a = 10$		Flex	$\boldsymbol{n}_7 = \lvert z\rvert \operatorname{sign}(x)\,\hat{\boldsymbol{i}} + \lvert x\rvert\,\hat{\boldsymbol{k}}$

Table 4.1: Parameters, volume formulas, values, and generalized motions for the cylinder, flap, and attenuator geometries

4.3.2 WEC types, geometries, and quantities

Four types of WECs are used in this study: a heaving point absorber, a surging point absorber, a terminator, and an attenuator. Descriptions of such WEC types are given in Cruz (2008) and Mei *et al.* (2005). Here, a point-absorber is defined to be a device that is small with respect to the wavelength and, in this case, its width and length are approximately equal, where width refers to a measurement across the designed wave direction and length refers to along the wave direction. A terminator is a device that is much wider than it is long, and an attenuator it a device that is longer than it is wide; for both geometries, the large dimension is of the same order of magnitude of the wavelength.

The heaving and surging point absorbers both use the same geometry, a cylinder. Both are single DOF devices and only move in each one's representative mode of motion. The diameter of the cylinder is d and its draft is c_c.

The terminator is a rectangular flap of width, d_f, length, l_f, and draft, c_f, that rotates about an axis parallel to its width and located at its bottom. It too only moves in a

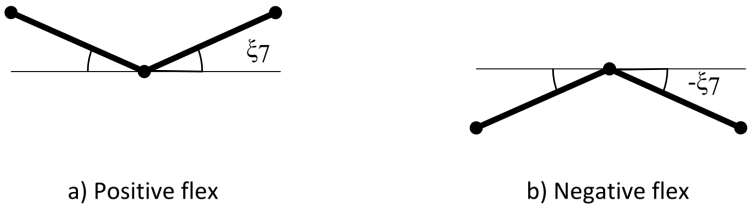

Figure 4.2: Schematic representation of the flex hinge motion.

single DOF.

The attenuator is a hinged raft, similar to a Hagen-Cockerall raft (Mei *et al.*, 2005) or a Pelamis device (Yemm *et al.*, 2012). It consists of two identical bodies that look like pencils sharpened at both ends, connected end-to-end by a hinge that rotates about an axis parallel to its width located at the origin. Power is absorbed through the relative motion about the hinge and this mode of motion shall be referred to as flex. The attenuator considered here is defined such that it has two DOFs, heave and flex, but only absorbs power in flex. Two DOFs were used because flex and heave are coupled in their inertial, hydrostatic, and hydrodynamic forces, which makes for more realistic motions and wave fields. The attenuator has a total length of l_a. The length of each cone portion is five percent of the total length, $0.05l_a$, and the width of the attenuator is d_a. Although the attenuator consists of completely cylindrical bodies, only half of it is submerged.

The flex motion of the attenuator is described by a generalized motion, $\boldsymbol{n}_7$:

$$\boldsymbol{n}_7 = |z| \operatorname{sign}(x)\, \hat{\boldsymbol{i}} + |x|\, \hat{\boldsymbol{k}} \tag{4.9}$$

The motion is symmetric about the origin, where the hinge is located. A flex motion of ξ_7 means that both bodies have been rotated by ξ_7 radians in the xz-plane but in opposite directions. See Figure 4.2. The angle between the bodies is twice the flex magnitude.

For the analysis, length quantities (geometric values, spatial coordinates, wavelength, and water depth) are non-dimensionalized by the diameter of the cylinder. In order to achieve some level of similarity between the different WEC designs, all WEC geometries have the same submerged volume. The geometric dimensions of each WEC were chosen 1) to conform to the definition of each device design, 2) to maintain the volume restriction, and 3) so that each WEC has its peak performance in a similar range of frequencies. The calculation of volume and the nondimensional parameter values are shown in Table 4.1, along with the generalized motion functions, $\boldsymbol{n}_i$. The resulting

submerged geometries along nondimensional axes are shown in Fig. 4.1.

The mass matrix for the cylinder consists of its scalar mass. For the flap, it is the moment of inertia of a box about an axis located at its bottom. Both of which can be computed analytically in a straightforward manner.

The mass matrix of the attenuator requires the evaluation of Eq. 3.130, where the density is taken to be constant. Values of the normal functions are given in Tab. 4.1:

$$\begin{aligned} M_{11} &= \rho_b \int\int\int_{\mathcal{V}_b^T} \boldsymbol{n}_3 \cdot \boldsymbol{n}_3 d\mathcal{V} \\ &= m && \text{heave-heave} && (4.10a) \\ M_{12} = M_{21} &= \rho_b \int\int\int_{\mathcal{V}_b^T} \boldsymbol{n}_3 \cdot \boldsymbol{n}_7 d\mathcal{V} \\ &= \rho_b \int\int\int_{\mathcal{V}_b^T} |x| \, d\mathcal{V} && \text{heave-flex/flex-heave} && (4.10b) \\ M_{22} &= \rho_b \int\int\int_{\mathcal{V}_b^T} \boldsymbol{n}_7 \cdot \boldsymbol{n}_7 d\mathcal{V} \\ &= \rho_b \int\int\int_{\mathcal{V}_b^T} \left(z^2 + x^2\right) d\mathcal{V} && \text{flex-flex} && (4.10c) \end{aligned}$$

As expected, the heave-heave term is simply the mass. The flex-flex term has the same value as would the pitch-pitch term as long, as the hinge is located at the center of gravity (CG). The flex-heave term needs to be evaluated independently, but for an simple geometry, it can be found by summing $m_i \cdot |x_{cg,i}|$ where m_i is the mass and $x_{cg,i}$ is the x location of the CG of the i^{th} component body. The attenuator is composed of two cylinders and four cones.

4.3.3 WEC wave field, motions, and power

The total WEC wave field is:

$$\phi = \phi^I + \phi^S + \sum_{i=1}^{N} \xi_i \phi_i^R \tag{4.11}$$

The incident wave is a plane wave traveling in the direction β (Eq. 3.71):

$$\phi^I = \mathrm{i}a\frac{g}{\omega} f(z) \, e^{-\mathrm{i}k(x\cos\beta + y\sin\beta)} \tag{4.12}$$

and the scattered and radiated wave fields are either those computed completely by WAMIT, the cylindrical wave fields (Eq. 4.1) or the far-field wave fields (Eq. 4.7), where the coefficients are computed using the cylindrical surface method.

The body motions are computed as (Eq. 3.132):

$$\left(-\omega^2 \left(\boldsymbol{M} + \boldsymbol{\mathcal{A}}\right) + \mathrm{i}\omega \left(\boldsymbol{D} + \boldsymbol{\mathcal{B}}\right) + \boldsymbol{K} + \boldsymbol{C}\right) \boldsymbol{\xi} = \boldsymbol{f}^D \tag{4.13}$$

For the single DOF devices, Eq. 4.13 becomes a scalar equation.

The excitation force, added mass and damping matrices are computed directly by WAMIT. For the flex motion of the attenuator, this required the use of the generalized modes functionality of WAMIT. A generalized mode is defined by writing a function in Fortran that describes the generalized motion, which is passed to WAMIT at run time via a DLL. For the definition of the newmodes see WAMIT, 2012, Chapter 9.3.

For the cylinder and the flap, the hydrostatic restoring force is scalar, can be computed in a straight-forward manner, and the values returned by WAMIT are used.

However, additional computation must be performed for the attenuator. For the standard 6 DOF rigid body motions, WAMIT returns an accurate hydrostatic matrix. However, WAMIT computes a generalized hydrostatic matrix, but it only includes the effect of the hydrostatic fluid force and not any effects of the body weight. That is, WAMIT computes:

$$C_{ij} = \rho g \int\int_{S_b} \left(\boldsymbol{n}_i \cdot \hat{\boldsymbol{k}} + \nabla \cdot \boldsymbol{n}_i\right) \boldsymbol{n}_j \cdot \boldsymbol{n} dS \tag{4.14}$$

but not

$$C_{ij} = \rho g \int\int_{S_b} \left(\boldsymbol{n}_i \cdot \hat{\boldsymbol{k}} + \nabla \cdot \boldsymbol{n}_i\right) \boldsymbol{n}_j \cdot \boldsymbol{n} dS + g \int\int_{S_b^T} \left(\rho_b \boldsymbol{n}_i \cdot \hat{\boldsymbol{k}}\right) \boldsymbol{n}_j \cdot \boldsymbol{n} dS \tag{4.15}$$

So, the hydrostatic force for the attenuator is computed externally to WAMIT using a custom panel approach. This computation was performed in the Matlab package mwave (See Appendix B.1).

For all devices, the power take-off (PTO) damping and spring matrices are linear mechanical force quantities that can be set arbitrarily to control the body motions and resulting power absorption. For the sake of realism, these values are limited to positive quantities and for the attenuator, the matrices are zeros everywhere except for a positive real quantity in the flex-flex location. Because each device only absorbs power in a single DOF, the power absorption computed from body motions is a scalar equation:

$$P = \frac{1}{2} \omega^2 D \left|\xi\right|^2 \tag{4.16}$$

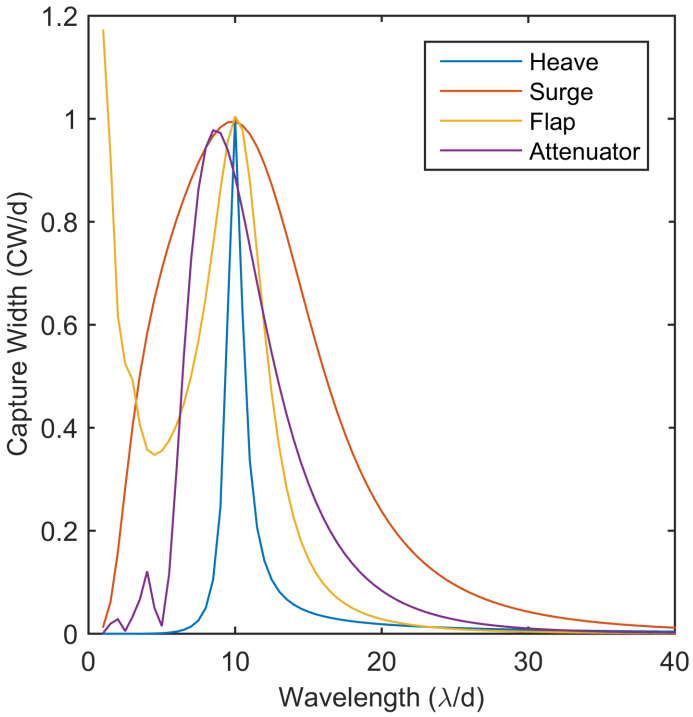

Figure 4.3: WEC performance as a function of nondimensional wavelength

To achieve similarity in the total wave field, the mechanical stiffness and PTO damping quantities are found so that for the wave: $\lambda/d = 10$, $\beta = 0°$, the capture for all geometries is close to $CW = 1$, where the capture width is given by Eq. 3.142. The capture width curves are shown in Fig. 4.3. It is important to note that the D and K values for each WEC are not the values for optimal power capture, and in fact may degrade the power absorption of the WEC significantly. With that in mind, the performance of each design should not be compared based on Fig. 4.3, and the comparison and evaluation of WEC designs is not the purpose of this chapter.

4.4 Results and discussion

In this section, the cylindrical wave fields and the far-field wave fields shall be compared to the BEM wave fields produced by WAMIT. Results from WAMIT have been validated (e.g. Payne *et al.* (2008)) and WAMIT is widely accepted as state-of-the-art for producing accurate linear wave results. Since the cylindrical coefficients and the Kochin function are computed from WAMIT results, it may seem circuitous then to compare their wave fields to those of WAMIT. However, the coefficients were computed from only a small portion of the WAMIT wave field, and the comparison assesses the accuracy

the cylindrical coefficients and the validity of Eq. 4.1 and Eq. 4.7 for representing the entire wave field.

To make this assessment, really only a comparison of the scattered wave fields and the unit-amplitude radiated wave fields, both of which depend on geometric shape but not body motions, needs to be made. Motions are not truly necessary to this analysis. However, it is convenient to look at the total wave field as described by Eq. 4.11 because 1) it is the wave field that exists in reality, 2) we can compare one wave field instead of two or three, and 3) for the purpose of measuring the relative error.

Take the relative error to be the absolute value of the difference between the approximate wave field (i.e. cylindrical or far-field) and the WAMIT wave field divided by the WAMIT wave field.

$$\text{Err}\,(\%) = \left| \frac{\phi_a - \phi_{WAM}}{\phi_{WAM}} \right| \times 100 \tag{4.17}$$

The magnitude of the total wave field goes to a value of 1 with increasing distance from the body, while the magnitudes of the scattered and radiated wave fields go to 0. Insignificant errors that appear far from the body may appear inappropriately large if they are measured in the scattered or radiated wave fields, but the error will be proportional to its actual impact if measured in the total wave field.

Although the wave field varies as a function of depth, it is convenient to plot the surface elevation, $\eta = -\frac{\mathrm{i}\omega}{g}\,\phi|_{z=0}$. As shall be seen, the progressive wave dominates and its depth dependence of $\cosh k\,(z+h)$ is well accepted in linear wave theory, so a comparison of the surface elevation seems sufficient. Each wave field is plotted as the absolute value of the surface elevation, $|\eta|$, as a function of space. Since the incident wave amplitude is 1, a value of $|\eta| = 1.1$ indicates that the wave height at that location is 10% higher than the undisturbed incident wave height. Four regular wave fields are considered: $\beta = 0°$ at three wavelengths $\lambda/d = 3,\ 10,\ 30$, and $\beta = 30°$ at $\lambda/d = 10$. All wave fields are computed for a water depth of $h/d = 10$.

4.4.1 Numerical considerations

As discussed in Section 4.3, a finite number of field points, $N\theta \times Nz$, covering a circular cylinder of radius r_0 are computed by WAMIT to find the cylindrical coefficients.

In θ, points are evenly spaced from 0 to $2\pi \times \left(1 - \frac{1}{N\theta}\right)$, and the number of points is taken to be a power of 2 in order to facilitate the use of the FFT. One could use a different range of angles (e.g. $-\pi$ to π) if the integral $\left(\int_{-\pi}^{\pi} \{\}\, e^{-\mathrm{i}m\theta} d\theta\right)$ is evaluated directly. However, if an FFT is used, the angles should begin at $\theta = 0$ so that the phase angles of the transformed coefficients are correct.

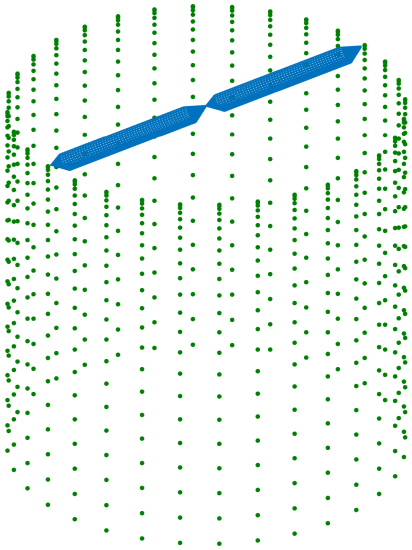

Figure 4.4: Attenuator geometry inside example cylindrical point surface of $N\theta = 32$, $Nz = 21$ points.

The number of points in the θ direction needs to be high enough to resolve each circular frequency, m, where M is the highest circular frequency employed. By Nyquist, $N\theta \geq 2M$, but in practice, $N\theta$ should be at least five or ten times greater than M.

A similar relation holds for the depth, $Nz \geq 2\left(\frac{k_N}{2\pi}\right)$, where k_N is the wave number of the highest evanescent wave component implemented. However, it was found that the value of Nz was actually driven by the progressive wave number, k. For high k (short waves), the velocity potential decays quickly with depth, and to accurately resolve this decay a high point density near the free surface is needed. Due to similar considerations, for the measurment of water run-up on emergent bodies, Newman and Lee (1992) recommend cosine spacing in the body's paneling for BEM computation. Here, cosine spacing is also used, where the z points were computed as $z = h\left(\cos\left(0, \frac{\pi}{2(Nz-1)}, \frac{\pi}{(Nz-1)}, \ldots, \frac{\pi}{2}\right) - 1\right)$. Figure 4.4 shows an example cylindrical surface of $N\theta = 32$, $Nz = 21$ points circumscribing the attenuator. However, for the results, for all geometries and wave fields a much higher point density of $N\theta = 256$, and $Nz = 201$, was used.

WAMIT wave fields were calculated using the low-order panel method. For which, the WAMIT manual, Section 3.6 warns against making field point measurements too close to the body. It suggests the minimum distance be greater than the distance from one panel center to its neighbor (WAMIT, 2012). For all geometries, the average panel side

length is about 0.065, and so the wave field was computed no closer than a distance of 0.1. That is, r_0 was taken to be the radius of the circle that circumscribes the geometry plus 0.1.

The M and N cutoff values varied for each geometry and wave condition. The cutoff M value was determined so that the progressive wave coefficients of circular modes $-M$ and M were at least 10^6 times as large as the largest progressive wave coefficient: $10^6 \times |b_M|\,,\ 10^6 \times |b_{-M}| \geq \max(|b_m|)$. If a coefficient was 10^6 times smaller than the largest coefficient, its impact could be ignored. Furthermore, WAMIT only returns 6 significant figures, so it would be unreasonable to expect that coefficients that were 10^6 times smaller than the largest coefficient had meaningful values.

The number of depth modes implemented was found by computing the relative error for increasing N values until a point of diminishing returns. Figure 4.5 shows the relative error (Eq. 4.17) in the total cylindrical heaving WEC wave fields for $\lambda/d = 10$, $\beta = 0°$ as a function of the number of evanescent wave modes included, N. Increasing N from 0 decreases the error - the red region gets smaller. However, above $N = 6$, increasing N has little effect. This can be seen more clearly in bottom figure in 4.5, which is a plot of the mean of the error at all points in the wave field outside the radius, r_0. As N goes from 0 to 6, the mean error decreases, and above $N = 6$, the mean error actually increases a bit. The cutoff N value was selected when the marginal reduction in the mean error of the wave field at $N + 1$ was less than 0.1%.

The accuracy of the heaving WEC wave field at this wave condition is improved with the inclusion of evanescent modes, but it should be noted that the error scale in Fig. 4.5 has a maximum value of 1%, and so the improvement is still relatively small. In the next Section, along with the plots of the wave field and error, the values of M and N are also included.

4.4.2 Wave fields

Figures 4.6-4.9 show the WAMIT, cylindrical, and far-field wave fields and error plots for each wave condition. The WAMIT wave fields show the geometry in white. No geometry is present in the computation of the cylindrical and the far-field wave fields, and so their plots show a white circle which represents the circumscribed circular cylinder used for the calculation of the coefficients. Both the geometry and circle are shown in the plots of the wave field error as it is a combination of both wave fields.

Figure 4.6 shows the wave fields for the $\lambda/d = 10$, $\beta = 0°$ wave. $\beta = 0°$ means the incident wave travels from left to right. All wave fields plots use the same color scale. The color scale of the cylindrical error is the same for all geometries and the color scale of the far-field error is the same for all geometries. All wave fields show standing waves

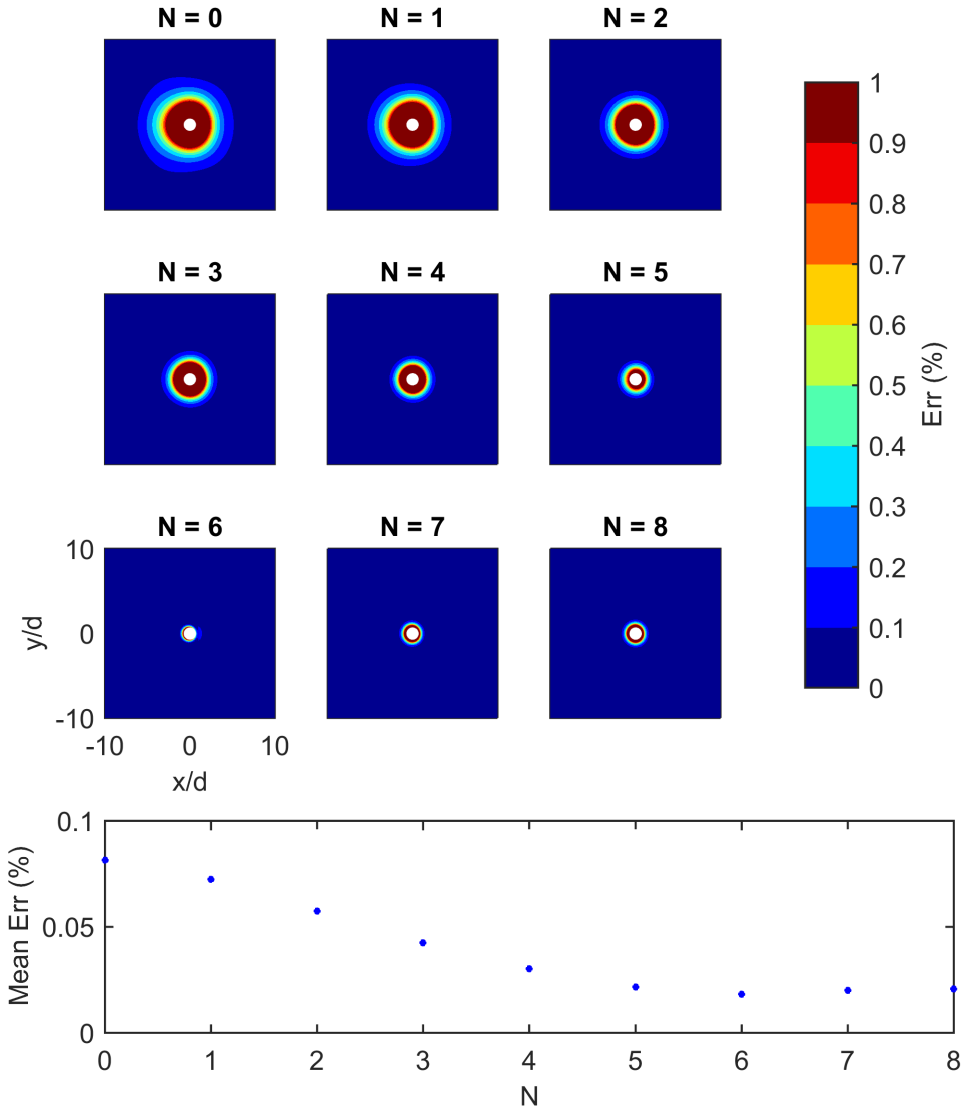

Figure 4.5: Accuracy of the wave field of the heaving cylinder for various evanescent cutoff values, N.

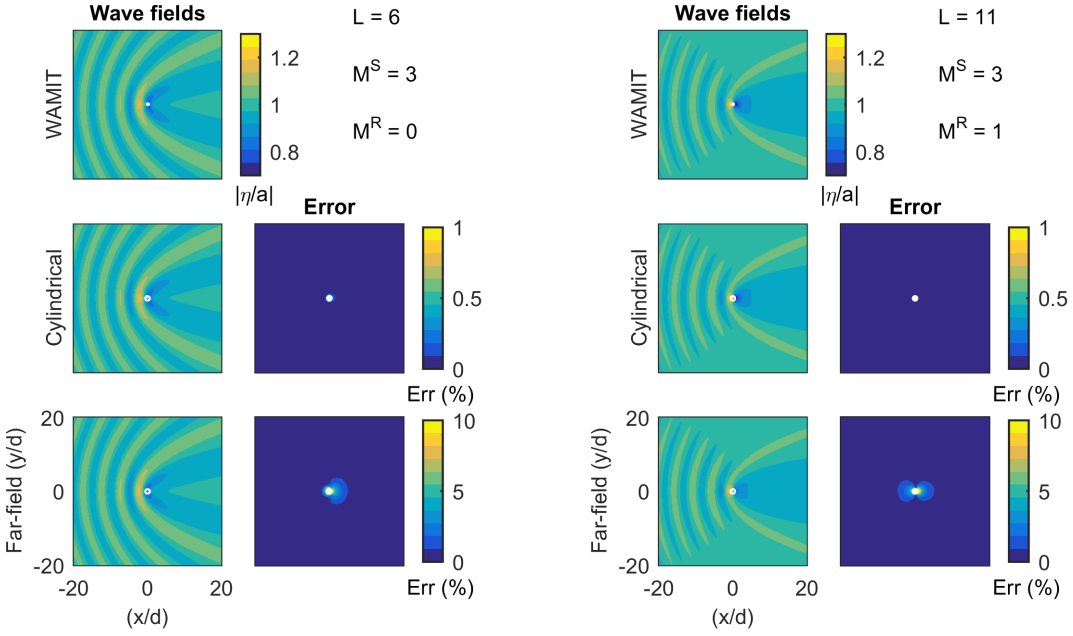

(a) Heaving cylinder

(b) Surging cylinder

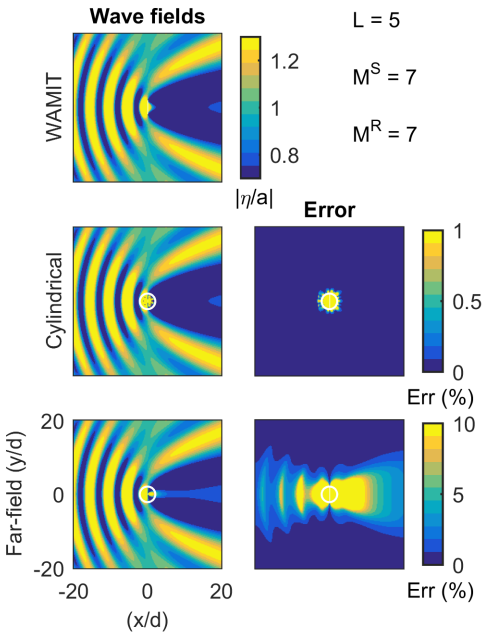

(c) Flap

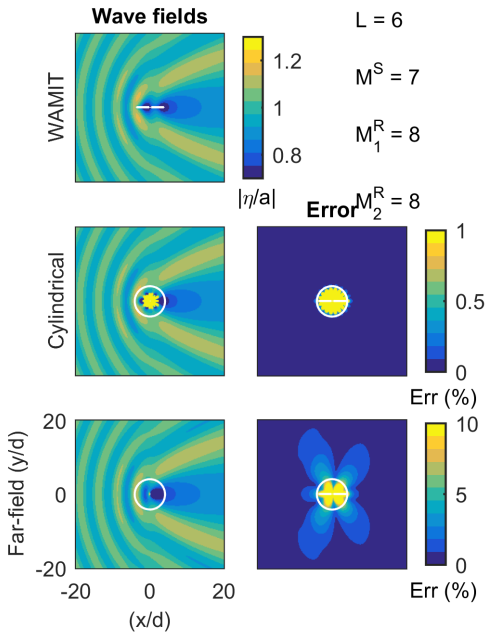

(d) Attenuator

Figure 4.6: Wave field results for $\lambda/a = 10$, $\beta = 0°$

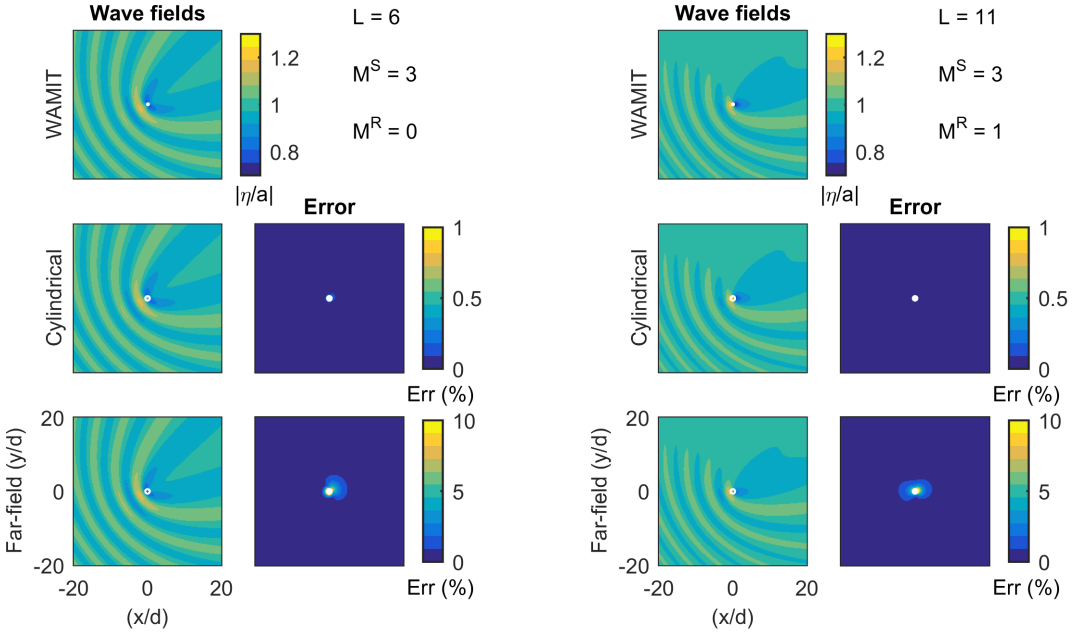

(a) Heaving cylinder

(b) Surging cylinder

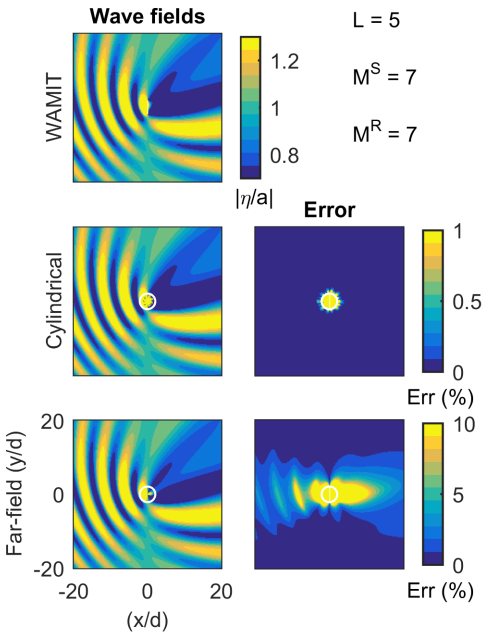

(c) Flap

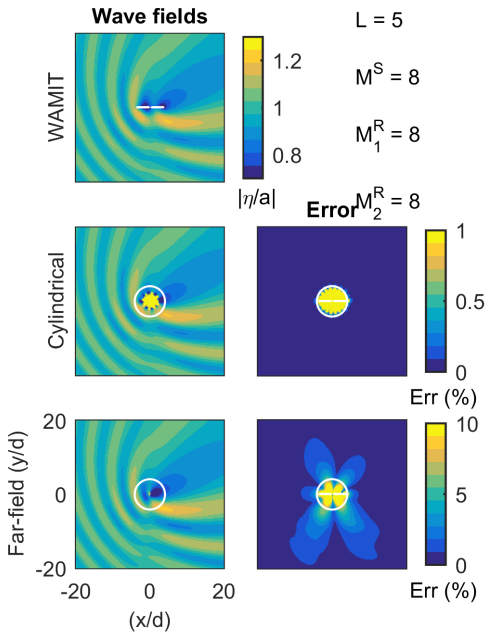

(d) Attenuator

Figure 4.7: Wave field results for $\lambda/a = 10$, $\beta = 30°$

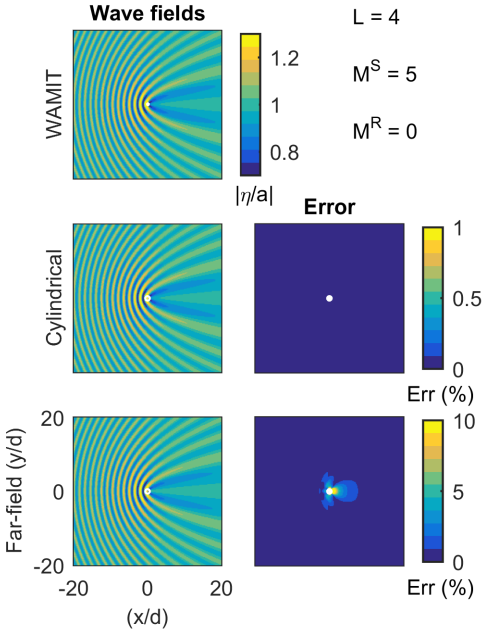

(a) Heaving cylinder

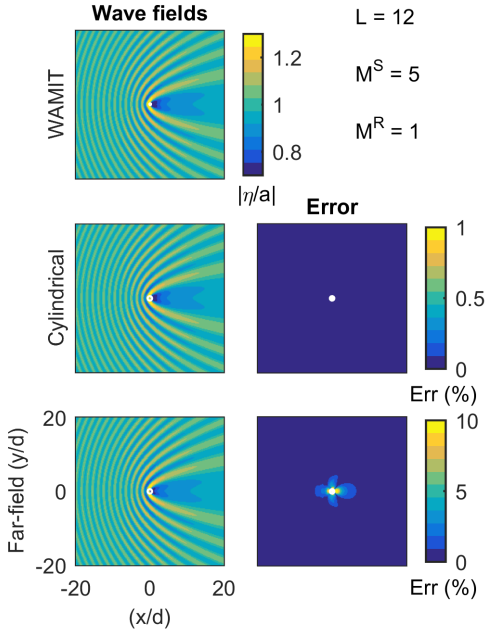

(b) Surging cylinder

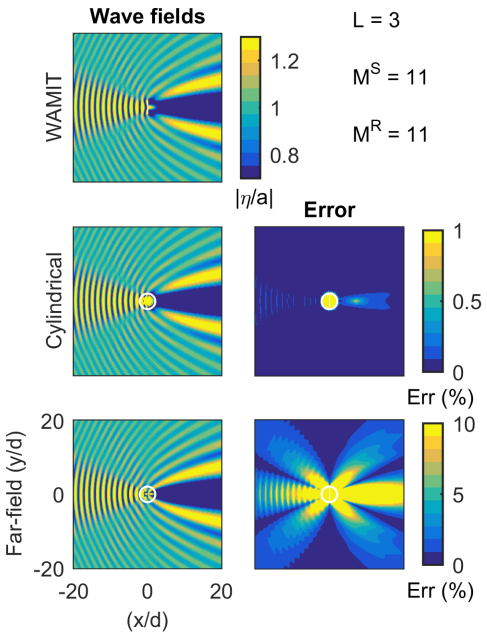

(c) Flap

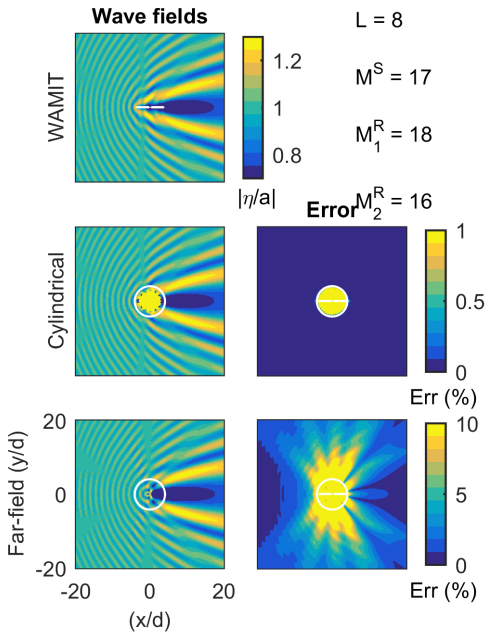

(d) Attenuator

Figure 4.8: Wave field results for $\lambda/a = 3$, $\beta = 0°$

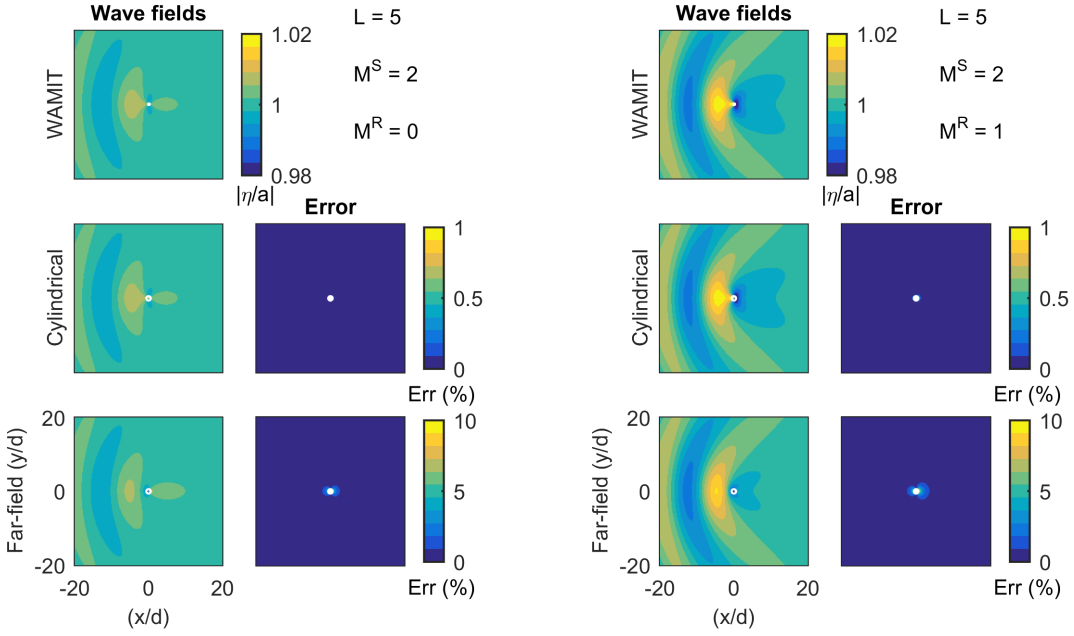

(a) Heaving cylinder

(b) Surging cylinder

(c) Flap

(d) Attenuator

Figure 4.9: Wave field results for $\lambda/a = 30$, $\beta = 0°$

(alternating hot and cool colors) shaped like parabolas wrapping around the device and a wave shadow (wave height less than 1.0) in its lee. Qualitatively, there appears to be agreement between the WAMIT, cylindrical, and far-field wave fields for all geometries.

However, a quantitative understanding is gained by considering the error plots. The cylindrical wave fields of the heaving and surging cylinders have a relative error less than 0.1% for the entire region outside the body. For the flap, the cylindrical wave field error is less than 0.1% for most of the wave field outside of the circumscribed circle, however, near the circle the error is a little higher. Within the circumscribed circle, the relative error is above the upper bound of the error range, but as discussed in Section 4.3, the wave fields in this region are not expected to match. For the cylindrical wave field of the attenuator, the error is less than 0.1% for the region outside and even slightly inside the circle. The cylindrical wave field of the attenuator is as good as that of the cylindrical WECs and the cylindrical flap wave field is only slightly worse.

Examination of the scattered, M^S, and radiated, M^R, truncation values also provides information. For the cylinder, $M^S = 3$; only a few partial waves are required to represent the scattered wave field. For the heaving cylinder, $M^R = 0$. As was discussed in Section 3.4.7, only the $m = 0$ partial wave component is needed to represent the isotropic wave due to a heaving axisymmetric body. Similarly, for the surging wave field, $M^R = 1$. Only the $m = -1$ and $m = 1$ wave components are needed to represent a surging wave. The numerically derived partial wave coefficients agree well with theory. The M^S and M^R values for the flap and attenuator are higher. More partial waves are need to represent their wave fields, because they are less geometrically circular.

The far-field wave field error is higher than the cylindrical wave field error for all geometries, and it is higher for the less-circular geometries (flap and attenuator) than for the cylinder. As the name implies, the far-field approximation should only be valid in the far field. That said, the error is still mostly less than 5% outside of the the circumscribed circle and as one would expect, it decreases with increasing distance from the geometry. For both the heaving cylinder and the surging cylinder, the relative error is less than 1% within a distance of half a wavelength from the origin. For the attenuator, the radial distance to a maximum far-field error of 1% is less than two wavelengths from the origin. And for the flap, within a distance of 4.5 wavelengths, the relative error less than 1%.

The asymptotic form of the Hankel function, $H_m^{(2)}(kr)$, is valid for $\frac{r}{\lambda} \gg \left|m^2 - \frac{1}{4}\right|$, which means that the more partial waves used (i.e. higher M) the greater the radial distance until the far-field approximation is valid. This corresponds to the results for far-field accuracy - the flap and the attenuator have higher M^S and M^R values and are less accurate near the body than the cylinder. The partial waves are also modified by the coefficient, b_m, which generally decreases with increasing m, which explains why the

M values of the attenuator are higher than that of the flap but the minimum accurate distance of the flap is greater. Perhaps a method can be derived to determine the minimum accurate distance based on the magnitude and number of partial waves.

Figure 4.7 shows the results for the wave $\lambda/d = 10$, $\beta = 30°$. Although they are skewed compared to the $\beta = 0°$ case, all wave fields show parabolic standing waves and a wave shadow. Both the cylindrical and the far-field wave approximations are as good at this angle of incidence as they are for the $\beta = 0°$ case. When a wave is incident at an angle of 0° to a geometry with port-starboard symmetry, the wave fields are port-starboard symmetric. The cylindrical wave field coefficients are also symmetric or antisymmetric about $m = 0$. However, when the incident wave angle is non-zero, the wave field is not symmetric, and correspondingly neither are the cylindrical wave field coefficients. The non-zero incident wave angle was selected to show that the cylindrical and far-field approximations can just as easily represent an asymmetric wave field as they can a symmetric one.

Figure 4.8 shows the result for the incident wave $\lambda/d = 3$, $\beta = 0°$, a short wave. For all WECs except the flap, the cylindrical wave field error is less than 0.1% outside of the circumscribed circle. However for the flap, there is a slightly higher error up to about 0.6% in the region behind the device. The error is due to inaccuracies in the computation of the depth integral. As discussed in Section 4.4.1, for short waves, the velocity potential decays quickly with depth, which requires a high point resolution near the free surface. The error could probably be decreased by improving this resolution, but here the error is not excessive and it helps to demonstrate where inaccuracies in the calculation can arise.

The $\lambda/d = 3$ far-field wave fields show more relative error than for $\lambda/d = 10$. For the heaving and surging cylinders, distances of slightly less than 3 wavelengths are required to reach a relative error less than 1%. And for the flap and attenuator the decay to 1% occurs after about 20 wavelengths for each device. High M values are employed for the scattering coefficients of the cylinder and for both the scattering and radiated coefficients of the flap and attenuator. More m partial waves are needed to describe how the relatively large bodies effect the wave field. The high M also explains why the far-field approximation is less accurate.

Figure 4.9 shows the result for the incident wave $\lambda/d = 30$, $\beta = 0°$, a long wave. None of the geometries significantly affect the wave field through scattering or power absorption, and the wave elevation plots are significantly scaled down as compared to the other wave conditions. The cylindrical and far-field wave fields are also more accurate than in previous wave cases. The cylindrical wave field error outside of the circumscribed circle is similar to results for other wavelengths. The far-field error is much improved. For all geometries, the far-field approximation reaches 1% accuracy

within a third of the wavelength from the origin.

4.5 Summary

Over a range of wave conditions, the linear wave fields of a variety of WECs are well represented by the summation of the product of coefficients and cylindrical partial waves. The method described herein for the computation of the coefficients is quite accurate for all geometries and waves considered. The asymptotic form of the cylindrical wave field, or the far-field wave field, is also shown to be a reasonable approximation. When a body is geometrically non-circular and/or when the body is large compared to the wavelength (short waves), more m partial waves are needed to accurately represent its cylindrical wave field. As more m partial waves are required, the far-field approximation is less accurate close to the body.

With the cylindrical coefficients for a given WEC and wave condition, one can analytically compute the linear wave field at any point over a constant depth bathymetry. The coefficients also enable the implementation of Kagemoto and Yue's (1986) interaction theory, which can expedite the computation of wave farm performance and wave field effects, and is considered in detail in Chapter 6. The cylindrical wave fields produced by the cylindrical surface method are not accurate inside the cylinder circumscribing the geometry, but this limitation does not affect the use of Kagemoto and Yue's (1986) theory, as theirs has a similar limitation - the origin of one geometry cannot be inside the circumscribed cylinder of another. Kagemoto and Yue (1986) also include the effects of evanescent waves by evaluating the scattered wave due to an incident evanescent wave. Because WAMIT only implements incident progressive waves, these effects cannot be included when the coefficients are found by the computational method presented here. However, as shown in Section 4.4.1, the magnitude and range of the evanescent waves can be isolated, and may not play a significant role in interactions.

Previous work has shown that the wave field of a cylinder or a point source could be formulated with circular-cylindrical waves, but it was not well understood that cylindrical waves are valid for an arbitrary geometry. Although the terminator and attenuator geometries are not circular in shape, their wave fields are well represented by the summation of circular cylindrical waves. Due to the interaction of the cylindrical radiated and scattered waves with the planar incident wave, the wave field patterns for all geometries, circular or not, show mostly parabolic standing waves due to wave reflections and a wave shadow. In general, for any geometry or wave condition, linear floating-body wave fields can be computed using the cylindrical surface method and represented as a summation of partial cylindrical waves.

Chapter 5

Cylindrical Surface Method: Experiments

5.1 Introduction

In the previous chapter a new method was developed for finding the cylindrical, progressive and evanescent, scattered and radiated coefficients by manipulating wave field measurements made over a circular cylindrical control surface that circumscribes the body. The method was applied computationally using WAMIT to find the coefficients for a variety of geometries under various wave conditions. The method is general and can be applied to numerical results or experiments as long as linearity is given or assumed.

In this chapter, wave tank experiments are described, in which the cylindrical surface method is applied to find the cylindrical coefficients. The experiments were conducted in the University of Edinburgh Curved Tank. An array of 59 wave gauges was arranged in a circle-spoke pattern, where the circle of wave gauges was necessary for deriving the cylindrical coefficients, and the spokes, which extended radially further afield, were used for validation. Two simple body geometries, each with a single degree-of-freedom (DOF) were considered: a flap and an attenuator. Tests were conducted with each body in forced harmonic motion to measure the radiated wave. The wave field was also measured in the absence of the body to find the incident wave field, and with each body held fixed to find the diffracted wave field. The difference of these two produced the scattered wave field.

Results are shown for the measured wave field, the cylindrical wave field where the coefficients were produced from the experimental measurements, and for a cylindrical wave field where the coefficients were found in WAMIT. In many cases the cylindrical wave field produced from measurements is a good representation of the complete measured wave field, and is almost always better than that produced by WAMIT. However, there are two issues: 1) the waves were not completely linear, and to varying degrees, higher-order harmonics were present; and 2) reflections of the radiated and scattered waves off the tank walls and paddles degraded the match and most likely caused errors in the

cylindrical coefficients, which may have been significant in some cases. Overall though, the results are very good, and serve to validate the cylindrical wave representation of the wave field of floating bodies.

The content of this chapter was published in McNatt *et al.* (2015b).

5.2 Theory

The theory behind the experimental approach is essentially the same as that presented in Section 4.2. The method given in Section 4.2 required that measurements be made over depth to isolate the progressive from the evanescent waves and the evanescent waves from one another. Making such measurements experimentally is challenging.

However, evanescent waves decay exponentially in the radial direction so that at a distance far enough from the origin, only progressive waves are significant. At such a distance, the scattered or radiated wave elevation can be approximated as:

$$\eta^{S,R}(r,\theta) \approx \sum_{m=-\infty}^{\infty} b_m^{S,R} H_m^{(2)}(kr)\, e^{\mathrm{i}m\theta} \tag{5.1}$$

which means that if one makes measurement of the surface elevation over a circle radius, $r = r_0$, which is large enough to neglect evanescent wave modes:

$$\eta_c^{S,R} = \eta^{S,R}(r = r_0, \theta) \tag{5.2}$$

the m^{th} cylindrical coefficient can be found using a Fourier transform as:

$$b_m^{S,R} = \frac{1}{2\pi} \frac{1}{H_m^{(2)}(kr_0)} \int_0^{2\pi} \eta_c^{S,R} e^{-\mathrm{i}m\theta} d\theta \tag{5.3}$$

An important aspect of implementing this version of the method is to determine the radius that is sufficiently large. To do so, preliminary computational work was performed to check the extent of the evanescent modes. This is discussed in Section 5.3.4.

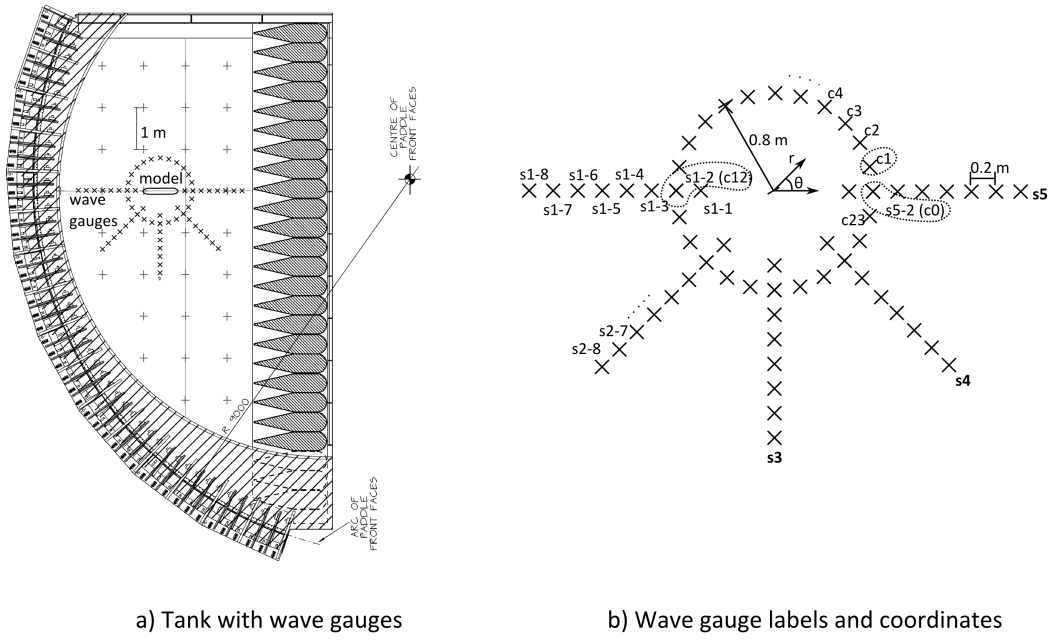

a) Tank with wave gauges

b) Wave gauge labels and coordinates

Figure 5.1: The figures show the experimental test setup including a) the location of wave gauges in the wave tank, and b) the wave gauges with their coordinate system and labels.

5.3 Experimental design

The experiments were designed to measure the wave elevation, so as to derive the cylindrical coefficients and test the analytical representation of the wave field. Critical to this analysis is the design of a wave gauge array. Furthermore, the scattered and radiated coefficients need to be derived separately, and so multiple experimental setups were devised to do this. For variety, the analysis was performed on two different wave-energy-converter (WEC) like geometries: a flap (or terminator) and an attenuator for three wave frequencies: 0.8, 1, and 1.25 Hz.

5.3.1 Wave tank

The experiments were conducted in The University of Edinburgh Curved Wave Tank. The tank was refurbished in June 2014, shortly before the experiments were conducted in November 2014. Prior to the refurbishment, the tank performance was analyzed by Gyongy *et al.* (2014) in order to validate a computational model of the tank. The tank (see Figure 5.1-a) has a curved array of force-feedback absorbing wave makers subtending an arc of 96 degrees at a radius of 9 m. Opposite the wave makers is a 12 m length of "beaches" made up of porous material, and along one side is a glass wall of

length 4.4 m. The wave makers are capable of generating waves over a frequency range of 0.5-1.5 Hz. The water depth at which the tests were performed was 1.16 m.

5.3.2 Wave measurements

The wave gauge array consisted of a circle of 24 wave gauges, and 5 spokes of 8 wave gauges each. Measurements from the circle of gauges are used to find the cylindrical coefficients via Eq. 5.3, and measurements along the spokes are used to validate the analytical wave field given by Eq. 5.1. The array is shown in Figure 5.1 in a schematic of the curved tank as well as close up with its coordinates and labels. The center of the circle was taken to be the origin of the wave gauge array. The directional coordinate, θ, was defined so that $\theta = 0$ corresponded to the $\beta = 0$ incident wave direction of the tank, which was also parallel to the tank's glass wall. Positive θ is counter-clockwise.

The circle of wave gauges was positioned at a radius of $0.8\,m$, and were numbered $c0 - c23$ over even increments in θ of $\pi/12$ radians. The spokes extended radially along constant θ. They were numbered $s1 - s5$, and along each spoke were 8 wave gauges, numbered for example: $s1 - 1$, $s1 - 2, \ldots$ going radially outward. The $s1$ spoke was located at $\theta = \pi$, $s2$ at $\theta = \frac{5}{4}\pi$, $s3$ at $\theta = \frac{3}{2}\pi$, $s4$ at $\theta = \frac{7}{4}\pi$, and $s5$ at $\theta = 0$. The spacing between gauges along the spokes was $0.2\,m$, and the first gauge was located at $r = 0.6\,m$. Five of the wave gauges were part of both the circle and the spokes; these were in the 2 position of the spokes (e.g. $s1 - 2$). The total number of wave gauges employed was 59.

The gauges were resistive wave gauges. They were made up of two $3\,mm$ diameter stainless steel round bars with a working length of $0.3\,m$ and a separation distance of $20mm$. The wave gauges were wired to one of 3 older model Wave Gauge 8 measurement boxes by Edinburgh Designs. Only 3 wave gauge boxes were available, each box had only 8 measurement channels, and one box had two broken channels, which meant that only 22 wave gauge channels were active for any given run. Consequently, each test was performed 3 times in order to capture all of the wave gauge information.

Calibration is a very important aspect of using wave gauges. Calibrating 59 wave gauges could be arduous, however, a calibration system was devised which allowed all the active wave gauges to be calibrated simultaneously. The entire wave gauge rig was supported by two beams that spanned the tank from the wave maker side to the beach side (see Figure 5.2). Each end of each beam was supported by a car scissor jack, next to which was a ruler. The entire rig could be raised and lowered by a known amount by adjusting these scissor jacks, which would in turn raise or lower the wave gauges in the tank. It was estimated that the rig could be set to a vertical accuracy of less than $0.5\,mm$.

A five point calibration over a range of $\pm 40\,mm$ was used for each gauge, and the

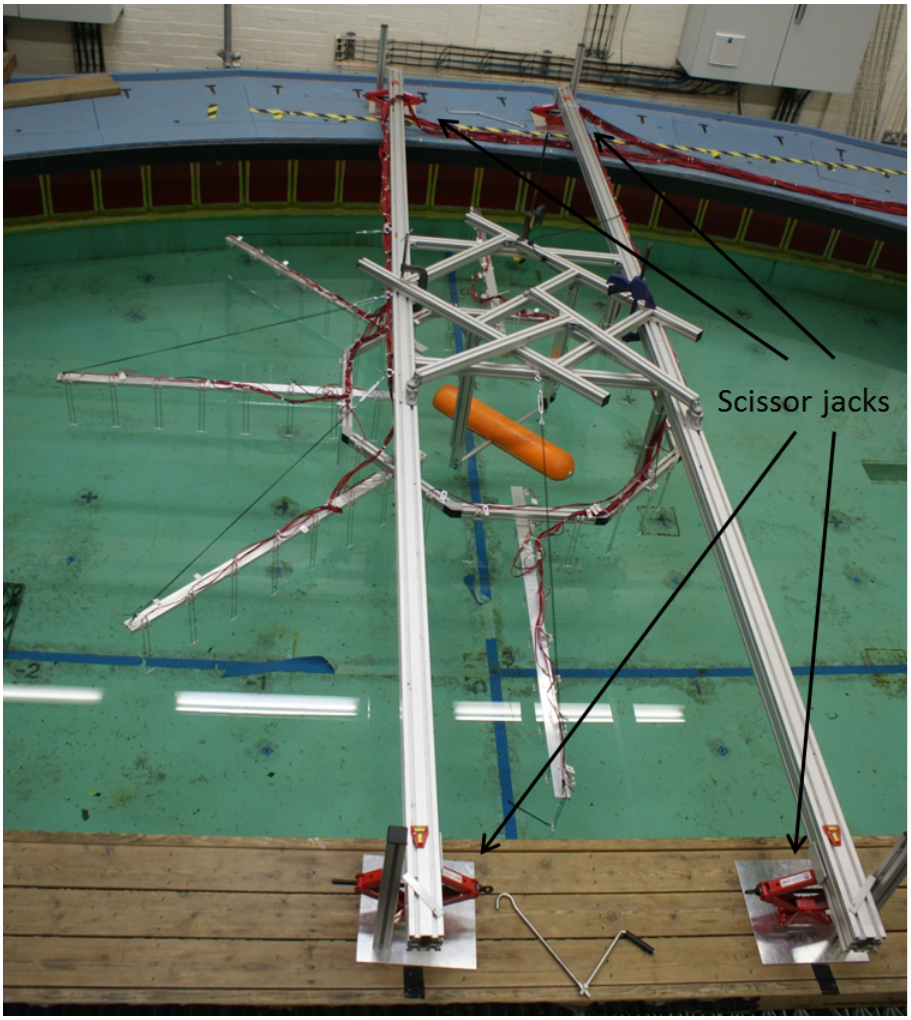

Figure 5.2: The picture shows the experimental setup in the wave tank. One can see the two cross-beams which support the wave gauges and model from overhead. The scissor jacks which were used to calibrate the wave gauges are indicated. The model is the attenuator at an orientation of $45°$.

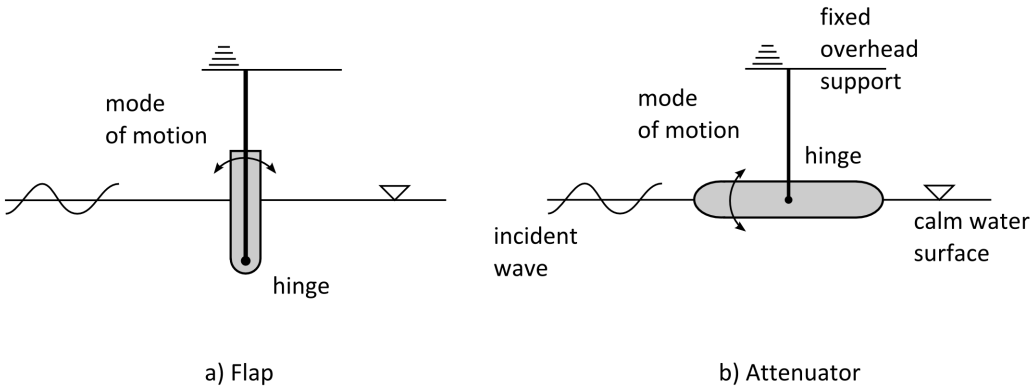

Figure 5.3: The diagram shows the bodies indicating specifically the location of the hinge and the mode of motion.

gauges were found to be very linear. The wave gauges were calibrated at least everyday, or multiple times per day if the active wave gauges were switched.

A calibrated wave gauge measures wave elevation as a function of time. The wave signal was periodic, but not necessarily sinusoidal (i.e. linear). For the theory, the complex linear amplitude is needed. To extract the amplitude, an FFT was performed on the time domain signal of each wave gauge, after a point in time when the waves appeared to have reached a steady state. Then the amplitude and phase of the lowest order signal, which always conformed to the frequency of interest was used for the complex linear amplitude. Care was taken to ensure that an integer number of periods were present in the measurement window to produce a frequency domain signal with minimal leakage.

5.3.3 Physical models

Two different types of WEC models were used in the analysis: a flap and an attenuator. Each only had a single degree of freedom. The flap model was hinged at the bottom and is the same conceptually as the terminator presented in Chapter 4, because its across-wave dimension was significantly larger that its along-wave dimension. However, the attenuator was different than the attenuator presented in Chapter 4. It was a horizontal cylinder with spherical ends that pitched about its midpoint, which was located at the still water level. The single degree of freedom was maintained through hinges that were fixed to a frame mounted on beams that were suspended above the water. Figures 5.3-a) and -b) show a diagram of the flap and attenuator and indicate each ones mode of motion. Figure 5.2 shows the attenuator in its setup.

Figures 5.4-a) and -b) show the dimensions of the flap and attenuator. The flap had a width of $0.6\,m$, a height of $0.5\,m$, a thickness of $0.08\,m$, and a draft of $0.4\,m$. The corners and edges were rounded slightly to reduce viscous effects. The attenuator had

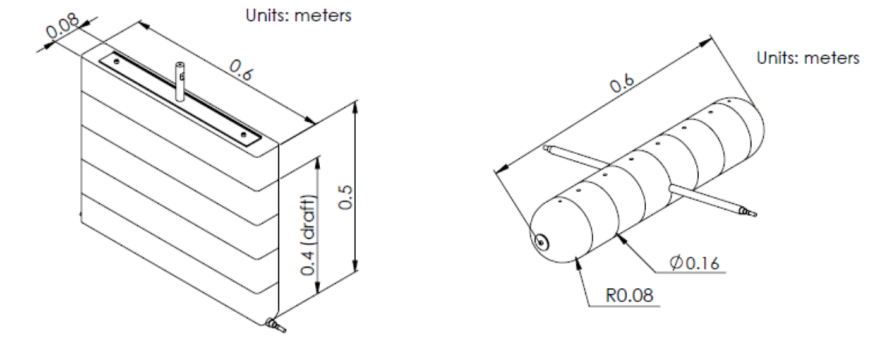

Figure 5.4: Shown are drawings of each geometry model assembly indicating dimensions in meters.

an overall length of $0.8\,m$, and a diameter of $0.16\,m$. The ends were hemispherical, and the attenuator was half submerged in still water. The models were constructed of a high-performance foam called Divinycell around an internal aluminium frame.

The physical setup also allowed the body orientation to be changed relative to the wave gauge coordinate system to achieve different incident wave directions. Two body orientations were considered: $0°$ and $45°$ (incident direction of $-45°$), where the orientation is a rotation of the body in the θ coordinate. See Figures 5.1-b and 5.2.

The models were not true WECs as they did not intentionally absorb wave power - there was no power-take-off (PTO) mechanism. This approach was taken, because a PTO was not necessary to the analysis, and the lack of one reduced the complexity of the physical model design.

5.3.4 Evanescent waves

As was discussed in Section 5.2, because only surface elevation is measured, one cannot separate the evanescent wave components from the progressive. The circular array of wave gauges was designed to be at a radius outside of the expected significant extent of the evanescent waves. This extent was estimated computationally during the experimental design phase. Using the computational cylindrical surface method, the progressive cylindrical coefficients were computed for the physical model geometries, and the wave field made up of just the progressive waves was compared to a wave field computed completely by WAMIT. The relative difference (or error) between the wave fields is defined as $100 \times \left|\eta^{Pr} - \eta^{W}\right|$, where η^{Pr} is the wave field of progressive waves and η^{W} is the total wave field computed with WAMIT.

Figure 5.5 shows the relative difference for the diffracted wave fields at an incident

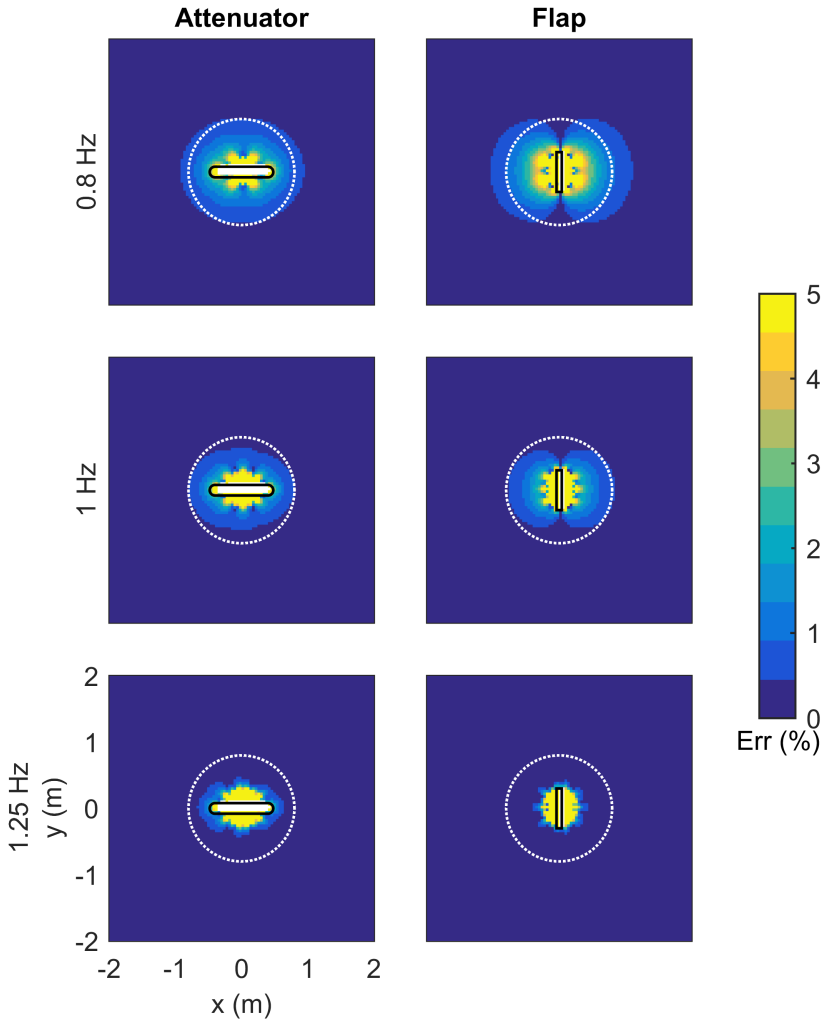

Figure 5.5: The figure shows the relative difference (error) between the diffracted wave fields with and without evanescent waves. The relative difference is defined as $100 \times \left|\eta^{Pr} - \eta^{W}\right|$, where η^{Pr} is the wave field of progressive waves and η^{W} is the total wave field computed with WAMIT. This gives the extent of the evanescent wave effects. The white dashed line is the location of the circle of wave gauges.

direction $\beta = 0$ for both the attenuator and the flap for waves at 0.8, 1, and 1.25 Hz. Also shown is a white dashed line that indicates the location of the circle of wave gauges. Note that the scale is from 0 to 5%. For 1 and 1.25 Hz, the relative difference at the location of the circle is $< 0.5\%$ and for 0.8 Hz it is on the order of 1%. The radiated wave fields and the diffracted wave fields at different angles showed similar results. It seems safe to assume that the wave field measured around the circle of gauges is purely progressive.

5.3.5 Run conditions

Three frequencies were considered for the tests: 0.8, 1, and 1.25 Hz. Plane waves were used as the incident waves, and for some conditions the body was rotated to change the incident wave angle. At each frequency, three tests were performed: incident, diffracted, and radiated. Each test was repeated at least twice, then the mean of the linear amplitude and mean of the linear phase were taken as the final results.

Incident, η^I

A plane wave at each frequency was measured with no body present.

Diffracted, $\eta^I + \eta^S$

For these tests, the models were fixed in their mean position and subjected to incident waves. The diffracted wave field is the sum of the incident and the scattered wave fields, and so the scattered wave field was then found by subtracting the incident from the diffracted. That is, the difference of the complex linear amplitudes was taken between the diffracted and the incident wave fields to get the scattered wave field. The diffracted wave field was computed for two body orientations: 0° and 45°. For both the incident and diffracted wave conditions, the start of the measurements was triggered by a signal from the wave makers, which ensured a phase coherence between the incident and diffracted wave measurements as well as between repeated tests.

Radiated, $\xi\eta^R$

The radiated wave field was created by forcing a harmonic motion on the body in its degree of freedom in the absence of incident waves. The radiated wave field is described by $\xi\eta^R$, where η^R is the unit amplitude wave field and ξ is the complex motion amplitude. The harmonic forcing was produced by driving the motion with a linkage connected to a cam, which was connected to a motor. To produce a sinusoidal motion in angle, the linkage was designed to be long with respect to the lever arm on

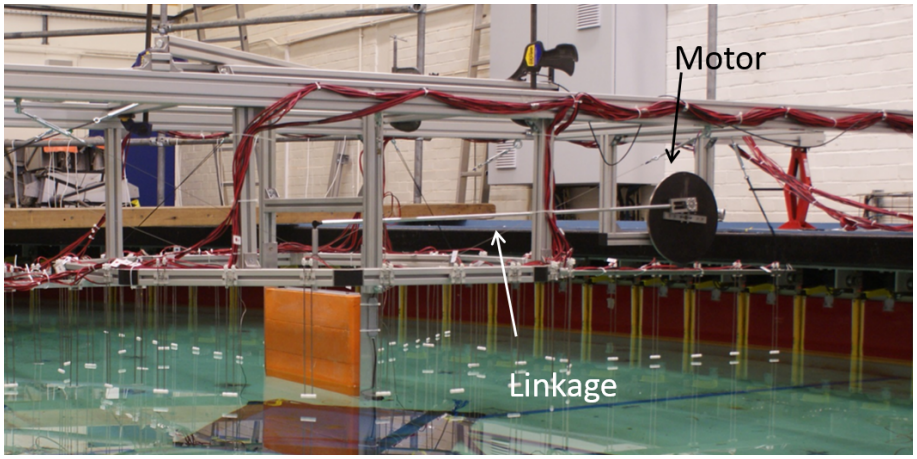

Figure 5.6: The picture shows the radiated wave setup for the flap. Indicated are the motor (one sees the steel wheel used as inertia) and the linkage to the body, which was designed to be long compared to the amplitude of motions. As shown the setup is not in its running position, but is raised out of the water.

the body and the radius of the cam. Figure 5.6 shows the radiated wave setup for the terminator.

The motor was run open loop to simplify the setup. A large steel plate was used as an inertial mass to help maintain a harmonic motion. However, it was difficult to tune the motion exactly to the frequency of interest, and the motion drifted slightly in frequency. In the radiated wave field tests, the drive frequency was off by a maximum of 2% of the desired frequency, which would result in approximately a 4% error in wavelength.

The motion of the body, ξ, was measured with a waterproof contactless sensor that was connected at the hinge location. The total radiated wave, $\xi\eta^R$, was measured by the wave gauges. There was no mechanism for triggering the measurements, and so measurements made by repeat tests were aligned in phase, by normalizing the wave phase to the phase of the body position.

5.3.6 Experimental data repository

All the experimental data from these tests, including raw data, setup descriptions, pictures and videos, and Matlab scripts are available for free online, see Appendix B. The author hopes that the data can be useful to other scientists and engineers.

5.4 Results and discussion

Results are shown in Figures 5.9-5.11 for a selection of conditions: the flap radiated wave field at 1 Hz, the flap oriented at 0° scattered wave field at 0.8 Hz, and the attenuator oriented at 45° scattered wave field at 1.25 Hz. The results were selected to show some of the best and worst matches as well as to cover all frequencies. The complete set of all experimental results can be found in Appendix C.

The plots show three lines:

Measured:
Magnitude of the linear wave amplitudes from tank measurements

Cylindrical:
Magnitude of the wave amplitudes predicted by Eq. 5.1, where the cylindrical coefficients were computed from the measurements via Eq. 5.3

WAMIT:
Magnitude of the wave amplitudes predicted by Eq. 5.1, where the cylindrical coefficients were computed with WAMIT following Chapter 4

The top plots show the points around the circle of wave gauges, where the abscissa is angular position. Plots along the left-hand side show the spokes of wave gauges. For the scattered results, the magnitude of the incident wave, $\left|\eta^I\right|$, is given, which was taken as the mean of the magnitudes of all wave gauges. For the radiated wave results, the magnitude of the angle of motion, $|\xi|$, is given.

Also shown in each figure are the magnitudes of the cylindrical coefficients, $|b_m|$, as a function of m, and the magnitude of the Kochin function, $|\mathcal{F}(\theta)|$, of the radiated or scattered wave. See Section 3.4.6.

The R^2 value for both the Cylindrical (R^2_C) and the WAMIT (R^2_W) data is given, where: $R^2 = 1 - \sum (y_i - f_i)^2 / \sum (y_i - \bar{y})^2$, and y_i is the measured data point, f_i is the Cylindrical or WAMIT point, and $\bar{y}$ is the mean of the measurements. The R^2 value indicates how well a model fits a given set of data relative the variance of the data, where a value closer to 1 indicates a better fit. R^2 was computed using only the data points along the spokes; the points over the circle are neglected, because this is where the Cylindrical values were fitted to the measurements originally. The R^2 values for all cases are summarized in Table 5.1.

Although the plots only show the magnitude of the wave amplitudes, the R^2 also takes into account the phase difference. Equation 5.1, of course, models both the amplitude and the phase. When results are plotted as $\mathrm{Re}\{\eta\}$ (or $\mathrm{Im}\{\eta\}$) which shows the phase of the wave, the match between the Measurements and the Cylindrical model is more striking, as can be seen in Figure 5.7, which shows the Flap radiated wave at 1 Hz along spoke s1.

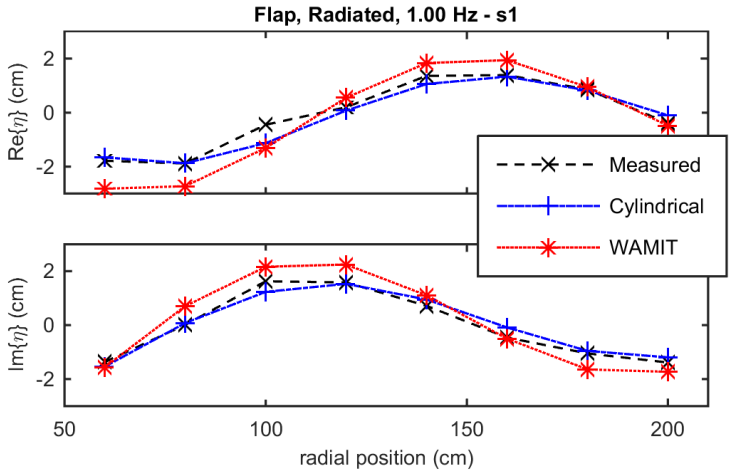

Figure 5.7: The figure shows the real and imaginary parts of the linear amplitude, which indicates the phase alignment, of spoke $s1$ for Flap in the radiated wave setup at 1 Hz. The full result is shown in Figure 5.9.

Body	Wave	Orient (deg)	Freq (Hz)	R_C^2	R_W^2
Flap	Radiated	-	0.8	0.78	0.68
			1	0.95	0.80
			1.25	0.90	0.78
	Scattered	0	0.8	0.93	0.91
			1	0.97	0.89
			1.25	0.91	0.80
		45	0.8	0.86	0.80
			1	0.92	0.84
			1.25	0.91	0.84
Attenuator	Radiated	-	0.8	0.60	0.61
			1	0.75	0.79
			1.25	0.86	0.86
	Scattered	0	0.8	0.68	0.64
			1	0.76	0.70
			1.25	0.75	0.74
		45	0.8	0.68	0.56
			1	0.82	0.57
			1.25	0.35	0.18

Table 5.1: The R^2 values for the Cylindrical fit to the data (R_C^2) and for the WAMIT fit to the data (R_W^2) for each condition. The complete set of all experimental results can be found in Appendix C.

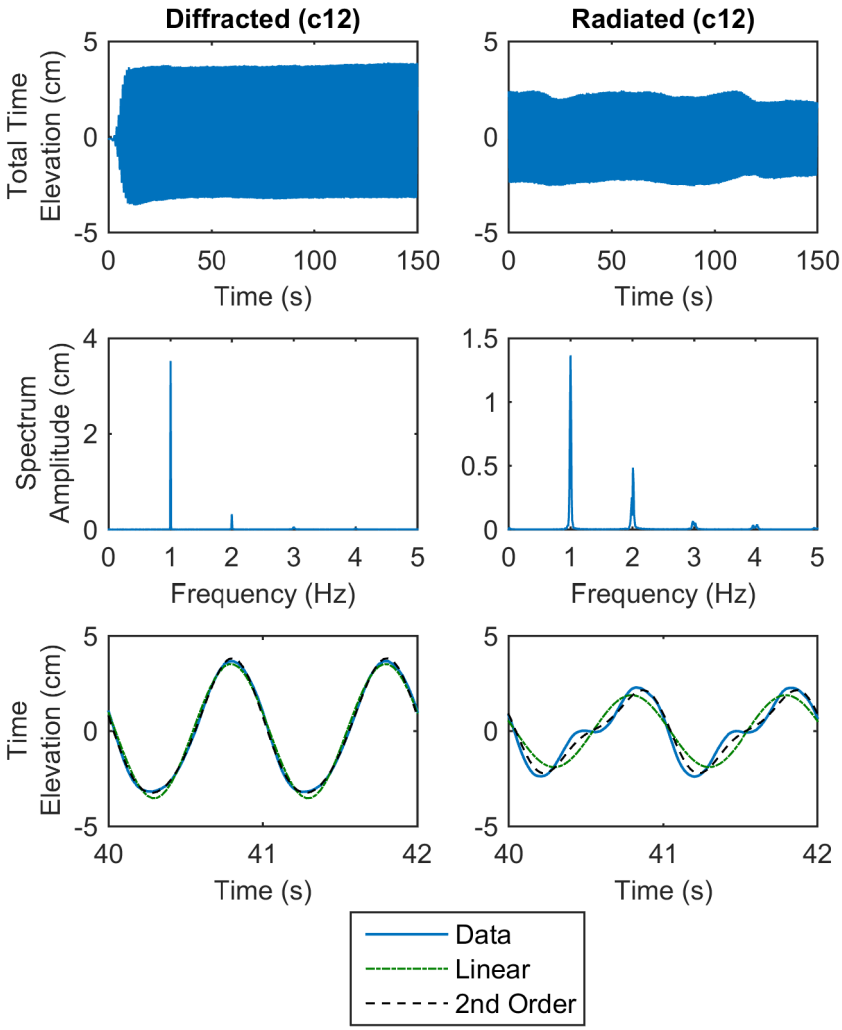

Figure 5.8: Figure shows plots of the full run-time time series, amplitude spectra, and close-up of the time series for wave gauge c12 (also s1-2) for both the diffracted and radiated wave field of the Flap at 1 Hz.

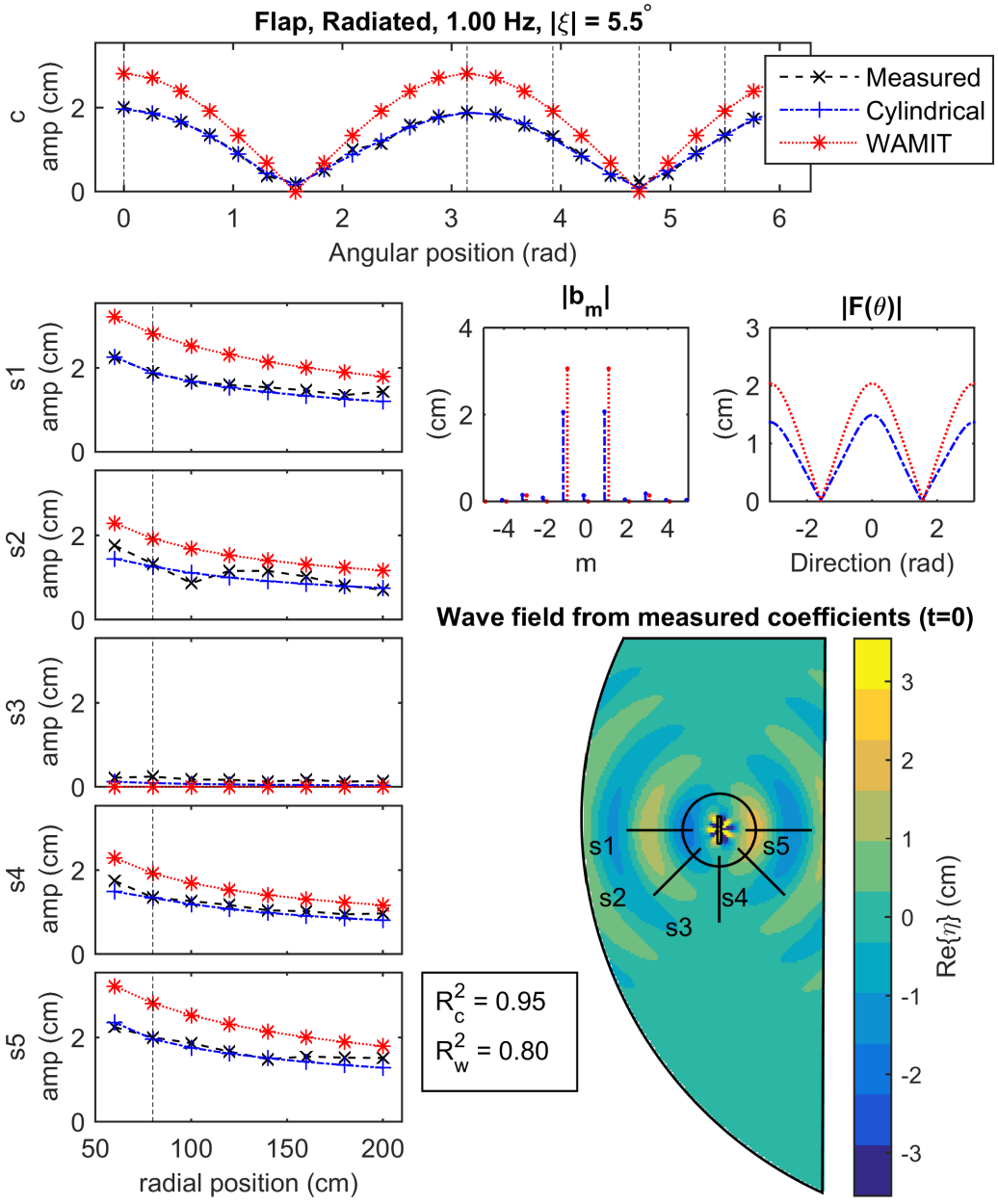

Figure 5.9: Flap, radiated wave field, 1 Hz

Figure 5.9 shows the results from the Flap radiating at 1 Hz. Around the circle of gauges, the Cylindrical results and the Measured results are virtually indistinguishable. In a way, this should not be surprising as the Cylindrical results are fitted around this circle with a Fourier transform. However, they do not necessarily match everywhere as the Cylindrical results are produced with 11 cylindrical (Fourier) coefficients (a truncation value of $M = 5$), which may not be sufficient to reproduce the circle Measurements exactly. However, in this case, the Flap produces a very nice clean pitch type radiated wave - a wave that has one phase on the front of the body and the opposite phase in the back. This type of wave is dominated by the $|m| = 1$ cylindrical coefficients. In Figure 5.9, the $m = \pm 1$, a_m, coefficients are dominant, while the other a_m coefficients are nearly 0. Comparison of the Cylindrical to the Measured out along the spokes is also very good, and here is where the judgment of the Cylindrical should be made - that is, the Cylindrical was devised from measurements around the circle, and comparison along the spokes shows the goodness-of-fit of Eq. 5.1, where the coefficients are computed with Eq. 5.3. There is some disagreement at the far ends of the spokes, but generally the trend of the Cylindrical matches the Measured well.

Comparison of the WAMIT modeled results shows that WAMIT over estimates the magnitude of the measured linear radiated wave. However, WAMIT does accurately predict the pitch wave behavior, and it shows the correct trends in magnitude and phase. One explanation for WAMIT's over-estimate is that the measurements shown in the plots are of the linear amplitudes, and in almost all cases, higher order harmonics were present, which WAMIT does not model. That is, for a given motion, WAMIT models the wave that is generated as completely linear, whereas in physical reality, some of the wave energy is in higher-order harmonics and the measurements given here only show the linear portion.

Figure 5.8 shows plots of the full run-time time series, amplitude spectra, and close-up of the time series for wave gauge c12 (also s1-2) for both the diffracted and radiated wave field of the Flap at 1 Hz. Firstly, as mentioned, higher-order components are present. For the diffracted case, the second-order component (the spike in the amplitude spectrum at 2 Hz) has an amplitude which is about about 9.1% of the linear component, which is only 0.8% by energy. (Energy is proportional to amplitude squared.) For the radiated case, which is the case considered in Figure 5.9, the amplitude of the second order harmonic is 32% of the primary, which means that it has about 10% of the energy, a fairly significant value. The plots at the bottom show a close up of the time-domain signal, and one can see that the 2nd order fit, which is the sum of the sinusoidal signal at the primary frequency and one at the second order frequency, does improve the fit to the data. For the diffracted case, it improves it only marginally, while for the radiated it makes a significant difference.

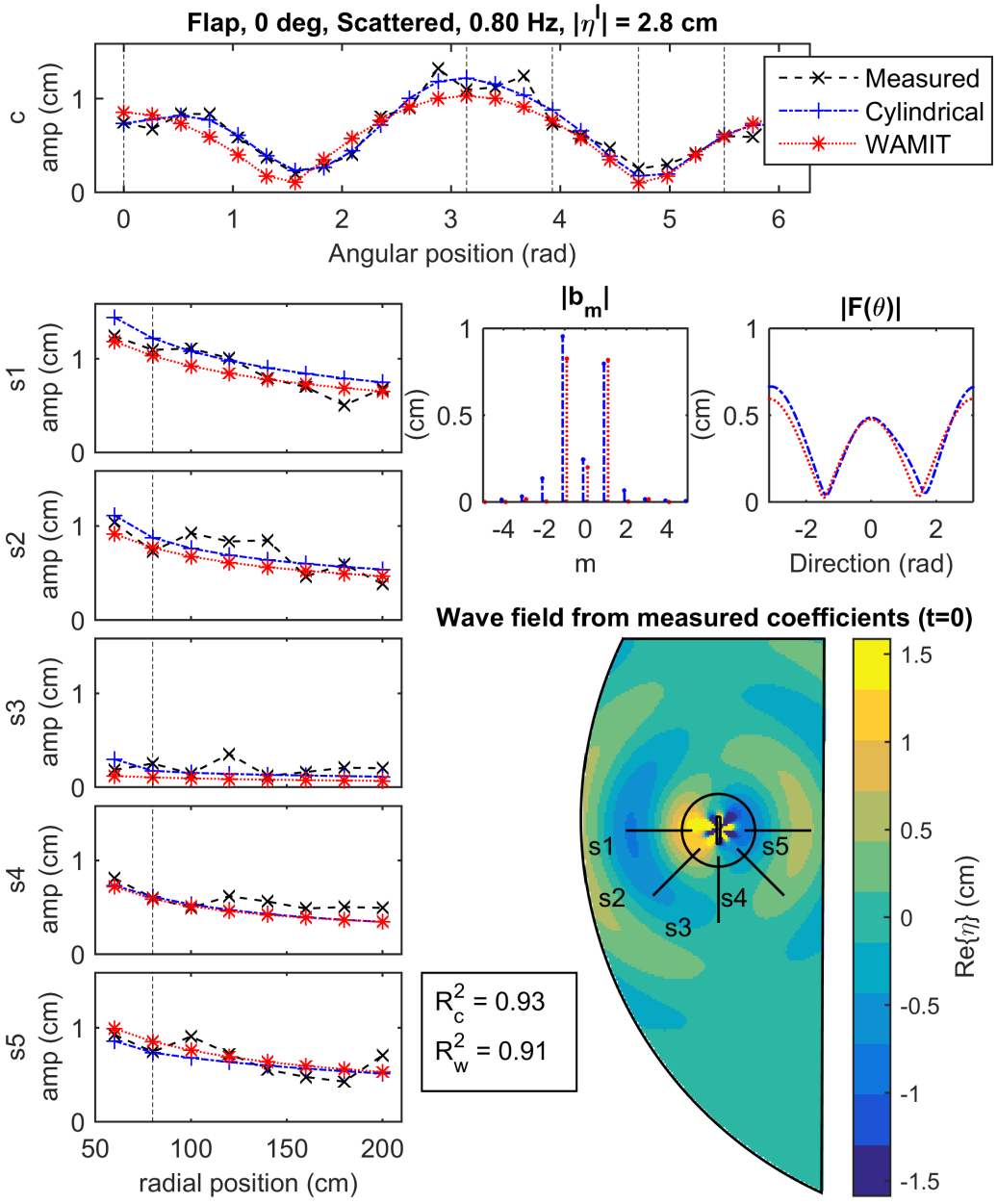

Figure 5.10: Flap, 0° orientation, scattered wave field, 0.8 Hz.

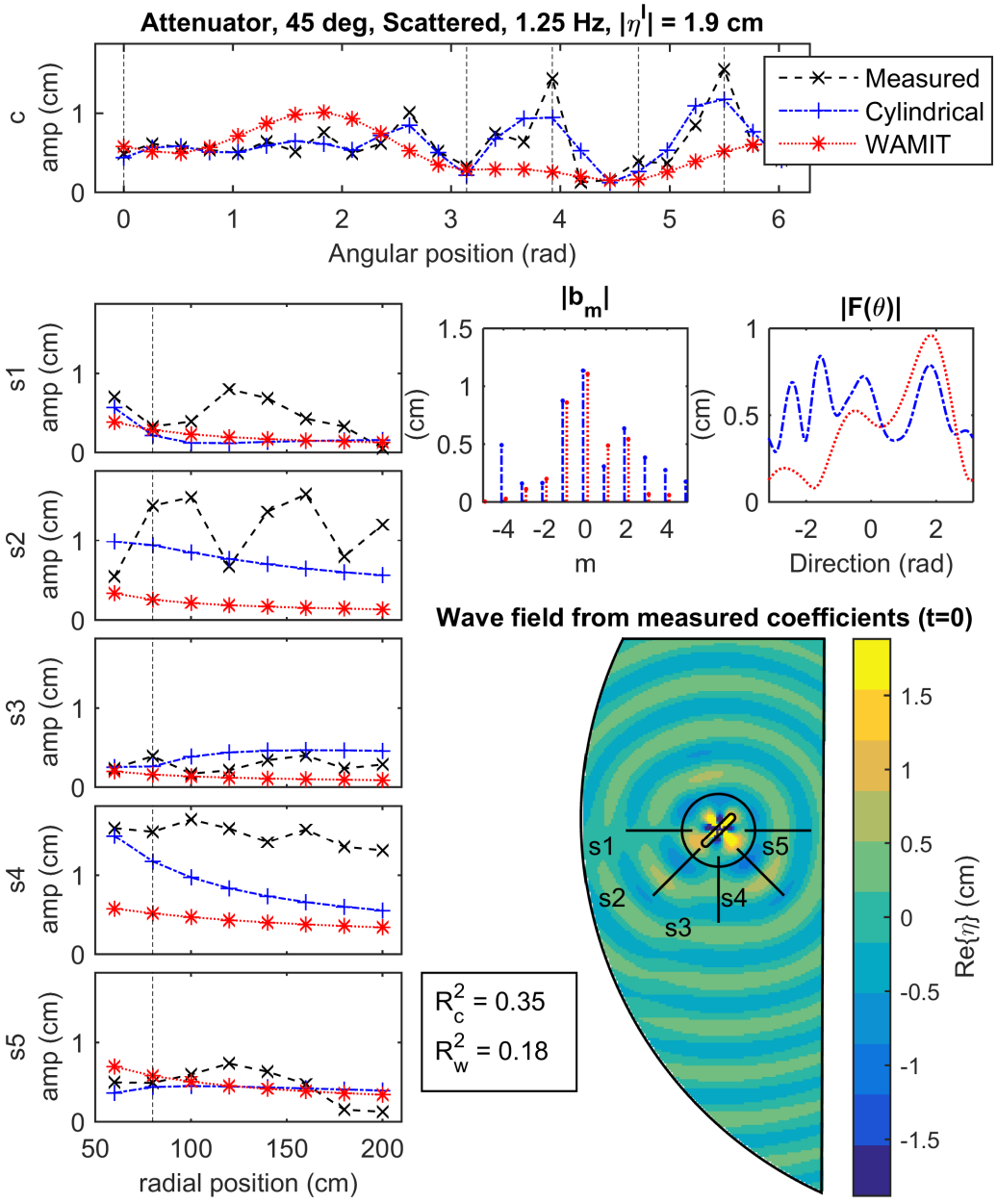

Figure 5.11: Attenuator, 45° orientation, scattered wave field, 1.25 Hz.

Although the second-order portion is significant in the radiated wave field, the cylindrical theory given herein only applies to linear waves, and so the second-order component cannot be addressed. This partially explains the disagreement between WAMIT and the Measured data. For example, at that wave gauge (c12), WAMIT predicts an amplitude of 2.8 cm, while the linear measured amplitude is only 1.9 cm, a difference of 50%.

Also here, it is important to note that the radiated wave signal is not as clean as the diffracted signal - the amplitude of the time-domain signal varies with time, the spectrum has a bit of what looks like leakage around the frequency peaks, and the close up of the time-domain signal show a fairly nonlinear wave. These issues were not necessarily intrinsic to the radiated wave with this body, but more likely due to the experimental setup. As was mentioned in Section 5.3.5, the motor was driven open loop and it was difficult to maintain its precision. If the experiments were to be repeated, it would be a good idea to have feedback control on the motor. In the amplitude spectrum, the spreading around the peaks is not leakage as the result of signal processing, but a real result due to a slight variation in the drive frequency of the motion over time. Because of this spreading, the sum, rather than a single peak, of all complex amplitudes with energy near each peak was used to produce the linear amplitudes and phases.

Figure 5.10 shows results for the scattered wave of the Flap oriented at 0° for a wave with $0.8\,Hz$. The Cylindrical is not as exact around the circle as it was for the radiated wave case, and going out along the spokes, one sees some slight oscillations in the measured data that are not present in the Fit or WAMIT. These oscillations are standing waves due to reflections of the scattered wave off of the wave tank walls and paddles. The reflections are not of the incident wave, because the total incident wave field, which includes reflections is subtracted out when the difference is taken between the diffracted and the incident waves.

Equation 5.1, which is used to represent the Cylindrical and WAMIT wave field, only describes outwardly propagating waves, that is, the Hankel function of the second kind, $H_m^{(2)}(kr)$, describes outwardly propagating wave energy. (See Section 3.4.2.) There is no mechanism to represent incident wave energy, such as reflections that would produce the oscillations in magnitude that are standing waves. In cylindrical coordinates, incident waves are described using a Bessel function of the first kind, $J_m(kr)$. (See Section 3.4.3) An arbitrary incident wave is: $\eta^I = \sum_m a_m J_m(kr)\, e^{\mathrm{i}m\theta}$.

The actual linear wave field including the outwardly propagating radiated and scattered waves as well as the reflections should be described as:

$$\eta = \sum_{m=-\infty}^{\infty} \left(\left(b_m^{S,R} + b_m^{S2} \right) H_m^{(2)}(kr) + a_m^{I2} J_m(kr) \right) e^{\mathrm{i}m\theta} \tag{5.4}$$

where $b_m^{S,R}$ are the scattered radiated wave amplitudes as before, a_m^{I2} are the incident wave amplitudes of the reflections off of the tank walls, beaches, and paddles. The amplitudes b_m^{S2} are the amplitudes of the scattering of the incident reflected waves. If one could find all of these coefficients, then the wave field including standing waves could be reproduced.

With only a single circle around which to measure, the outwardly propagating waves cannot be distinguished from the incoming reflections. This is completely analogous to the two-dimensional case where a single wave gauge cannot separate incident and reflected waves, while two or more wave gauges can. Similarly, if one had two concentric circles at radii r_0 and r_1, one could separate the outwardly propagating from the incoming waves by solving a system of equations:

$$\left(b_m^{S,R} + b_m^{S2}\right) H_m^{(2)}(kr_0) + a_m^{I2} J_m(kr_0) = \frac{1}{2\pi}\int_{-\pi}^{\pi} \eta(r_0,\theta)\, e^{-\mathrm{i}m\theta} \tag{5.5}$$

$$\left(b_m^{S,R} + b_m^{S2}\right) H_m^{(2)}(kr_1) + a_m^{I2} J_m(kr_1) = \frac{1}{2\pi}\int_{-\pi}^{\pi} \eta(r_1,\theta)\, e^{-\mathrm{i}m\theta} \tag{5.6}$$

For each m, the right-hand side is known, and one seeks the pair of unknowns: $\left(b_m^{S,R} + b_m^{S2}\right)$ and a_m^{I2}. However, the radiated wave or the primary scattered wave ($b_m^{S,R}$) still cannot be separated from the scattered waves due to reflections (b_m^{S2}). The locations of the zeros of the Bessel function must also be considered.

The wave field that is measured around the circle includes both the outwardly propagating and inwardly propagating waves, and in the single circle method used herein, the Cylindrical coefficients are fitted to a model which assumes all wave energy is propagating outwardly. This means that if there is significant reflected energy present around the circle, the coefficients and resulting Cylindrical wave field will be inaccurate. This can be seen in Figure 5.11, which shows the scattered wave field of the Attenuator oriented at 45° in 1.25 Hz, and is the worst result from this study. There are significant standing waves shown along s1 and s2, and s4 shows a line of very high measurements that are not captured by the model.

It may be difficult to determine where the reflections are coming from, why the Attenuator at 45°, 1.25 Hz, was the worst case, and why the spokes s1, s2, and s4 show such disagreement. Reflections propagated in all directions, but given the location of the standing waves, it may be that the reflections were from the wave paddles. Although the paddles were force feedback, they may not have been able to respond to the small

amplitude of the scattered waves (< 1 cm).

The inability to distinguish incoming from outgoing waves is a flaw in the experimental design. Perhaps for future work, the two-circle design should be used to determine reflections. However, other research being done suggests that these reflections would have very high m cylindrical values, which would be difficult to capture accurately from the circle of wave gauges. A better approach would be to minimize the reflected energy, perhaps with absorbing wave paddles and floating beach in a wave tank like FloWave (FloWave, 2015).

Given the issues with higher-order harmonics and reflections, the results still show that a wave field represented by the cylindrical solutions is good approximation of the wave field produced by physical reality within the linear signal domain.

5.5 Summary

Experiments were conducted in The University of Edinburgh Curved Wave Tank to measure the cylindrical coefficients of the scattered and radiated wave fields of two different geometries of WECs at three different frequencies. The resulting cylindrical analytical wave fields were then compared to measurements at other points in the wave tank and with a cylindrical wave field created numerically with the boundary-element method (BEM) software WAMIT. The measured cylindrical wave field generally agreed very well with the measured wave field. The numerical wave field did not agree quite as well, and one reason for this was that there was energy at higher order components, which could not be modelled by WAMIT. Additionally, reflections of the scattered and radiated waves off of the wave tank paddles, walls, and beaches caused some inaccuracies in the derivation of the cylindrical coefficients, which proved to be more significant in some conditions than in others. Ultimately, the experiments have served as validation for the use of cylindrical wave fields for representing the scattered and radiated waves of floating bodies.

Chapter 6

Multi-body Wave Interactions

6.1 Introduction

In the previous two chapters, a method was presented by which the cylindrical coefficients of the scattered or radiated wave fields could be computed computationally or experimentally from a circle of points circumscribing the body. However, the utility of the cylindrical coefficients was shown only in that they could be used to represent the wave field analytically. While this is useful for visually assessing, for example, the wave shadow, there are more powerful applications.

Consider a simple array of two floating bodies in the presence of incident waves. Body one scatters the incident waves and radiates waves from its movements; these waves are then incident upon body two. Body two scatters the ambient incident waves and the incident waves that were sent by body one; it also radiates waves; all of which is then incident upon body one. In linear wave theory, because of the steady-state harmonic time dependence, this multiple scattering is also in a steady state. For multiple bodies, the goal of the so-called interaction problem is to find the magnitudes and phases of the scattered and radiated waves that satisfies the array interactions.

Because the cylindrical representation of the scattered and radiated wave fields is an analytical representation based on a finite number of complex variables, it is the perfect system for solving the interaction problem. As discussed in Section 2.3, the interaction problem has been studied across a variety of wave related fields including water, electromagnetics and sound.

In water waves, probably the most influential work on interactions has been the multiple scattering theory of Kagemoto and Yue (1986), which is exact within limits of linear wave theory, accounts for both progressive and evanescent waves, and has only a minimal restriction with respect to the bodies' positions. The essence of the theory is that hydrodynamic properties only need to be computed for each unique geometry and the interaction effects between multiple geometries are computed with linear algebra based on the knowledge that waves scattered and radiated by one body are the incident waves on another. For an array of devices of the same geometry, the method provides

significant computational savings over the direct method of computing linear wave effects on an array. In the direct method, the linear-wave boundary value problem is solved using the surface of all bodies simultaneously, and is typically performed computationally with a boundary-element method (BEM) solver. In contrast, Kagemoto and Yue's (1986) interaction theory uses a linear operator called a diffraction transfer matrix that represents the scattering properties of a body and is found by solving the boundary-value problem (BVP) for the body in isolation. The diffraction transfer matrix transforms vectors of incident, cylindrical, partial-wave coefficients into vectors of outgoing, partial-wave coefficients representing waves scattered by the body.

Although the method is extremely powerful and general, it requires the computation of the diffraction transfer matrix. In Kagemoto and Yue (1986), the diffraction transfer matrix was computed with a hybrid element method but only for axisymmetric geometries. Goo and Yoshida (1990) and later Chakrabarti (2000) found the diffraction transfer matrix for arbitrary geometries using the method described in Section 3.5.2. However, as was discussed in Chapter 4, there is no off-the-shelf software that computes the diffraction transfer matrix, and implementing the method of Goo and Yoshida (1990) in a custom BEM is not a simple task.

In this chapter, a method is developed for computing the diffraction transfer matrix, in which the cylindrical surface method is applied iteratively to a vector of incident plane waves with directions from 0 to 2π. The method is straight-forward and can be performed with results from most standard software or experiments as long as linearity is assumed or given. A new operator called the force transfer matrix is introduced. The force transfer matrix transforms a vector of incident partial cylindrical wave coefficients into forces on the body. It is used in both the diffraction and radiation problems, and is computed in a manner similar to that of the diffraction transfer matrix. With the inclusion of the force transfer matrix, the interaction problem becomes purely algebraic and programming it is relatively uncomplicated.

A deficiency of the method presented here is that only propagating wave modes are included. This is unavoidable because only propagating incident waves are practical to use to compute the diffraction transfer and force transfer matrices. The absence of evanescent wave modes results in differences as compared to a full linear wave theory computation when bodies are spaced very close together. However, it is shown for the geometries considered in this chapter that this error is very small and is negligible for most inter-body spacing of practical interest.

In the following sections, the methodology for deriving the diffraction transfer and force transfer matrices and the results from their applications to interaction theory are shown. First, a useful vector representation of cylindrical wave solutions is presented. Next Kagemoto and Yue's (1986) interaction theory is reviewed, into which the force

transfer matrix is introduced for the computation of excitation forces and the added mass and damping matrices. Then, new techniques are presented for deriving the diffraction transfer and force transfer matrices from incident plane waves. Following the methodology, a summary section is presented to further clarify the computational procedures. Results are shown for a cylinder and an attenuator-type wave energy converter (WEC) and verified with comparison to direct computation using the BEM software, WAMIT. Finally, the method is used to compute the power absorption and wave field of a medium-sized array of WECs in spectral seas and of a very large wave farm of 101 WECs in regular waves - computations that are not practical with direct methods given current computational resources.

The results of this chapter were published in McNatt *et al.* (2015a). However, improvements and corrections have been made since that publication and are given in this chapter. 1) More elegant methods for deriving the diffraction transfer and force transfer matrices are shown. 2) A sign error is corrected in the formulation of the added mass and damping matrices. 3) Body symmetry calculations of the diffraction transfer and force transfer matrices are presented. And 4) an error in the computation of the attenuator hydrostatic matrix has been corrected; the error does not effect the interaction theory, but does effect the motions and performance of the device, and so some figures in this chapter are slightly different than those of McNatt *et al.* (2015a).

6.2 The interaction problem

For an array of floating bodies in proximity to one another, the total wave field is the superposition of an incident wave potential, ϕ^I, scattered wave potentials due to all bodies when held fixed, ϕ^S, and the radiation potentials, $\phi^R_{q_i}$ due to each body i, moving in each of its degrees-of-freedom, q_i,

$$\phi = \phi^I + \phi^S + \sum_{i=1}^{N} \sum_{q_i=1}^{Q_i} \xi_{q_i} \phi^R_{q_i} \tag{6.1}$$

In previous chapters, i has indexed the degree-of-freedom (DOF), and N has been the total number of DOF. Here it is more convenient to use i to index the bodies in the array and N as the total number of bodies. Each body i has Q_i generalized modes of motion indexed as q_i with amplitudes ξ_{q_i}. For the entire system, Q is the total DOF and is equal to: $Q = \sum Q_i$.

The BVP can be solved for the interaction between bodies in the array under the assumption that hydrodynamic quantities for each body are known. This is called an interaction problem. The necessary hydrodynamic quantities are the added mass and

damping, the diffraction transfer matrix, and the force transfer matrix. The added mass and damping are familiar quantities and their derivation is discussed in Section 3.6. The diffraction transfer matrix is essential to this interaction theory and although not widely employed, it is not new to literature. The force transfer matrix is a new quantity introduced herein. The derivations of the diffraction transfer matrix and the force transfer matrix are given in Section 6.3, and their meanings are discussed throughout this paper.

The interaction problem described in this section follows that of Kagemoto and Yue (1986) with a few differences in notation. Lower-case $\boldsymbol{a}$ and $\boldsymbol{b}$ are used for incident and body partial wave amplitudes, where superscripts distinguish the type of wave instead of Kagemoto and Yue's (1986) use of capital $\boldsymbol{A}$ for the scattered wave amplitudes and lower-case $\boldsymbol{a}$ for the planar incident wave amplitudes. The transformation matrix has the same notation, $\mathbf{T}_{ij}$, but the opposite meaning: $\boldsymbol{\Psi}_j^S = \mathbf{T}_{ij}\boldsymbol{\Psi}_i^I$ rather than Kagemoto and Yue (1986): $\boldsymbol{\Psi}_i^S = \mathbf{T}_{ij}\boldsymbol{\Psi}_j^I$, because the usage herein results in a more logical matrix equation for the complete system, as shall be seen at the end of this section. And so, instead of the interaction being solved about a body j, as in Kagemoto and Yue (1986), the problem is solved about body i. $\mathbf{D}_i$ rather than $\boldsymbol{B}_j$, is used to denote the diffraction transfer matrix. Finally, only propagating wave modes are considered.

6.2.1 Vectorized cylindrical solutions

For the application of Kagemoto and Yue's (1986) theory, it is convenient to write the cylindrical solutions as the product of infinitely long vectors of coefficients and basis functions. These are written in the cylindrical coordinates about body i, $\{r_i, \theta_i, z\}$. The plane wave incident to body i is:

$$\phi_i^P(\beta) = \mathrm{i}\frac{g}{\omega}\left(\boldsymbol{a}_i^P\right)^{\mathsf{T}}\boldsymbol{\Psi}_i^I \tag{6.2}$$

where T indicates the vector transpose. $\boldsymbol{a}_i^P$ is a vector of plane wave coefficients whose m^{th} coefficient is:

$$\left(\boldsymbol{a}_i^P\right)_m = ae^{-\mathrm{i}k(X_i\cos\beta + Y_i\sin\beta)}e^{-\mathrm{i}m\left(\beta+\frac{\pi}{2}\right)} \tag{6.3}$$

This is the same as the formulation given in Section 3.4.3, but with the addition of a phase term, $e^{-\mathrm{i}k(X_i\cos\beta+Y_i\sin\beta)}$, which varies the phase of the incident plane wave based on the location, $\{X_i, Y_i\}$, of body i in a global coordinate system. The body axis x_i is parallel to the global X axis.

$\boldsymbol{\Psi}_i^I$ is a vector of incident basis functions whose m^{th} value is:

$$\left(\boldsymbol{\Psi}_i^I\right)_m = \frac{\cosh k\left(h+z\right)}{\cosh kh} J_m\left(kr_i\right) e^{\mathrm{i}m\theta_i} \tag{6.4}$$

In an analogous manner, considering only the propagating wave modes, the velocity potential of the waves scattered or radiated by a floating body i can be written as product of complex coefficients and scattered basis functions:

$$\phi_i^{S,R} = \mathrm{i}\frac{\mathrm{g}}{\omega}\left(\boldsymbol{b}_i^{S,R}\right)^{\mathsf{T}} \boldsymbol{\Psi}_i^S \tag{6.5}$$

where $\boldsymbol{b}_i^{S,R}$ is a vector of the coefficients that depends on the geometry and for radiated waves the mode of motion, of body i. $\boldsymbol{\Psi}_i^S$ is a vector of scattered basis functions (which also apply to radiated waves):

$$\left(\boldsymbol{\Psi}_i^S\right)_m = \frac{\cosh k\left(h+z\right)}{\cosh kh} H_m^{(2)}\left(kr_i\right) e^{\mathrm{i}m\theta_i} \tag{6.6}$$

In general, the coefficient and basis function vectors are infinitely long, and their scalar product is an infinite summation centered about $m = 0$. As discussed in previous sections, in practice, this is truncated with a value M, so that the summation goes from $m = -M$ to M.

6.2.2 Solution to the interaction problem

For an array of N fixed bodies, the incident waves to a given body i are the sum of the ambient incident waves, $\phi_i^A = \mathrm{i}\frac{\mathrm{g}}{\omega}\left(\boldsymbol{a}_i^A\right)^{\mathsf{T}} \boldsymbol{\Psi}_i^I$, and waves scattered by all other bodies, $\phi_j^S = \mathrm{i}\frac{\mathrm{g}}{\omega}\left(\boldsymbol{b}_j^S\right)^{\mathsf{T}} \boldsymbol{\Psi}_j^S$.

$$\phi_i^I = \mathrm{i}\frac{\mathrm{g}}{\omega}\left(\begin{array}{cc} \left(\boldsymbol{a}_i^A\right)^{\mathsf{T}} \boldsymbol{\Psi}_i^I + & \sum_{\substack{j=1 \\ j\neq i}}^{N} \left(\boldsymbol{b}_j^S\right)^{\mathsf{T}} \boldsymbol{\Psi}_j^S \end{array}\right) \tag{6.7}$$

Here, the terminology incident wave means any wave component traveling towards a body. The ambient incident waves are the waves that drive the hydrodynamic interaction - without them, there would be no scattered waves. However, they are not necessarily plane incident waves; in the radiation problem, they are the radiated waves. The scattered waves of each body are the result of scattering of the ambient incident wave and scattering of incident waves that are the scattered waves of other bodies.

The relationship between an m^{th} order Hankel function of the second kind in body

coordinate system i and an n^{th} order Bessel function of the first kind in body coordinate system j is given by Graf's addition theorem (Abramowitz and Stegun, 1964):

$$H_m^{(2)}\left(kr_j\right)e^{\mathrm{i}m\theta_j} = \sum_{n=-\infty}^{\infty} H_{m-n}^{(2)}\left(kL_{ij}\right)e^{\mathrm{i}(m-n)\alpha_{ij}} J_n\left(kr_i\right)e^{\mathrm{i}n\theta_i} \tag{6.8}$$

where $L_{ij} = \sqrt{\left(X_i - X_j\right)^2 + \left(Y_i - Y_j\right)^2}$ and $\alpha_{ij} = \arctan\left(\frac{Y_i - Y_j}{X_i - X_j}\right)$, and are the distance and angle respectively of body i to body j. (Again, j and i are switched as compared to Kagemoto and Yue (1986)). Define a transformation matrix, T_{ij}, that transforms scattered basis functions in the coordinates of body j into incident basis functions in the coordinates of body i, $\boldsymbol{\Psi}_j^S = \mathsf{T}_{ij}\boldsymbol{\Psi}_i^I$. The mn^{th} element of the transformation matrix T_{ij} is:

$$\left(\mathsf{T}_{ij}\right)_{mn} = H_{m-n}^{(2)}\left(kL_{ij}\right)e^{\mathrm{i}(m-n)\alpha_{ij}} \tag{6.9}$$

Applying Eq. 6.9 to Eq. 6.7, the waves incident to body i in terms of incident basis functions of i are:

$$\phi_i^I = \mathrm{i}\frac{\mathrm{g}}{\omega}\left(\left(\boldsymbol{a}_i^A\right)^{\mathsf{T}} + \sum_{\substack{j=1 \\ j\neq i}}^{N}\left(\boldsymbol{b}_j^S\right)^{\mathsf{T}}\mathsf{T}_{ij}\right)\boldsymbol{\Psi}_i^I \tag{6.10}$$

Equation 6.10 is of the form, $\phi_i^I = \mathrm{i}\frac{\mathrm{g}}{\omega}\left(\boldsymbol{a}_i^I\right)^{\mathsf{T}}\boldsymbol{\Psi}_i^I$, where the incident wave coefficients, $\boldsymbol{a}_i^I$, are the sum of the ambient incident waves and the transformed scattered waves from all other bodies.

Now consider the diffraction transfer matrix of body i. The diffraction transfer matrix is a linear operator that transforms incident wave amplitudes to body i into the scattered wave amplitudes of body i, $\boldsymbol{b}_i^S = \mathsf{D}_i\boldsymbol{a}_i^I$. With the use of the diffraction transfer matrix, Eq. 6.10 becomes:

$$\boldsymbol{b}_i^S = \mathsf{D}_i\left(\boldsymbol{a}_i^A + \sum_{\substack{j=1 \\ j\neq i}}^{N}\mathsf{T}_{ij}^{\mathsf{T}}\boldsymbol{b}_j^S\right) \tag{6.11}$$

If the ambient incident wave amplitudes and the diffraction transfer matrices are known,

then the scattered wave amplitudes can be found by solving Eq. 6.11 as a system of linear equations in the form:

$$\begin{bmatrix} \boldsymbol{b}_1^S \\ \boldsymbol{b}_2^S \\ \vdots \\ \boldsymbol{b}_N^S \end{bmatrix} = \begin{bmatrix} \mathbf{D}_1 & \mathbf{0} & \cdots & \mathbf{0} \\ \mathbf{0} & \mathbf{D}_2 & & \vdots \\ \vdots & & \ddots & \mathbf{0} \\ \mathbf{0} & \cdots & \mathbf{0} & \mathbf{D}_N \end{bmatrix} \times \left(\begin{bmatrix} \boldsymbol{a}_1^A \\ \boldsymbol{a}_2^A \\ \vdots \\ \boldsymbol{a}_N^A \end{bmatrix} + \begin{bmatrix} \mathbf{0} & \mathbf{T}_{12}^{\mathsf{T}} & \cdots & \mathbf{T}_{1N}^{\mathsf{T}} \\ \mathbf{T}_{21}^{\mathsf{T}} & \mathbf{0} & & \vdots \\ \vdots & & \ddots & \mathbf{T}_{(N-1)N}^{\mathsf{T}} \\ \mathbf{T}_{N1}^{\mathsf{T}} & \cdots & \mathbf{T}_{N(N-1)}^{\mathsf{T}} & \mathbf{0} \end{bmatrix} \begin{bmatrix} \boldsymbol{b}_1^S \\ \boldsymbol{b}_2^S \\ \vdots \\ \boldsymbol{b}_N^S \end{bmatrix} \right) \tag{6.12}$$

Here the advantage of using the given definition of $\mathbf{T}_{ij}$ becomes apparent - $\mathbf{T}_{ij}$ means the i^{th} row j^{th} column transformation matrix of the super transformation matrix.

6.2.3 Forces due to the interaction problem

The incident waves on each body resulting from the interaction theory are a summation of partial cylindrical waves of various amplitudes. Because Kagemoto and Yue (1986), and subsequent authors who employed their method, had software designed to handle cylindrical incident waves, they could compute excitation forces by solving the BVP for incident cylindrical partial waves and then directly integrating the dynamic pressure. Unfortunately, standard, linear-wave software only solves for forces due to incident plane waves.

To overcome this short-coming, and in keeping with the simplicity of the diffraction transfer matrix, another linear operator, which can be derived from plane incident waves, is introduced to compute the forces - the force transfer matrix. The force transfer matrix, $\mathbf{G}_i$, transforms incident partial wave amplitudes on body i into linear excitation forces on body i in each degree of freedom, $\boldsymbol{f}_i^D = \mathbf{G}_i \boldsymbol{a}_i^I$. The derivation of the force transfer matrix is given in Section 6.3.2.

For the excitation forces on all bodies held fixed due to an incident plane wave at a direction, β, the ambient incident wave amplitudes are given by $\boldsymbol{a}_i^A = \boldsymbol{a}_i^P(\beta)$ (Eq. 6.3). The scattered wave problem is solved as described in Section 6.2.2. The incident waves to body i are the quantities in the brackets in Eq. 6.11, and the excitation force on body i is:

$$\boldsymbol{f}_i^D(\beta) = \mathsf{G}_i \left(\boldsymbol{a}_i^P(\beta) + \sum_{\substack{j=1 \\ j \neq i}}^{N} \mathsf{T}_{ij}^{\mathsf{T}} \boldsymbol{b}_j^S \right) \tag{6.13}$$

The added mass, $\boldsymbol{\mathcal{A}}$, and damping, $\boldsymbol{\mathcal{B}}$, matrices for the complete system are found by solving an interaction problem for each degree of freedom of the entire array. (The derivation of the added mass and damping matrices for a single body is given in Section 3.6). For motion of the q_j^{th} mode, the ambient incident wave amplitudes to body i are the transformed radiated wave amplitudes, $\mathsf{T}_{ij}^{\mathsf{T}} \boldsymbol{b}_{q_j}^R$, where $\boldsymbol{b}_{q_j}^R$are the radiated wave amplitudes of body j moving in mode q_j. On body j the ambient incident waves are zero.

$$\boldsymbol{a}_{i,q_j}^A = \begin{cases} \mathsf{T}_{ij}^{\mathsf{T}} \boldsymbol{b}_{q_j}^R & i \neq j \\ \mathbf{0} & i = j \end{cases} \tag{6.14}$$

For all bodies beside the body undergoing motion, the radiation force is due solely to incident waves from other bodies. For the body undergoing motion, the total radiation force must include the radiation forces of the body on itself, that is, its own added mass and damping matrices. The radiation force on body i due to motion in mode q_j is:[1]

$$\left(\boldsymbol{\mathcal{F}}_i^R\right)_{\bullet q_j} = \begin{cases} \mathsf{G}_i \boldsymbol{a}_i^I & i \neq j \\ \omega^2 \left(\boldsymbol{\mathcal{A}}_j\right)_{\bullet q_j} - \mathrm{i}\omega \left(\boldsymbol{\mathcal{B}}_j\right)_{\bullet q_j} + \mathsf{G}_j \boldsymbol{a}_j^I & i = j \end{cases} \tag{6.15}$$

where $\left(\boldsymbol{\mathcal{F}}_i^R\right)_{\bullet q_j}$ is the q_j^{th} column of the radiation force matrix on body i, $\boldsymbol{\mathcal{F}}_i^R$, and $\left(\boldsymbol{\mathcal{A}}_j\right)_{\bullet q_j}$ and $\left(\boldsymbol{\mathcal{B}}_j\right)_{\bullet q_j}$ are the q_j^{th} column vector of the added mass and damping matrices of body j in isolation. $\boldsymbol{\mathcal{F}}_i^R$ is $Q_i \times Q$ matrix, and the radiation force matrix for the complete system of bodies is:

$$\boldsymbol{\mathcal{F}}^R = \begin{bmatrix} \boldsymbol{\mathcal{F}}_1^R \\ \boldsymbol{\mathcal{F}}_2^R \\ \vdots \\ \boldsymbol{\mathcal{F}}_N^R \end{bmatrix} \tag{6.16}$$

where the added mass and damping matrices of the entire system of bodies are given by $\boldsymbol{\mathcal{A}} = \frac{1}{\omega^2}\mathrm{Re}\left\{\boldsymbol{\mathcal{F}}^R\right\}$ and $\boldsymbol{\mathcal{B}} = -\frac{1}{\omega}\mathrm{Im}\left\{\boldsymbol{\mathcal{F}}^R\right\}$.

---

1. In McNatt *et al.* (2015a), the radiation force of the body on itself was given as $-\omega^2 \left(\boldsymbol{\mathcal{A}}_j\right)_{\bullet q_j} + \mathrm{i}\omega \left(\boldsymbol{\mathcal{B}}_j\right)_{\bullet q_j}$ rather than the correct form: $\omega^2 \left(\boldsymbol{\mathcal{A}}_j\right)_{\bullet q_j} - \mathrm{i}\omega \left(\boldsymbol{\mathcal{B}}_j\right)_{\bullet q_j}$

6.3 Derivations of the diffraction transfer and force transfer matrices

The diffraction transfer matrix is a linear operator for a body that transforms an incident wave into a scattered wave. Historically, it has not been widely used, because the incident and scattered waves are of a somewhat unusual forms - infinite summations of cylindrical partial waves; see Section 3.4.7. Previously, each component of the diffraction transfer matrix, $(\mathbf{D})_{mn}$, was derived by solving the scattering BVP to find the m^{th} scattered wave coefficient due to an incident cylindrical wave component, n.

In the following sections, it is shown how the diffraction transfer matrix as well as the force transfer matrix can be derived from numerical or physical measurements of the scattered wave field and excitation forces due to a series of incident plane waves at directions from 0 to 2π. In the following sections, only a single body at a time is considered, and so the subscript, i, is omitted, and the position of the body coordinates is taken to be the origin.

6.3.1 The diffraction transfer matrix from incident plane waves

Here two methods are presented for finding the diffraction transfer matrix by probing the body with incident plane waves. They are computationally slightly different but conceptually the same. The second was put forward in McNatt *et al.* (2015a), however, the first is more elegant.

For a unit amplitude plane wave at an incident direction, β, one can can find the cylindrical scattered wave coefficients, $\boldsymbol{b}^S(\beta)$, using the cylindrical surface method presented in Chapter 4. By definition, the diffraction transfer matrix causes the following transformation, $\boldsymbol{b}^S(\beta) = \mathbf{D}\boldsymbol{a}^P(\beta)$, where both $\boldsymbol{a}^P(\beta)$ and $\boldsymbol{b}^S(\beta)$ are known. This can be rewritten as:

$$\left(\boldsymbol{b}^S(\beta)\right)_m = \sum_{n=-\infty}^{\infty} (\mathbf{D})_{mn}\, e^{-\mathrm{i}n\left(\beta+\frac{\pi}{2}\right)} \tag{6.17}$$

where the $e^{-\mathrm{i}n\left(\beta+\frac{\pi}{2}\right)}$ is the n^{th} cylindrical amplitude of a unit amplitude incident plane wave traveling in the direction β. The m^{th} coefficient of the scattered wave field is a Fourier series of diffraction transfer matrix coefficients in plane wave direction coordinate, β.

The mn^{th} term of the diffraction transfer matrix can be found as:

$$(\mathbf{D})_{mn} = \frac{1}{2\pi} e^{\mathrm{i}n\frac{\pi}{2}} \int_0^{2\pi} \left(\boldsymbol{b}^S(\beta)\right)_m e^{\mathrm{i}n\beta} d\beta \tag{6.18}$$

Equation 6.18 is a Fourier transform in incident wave direction of the scattered coefficients as a function of incident direction. In practice, one evaluates Equation 6.18 by computing the scattered coefficients due to plane waves for a discrete number of incident directions, L, where β_l, is the l^{th} direction, $\Delta\beta$ is the equal spacing, $\beta_1 = 0$, and $\beta_L = 2\pi - \Delta\beta$. The discrete Fourier transform is:

$$(\mathbf{D})_{mn} = e^{\mathrm{i}n\frac{\pi}{2}} \frac{1}{L} \sum_{l=1}^{L} \left(\boldsymbol{b}^S(\beta_l)\right)_m e^{\mathrm{i}n\beta_l} \tag{6.19}$$

Note that the sign of $e^{\mathrm{i}n\beta}$ is the opposite of the standard Fourier transform. In fact, the positive exponent is usually used to represent the inverse Fourier transform. Computationally, to evaluate Eq. 6.19, one should use an IFFT.

The diffraction transfer matrix is typically square going from index $-M$ to index M in both rows and columns. By Nyquist, the number of directions, L, must be at least twice as high as the expected truncation value. However, as was the case with computing the cylindrical surface, it is better to exceed the truncation value by 5 or 10 times.

In McNatt *et al.* (2015a), the method of finding the diffraction transfer matrix was presented as a least squares solution, fitting the rows of the diffraction transfer matrix to the solutions due to incident plane waves over all directions. As the Fourier transform is essentially a least squares fit to sinusoidal functions, this is effectively the same as the method given above. However, for completeness it is repeated here.

For an incident propagating plane wave at a direction β_l, the diffraction transfer matrix defines the relationship: $\boldsymbol{b}^S(\beta_l) = \mathbf{D}\boldsymbol{a}^P(\beta_l)$. $\boldsymbol{b}^S(\beta_l)$ and $\boldsymbol{a}^P(\beta_l)$ are known, and $\mathbf{D}$ is a matrix of unknown elements. For a single wave direction, this is an underdetermined matrix equation. Using the truncation value, M, the incident and scatter coefficient matrices are vectors of length $2M+1$, and diffraction transfer matrix is of size $(2M+1)\times(2M+1)$. To find $\mathbf{D}$, $2M$ more equations are needed. The additional equations are produced by solving for the scattered coefficients for at least $2M$ more wave directions going from 0 to 2π. By calling the vector of incident wave directions $\boldsymbol{\beta}$, $\left[\boldsymbol{b}^S(\boldsymbol{\beta})\right]$ is a matrix whose value at the m^{th} row and l^{th} column is the scattered wave coefficient of the m^{th} partial wave due to an incident wave in the direction β_l. Similarly, $\left[\boldsymbol{a}^P(\boldsymbol{\beta})\right]$ is a matrix whose value at the m^{th} row and l^{th} column is the incident regular wave amplitude given by Eq. 6.3. With this, the relationship become a full matrix equation:

$$\left[\boldsymbol{b}^S(\boldsymbol{\beta})\right] = \mathbf{D}\left[\boldsymbol{a}^P(\boldsymbol{\beta})\right] \tag{6.20}$$

$\left[\boldsymbol{b}^S(\boldsymbol{\beta})\right]_{m\bullet}$ is the m^{th} row vector of $\left[\boldsymbol{b}^S(\boldsymbol{\beta})\right]$ - the scattered wave coefficients of circular

mode m for different incident wave directions. The m^{th} row of the diffraction transfer matrix, $(\mathbf{D})_{m\bullet}$, can be found by solving the system of equations:

$$\left[\boldsymbol{a}^S(\boldsymbol{\beta})\right]_{m\bullet}^{\mathsf{T}} = \left[\boldsymbol{a}^P(\boldsymbol{\beta})\right]^{\mathsf{T}} (\mathbf{D})_{m\bullet}^{\mathsf{T}} \tag{6.21}$$

Only $2M+1$ incident wave directions are needed to solve for a diffraction transfer matrix of size $(2M+1)\times(2M+1)$. However, again, it was found to be more accurate to compute scattered wave coefficients for greater than $(2M+1)$ incident directions to create an over determined system and then fit row vectors $(\mathbf{D})_{m\bullet}$.

Using the cylindrical surface method, one can also compute the scattering coefficients of the evanescent wave modes due to incident waves. However, to use the evanescent modes in the interaction problem, one would need to find scattering coefficients due to incident evanescent waves. Incident partial evanescent wave modes do not exist in isolation and so would be challenging to create experimentally or with nonlinear computational software, and they are not included in commercial linear wave software. The derivation of a diffraction transfer matrix that includes evanescent wave modes is not practical experimentally or computationally following the methods given here.

Here, the diffraction transfer matrix is found by probing the body with incident plane waves from different directions. In the BEM of Goo and Yoshida (1990), the diffraction transfer matrix was found by probing the body directly with incident cylindrical waves. To find column n of $\mathbf{D}$, the n^{th} order incident cylindrical wave was used (each row m was found by integrating over the body surface with the m^{th} incident basis function). So, to compute to a truncation value of M, the Goo and Yoshida (1990) method requires $2M+1$ incident waves. The Fourier transform method presented here requires that $L \geq 2M$ by the Nyquist criterion, and the second method requires $2M+1$ incident waves. That is, theoretically, there are no computational savings for the Goo and Yoshida (1990) method as compared to the two methods presented here. However, in practice, for a general geometry one does not know an appropriate truncation value a priori, which means that one tends to over estimate the number of incident waves required to ensure accuracy. In this respect, the method of Goo and Yoshida (1990) is computationally more efficient, but the methods presented here are more general.

6.3.2 The force transfer matrix from incident plane waves

The derivation of the force transfer matrix is analogous to that of the diffraction transfer matrix and like in Section 6.3.1, two methods are presented. The first is more elegant and mathematically clear, and the second was given first in McNatt *et al.* (2015a).

The force transfer matrix defines the relationship: $\boldsymbol{f}^D(\beta) = \mathbf{G}\boldsymbol{a}^P(\beta)$, where both $\boldsymbol{f}^D(\beta)$ and $\boldsymbol{a}^P(\beta)$ are known. The force in DOF q can be written as:

$$\left(\boldsymbol{f}^D(\beta)\right)_q = \sum_{m=-\infty}^{\infty} (\mathbf{G})_{qm}\, e^{-\mathrm{i}m\left(\beta+\frac{\pi}{2}\right)} \tag{6.22}$$

and so the $(\mathbf{G})_{qm}$ term of the force transfer matrix can be found as the Fourier transform:

$$(\mathbf{G})_{qm} = \frac{1}{2\pi} e^{\mathrm{i}m\frac{\pi}{2}} \int_0^{2\pi} \left(\boldsymbol{f}^D(\beta)\right)_q e^{\mathrm{i}m\beta} d\beta \tag{6.23}$$

This is again computed in practice with a discrete number of plane incident waves, so that the discrete inverse Fourier transform from $\beta_1 = 0$ to $\beta_L = 2\pi - \Delta\beta$ is:

$$(\mathbf{G})_{qm} = e^{\mathrm{i}m\frac{\pi}{2}} \frac{1}{L} \sum_{l=1}^{L} \left(\boldsymbol{f}^D(\beta_l)\right)_q e^{\mathrm{i}m\beta_l} d\beta \tag{6.24}$$

As before, the force transfer matrix can also be computed via a least squares fitting method as presented in McNatt *et al.* (2015a). $\boldsymbol{f}^D(\beta_l)$ is a $Q \times 1$ vector of diffraction forces due to incident direction β_l. $\mathbf{G}$ is a $Q \times (2M+1)$ matrix. One may find $\mathbf{G}$ by solving for a vector of different incident wave directions, $\boldsymbol{\beta}$, where the number of wave directions is at least but preferably greater than $2M+1$.

$$\left[\boldsymbol{f}(\boldsymbol{\beta})\right] = \mathbf{G}\left[\boldsymbol{a}^P(\boldsymbol{\beta})\right] \tag{6.25}$$

The q^{th} row of the matrix, $\left[\boldsymbol{f}(\boldsymbol{\beta})\right]_{q\bullet}$, represents the forces on mode q at each incident wave direction. The q^{th} row of the force transfer matrix can be solved as:

$$\left[\boldsymbol{f}(\boldsymbol{\beta})\right]_{q\bullet}^{\mathsf{T}} = \left[\boldsymbol{a}^P\left(\boldsymbol{\beta}^{\mathsf{T}}\right)\right]^{\mathsf{T}} (\mathbf{G})_{q\bullet}^{\mathsf{T}} \tag{6.26}$$

6.3.3 Rotation of the body

In some cases for an interaction computation, a body in the array may be rotated with respect to the orientation for which its diffraction transfer and force transfer matrices were computed. This does not present a problem, and a rotation was shown originally by Peter and Meylan (2004a).

A body rotation is akin to a redefining the body coordinate system. For the rotation of the diffraction transfer matrix, this must be done for the scattered wave amplitudes as well as the incident wave amplitudes.

Consider the rotation angle, γ, of the body, the modified scattered basis function is:

$$\begin{aligned}\left(\boldsymbol{\Psi}_{\gamma}^{S}\right)_{m} &= \frac{\cosh k\left(h+z\right)}{\cosh kh} H_{m}^{(2)}\left(kr\right) e^{\mathrm{i}m(\theta-\gamma)} \\ &= e^{-\mathrm{i}m\gamma}\left(\boldsymbol{\Psi}^{S}\right)_{m}\end{aligned} \tag{6.27}$$

Here γ is used as a subscript to represent coefficients or basis functions in a coordinate system rotated by γ relative to the original coordinates. The rotated basis function, $\left(\boldsymbol{\Psi}_{\gamma}^{S}\right)_{m}$, is the product of $e^{-\mathrm{i}m\gamma}$ and the standard basis function, $\left(\boldsymbol{\Psi}^{S}\right)_{m}$. The same rotation applies to the incident basis function. Applying this to the diffraction transfer matrix relationship:

$$\begin{aligned}e^{-\mathrm{i}m\gamma}\left(\boldsymbol{b}^{S}\right)_{m} &= \left(\mathbf{D}\right)_{mn} e^{-\mathrm{i}n\gamma}\left(\boldsymbol{a}^{I}\right)_{n} \\ \left(\boldsymbol{b}^{S}\right)_{m} &= e^{\mathrm{i}(m-n)\gamma}\left(\mathbf{D}\right)_{mn}\left(\boldsymbol{a}^{I}\right)_{n}\end{aligned} \tag{6.28}$$

Clearly, $e^{\mathrm{i}(m-n)\gamma}$ is the adjustment of diffraction transfer coefficient $\left(\mathbf{D}\right)_{mn}$ due to a body rotation, γ.

For the force transfer matrix, the situation is simpler, only the incident waves need to be rotated, $\boldsymbol{f}_{\gamma}^{D} = \sum e^{-\mathrm{i}m\gamma}\left(\mathbf{G}\right)_{\bullet m}\left(\boldsymbol{a}^{I}\right)_{m}$. Similarly, the radiation coefficients must be rotated by $e^{-\mathrm{i}m\gamma}$. The complete set of rotations is then:

$$\left(\mathbf{D}_{\gamma}\right)_{mn} = e^{\mathrm{i}(m-n)\gamma}\left(\mathbf{D}\right)_{mn} \tag{6.29a}$$

$$\left(\mathbf{G}_{\gamma}\right)_{\bullet m} = e^{-\mathrm{i}m\gamma}\left(\mathbf{G}\right)_{\bullet m} \tag{6.29b}$$

$$\left(\boldsymbol{b}_{\gamma,q}^{R}\right)_{m} = e^{-\mathrm{i}m\gamma}\left(\boldsymbol{b}_{q}^{R}\right)_{m} \tag{6.29c}$$

6.3.4 Body symmetry

Man-made offshore structures are often symmetric in some manner: axisymmetric, symmetric about the x-axis, symmetric about the y-axis, or symmetric about both axes. For symmetric bodies, fewer incident wave directions are needed to find the diffraction transfer and force transfer matrices, and the matrices, particularly the diffraction transfer matrix for axisymmetric bodies, have distinctive properties. The symmetry relationships are found by first determining the symmetry of the scattered coefficients or the forces about the respective axis and then applying that symmetry to the Fourier transform formulation of the matrices.

Consider the case of the diffraction transfer matrix for an axisymmetric body. The scattered wave field of any body due to an incident plane wave in direction β is the same as the wave field of a body oriented at an angle $\gamma = -\beta$ due to an incident wave at $\beta_\gamma = 0$, whose coordinates are then rotated by $\gamma = \beta$ back to the original. That is:

$$\begin{aligned} \left(\boldsymbol{b}^S(\beta)\right)_m \left(\boldsymbol{\Psi}^S\right)_m &= \left(\boldsymbol{b}^S_{\gamma=-\beta}(0)\right)_m \left(\boldsymbol{\Psi}^S_{\gamma=\beta}\right)_m \\ \left(\boldsymbol{b}^S(\beta)\right)_m &= e^{-\mathrm{i}m\beta} \left(\boldsymbol{b}^S_{-\beta}(0)\right)_m \end{aligned} \tag{6.30}$$

For an axisymmetric body, the scattered coefficients due to a wave at $\beta = 0$ are independent of the body orientation, and the scattered coefficients due to any incident direction are $e^{-\mathrm{i}m\beta}$ times the coefficients at $\beta = 0$: $\left(\boldsymbol{b}^S(\beta)\right)_m = e^{-\mathrm{i}m\beta}\left(\boldsymbol{b}^S(0)\right)_m$. Returning to Fourier transform derivation of the diffraction transfer matrix (Eq. 6.18), because it is independent of direction, $\left(\boldsymbol{b}^S(0)\right)_m$ is pulled outside the integral:

$$(\mathbf{D})_{mn} = \frac{1}{2\pi} e^{\mathrm{i}n\frac{\pi}{2}} \left(\boldsymbol{b}^S(0)\right)_m \int_0^{2\pi} e^{\mathrm{i}(n-m)\beta} d\beta \tag{6.31}$$

which evaluates to 0, except when $m = n$, and so for axisymmetric bodies, the mn^{th} term of the diffraction transfer matrix is:

Axisymmetry:

$$(\mathbf{D})_{mn} = \begin{cases} e^{-\mathrm{i}m\frac{\pi}{2}} \left(\boldsymbol{b}^S(0)\right)_m & m = n \\ 0 & \text{otherwise} \end{cases} \tag{6.32}$$

That is, for an axisymmetric body, the diffraction transfer matrix is a diagonal matrix of the scattered coefficients for $\beta = 0$ modified by $e^{-\mathrm{i}m\frac{\pi}{2}}$.

Now consider the diffraction transfer matrix of a body symmetric about the x-axis. The

scattered wave field of a symmetric body due to an incident plane wave at a direction, β, is the same as that due to a wave at a direction, $-\beta$, which is flipped about the x-axis so that $\theta' = -\theta$, where θ' is the angular coordinate of the flipped coordinate system:

$$\begin{aligned}\left(\boldsymbol{b}^S(-\beta)\right)_m H_m^{(2)}(kr)\, e^{-\mathrm{i}m\theta} &= \left(\boldsymbol{b}^S(\beta)\right)_m H_m^{(2)}(kr)\, e^{\mathrm{i}m\theta} \\ \left(\boldsymbol{b}^S(-\beta)\right)_m &= e^{-\mathrm{i}m\pi}\left(\boldsymbol{b}^S(\beta)\right)_{-m}\end{aligned} \tag{6.33}$$

where the relationship, $H_{-m}^{(2)}(kr) = e^{-\mathrm{i}m\pi} H_m^{(2)}(kr)$, has been used. The m^{th} scattered coefficient due to an incident direction, $-\beta$, is $e^{-\mathrm{i}m\pi}$ times the $-m^{th}$ scattered coefficient due to an incident wave at β. By splitting the integral from 0 to 2π into integrals from 0 to π and $-\pi$ to 0, the Fourier transform derivation of the diffraction transfer matrix can be rewritten as:

x-axis symmetry:

$$(\mathbf{D})_{mn} = \frac{1}{2\pi} e^{\mathrm{i}n\frac{\pi}{2}} \int_0^{\pi} \left(\left(\boldsymbol{b}^S(\beta)\right)_m e^{\mathrm{i}n\beta} + e^{-\mathrm{i}m\pi}\left(\boldsymbol{b}^S(\beta)\right)_{-m} e^{-\mathrm{i}n\beta} \right) d\beta \tag{6.34}$$

which means that the diffraction transfer matrix for bodies symmetric about the x-axis can be found by only solving for incident waves from 0 to π.

Symmetry about the y-axis occurs for incident direction pairs, β and $-\beta + \pi$. It can be interpreted as symmetry about the x-axis of a body rotated by $\pi/2$. That is, rotate the coordinate system by $\frac{\pi}{2}$ (i.e. multiply both wave field basis functions by $e^{-\mathrm{i}m\frac{\pi}{2}}$) and then flip one coordinate system ($\theta' = -\theta$):

$$\begin{aligned}\left(\boldsymbol{b}^S(-\beta+\pi)\right)_m H_m^{(2)}(kr)\, e^{-\mathrm{i}m\frac{\pi}{2}} e^{-\mathrm{i}m\theta} &= \left(\boldsymbol{b}^S(\beta)\right)_m H_m^{(2)}(kr)\, e^{-\mathrm{i}m\frac{\pi}{2}} e^{\mathrm{i}m\theta} \\ \left(\boldsymbol{b}^S(-\beta+\pi)\right)_m e^{-\mathrm{i}m\frac{\pi}{2}} &= \left(\boldsymbol{b}^S(\beta)\right)_{-m} e^{-\mathrm{i}m\pi} e^{\mathrm{i}m\frac{\pi}{2}} \\ \left(\boldsymbol{b}^S(-\beta+\pi)\right)_m &= \left(\boldsymbol{b}^S(\beta)\right)_{-m}\end{aligned} \tag{6.35}$$

Split the integral from 0 to 2π into integrals from $-\pi/2$ to $\pi/2$ and $\pi/2$ to $-\pi/2$, the Fourier transform form of the diffraction transfer matrix is:

$$(\mathbf{D})_{mn} = \frac{1}{2\pi} e^{\mathrm{i}n\frac{\pi}{2}} \left(\int_{-\frac{\pi}{2}}^{\frac{\pi}{2}} \left(\boldsymbol{b}^S(\beta)\right)_m e^{\mathrm{i}n\beta} d\beta + \int_{\frac{\pi}{2}}^{-\frac{\pi}{2}} \left(\boldsymbol{b}^S(\beta)\right)_m e^{\mathrm{i}n\beta} d\beta \right) \tag{6.36}$$

Make the substitution: $\beta = -\beta + \pi$, and the second term becomes:

$-e^{\mathrm{i}n\pi}\int_{\frac{\pi}{2}}^{-\frac{\pi}{2}}\left(\boldsymbol{b}^S\left(-\beta+\pi\right)\right)_m e^{-\mathrm{i}n\beta}d\beta$. Then substitute in Eq. 6.35 and flip the limits of integration, and the diffraction transfer matrix is:

y-axis symmetry:

$$(\mathbf{D})_{mn} = \frac{1}{2\pi}e^{\mathrm{i}n\frac{\pi}{2}}\int_{-\frac{\pi}{2}}^{\frac{\pi}{2}}\left(\left(\boldsymbol{b}^S\left(\beta\right)\right)_m e^{\mathrm{i}n\beta} + e^{\mathrm{i}n\pi}\left(\boldsymbol{b}^S\left(\beta\right)\right)_{-m} e^{-\mathrm{i}n\beta}\right)d\beta \tag{6.37}$$

and again, only half of the incident wave directions are required.

For a body that is symmetric about the x and y axes, the integral in the y-axis symmetry formulation, Eq. 6.37, can be split into integrals from $-\pi/2$ to 0 and 0 to $\pi/2$, and the relationship for x-axis symmetry, Eq. 6.33, can be applied, so that one gets:

xy-axes symmetry:

$$\begin{aligned}(\mathbf{D})_{mn} =& \frac{1}{2\pi}e^{\mathrm{i}n\frac{\pi}{2}}\left(\cos\left(m+n\right)\pi+1\right)\\ &\times\left(\int_0^{\frac{\pi}{2}}\left(\left(\boldsymbol{b}^S\left(\beta\right)\right)_m e^{\mathrm{i}n\beta} + e^{-\mathrm{i}m\pi}\left(\boldsymbol{b}^S\left(\beta\right)\right)_{-m} e^{-\mathrm{i}n\beta}\right)d\beta\right)\end{aligned} \tag{6.38}$$

for which only the incident directions from 0 to $\frac{\pi}{2}$ are needed, and all terms where $m+n$ is odd are zero.

The application of symmetry to the computation of the force transfer matrix requires a priori knowledge of the symmetry of the forces. For example, for an axisymmetric body one knows that the surge and pitch forces go as the cosine of the incident wave direction while the sway and roll forces go as the sine and negative sine respectively (roll has the opposite sign of pitch because positive pitch is a motion towards the x-axis, while positive roll is away from the y-axis). Heave is independent of incident wave angle and yaw is zero (because the motion normal is always tangential to the body surface). Generalized forces can be defined and they can always be solved by evaluating the force over all incident wave angles. However, if one knows the functional relationship, then symmetry can be used to reduce the problem. The force transfer matrix for an axisymmetric body for each mode of motion can be found as:

Axisymmetry:

$$(\mathbf{G})_{1m} = \frac{1}{2\pi} e^{\mathrm{i}m\frac{\pi}{2}} \left(\boldsymbol{f}_1^D(\beta=0)\right)_m \int_0^{2\pi} \cos\beta e^{\mathrm{i}m\beta} d\beta$$
$$= \begin{cases} \operatorname{sign}(m)\, \frac{\mathrm{i}}{2} \left(\boldsymbol{f}_1^D(0)\right)_m & m = -1, 1 \\ 0 & \text{otherwise} \end{cases} \quad \text{surge} \quad (6.39a)$$

$$(\mathbf{G})_{2m} = \frac{1}{2\pi} e^{\mathrm{i}m\frac{\pi}{2}} \left(\boldsymbol{f}_1^D(0)\right)_m \int_0^{2\pi} \sin\beta e^{\mathrm{i}m\beta} d\beta$$
$$= \begin{cases} -\frac{1}{2} \left(\boldsymbol{f}_1^D(0)\right)_m & m = -1, 1 \\ 0 & \text{otherwise} \end{cases} \quad \text{sway} \quad (6.39b)$$

$$(\mathbf{G})_{3m} = \frac{1}{2\pi} e^{\mathrm{i}m\frac{\pi}{2}} \left(\boldsymbol{f}_3^D(0)\right)_m \int_0^{2\pi} e^{\mathrm{i}m\beta} d\beta$$
$$= \begin{cases} \boldsymbol{f}_3^D(\beta=0) & m = 0 \\ 0 & \text{otherwise} \end{cases} \quad \text{heave} \quad (6.39c)$$

$$(\mathbf{G})_{4m} = \frac{1}{2\pi} e^{\mathrm{i}m\frac{\pi}{2}} \left(\boldsymbol{f}_5^D(0)\right)_m \int_0^{2\pi} -\sin\beta e^{\mathrm{i}m\beta} d\beta$$
$$= \begin{cases} \frac{1}{2} \left(\boldsymbol{f}_5^D(0)\right)_m & m = -1, 1 \\ 0 & \text{otherwise} \end{cases} \quad \text{roll} \quad (6.39d)$$

$$(\mathbf{G})_{5m} = \frac{1}{2\pi} e^{\mathrm{i}m\frac{\pi}{2}} \left(\boldsymbol{f}_5^D(0)\right)_m \int_0^{2\pi} \cos\beta e^{\mathrm{i}m\beta} d\beta$$
$$= \begin{cases} \operatorname{sign}(m)\, \frac{\mathrm{i}}{2} \left(\boldsymbol{f}_5^D(0)\right)_m & m = -1, 1 \\ 0 & \text{otherwise} \end{cases} \quad \text{pitch} \quad (6.39e)$$

$$(\mathbf{G})_{6m} = 0 \quad \text{yaw} \quad (6.39f)$$

For a body with x-symmetry, the forces have even ($\boldsymbol{f}(-\beta) = \boldsymbol{f}(\beta)$) or odd ($\boldsymbol{f}(-\beta) = -\boldsymbol{f}(\beta)$) symmetry about the x-axis, which results in integrals of cosine or sine:

x-axis symmetry:

$$(\mathbf{G})_{qm} = \frac{1}{\pi} e^{\mathrm{i}m\frac{\pi}{2}} \int_0^{\pi} \left(\boldsymbol{f}_q^D(\beta)\right)_m \cos(m\beta)\, d\beta \quad \text{surge, heave, pitch} \quad (6.40a)$$

$$(\mathbf{G})_{qm} = \frac{\mathrm{i}}{\pi} e^{\mathrm{i}m\frac{\pi}{2}} \int_0^{\pi} \left(\boldsymbol{f}_q^D(\beta)\right)_m \sin(m\beta)\, d\beta \quad \text{sway, roll, yaw} \quad (6.40b)$$

Similarly, for a body with y-symmetry, the forces have even ($\boldsymbol{f}(-\beta+\pi) = \boldsymbol{f}(\beta)$) or odd ($\boldsymbol{f}(-\beta+\pi) = -\boldsymbol{f}(\beta)$) symmetry about the y-axis, which results in integrals that

depend on whether m is even or odd:

y-axis symmetry:

$$(\mathbf{G})_{qm} = \begin{cases} \frac{1}{\pi} e^{\mathrm{i}m\frac{\pi}{2}} \int_{-\frac{\pi}{2}}^{\frac{\pi}{2}} \left(\boldsymbol{f}_q^D(\beta)\right)_m \cos(m\beta)\, d\beta & m \text{ even} \\ \frac{\mathrm{i}}{\pi} e^{\mathrm{i}m\frac{\pi}{2}} \int_{-\frac{\pi}{2}}^{\frac{\pi}{2}} \left(\boldsymbol{f}_q^D(\beta)\right)_m \sin(m\beta)\, d\beta & m \text{ odd} \end{cases} \quad \text{sway, heave, roll} \tag{6.41a}$$

$$(\mathbf{G})_{qm} = \begin{cases} \frac{\mathrm{i}}{\pi} e^{\mathrm{i}m\frac{\pi}{2}} \int_{-\frac{\pi}{2}}^{\frac{\pi}{2}} \left(\boldsymbol{f}_q^D(\beta)\right)_m \sin(m\beta)\, d\beta & m \text{ even} \\ \frac{1}{\pi} e^{\mathrm{i}m\frac{\pi}{2}} \int_{-\frac{\pi}{2}}^{\frac{\pi}{2}} \left(\boldsymbol{f}_q^D(\beta)\right)_m \cos(m\beta)\, d\beta & m \text{ odd} \end{cases} \quad \text{surge, pitch, yaw} \tag{6.41b}$$

Combining the relationships for x and y symmetry, one gets:

xy-axes symmetry:

$$(\mathbf{G})_{qm} = \begin{cases} 0 & m \text{ even} \\ \frac{2}{\pi} e^{\mathrm{i}m\frac{\pi}{2}} \int_{0}^{\frac{\pi}{2}} \left(\boldsymbol{f}_q^D(\beta)\right)_m \cos(m\beta)\, d\beta & m \text{ odd} \end{cases} \quad \text{surge, pitch} \tag{6.42a}$$

$$(\mathbf{G})_{qm} = \begin{cases} 0 & m \text{ even} \\ \frac{2\mathrm{i}}{\pi} e^{\mathrm{i}m\frac{\pi}{2}} \int_{0}^{\frac{\pi}{2}} \left(\boldsymbol{f}_q^D(\beta)\right)_m \sin(m\beta)\, d\beta & m \text{ odd} \end{cases} \quad \text{sway, roll} \tag{6.42b}$$

$$(\mathbf{G})_{qm} = \begin{cases} \frac{2}{\pi} e^{\mathrm{i}m\frac{\pi}{2}} \int_{0}^{\frac{\pi}{2}} \left(\boldsymbol{f}_q^D(\beta)\right)_m \cos(m\beta)\, d\beta & m \text{ even} \\ 0 & m \text{ odd} \end{cases} \quad \text{heave} \tag{6.42c}$$

$$(\mathbf{G})_{qm} = \begin{cases} \frac{2\mathrm{i}}{\pi} e^{\mathrm{i}m\frac{\pi}{2}} \int_{0}^{\frac{\pi}{2}} \left(\boldsymbol{f}_q^D(\beta)\right)_m \sin(m\beta)\, d\beta & m \text{ even} \\ 0 & m \text{ odd} \end{cases} \quad \text{yaw} \tag{6.42d}$$

6.4 Summary of computational procedures

The preceding theory is long and complex, and so it helps to have the computational steps summarized in the order they are applied. The following quantities need to be computed for each unique geometry in isolation prior to solving the interaction problem.

1. *Standard linear hydrodynamic properties* - For each unique geometry in isolation, one needs to compute the added mass, damping, and hydrostatic matrices.
2. *The force transfer matrix* - Excitation forces are found for each mode of motion due to incident plane waves for at least $2M + 1$ directions from 0 to 2π. Body symmetry can be exploited to reduce the number of directions required. These forces are used derive the force transfer matrix as in Section 6.3.2.
3. *The diffraction transfer matrix* - Each scattered wave field is measured over a cylindrical surface surrounding the body due to incident plane waves for at least $2M + 1$ directions from 0 to 2π. Body symmetry can be exploited to reduce the number of directions required. These measured points are used to compute the diffraction transfer matrix as in Section 6.3.1 where the cylindrical surface method is described in Section 4.2.
4. *Radiated wave coefficients* - For each mode of motion, wave field points are measured over a cylindrical surface surrounding the body due to unit-amplitude forced motion. These measured points are used to compute the radiated wave coefficients for each mode of motion using the cylindrical surface method described in Section 4.2.

Once these hydrodynamic quantities have been found, they can be used in the interaction theory to find the hydrodynamic quantities for an array of bodies.

1. *Rotate bodies* - If any of the bodies in the interaction problem are rotated relative to the orientation at which their hydrodynamic quantities were computed, the hydrodynamic quantities are modified as in Section 6.3.3.
2. *The scattering problem* - The scattering problem is used to find the excitation forces for the entire array. First the scattering problem is solved as in Section 6.2.2, where the ambient incident wave is a plane wave at the direction of interest. Next the excitation force on each body is found with the force transfer matrix as in Section 6.2.3.
3. *The radiation problem* - The radiation problem is used to find the added mass and damping matrices for the entire array. For each mode of motion in the array, a scattering problem is solved (Section 6.2.2), where the ambient incident wave is the wave radiated by that mode of motion. The added mass and damping matrices are assembled for the array following Section 6.2.3.

The added mass, damping, and excitation forces for the array can then be used to calculate body motions and wave power absorption in the standard manner, where the

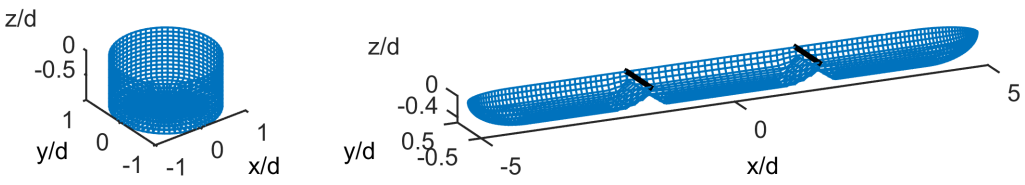

a) Cylinder b) Attenuator

Figure 6.1: Cylinder and attenuator geometries shown as their panelization for the BEM computation. Black lines indicate attenuator hinges. All dimensions are nondimensionalized by the cylinder's radius, d.

matrices (added mass, damping, stiffness, etc.) and vectors (motions and forces) are taken to be those for the entire system. Results from the application of the method are shown and discussed in the next section and, where possible, are verified against direct method results computed with WAMIT.

6.5 Results

In the results section, the interaction theory computational method is verified against the direct method computed with the commercial BEM software, WAMIT. Also presented are two cases where a direct BEM computation is not practical due to lengthy computation time, and which therefore can only be computed with interaction theory. Two geometries are considered - a floating cylinder and an attenuator-type WEC. Two array cases are examined for verification - two bodies at various distances, and a medium sized array of greater than 10 bodies. Finally, using only interaction theory, a computation is made on a medium-sized array of WECs in spectral seas, and on a very large array of 101 WECs in regular waves.

6.5.1 Geometries

The cylinder has a radius d, a height, $1.5d$, and a draft d (portion below the still water level). It is uniform in density and free to move in the standard 6 DOF rigid-body motions with no external mechanical forces applied. All values are non-dimensionalized by the cylinder radius, d. It is shown as its low-order panelization in Figure 6.1-a. All computations are performed in a water depth of $h/d = 10$.

The attenuator is similar to the attenuator considered in Chapter 4, but here it is slightly more realistic. It consists of three cylindrical bodies hinged together to rotate

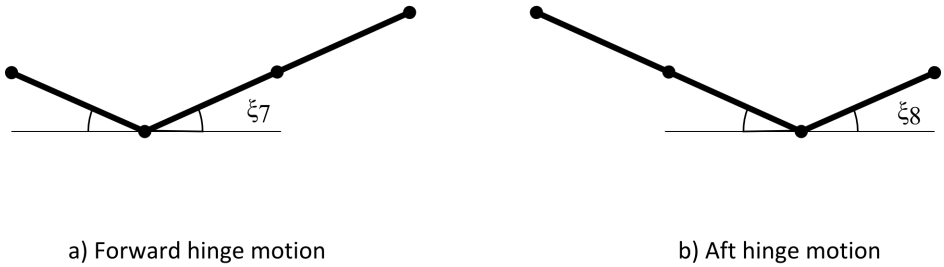

Figure 6.2: Diagram of definitions of hinged motions for attenuator. ξ_7 is Forward Flex, where the front of the attenuator is taken to be the end which meets the waves first at an incident wave direction of $\beta = 0$. ξ_8 is Aft Flex.

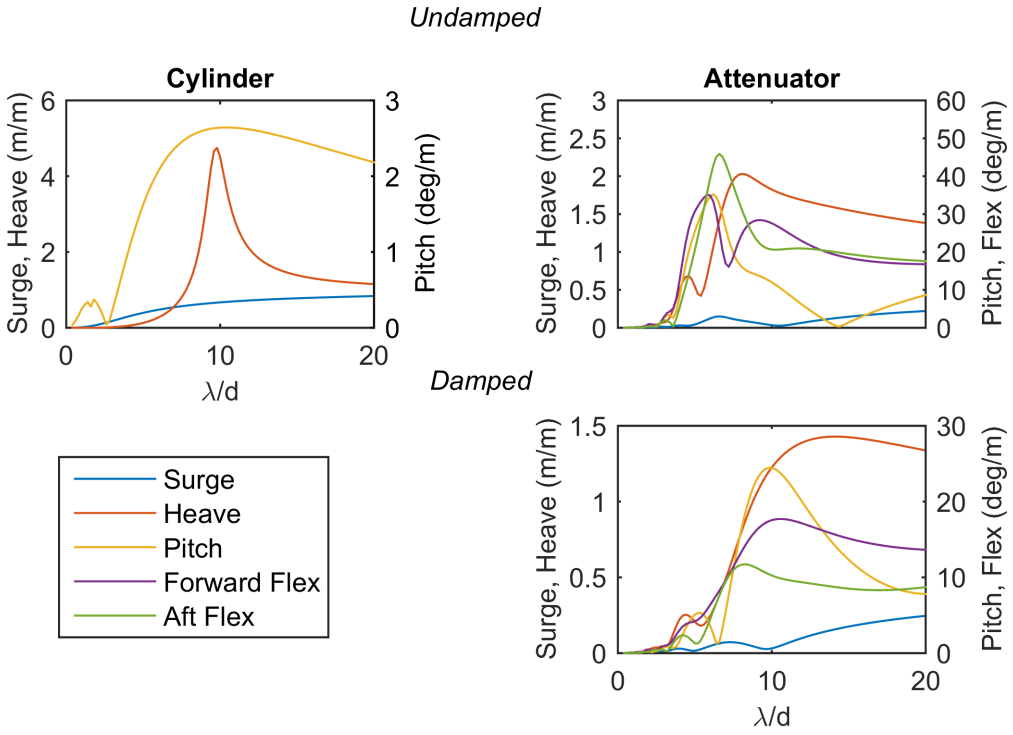

Figure 6.3: Cylinder and attenuator body motions as response amplitude operators as functions of nondimensional wavelength. Linear motions are shown on left-hand axes as meters of response per meter of incident wave amplitude, and rotational motions are shown on right-hand axes as degrees of response per meter of incident wave amplitude. Attenuator body motions are for head-seas ($\beta = 0$) and are shown for both damped and undamped case.

about axes parallel to the y-axis. It has 8 DOF - 6 rigid body motions and 2 flex motions (mode 7 is flex in the forward hinge, and 8 is flex in the aft hinge). A unit amplitude flex motion defined as shown in Figure 6.2. It has a beam of d, and a total length of $10d$. Its ends are spheroidal; there are notches at the hinges; and it is semi-submerged - see Figure 6.1-b.

The generalized normal of an attenuator hinge is:

$$\boldsymbol{n}_i = |z - z_i| \operatorname{sign}(x - x_i)\, \hat{\boldsymbol{i}} + |x - x_i|\, \hat{\boldsymbol{k}} \tag{6.43}$$

where $\{x_i, z_i\}$ are the coordinates of the hinge. The hinge positions of the attenuator in body coordinates are: $\{x_7, z_7\} = \left\{-\frac{5}{3}d, 0\right\}$, and $\{x_8, z_8\} = \left\{\frac{5}{3}d, 0\right\}$. As was discussed in Sections 4.3.2 and 4.3.3, the hydrodynamic quantities of the generalized hinge motions are computed in WAMIT using the Generalized modes feature (see Chapter 9.3). However, the body mass matrix and the hydrostatic matrix require special attention and must be computed externally. Both are computed numerically using the mwave Matlab software package (see Appendix B.1). The mass matrix is found by discretizing the body volume into mass elements and evaluating the integral given in Section 3.6.3. The hydrostatic matrix is computed by panelizing both the submerged and emergent surfaces of the body and following the theory given in Section 3.6.2. For both computations, the body is assumed to have a constant density, which is half the fluid density.

The dimensions of both geometries were chosen so that each had significant motions around $\lambda/d = 10$. The cylinder and attenuator motions as the response amplitude operator, $|\xi_{q_i}/d|$, plotted as a function of non-dimensional wavelength are shown in figure 6.3. However, besides the motion response condition, the dimensions of the geometries are arbitrary and the interaction theory method could be applied to any shape. Figure 6.3 shows the motions of the attenuator for normally incident waves with no external mechanical forces. The power take-off (PTO) value for the WEC was set to a constant damping for all wavelength in order to give a reasonable power capture. However, no attempt was made to optimize its value in order to maximize power capture.

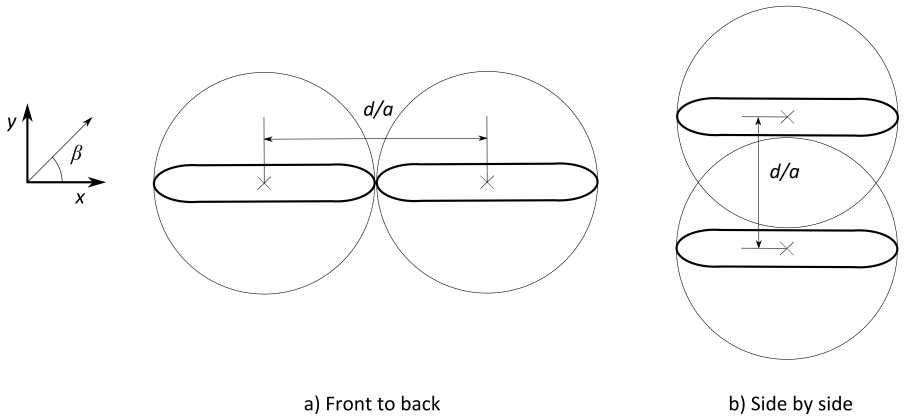

Figure 6.4: Two arrangements of the attenuator for the distance verification computation. The outline of the attenuator is shown as the thick line; it origin is given by the 'x'; and its circumscribing cylinder is given by the thin line. Because the cylindrical solutions are only valid for the region outside of a body's circumscribing circle, no part of another body may be inside this region.

6.5.2 Excitation force and radiation values

In this section, excitation force and radiation values for an array of two bodies are considered as a function of body separation distance, δ/d, at three wavelengths: $\lambda/d =$ 3, 10, 30, and a constant water depth of $h/d = 10$. Three incident wave directions are considered for the excitation force computation: $\beta = 0,\ \frac{\pi}{4},\ \frac{\pi}{2}$.

The separation distance is the origin-to-origin distance between the geometries. The cylinders are aligned along the x-axis. Due to the axisymmetry of the cylinder, only the separation distance needs be considered; body orientation is irrelevant. However, for the attenuator pairs, there are three parameters - body separation, direction of separation, and the relative orientation of the second body to the first. For the separation analysis - two cases were considered: 1) two attenuators, parallel in orientation, and set up in-line and front to back and 2) two attenuators, parallel in orientation, and set side by side. These arrangements can be seen in Figure 6.4.

A restriction imposed by Graf's addition theorem is that the center of the second body must be outside the circumscribing circle of the first body and vice versa. However, the cylindrical solutions themselves impose a stronger restriction. Because the cylindrical solutions are only valid for the region outside of a body's circumscribing circle, no part of another body may be inside this region. In McNatt *et al.* (2015a), this criterion was not correctly identified. For the front to back orientation, even though the bodies themselves are closer (nearly touching at the minimum distance), the body spacing in terms of interaction theory is in fact further than for the side by side case.

The only theoretical difference between the results of the interaction theory compu-

tation and WAMIT is the absence of evanescent waves in the interaction theory. The effect should only be present at small separation distances.

For each of the layouts, all of the excitation force values and all important added mass and damping values were examined. The agreement in almost all cases was excellent with the only differences being found at short separation distances.

Example plots, selected because they show some of the largest disagreement, are given for the cylinders in Figure 6.5 and for the attenuators in Figure 6.6. The benchmark WAMIT computations are represented as dashed lines, and the interaction theory computations are solid lines. In some figures, only solid lines are visible, which means that the interaction theory and WAMIT computations are in excellent agreement. For the cylinder computation, one can see differences between the two computations at short distances due to the evanescent wave effects, particularly so in the added mass. For the attenuator in the front to back configuration, one also sees evanescent wave effects at short distances. In both of these cases, the two bodies are almost touching.

6.5.3 Medium sized arrays

In this section, the interaction theory computation is verified by examining the wave fields of medium sized arrays. The wave field is plotted as the magnitude of the total wave elevation normalized by the incident wave amplitude, $|\eta/a|$, which centers the value around 1. The total wave elevation is the sum of the incident, scattered, and radiated wave elevations, and inherently includes the effects of the computed body motions. Also shown is 100 times absolute value of the difference between the wave fields: $100 \times \left|\left(\eta^{IT} - \eta^{WAM}\right)/a\right|$, which can be thought of as a percentage difference relative to the incident wave amplitude.

Figure 6.7 shows the results for an array of 16 cylinders in a square 4×4 grid, with a spacing of $\delta/d = 5$. In general, for all wave fields there is very good agreement. The difference is less than 0.2% for most of the wave fields. At $\lambda/d = 10$, $\beta = 0$, one can see differences in the wave fields near the cylinders themselves resulting from the evanescent waves (at a distance of $1d$ from the wall of any given cylinder, the difference is less than 4%). This difference dies out in the far-field wave field. In contrast at $\lambda/d = 10$, $\beta = \frac{\pi}{4}$, there is a small difference that propagates into the far-field. At this incident wave angle, some of the heave body motions are larger than at $\beta = 0$, which results in larger radiated evanescent waves and leads to differences in the body motions.

Figure 6.8 shows the results for an array of 11 attenuator WECs, setup in two offset rows. The bodies are shown as well as the circumscribing circle from which the cylindrical coefficients were computed. One would not expect agreement in the wave fields inside this circle. The center to center distance between bodies in a row is $\delta/d = 20$,

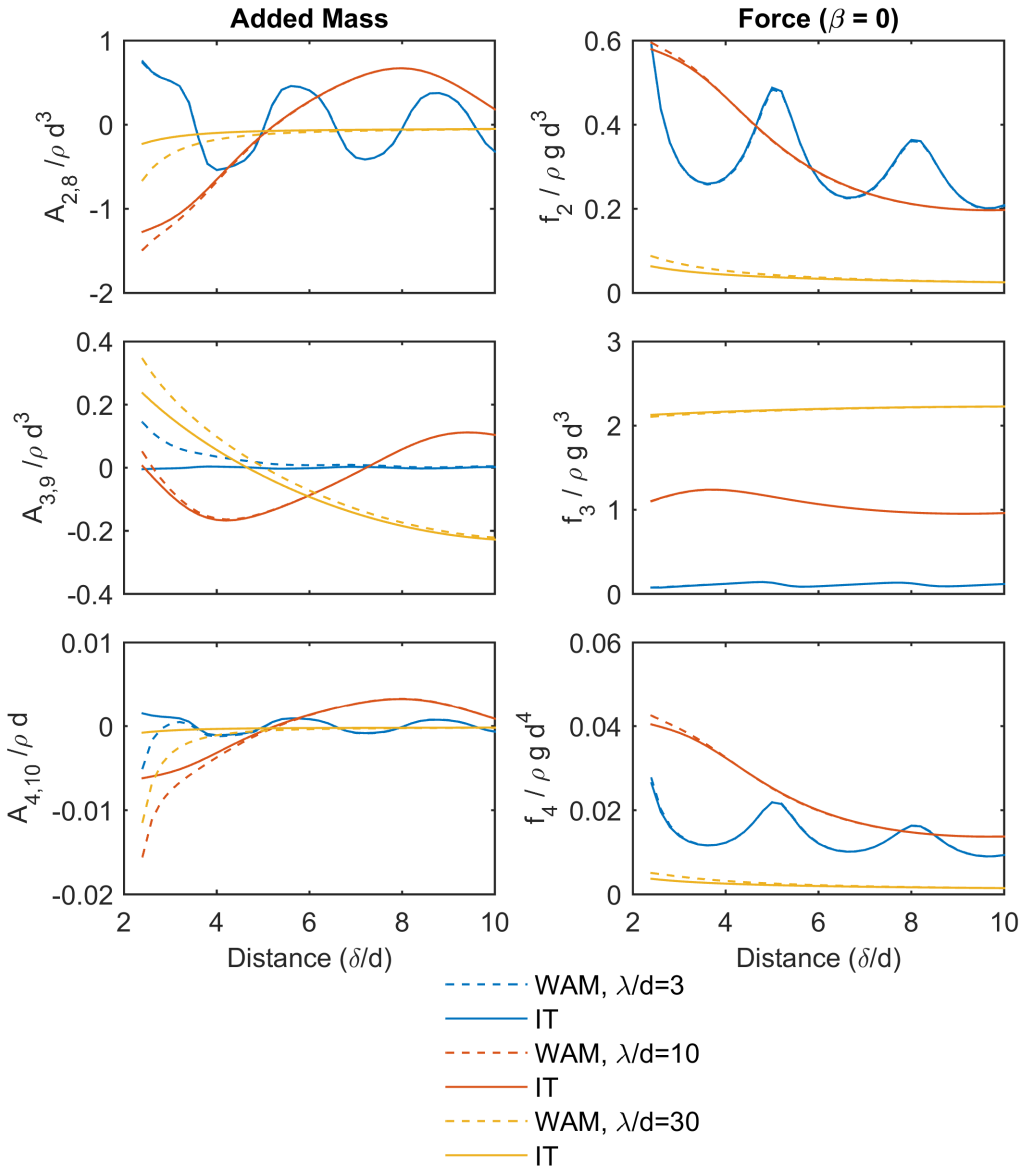

Figure 6.5: Plots of added mass ($\boldsymbol{\mathcal{A}}$) and excitation force ($\boldsymbol{f}^D$) for plane incident waves at a direction $\beta = 0$ for two cylinders as a function of nondimensional separation distance. Subscripts $1-6$ are the six DOFs of the first body, and subscripts $7-12$ are the 6 DOFs of the second body. For example, $\mathcal{A}_{2,8}$ is the added mass of sway-sway coupling between the bodies. WAM - WAMIT computation; IT - interaction theory computation.

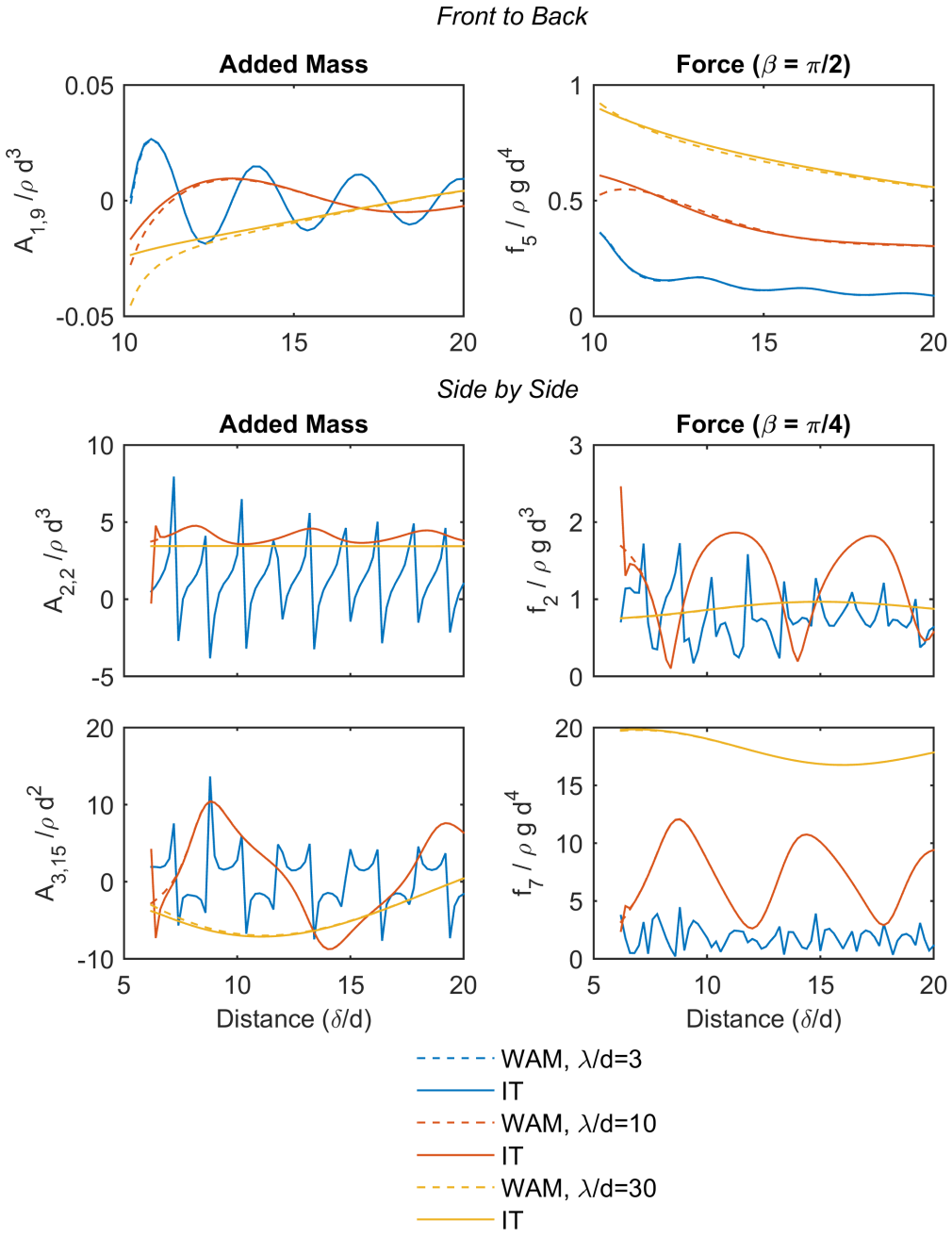

Figure 6.6: Plots of added mass ($\mathcal{A}$) and excitation force ($\boldsymbol{f}^D$) for plane incident waves for two attenuators as a function of nondimensional separation distance in the Front-to-Back and Side-by-Side arrangements (see figure 6.4). Subscripts $1-8$ are the six standard DOFs plus the two flex modes of body one, and subscripts $9-16$ are the 8 DOFs of the second body. For example, $\mathcal{A}_{3,15}$ is the added mass of heave-forward flex coupling between the bodies. WAM - WAMIT computation; IT - interaction theory computation.

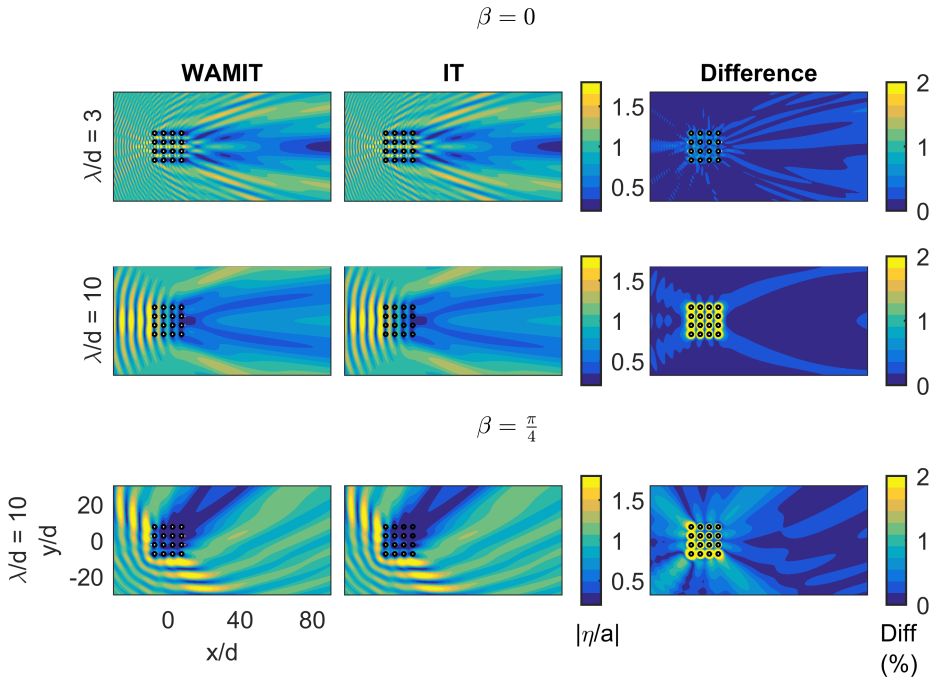

Figure 6.7: The figures show wave fields produced with WAMIT and the interaction theory (IT) computations, plotted as the magnitude of surface elevation, $|\eta| = |-(\mathrm{i}\omega/g)\,\phi|_{z=0}|$, at two nondimensional wavelengths and for two incident wave directions, for an array of 16 cylinders. Also shown is the percentage difference between the wave fields, $100\% \times |\eta_{IT} - \eta_{WAM}|$.

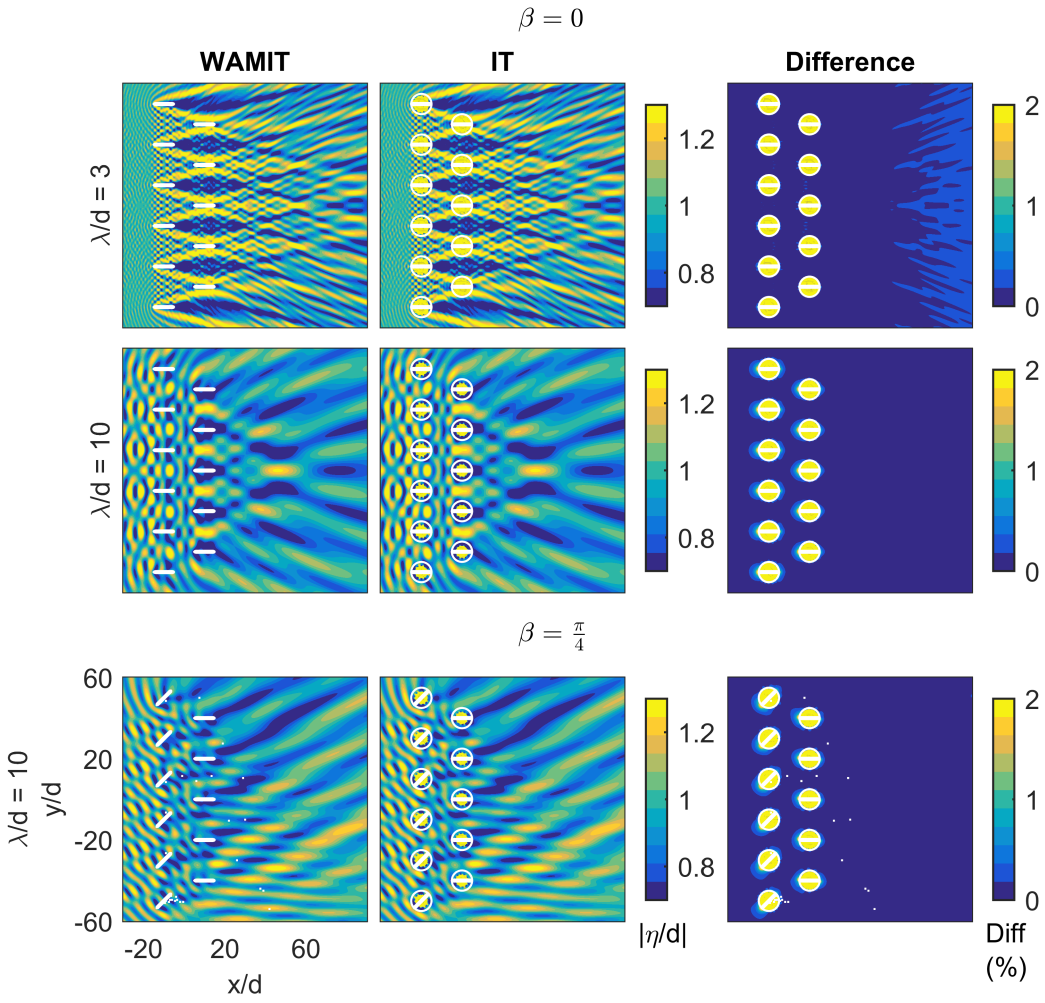

Figure 6.8: The figures show wave fields produced with WAMIT and the interaction theory (IT) computations, plotted as the magnitude of surface elevation, $|\eta| = |-(\mathrm{i}\omega/g)\ \phi|_{z=0}|$, at two nondimensional wavelengths and for two incident wave directions, for the 11 attenuator array. Also shown is the percentage difference between the wave fields, $100\% \times |\eta_{IT} - \eta_{WAM}|$. At $\beta = \frac{\pi}{4}$, the front row of attenuators is rotated to face the incident waves to demonstrate the rotation given in section 6.3.3.

and the row spacing is $\delta/d = 20$. At an incident direction, $\beta = \pi/4$, the front row of bodies has been rotated to demonstrate the calculation described in Section 6.3.3. At this spacing evanescent wave effects are non-existent and the agreement between the wave fields for all conditions is excellent (generally less than a 0.2% difference).

In the difference plots at $\lambda/d = 3$ of both the cylinder and the attenuator arrays, there are errors that appear not to decay with distance as one would expect. This is particularly visible in the attenuator plot at the far right edge. The reason for this is not currently known, although it may be due to errors in the evaluation of the Hankel function for large orders, m, at large arguments, kr.

6.5.4 Spectral array

In this section, a spectral wave field is considered. The incident sea spectrum is a Bretschneider spectrum with a peak at a wavelength, $\lambda/d = 10$, and a cosine-squared spreading, $A_2 \cos^{2s}\left(\frac{1}{2}\theta\right)$, where A_2 is the normalizing constant and $s = 10$ (Holthuijsen, 2007). 24 frequency components and 5 directions were implemented for a total of 120 incident wave components. The computation time for the array with this many wave components would be very long using the direct method, and so it was only performed using interaction theory.

For WEC arrays, a common measure of the impact of the array effects on device performance is the interaction factor. Although it has slightly varying definitions throughout literature, here it is defined for a single WEC in the array, i, as ratio of power absorbed by that WEC to the power absorbed by the same single WEC in isolation - $q_i = \frac{P_i}{P_{isolated}}$. For the attenuator, the power absorbed is the total power for both hinges over all incident wave frequencies and directions. A q greater than 1 indicates that the given WEC performs better due to array effects, and conversely, for q less than one, the WEC performs worse.

Figure 6.9 shows the interaction factor and the wave field for the 11 WEC array in spectral seas. The wave field is plotted as the disturbance coefficient - the ratio of significant wave height at a field point to the incident significant wave height $\left|H_s/H_s^I\right|$. The interaction factor shows that the front row of WECs receives a slight boost in performance (+2% to +11%), likely due to reflection of waves from the rear row. The performance of the rear row is slightly diminished (−4% to −12%) due to wave shadowing from the front row. The wave field shows wave energy reflection in front of the WECs and a wave shadow behind the array.

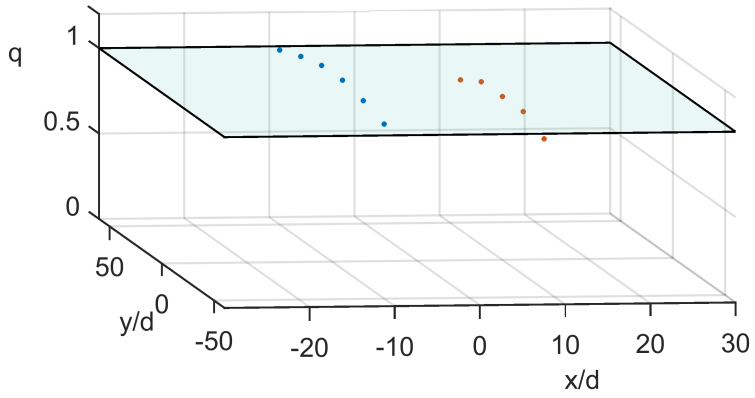

a) Interaction factor

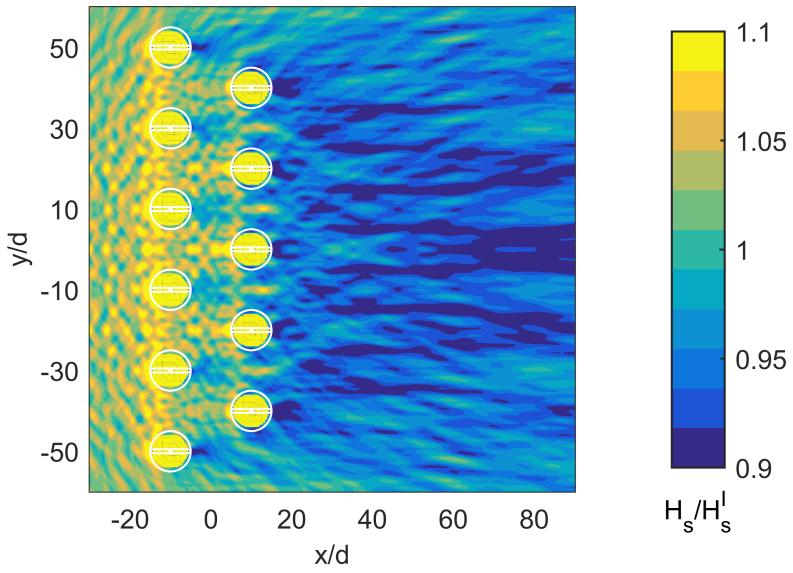

b) Wave field

Figure 6.9: The plots are for the 11 attenuator array in spectral seas. Figure (a) shows the interaction factor, q, for each body as a function of its position. q is a measure of the effect of multi-body interactions on power absorption. Figure (b) shows the wave field as the disturbance coefficient, $\left|H_s/H_s^I\right|$.

6.5.5 Large WEC array

In this section, an example of a very large WEC array of 101 bodies (808 degrees-of-freedom) is computed for a regular wave: $\lambda/d = 10$ at $\beta = 0$. The array is divided into 3 rows and the spacing between WECs in a row and between rows is $\delta/d = 20$. To the authors' knowledge no computations of arrays this large have been made with the direct method due to the limitations of computational resources.

Results for the very large WEC array are shown in Figure 6.10 as the interaction factor and the wave field. The interaction factor results are similar to those of the spectral array - the first row receives a performance gain, likely due to reflections from the back rows, and the back two rows have performance drops, likely due to wave shadowing[2]. Looking across the rows, both the front and middle rows have slight gains in performance near the middle and dips at the ends. At individual frequencies, the coherent interaction between the incident wave and scattered and radiated waves, creates standing waves, which act to increase or reduce wave energy at localized points in the wave field. These standing waves can be seen clearly in the wave fields of individual bodies shown in Chapter 4. Performance gains or losses due to these standing wave effects are very sensitive to the ratio of wavelength to body spacing. The effects shown here are for a particular device and a single-frequency, long-crested wave, and should not be generalized.

6.6 Discussion

The purpose of interaction theory is to accelerate the linear hydrodynamic computation of arrays without losing accuracy. The method developed in this chapter enables the interaction theory calculation with minimal requirements for complex custom software development. With that in mind, it is important to first consider the extent of the computational acceleration and why it results. After which, shortcomings of the method, including the absence of evanescent waves, the flat bottom condition, and the long-crested incident wave, are discussed and their significance assessed.

The most time-consuming computation in both the direct BEM and the interaction theory calculations is the solution to the resulting system of linear equations. For interaction theory the system is given by Eq. 6.12. Solving a system of equations using an iterative method leads to a computation time of $O\left(L^2\right)$, where L is the number of unknowns (Newman and Lee, 2002). For the low-order BEM, the number of unknowns is equal to the total number of panels in the system. For an array of N identical bodies,

2. This result is different than that of McNatt *et al.* (2015a) where the performance in the final row is actually increased. The discrepancy is due to the correction of the hydrostatic term of the attenuator.

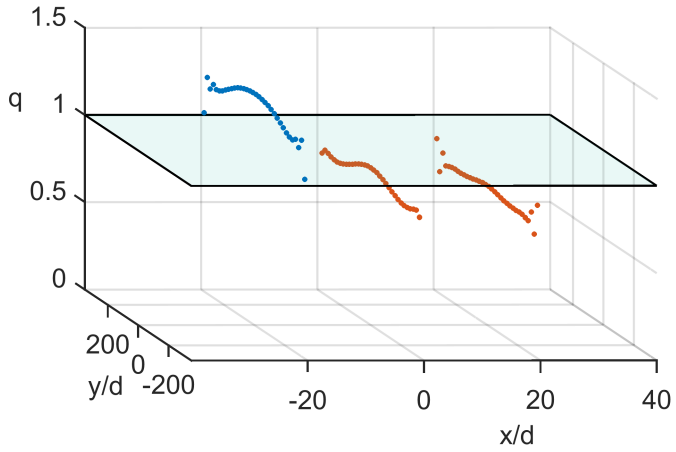

a) Interaction factor

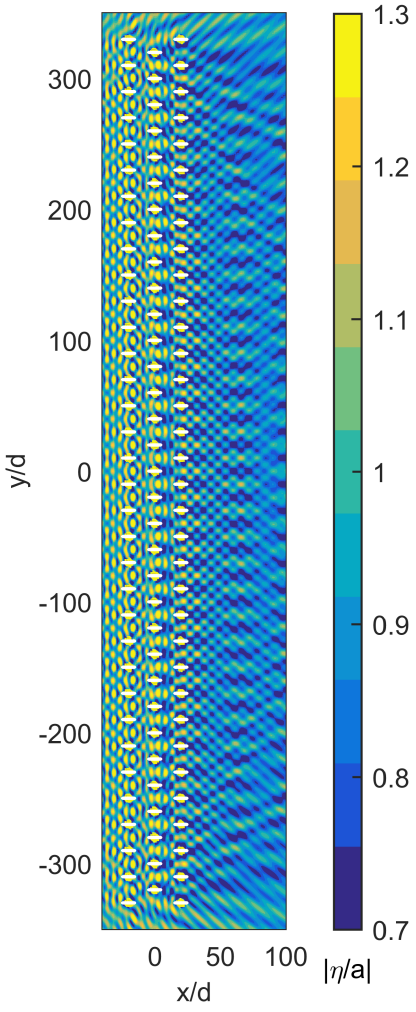

b) Wave field

Figure 6.10: The plots are for the 101 attenuator array in regular waves, $\lambda/a = 10$, $\beta = 0$. Figure (a) shows the interaction factor, q, for each body as a function of its position. q is a measure of the effect of multi-body interactions on power absorption. Figure (b) shows the wave field, as the magnitude of wave elevation, $|-(\mathrm{i}\omega/g)\ \phi|_{z=0}|$.

		Cylinder	Attenuator
Panels (P)		1280	1920
	$\lambda/a = 3$	17	47
Scattered Waves	$\lambda/a = 10$	9	25
$(2M+1)$	$\lambda/a = 30$	9	15

Table 6.1: Panel and scattered wave count for each geometry

each with P panels, the total number of unknowns is NP, and the computation time is $O\left(N^2P^2\right)$.

For the interaction theory, the number of unknowns is equal to the number of scattered wave modes included in the problem. The number of scattered waves is determined by the cylindrical partial-wave truncation value, M, where the number of scattered waves is $2M+1$. For an array of N identical bodies, the total number of unknowns is $N\left(2M+1\right)$ and the computation time is $O\left(N^2\left(2M+1\right)^2\right)$. Herein, the truncation value is determined based on the accuracy and precision of the measured wave field values used to compute the cylindrical wave field coefficients. M was determined as the point where all coefficients beyond M were smaller than the designated accuracy/precision floor of the wave field measurements used to determine the diffraction transfer matrix. For example, WAMIT returns field points to 6 significant figures. In computing the partial wave amplitudes with other software, these measurements are padded with zeros, and the FFT returns values at accuracies greater than that of the original measurement, which of course are not real. In fact, it was found that these phantom accuracies adversely affect computational results, and all the coefficients should be rounded to the accuracy/precision floor.

The number of panels and the number of scattered waves used for the cylinder and attenuator geometries are shown in Table 6.1. In all cases, the number of geometry panels is two orders of magnitude greater than the number of scattered waves. Consider the attenuator at a wavelength of $\lambda/d = 10$, the number of panels is 1920, and the number of scattered waves is 25, which means that for a given array computation, regardless of the number of bodies, the direct method will take on the order of $(1920/25)^2$ (about 5900) times longer to compute.

There is an upfront computational cost to the interaction theory computation. To compute the diffraction transfer matrix, force transfer matrix, and radiation wave field coefficients - values must be found at field points for $20-100$ incident wave directions on a single body for each wave frequency and water depth. However, once those quantities are found, they can be reused to significantly reduce array computation time.

Here a few representative computation times are given. Both the WAMIT and interaction theory computations were performed on a desktop computer with a 3.3

GHz processor. WAMIT is written in Fortran and the interaction theory routine was coded in Matlab and uses the built-in 'mldivide' routine to solve the system of linear equations. No significant consideration was given to speeding up computation time for either the direct method or the interaction computation via parallel processing or other techniques. The following values should only be taken as rough estimates. The computation time of a spectral sea as performed in Section 6.5.4 increases linearly with the number of incident wave components for both interaction theory and the direct method. With interaction theory, the spectral solution was found for the entire array at all 24 frequencies and 5 wave directions in approximately 8 minutes. However using the direct method, it took roughly 40 minutes to find the the array solution at a single frequency and direction, and so one may surmise that the spectral computation would take about 80 hours. For the very large array of 101 WECs each with 8 DOF, the interaction theory computation at a single wave frequency and direction took about 40 minutes. No equivalent computation was made with the direct method, although based on the computation with 11 bodies, theory suggests that the computation time for such an array would be about $2-3$ days.

In essence what interaction theory expresses is that to compute the linear-wave forces on an array of floating bodies, a detailed representation of each body is not needed; one only needs to know the shape, magnitude and phase of the waves it scatters. As solutions to the BVP, linear waves have a somewhat limited functional representation (i.e. sinusoidal), and so the scattered wave can be described by far fewer variables than are generally used to describe a geometric shape in BEM computation. Additionally, it was noticed that near the body, higher-order coefficients ($\left(\boldsymbol{b}_i^S\right)_m$ at large m values), even with very small amplitudes, were important to computations due to the exponential nature of the Hankel function, but far from the body the impact of the coefficients decayed exponentially with the Hankel function. So, even fewer partial cylindrical waves are required to compute bodies that are spaced far apart, and in essence as the distance from the body increases, the propagating wave effectively becomes more circular in shape.

The scattered wave solutions are only valid for the circular region outside the body. Near the body, another solution is required, for which the BEM is appropriate. The interaction computation can only be performed between two bodies, when the surface of one body is outside the circle that circumscribes the other body. This restriction is not constrictive, because the theory presented herein does not include evanescent waves, and so one should only use it at very close separation distances with caution.

In open water, linear theory states that waves are propagating waves with a exponential depth dependence, but near the body, to meet the body boundary condition, evanescent modes fit the propagating wave to the body's shape. Since evanescent waves

are neglected in the interaction theory herein, this will naturally lead to errors when bodies are spaced very closely together. One can see these errors in Figures 6.5 and 6.6 as hydrodynamic quantities and 6.7 in the wave fields around the bodies. For the 16 cylinder array, the absence of evanescent waves does not effect the computation of motions for an incident wave direction of $\beta = 0$. It does create small errors at $\beta = \frac{\pi}{4}$, but the errors are less than 2% in the body motions and wave field. For the attenuator array, where the body spacing is larger, and more representative of the spacing in a wave farm, the agreement between the motions computed with interaction theory and with the direct BEM computation is excellent. In general, for arrays like wave farms or wind farms, where the spacing is relatively large, the interaction theory can be used with confidence, but for more compact arrays, it should be used with caution and some results should be checked with direct BEM computations.

The interaction theory assumes a constant depth over the domain of the computation. For medium-sized arrays, like those shown in Figures 6.8 and 6.9, constant depth is not unreasonable. However, for the very large array shown in Figure 6.10 it may not be a good assumption. For example, take the attenuators to have a beam of $d = 5\,m$, then the area of the wave field computed in that problem would be $0.7\,km \times 3.5\,km$, which may be too large of an area over which to assume a constant depth. Also, herein, only a finite depth theory has been given. Peter and Meylan (2004a) extended Kagemoto and Yue's (1986) theory to infinite depth, but more research is needed to determine how to derive the radiated and scattered wave coefficients following the methodology given here.

Another assumption that may be dubious for such a large array is that the incident wave is a coherent long-crested wave. Using the large array example above, this would be a $3.5\,km$ long crest. The coherent motions and standing waves found throughout the entire array that result from such an incident wave will likely not exist in reality. However, locally over a smaller array subset, there may be such coherent interactions.

The linear wave interaction theory is probably best applied to with spectral seas to medium-sized arrays, where the bodies are not spaced too closely together and the flat bottom assumption is reasonable. Because of the significant speed up afforded by the interaction computation, the method can be employed as a tool for the optimization of the layout of the array by iterative calculations. Examples of such problems would be in the design of a wave farm to maximize power production or of an offshore wind farm to minimize loads or body motions.

6.7 Summary

A novel method has been presented to compute the diffraction transfer matrix and the new force transfer matrix by probing a body with a series of incident plane waves. Inputs to the calculation can be derived from standard numerical or experimental measurements. This computation enables the use of a theory for water wave interactions between multiple bodies developed by Kagemoto and Yue (1986), which leads to improvements in array computation time on the order of 10^3 over direct methods. The method was verified against direct method computations using the BEM solver WAMIT for two geometries, a cylinder and an attenuator type WEC, in a variety of array arrangements and wave conditions, but is general and can be applied to arbitrary geometries and modes of motions. The method presented herein neglects evanescent waves, but their effects are shown to be very small - for the 16 cylinder array, the evanescent waves represented about 4% of the wave field near a given body, and decayed exponentially with distance from the body. For arrays where the inter-device spacing is of practical interest, such as the wave farm examples, evanescent waves are negligible and the interaction theory matches the BEM computation to differences of less than 0.2% for most of the wave field. Finally, two cases of array computations are considered that could only be computed with interaction theory due to the computational acceleration it affords - a medium-sized array in spectral seas and a very large array of 101 WECs.

Chapter 7

Wave Power Absorption

7.1 Introduction

Efficiency is a fundamental concept in any energy conversion process, where efficiency is the ratio of output energy to the available input energy for a system or a conversion step. Efficiency provides a nondimensional, objective, quantitative measure of performance. However, in renewable ocean wave energy conversion, a good measure of hydrodynamic efficiency has not been defined. That is, given the current state of physics, one cannot describe a given wave energy converter (WEC) as being XX% efficient at converting water wave energy into another form of energy. The reason arises not because of difficulty in computing the power absorbed, in fact, that is well understood, but because of difficulties in characterizing the available wave power.

Waves of all sorts, water waves, sound waves, and electromagnetic waves, diffract - they spread laterally from regions of high energy to those of lower energy. In the process of wave energy absorption, this means that a wave absorbing device effectively sucks energy in from surrounding areas. This is indeed a benefit. However, it creates confusion as to the incident energy and the hydrodynamic efficiency of WECs. Further background on wave energy absorption and the WEC wave field is given in Section 2.5.

In this chapter, from the general form of cylindrical progressive waves representing the wave field of floating bodies, a new expression for power absorption using cylindrical coefficients is shown, which is similar to John's (1950) but is derived in a different manner. From the power absorption relationships, it becomes clear that the radiated partial cylindrical waves absorb power by canceling the outgoing diffracted partial cylindrical waves. The relationship between radiated and diffracted waves leads to a new measure of efficiency on a per cylindrical wave component basis. The sum of the per wave efficiencies is shown to correspond to the nondimensional measure, $k \cdot CW$, given by Mei *et al.* (2005), as well as relate to the gain of an antenna. A new formulation for optimal body motions from the cylindrical partial wave coefficients is presented. Finally, a generalized incident wave is found that can be completely absorbed by a given body. The interaction of the body with this incident wave represents 100% efficiency.

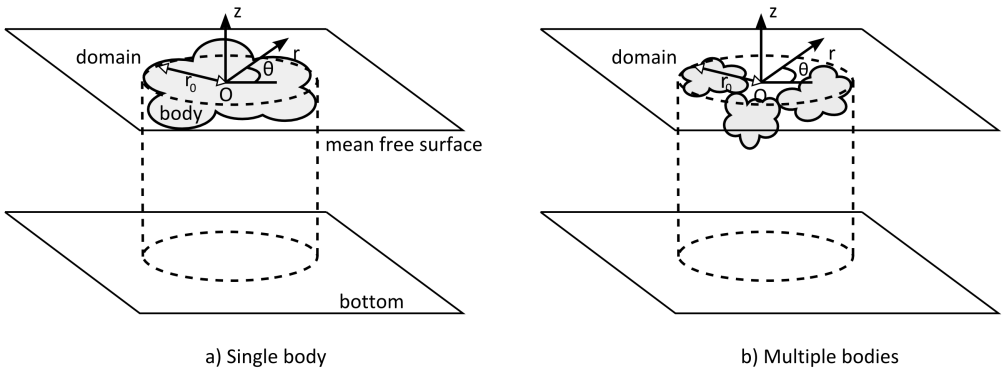

Figure 7.1: The domain of validity for the general cylindrical solutions for progressive waves is outside of a cylinder that circumscribes the body or bodies.

Using the cylindrical wave formulation of the floating body power absorption, the classic solutions for heaving and surging point absorbers are found easily. Cylindrical wave power absorption is then applied to a real finite sized body in three dimensions (3D), the Bristol Cylinder. Various beam lengths of the Bristol Cylinder are examined and the analysis proves very useful in connecting two-dimensional (2D) theory, in which the Bristol Cylinder can be 100% efficient, to point absorber theory, to the theory of the finite sized bodies in 3D. Additionally, examination of the cylindrical coefficients reveals opportunities for improving performance of a given WEC by increasing component efficiency and reducing "end effects". By modifying its shape to make the radius of the ends larger than that of the center, the performance of the Bristol Cylinder is improved by 15%. Finally a generalized incident wave is found for the Bristol Cylinder that is 100% absorbed.

7.2 Theory

Begin with the general form for progressive waves in terms of cylindrical eigenfunctions (see Eq. 3.84), which is valid for one or more bodies in the region outside of a circular cylinder of radius, r_0, circumscribing the bodies as in Figure 7.1:

$$\eta = \sum_{m=-\infty}^{\infty} \left(c_m^{(i)} H_m^{(1)}(kr) + c_m^{(o)} H_m^{(2)}(kr) \right) e^{\mathrm{i}m\theta} \tag{7.1}$$

where the $c_m^{(i)} H_m^{(1)}(kr)\, e^{\mathrm{i}m\theta}$ terms represent incoming wave energy, while the $c_m^{(o)} H_m^{(2)}(kr)\, e^{\mathrm{i}m\theta}$ terms represent outgoing wave energy.

The wave field of one or more more floating bodies is:

$$\eta = \eta^I + \eta^S + \sum_{i=1}^{N} \xi_i \eta_i^R \tag{7.2}$$

From Eq. 3.87, and using $J_m(kr) = \frac{1}{2}\left(H_m^{(1)}(kr) + H_m^{(2)}(kr)\right)$, the general cylindrical form of the incident wave is:

$$\eta^I(r,\theta) = \sum_{m=-\infty}^{\infty} \frac{1}{2} a_m \left(H_m^{(1)}(kr) + H_m^{(2)}(kr)\right) e^{\mathrm{i}m\theta} \tag{7.3}$$

The scattered and radiated waves are of the form:

$$\eta^{S,R}(r,\theta) = \sum_{m=-\infty}^{\infty} b_m^{S,R} H_m^{(2)}(kr)\, e^{\mathrm{i}m\theta} \tag{7.4}$$

Combining Eqs. 7.2, 7.3, 7.4, and writing the solution of the form of Eq. 7.1:

$$\eta = \sum_{m=-\infty}^{\infty} \left(\frac{1}{2} a_m H_m^{(1)}(kr) + \left(\frac{1}{2} a_m + b_m^S + \sum_{i=1}^{N} \xi_i b_{m,i}^R\right) H_m^{(2)}(kr)\right) e^{\mathrm{i}m\theta} \tag{7.5}$$

The incoming wave is 1/2 of the incident wave, and the outgoing wave is the sum of the 1/2 of the incident, the scattered, and all radiated waves.

The general solution for the linear progressive wave-body boundary-value problem (BVP) given by John (1950) only includes Hankel functions for sources or outgoing waves, because the wave created by the body must propagate away from it (i.e. the Sommerfeld radiation condition). However, when the general solution is written as above, one can see that Hankel function for incoming waves (in this case, $H_m^{(1)}$) is a valid solution that represents a wave energy sink. For example, at a given m, if one can make $\frac{1}{2}a_m + b_m^S + \sum_{i=1}^{N} \xi_i b_{m,i}^R = 0$, then the wave field at that m is $\eta = \frac{1}{2} a_m H_m^{(1)}(kr)$, which represents wave energy propagating into the origin and disappearing.

7.2.1 The body coefficients

The understanding of wave energy absorption with the cylindrical formulation is aided by understanding more about the body coefficients. The method of Goo and Yoshida (1990) for finding the cylindrical body coefficients is given in Section 3.5.2. From that, the progressive cylindrical scattered or radiated coefficients can be found as an integral over the body's surface of the product of source strengths and the eigenfunctions:

$$b_m^{S,R} = \frac{1}{2}\frac{\omega}{g} C_0 \cosh kh \int\int_{S_b} \sigma^{S,R}(R,\Theta,Z) \cosh k(Z+h)\, J_m(kR)\, e^{-\mathrm{i}m\Theta} dS \tag{7.6}$$

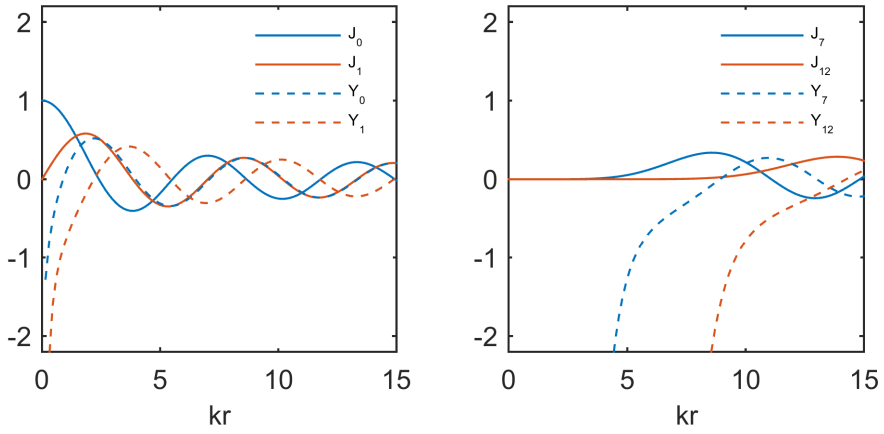

Figure 7.2: The plots show Bessel functions of the first, J_m, and second kind, Y_m, for $m = 0, 1, 7, 12$. Note that for the large orders, $m = 7, 12$, J_m is nearly zero for small arguments, while Y_m is very large.

For a given wave component m, a body may have no effect; that is $b_m^{S,R} = 0$. For example, by definition a point absorber does not have a scattered wave field, $b_m^S = 0$ for all m. A heaving point absorber generates only an isotropic radiated wave. One can see that to create such a wave, the directionally independent, 0^{th} order term must have a finite value of b_0^R, while $b_m^R = 0$ for all $m \neq 0$.

One can also see how the magnitudes of the coefficients relate to the depth of submergence of the body and the body size by examining Eq. 7.6. The coefficients are proportional to the integral of $\sigma^{S,R}(R, \Theta, Z) \cosh k(Z + h)$ over the body surface. A given body that is located deep in the water will have smaller cylindrical coefficients than another body of the same geometry located higher in the water column.

The dependence in the radial direction gives an indication of how the horizontal size of a body relates the magnitudes of the coefficients. The coefficients are proportional to $\sigma^{S,R}(R, \Theta, Z) J_m(kR)$. Figure 7.2 shows the Bessel functions of the first kind and second kind for $m = 0, 1, 7, 12$. For negative orders, $J_{-m} = (-1)^m J_m$ and $Y_{-m} = (-1)^m Y_m$. At $kr = 0$, $J_0(0) = 1$, and $J_m(0) = 0$ for all other m. From this it is clear, that for a body that is infinitesimally small, $kr_0 \approx 0$, only the $m = 0$ coefficient can be non-zero. At higher orders of m, J_m is nearly zero for significant range of small kr.

From its summation form (Abramowitz and Stegun, 1964), one may get an asymptotic form of the Bessel function valid for small arguments:

$$|J_m(kr)| \approx \left(\frac{kr}{2}\right)^{|m|} \frac{1}{\Gamma(|m| + 1)}, \qquad kr \ll 2\sqrt{|m| + 1} \tag{7.7}$$

If $kr \ll 2\sqrt{|m|+1}$, then $\left(\frac{kr}{2}\right)^{|m|} \ll \Gamma\left(|m|+1\right)$, which means that:

$$|J_m\left(kr\right)| \approx 0, \qquad kr \ll 2\sqrt{|m|+1} \tag{7.8}$$

and so for a body of a given size defined by kr_0, one can find a value of m, called say m_c, where $kr_0 \ll 2\sqrt{|m_c|+1}$, so that $|b_m| \approx 0$ for all $|m| > |m_c|$.

Another way to show that the magnitudes of the body coefficients go to zero as the order increases is to consider the Kochin function, $\mathcal{F}\left(\theta\right)$ (see Section 3.4.6). As John (1950) points out, $\mathcal{F}\left(\theta\right)$, is analytic over the period $-\pi$ to π, which means that the integral, $\int_{-\pi}^{\pi} \left|\mathcal{F}\left(\theta\right)\right|^2 < \infty$. Therefore $\sum \left|b_m^{S,R}\right|^2 < \infty$, and so there are a finite number of non-zero coefficients, or $\left|b_m^{S,R}\right| \to 0$, as $m \to \infty$.

7.2.2 Derivation of cylindrical power absorption

In this section, a formula for wave power absorption in terms of cylindrical coefficients is derived, where the wave field is given by the general cylindrical form of progressive waves, Eq. 7.1. Cylindrical power absorption is then considered in the context of incident waves, and the wave fields of floating and fixed bodies in subsequent sections.

The power or energy flux of a fluid through a surface is the product of the dynamic pressure and the velocity in the direction of the surface normal: $P^{(t)} = \int\int_S p^{(t)} \boldsymbol{U} \cdot \boldsymbol{n} dS$, where $p^{(t)}$ is the dynamic pressure and $\boldsymbol{U} \cdot \boldsymbol{n}$ is the scalar product of the velocity and the surface normal. Here, $p^{(t)} = \mathrm{Re}\left\{-\mathrm{i}\omega\rho\phi e^{\mathrm{i}\omega t}\right\}$, and $\boldsymbol{U} \cdot \boldsymbol{n} = \mathrm{Re}\left\{\frac{\partial\phi}{\partial n} e^{\mathrm{i}\omega t}\right\}$, where $\frac{\partial\phi}{\partial n}$ is the normal derivative of the velocity potential into the surface. As the wave is harmonic, one should consider the time-average power $P = \frac{\omega}{2\pi}\int_t^{t+\frac{2\pi}{\omega}} P^{(t)} dt$. In terms of the velocity potential, the time-averaged linear energy flux through an arbitrary surface, S, is (Mei *et al.* (2005)):

$$P = \frac{\rho\omega}{2} \int\int_S \mathrm{Im}\left\{\phi \frac{\partial \phi^*}{\partial n}\right\} dS \tag{7.9}$$

Now, consider the surface to be a circular cylinder of radius, $r = r_0$. Take the velocity potential to be the general form of cylindrical progressive waves (Eq. 3.84):

$$\phi = \mathrm{i}\frac{g}{\omega} f\left(z\right) \eta\left(r,\theta\right) \tag{7.10a}$$

$$\eta = \sum_{m=-\infty}^{\infty} \left(c_m^{(i)} H_m^{(1)}\left(kr\right) + c_m^{(o)} H_m^{(2)}\left(kr\right)\right) e^{\mathrm{i}m\theta} \tag{7.10b}$$

The normal velocity is $-\left.\frac{\partial \eta}{\partial r}\right|_{r=r_0}$, where the negative appears because positive r points outwards and the normal of the surface is defined as into the cylinder, such that a positive value of power means that there is a net flux of energy into the cylinder. The power through the cylinder can be written as the product of an integral over the depth of the depth function and an integral over direction of the elevation:

$$P = -\frac{\rho g^2}{2\omega} \int_{-h}^{0} f\left(z\right)^2 dz \int_{-\pi}^{\pi} \mathrm{Im}\left\{ \eta\left(r_0, \theta\right) \left.\frac{\partial \eta^*}{\partial r}\right|_{r=r_0} \right\} r_0 d\theta \tag{7.11}$$

The coefficients and the depth term are rearranged as:
$-\frac{\rho g^2}{2\omega} \int_{-h}^{0} f\left(z\right)^2 dz = -\frac{\rho g}{2} \left(\omega \frac{g}{\omega^2} \int_{-h}^{0} f\left(z\right)^2 dz \right)$, where the term inside the parentheses is evaluated as:

$$\begin{aligned} \omega \frac{g}{\omega^2} \int_{-h}^{0} f\left(z\right)^2 dz &= \omega \frac{g}{\omega^2} \frac{1}{\cosh^2 kh} \int_{-h}^{0} \cosh^2 k\left(z+h\right) dz \\ &= \frac{1}{2} \omega \frac{g}{\omega^2} \frac{h}{\cosh^2 kh} \left(1 + \frac{\sinh 2kh}{2kh} \right) \end{aligned} \tag{7.12}$$

Make a substitution of the dispersion relation, $\frac{g}{\omega^2} = \frac{1}{k \tanh kh} = \frac{1}{k} \frac{\cosh kh}{\sinh kh}$:

$$\begin{aligned} \frac{1}{2} \omega \frac{g}{\omega^2} \frac{h}{\cosh^2 kh} \left(1 + \frac{\sinh 2kh}{2kh} \right) &= \frac{\omega}{k} \frac{h}{2 \sinh kh \cosh kh} \left(1 + \frac{\sinh 2kh}{2kh} \right) \\ &= \frac{\omega}{2k^2} \left(1 + \frac{2kh}{\sinh 2kh} \right) \end{aligned} \tag{7.13}$$

and then using the group velocity, $c_g = \frac{1}{2} \frac{\omega}{k} \left(1 + \frac{2kh}{\sinh 2kh} \right)$, the depth integral becomes:

$$\omega \frac{g}{\omega^2} \int_{-h}^{0} f\left(z\right)^2 dz = \frac{c_g}{k} \tag{7.14}$$

Considering now the surface elevation, the power into a circle of any radius r_0 is:

$$P = -\frac{\rho g}{2} \frac{c_g}{k} \int_{-\pi}^{\pi} \mathrm{Im}\left\{ \eta\left(r_0, \theta\right) \left.\frac{\partial \eta^*}{\partial r}\right|_{r=r_0} \right\} r_0 d\theta \tag{7.15}$$

where the wave elevation is:

$$\eta\left(r, \theta\right) = \sum_{m=-\infty}^{\infty} \left(c_m^{(i)} H_m^{(1)}\left(kr\right) + c_m^{(o)} H_m^{(2)}\left(kr\right) \right) e^{\mathrm{i}m\theta} \tag{7.16}$$

The complex conjugate normal derivative evaluated at r_0 is:

$$\left.\frac{\partial \eta^*}{\partial r}\right|_{r=r_0} = \sum_{m=-\infty}^{\infty} \left(c_m^{(i)*} \left.\frac{\partial H_m^{(2)}}{\partial r}\right|_{r_0} + c_m^{(o)*} \left.\frac{\partial H_m^{(1)}}{\partial r}\right|_{r_0} \right) e^{\mathrm{i}m\theta} \tag{7.17}$$

Calling the integral over the surface elevation: $I = \int_{-\pi}^{\pi} \mathrm{Im}\left\{ \eta\left(r_0,\theta\right) \left.\frac{\partial \eta^*}{\partial r}\right|_{r=r_0} \right\} r_0 d\theta$,

$$\begin{aligned} I = \int_{-\pi}^{\pi} \mathrm{Im}\Bigg\{ \sum_{m=-\infty}^{\infty} \sum_{n=-\infty}^{\infty} \Bigg(& c_m^{(i)} c_n^{(i)*} H_m^{(1)} \frac{\partial H_n^{(2)}}{\partial r} + c_m^{(o)} c_n^{(o)*} H_m^{(2)} \frac{\partial H_n^{(1)}}{\partial r} \\ & + c_m^{(i)} c_n^{(o)*} H_m^{(1)} \frac{\partial H_n^{(1)}}{\partial r} + c_m^{(o)} c_n^{(i)*} H_m^{(2)} \frac{\partial H_n^{(2)}}{\partial r} \Bigg) e^{\mathrm{i}(m-n)\theta} \Bigg\} r_0 d\theta \end{aligned} \tag{7.18}$$

Evaluating the integral over θ, the cross terms are 0, and when $m = n$, it is 2π, So the equation becomes a single summation over m:

$$\begin{aligned} I = & 2\pi r_0 \mathrm{Im}\Bigg\{ \sum_{m=-\infty}^{\infty} \Bigg(\left|c_m^{(i)}\right|^2 H_m^{(1)} \frac{\partial H_m^{(2)}}{\partial r} + \left|c_m^{(o)}\right|^2 H_m^{(2)} \frac{\partial H_m^{(1)}}{\partial r} \\ & + c_m^{(i)} c_m^{(o)*} H_m^{(1)} \frac{\partial H_m^{(1)}}{\partial r} + c_m^{(i)*} c_m^{(o)} H_m^{(2)} \frac{\partial H_m^{(2)}}{\partial r} \Bigg) \Bigg\} \end{aligned} \tag{7.19}$$

The final two terms, $c_m^{(i)} c_m^{(o)*} H_m^{(1)} \frac{\partial H_m^{(1)}}{\partial r} + c_m^{(i)*} c_m^{(o)} H_m^{(2)} \frac{\partial H_m^{(2)}}{\partial r}$, are of the form $\mathrm{Im}\left\{C + C^*\right\} = 0$, and one is left with:

$$I = 2\pi r_0 \sum_{m=-\infty}^{\infty} \left(\left|c_m^{(i)}\right|^2 \mathrm{Im}\left\{ H_m^{(1)} \frac{\partial H_m^{(2)}}{\partial r} \right\} + \left|c_m^{(o)}\right|^2 \mathrm{Im}\left\{ H_m^{(2)} \frac{\partial H_m^{(1)}}{\partial r} \right\} \right) \tag{7.20}$$

Here,

$$\begin{aligned} \mathrm{Im}\left\{ H_m^{(1)} \frac{\partial H_m^{(2)}}{\partial r} \right\} &= -\left(J_m \frac{\partial Y_m}{\partial r} - Y_m \frac{\partial J_m}{\partial r} \right) \\ &= -W\left(J_m, Y_m\right) \\ &= -\frac{2}{\pi k r_0} k \\ &= -\frac{2}{\pi r_0} \end{aligned} \tag{7.21}$$

where the fact that $J_m \frac{\partial Y_m}{\partial r} - Y_m \frac{\partial J_m}{\partial r}$ is the Wronskian of J_m, and Y_m, and $W\left(J_m\left(x\right), Y_m\left(x\right)\right) =$

$\frac{2}{\pi x}$ is used. The final k came from applying the chain rule to the derivatives. Likewise,

$$\mathrm{Im}\left\{H_m^{(2)}\frac{\partial H_m^{(1)}}{\partial r}\right\} = \frac{2}{\pi r_0} \tag{7.22}$$

And the elevation integral is:

$$I = 4\sum_{m=-\infty}^{\infty}\left(-\left|c_m^{(i)}\right|^2 + \left|c_m^{(o)}\right|^2\right) \tag{7.23}$$

Finally, the total power in the wave field given by Eq. 7.1 can be computed as:

$$P = 2\rho g\frac{c_g}{k}\sum_{m=-\infty}^{\infty}\left(\left|c_m^{(i)}\right|^2 - \left|c_m^{(o)}\right|^2\right) \tag{7.24}$$

The value c_g is the group velocity of a plane wave. Wypych *et al.* (2012) note that in reality the group velocity of a cylindrical wave is more complicated and is a function of the radial distance. However, they also show that it asymptotes to c_g.

Equation 7.24 describes the power absorption through a generic linear wave field in terms of the cylindrical coefficients of its incoming, $c_m^{(i)}$, and outgoing, $c_m^{(o)}$, partial cylindrical waves, and to the author's knowledge, it is the first time that a relationship of this form has been given. A positive value of power means that power is absorbed; a negative value means that power is radiated; and zero power indicates that there is no net power transferred through the wave field. Equation 7.24 shows clearly that partial wave components of different orders, m, do not interact to absorb power, nor do the incoming and outgoing portions of the wave field interact with one another. This should not be surprising as each partial wave is an orthogonal eigenfunction.

In the following sections, the cylindrical wave power formulation is applied to the incident wave field, the wave field of a floating body and the wave field of a fixed body.

7.2.3 Power in the incident wave field

For an incident wave, $c_m^{(i)} = c_m^{(o)} = \frac{1}{2}a_m$ (see Section 3.4.3). From Eq. 7.24, it is clear that the net power is zero. This result is also logical - in an incident wave field there is no means for power to be sourced or sinked. However, one may consider just the incoming portion of the incident wave, for which the power is:

$$P^{(i)} = \frac{1}{2}\rho g\frac{c_g}{k}\sum_{m=-\infty}^{\infty}|a_m|^2 \tag{7.25}$$

Equation 7.25 has a familiar form that is similar to the incident power per crest width of a plane wave:

$$\mathcal{E}_f^P = \frac{1}{2}\rho g c_g a^2 \tag{7.26}$$

Compared to the power per crest width of a plane wave, Eq. 7.25 has an additional a factor of $1/k$, and it is an infinite summation. $\mathcal{E}_f^P$ is a power density, while Eqs. 7.24 and 7.25 represent the power in the entire wave field. In the case of the plane wave, the coefficients given by Eq. 3.89 have an magnitude of $|a|$ for all m, which means that over the infinite summation of non-decaying coefficients, there is an infinite amount of power. This is consistent with using a constant power per crest width, and recognizing that in an infinite wave field, a plane wave has an infinitely long crest.

7.2.4 Power in the floating body wave field

When one or more bodies are present using Eqs. 7.5 and 7.24, the power absorbed or radiated by the bodies is:

$$P = 2\rho g \frac{c_g}{k} \sum_{m=-\infty}^{\infty} \left(\frac{1}{4} |a_m|^2 - |d_m|^2 \right) \tag{7.27}$$

where:

$$d_m = \frac{1}{2} a_m + b_m^S + \sum_{i=1}^{N} \xi_i b_{m,i}^R \tag{7.28}$$

The relationship between $|a_m|$ and $|d_m|$ indicates the flow of power through the wave field at a given m component:

$$|d_m| > \frac{1}{2}|a_m| \qquad \text{power radiated into wave field} \tag{7.29a}$$

$$|d_m| = \frac{1}{2}|a_m| \qquad \text{zero net energy flux} \tag{7.29b}$$

$$|d_m| < \frac{1}{2}|a_m| \qquad \text{power absorbed} \tag{7.29c}$$

$$|d_m| = 0 \qquad \text{maximum power absorbed} \tag{7.29d}$$

When $|d_m| = 0$ the maximum possible power is absorbed, where d_m is the coefficient of the net interaction of the outgoing incident with the scattered and the radiated waves. Wave energy absorption is a wave cancellation process and as Farley (2012) explains, the outgoing scattered and radiated waves can only interact with the outgoing portion of

the incident wave. However, when considering its cylindrical representation, the incident wave contains energy that propagates in and out from *all* directions, not just a single direction as is the case of a plane wave.

7.2.5 Power in the fixed body wave field

The diffracted wave field is the wave field of the bodies held fixed. It is the sum of the incident and the scattered in the absence of radiated waves. As the body is fixed and not absorbing power, by conservation of energy, the net power through the wave field must be zero. One can also show this by an application of Green's theorem to the diffracted wave field, noting that the no-penetration boundary condition on the body is $\frac{\partial \phi^I}{\partial n} + \frac{\partial \phi^S}{\partial n} = 0$.

Setting Eq. 7.27 equal to 0, and setting $d_m = \frac{1}{2}a_m + b_m^S$, the total incoming power is equal to the total outgoing power:

$$\sum_{m=-\infty}^{\infty} \frac{1}{4} |a_m|^2 = \sum_{m=-\infty}^{\infty} \left| \frac{1}{2}a_m + b_m^S \right|^2 \tag{7.30}$$

For an individual wave component, it may be that $\frac{1}{4}|a_m|^2 = \left|\frac{1}{2}a_m + b_m^S\right|^2$, in which case $\mathrm{Re}\left\{a_m^* b_m^S\right\} = -\left|b_m^S\right|^2$. However, this is not necessarily the case, as the process of diffraction may redistribute the incoming wave energy at component m to other the components, just so long as it maintains the net total power.

7.2.6 Wave component absorption efficiency

While a given incident wave, such as a plane wave, may have an infinite amount of total incoming power, each cylindrical m wave component has a finite amount of power. One may then define an efficiency on a per wave component basis.

The radiated wave is the only wave that is capable of absorbing energy from the wave field. As the radiated wave is necessarily outgoing, it can only interact with the outgoing portion of the diffracted wave field. As discussed in Section 7.2.5, the process of diffraction redistributes the incoming energy to different outgoing wave components, and so rather than considering the incoming incident wave, one needs to consider the outgoing diffracted wave as the available energy.

Using Eq. 7.30, the power absorbed, Eq. 7.27 can be written as:

$$P = 2\rho g \frac{c_g}{k} \sum_{m=-\infty}^{\infty} \left(\left| \frac{1}{2}a_m + b_m^S \right|^2 - |d_m|^2 \right) \tag{7.31}$$

At a given wave component, the available power that can be absorbed is $2\rho g\frac{c_g}{k}\left|\frac{1}{2}a_m + b_m^S\right|^2$and the actual absorbed power is $2\rho g\frac{c_g}{k}\left(\left|\frac{1}{2}a_m + b_m^S\right|^2 - |d_m|^2\right)$, which means that one can define the efficiency of the power absorption of component m as:

$$e_m = \frac{\left|\frac{1}{2}a_m + b_m^S\right|^2 - |d_m|^2}{\left|\frac{1}{2}a_m + b_m^S\right|^2} \tag{7.32}$$

When a body has no components at m, that is, $b_m^S = 0$ and $b_{m,i}^R = 0$ for all i, then $d_m = \frac{1}{2}a_m$, no power is absorbed, and the efficiency is $e_m = 0$. Similarly, one can see that in the diffracted case, when $b_m^S \neq 0$ but $b_{m,i}^R = 0$, the efficiency is 0. However, when the body radiates waves at a given order m, power may be absorbed, and the maximum is reached when, $d_m = 0$, which gives an efficiency of 1.

Setting $d_m = 0$, one finds the relationship for the maximum energy absorption between all the radiated wave components, and the diffracted wave components is:

$$\sum_{i=1}^{N} \xi_i b_{m,i}^R = -\left(\frac{1}{2}a_m + b_m^S\right) \tag{7.33}$$

For a given wave component m, the maximum energy is absorbed when the sum of all radiated waves equals the magnitude of the half the incident wave plus the scattered wave and is 180° out of phase. For the point absorber case, where $b_m^S = 0$, Wypych *et al.* (2012) show the same result for surging and heaving radiated waves.

e_m can never be greater than 1, but it can be negative. When $e_m < 0$, it means that at wave component m the body is radiating energy into the wave field rather than absorbing it. This can occur due to the relative phase between the radiated and diffracted waves or because the magnitude of the radiated wave is greater than that of the outgoing diffracted wave.

The component version suggests another nondimensional measure of power absorption, which is the sum of the efficiencies:

$$E = \sum_{m=-\infty}^{\infty} e_m \tag{7.34}$$

In a sense, E describes how many wave components are "absorbed completely." It is not in fact an efficiency itself, as it can obtain values greater than 1.

When a single wave component is absorbed completely, $d_m = 0$, the power is $\frac{1}{2}\rho g\frac{c_g}{k}|a_m|^2$. For a plane wave, $|a_m| = |a|$, and the capture width of a single component absorbed completely is: $CW_m = 1/k$. As E is the number of components absorbed completely and as the capture with is the sum of all the component capture widths: $E \cdot CW_m =$

$E \cdot 1/k = CW$ or the number of components absorbed completely is:

$$E = k \cdot CW \tag{7.35}$$

Another analogue can be made here with antenna theory. The gain of an antenna is the ratio of the actual power absorbed to the maximum power absorbed by the isotropic wave, where the maximum power absorbed by the isotropic wave is: $\frac{1}{2}\rho g \frac{c_g}{k} |a_0|^2$. For any wave, long or short crested, the power in the isotropic wave (or omnidirectional wave), it the total wave energy flux in all directions at that frequency, which one would naturally denote as $|a|^2$. So the gain is:

$$\begin{aligned} G &= \frac{P}{\frac{1}{2}\rho g \frac{c_g}{k} |a|^2} \\ &= k \cdot CW \\ &= E \end{aligned} \tag{7.36}$$

Gain in antenna theory represents the focusing ability of the antenna, and gain, (G or $k \cdot CW$ or E) has the same meaning for water waves. A device with a high gain will be able to absorb a significant amount of power from a highly focused incident wave. A long-crested plane wave is the most focused a wave can be: it is a delta function in the direction that the wave travels.

Another useful meaning of E is that E indicates whether at a given wave frequency, a WEC performs better ($E > 1$) or worse ($E < 1$) than an optimal heaving point absorber. E is clearly a very meaningful value.

7.2.7 Optimal motions

For a body with a given geometry and set of modes of motion, the scattered and radiated waves are determined, and one can affect the power absorption only by varying the amplitude and phase of the body motions. In which case, a classical problem is to find the optimal motions that generate the most power. For example, Evans (1980) provides an elegant solution for optimal motions for a single WEC or a WEC array with and arbitrary number of degrees of freedom (DOFs) using only the hydrodynamic damping and excitation forces.

Here the problem will be solved using cylindrical wave components. It may not be possible to cancel out each wave component, such that $d_m = 0$, instead one wants to minimize the sum of the squares: $\sum |d_m|^2$, which will maximize the absorbed power.

To find this point, set the partial derivatives of the power with respect to each motion to zero:

$$\frac{\partial P}{\partial \xi_i} = -2\rho g \frac{c_g}{k} \sum_{m=-\infty}^{\infty} \left(\frac{\partial d_m}{\partial \xi_i} d_m^* + d_m \frac{\partial d_m^*}{\partial \xi_i} \right)$$

$$0 = \sum_{m=-\infty}^{\infty} \mathrm{Re}\left\{ b_{m,i}^R d_m^* \right\} \tag{7.37}$$

Now it is convenient to write the equation as matrices and vectors. Take $\boldsymbol{a}$ to be the column vector of incident amplitudes (a_m), $\boldsymbol{b}^S$ to be the column vector of scattered amplitudes, (b_m^S), $\boldsymbol{\xi}$ to be the column vector of body motions, $\boldsymbol{b}_i^R$ to be the column vector of radiated amplitudes of motion ξ_i, and $\mathbf{B}^R$ to be the matrix of radiated wave amplitudes, whose columns are $\boldsymbol{b}_i^R$. Eq. 7.37 combined with Eq. 7.28, written in matrix form is:

$$\mathrm{Re}\left\{ \left(\frac{1}{2}\boldsymbol{a} + \boldsymbol{b}^S + \mathbf{B}^R \boldsymbol{\xi} \right)^\dagger \boldsymbol{b}_i^R \right\} = 0 \tag{7.38}$$

where † indicates the complex conjugate transpose. The power is maximized by solving the system of equations:

$$\mathbf{B}^R \boldsymbol{\xi} = -\left(\frac{1}{2}\boldsymbol{a} + \boldsymbol{b}^S \right) \tag{7.39}$$

If $\mathbf{B}^R$ has a left inverse then the optimal motions are: $\boldsymbol{\xi} = -\left(\mathbf{B}^R\right)^{-1}\left(\frac{1}{2}\boldsymbol{a} + \boldsymbol{b}^S\right)$.

Although, $\boldsymbol{a}$ may be infinitely long and non-decaying, for finite-sized bodies, $\mathbf{B}^R$ and $\boldsymbol{b}^S$ have a finite number of non-zero coefficients. Call the number of non-zero body coefficients, L, and recall that the number of DOF is N, $\mathbf{B}^R$ is an $L \times N$ matrix. If $L = N$, then the system is critically determined; if $L < N$, the system is underdetermined, and if $L > N$, the system is overdetermined. Furthermore, the rank of $\mathbf{B}^R$ may be less than L, and in which case, the system can be underdetermined.

Equation 7.39 cannot be simply substituted back into Eqs. 7.27 and 7.28 for power, as when it is an overdetermined system, it does not represent an equivalence.

7.2.8 The perfect wave

In reality, one does not have control over the incident wave. The incident wave exists, and WEC should be designed to effectively absorb its power. However, as a theoretical exercise, consider the incident wave as variable. Using the diffraction transfer matrix, one can find an incident wave that can be completely absorbed by a given body.

Equation 7.39 gives the relationship for optimal power absorption, substituting the diffraction transfer matrix, $\boldsymbol{b}^S = \mathbf{D}\boldsymbol{a}$:

$$\mathbf{B}^R\boldsymbol{\xi} = -\left(\frac{1}{2}\mathbf{I} + \mathbf{D}\right)\boldsymbol{a} \tag{7.40}$$

For an arbitrary motion, $\boldsymbol{\xi}$, (e.g. unit motion), assuming the inverse of $\left(\frac{1}{2}\mathbf{I} + \mathbf{D}\right)$ exists, the incident wave amplitudes that can be completely absorbed are:

$$\boldsymbol{a}^C = -\left(\frac{1}{2}\mathbf{I} + \mathbf{D}\right)^{-1}\mathbf{B}^R\boldsymbol{\xi} \tag{7.41}$$

where $\boldsymbol{a}^C$ are the coefficients of the "perfect" incident wave for the given body. This system of incident wave and body represent true 100% efficient wave energy absorption.

Because the number of body coefficients must be finite, the completely absorbed incident wave must also have a finite number of coefficients, which means that the incoming power, given by Eq. 7.25, must also be finite. Within linear wave theory in 3D to completely absorb an incident wave with a finite sized body, the incident wave itself must also be finite.

7.3 Results

In this section, the cylindrical wave power computation is applied to the classical examples of a heaving and surging (and swaying) point absorbers, and well-known results are found. The computation is then applied to a finite sized Bristol Cylinder type WEC. The implications of the body size on wave component absorption are considered. Examination of the coefficients is used to optimize the body shape. Finally, for a particular Bristol Cylinder, the perfect wave is found.

7.3.1 Heaving point absorber

Equations 7.27 and 7.28 are quite powerful and from them, the results for heaving and surging point absorbers are readily obtained. To demonstrate their utility, the heaving and surging point absorber cases will be shown in a somewhat backwards fashion. That is, first it will be shown that one can obtain the correct power absorption by canceling out the correct wave components, and then it shall be shown that the waves at these components are heaving and surging radiated waves respectively.

In Eq. 7.27, set $d_0 = 0$. For all other m, $d_m = \frac{1}{2}a_m$, and the power in those terms is 0. The total power absorbed is then:

$$P = \frac{1}{2}\rho g \frac{c_g}{k} |a_0|^2 \tag{7.42}$$

Consider now the incident wave to be a plane wave, $a_0 = a$ (Eq. 3.89). The capture width is $CW = \frac{1}{k}$, or the more familiar:

$$CW = \frac{\lambda}{2\pi} \tag{7.43}$$

What wave makes $d_0 = 0$? A point absorber is defined by having no scattered wave, that is, $b_m^S = 0$, for all m, which means that from Eq. 7.28, the radiated wave is completely defined by the 0^{th} order wave component:

$$\eta^R = b_0^R H_0^{(2)}(kr) \tag{7.44}$$

where for optimal motion, the product of the body motion and the radiated wave amplitude must be half the incident amplitude and 180° out of phase: $\xi b_0^R = -\frac{1}{2}a$. As discussed by Wypych *et al.* (2012), intuitively, one can see that this is the wave produced by an axisymmetric body moving in heave. By definition, a heaving point absorber is defined as generating an isotropic radiated wave. That means that the radiated wave per motion amplitude is the product of a complex coefficient, b^R, and some function in the radial direction, $g(r)$, but independent of the angular direction: $\eta^R = b^R g(r)$. Setting this equal to the solutions to the BVP, Eq. 7.4, and then taking a Fourier transform over direction, $\int_{-\pi}^{\pi} \{\} e^{-\mathrm{i}n\theta} d\theta$, It is clear that $b^R = b_0^R$ and $g(r) = H_0^{(2)}(kr)$.

7.3.2 Surging-swaying point absorber

Taking a similar approach to that of the heaving point absorber, in Eq. 7.27, set $d_{-1} = d_1 = 0$, and for all other m, $d_m = \frac{1}{2}a_m$. The total power absorbed is:

$$P = \frac{1}{2}\rho g \frac{c_g}{k}\left(|a_{-1}|^2 + |a_1|^2\right) \tag{7.45}$$

Considering the incident wave to be a plane wave, from Eq. 3.89, $a_{-1} = \mathrm{i}ae^{\mathrm{i}\beta}$, and $a_1 = -\mathrm{i}ae^{-\mathrm{i}\beta}$, and so $|a_{-1}|^2 = |a_1|^2 = |a|^2$, and finally the capture width is $CW = \frac{2}{k}$, or:

$$CW = \frac{\lambda}{\pi} \tag{7.46}$$

What wave makes $d_{-1} = d_1 = 0$? Again, $b_m^S = 0$, for all m. As two wave components are involved, $m = -1, 1$, first take the case where there are two DOF. One gets the matrix equation:

$$\begin{bmatrix} b_{-1,1}^R & b_{-1,2}^R \\ b_{1,1}^R & b_{1,2}^R \end{bmatrix} \begin{bmatrix} \xi_1 \\ \xi_2 \end{bmatrix} = -\frac{a}{2} \begin{bmatrix} \mathrm{i}e^{\mathrm{i}\beta} \\ -\mathrm{i}e^{-\mathrm{i}\beta} \end{bmatrix} \tag{7.47}$$

The radiated waves due to each motion are essentially undefined. However, in order to get a more concrete picture, consider the motion, ξ_1 to be surge, and ξ_2 to be sway. A surging point absorber is characterized by a wave with a cosine shape in the angular direction, and a swaying point absorber has a sine shaped wave. Assuming the body is axisymmetric, then the amplitude of the surging and swaying waves would be the same. The waves are:

$$\eta_1^R = b^R \cos\theta g\left(r\right) \qquad \text{surge} \tag{7.48a}$$

$$\eta_2^R = b^R \sin\theta g\left(r\right) \qquad \text{sway} \tag{7.48b}$$

Set these equations equal to Eq. 7.4, take the Fourier transform, $\int_{-\pi}^{\pi}\{\}\, e^{-\mathrm{i}n\theta}d\theta$, and use the relations, $\cos\theta = \frac{1}{2}\left(e^{\mathrm{i}\theta} + e^{-\mathrm{i}\theta}\right)$, $\sin\theta = \frac{\mathrm{i}}{2}\left(e^{\mathrm{i}\theta} - e^{-\mathrm{i}\theta}\right)$, and $H_{-m}^{(2)} = e^{-\mathrm{i}m\pi}H_m^{(2)}$. For surge:

$$\int_{-\pi}^{\pi}\left\{b^R\cos\theta g\left(r\right)\right\}e^{-\mathrm{i}n\theta}d\theta=\int_{-\pi}^{\pi}\left\{\sum_{m=-\infty}^{\infty}b_{m,1}^R H_m^{(2)}\left(kr\right)e^{\mathrm{i}m\theta}\right\}e^{-\mathrm{i}n\theta}d\theta$$
$$\left(\frac{1}{2}b^R e^{-\mathrm{i}\theta}+\frac{1}{2}b^R e^{\mathrm{i}\theta}\right)g\left(r\right)=\left(-b_{-1,1}^R e^{-\mathrm{i}\theta}+b_{1,1}^R e^{\mathrm{i}\theta}\right)H_1^{(2)}\left(kr\right) \tag{7.49}$$

and for sway:

$$\int_{-\pi}^{\pi}\left\{b^R\sin\theta g\left(r\right)\right\}e^{-\mathrm{i}n\theta}d\theta=\int_{-\pi}^{\pi}\left\{\sum_{m=-\infty}^{\infty}b_{m,1}^R H_m^{(2)}\left(kr\right)e^{\mathrm{i}m\theta}\right\}e^{-\mathrm{i}n\theta}d\theta$$
$$\left(-\frac{\mathrm{i}}{2}b^R e^{-\mathrm{i}\theta}+\frac{\mathrm{i}}{2}b^R e^{\mathrm{i}\theta}\right)g\left(r\right)=\left(-b_{-1,2}^R e^{-\mathrm{i}\theta}+b_{1,2}^R e^{\mathrm{i}\theta}\right)H_1^{(2)}\left(kr\right) \tag{7.50}$$

From which it is clear that $b_{-1,1}^R=-\frac{1}{2}b^R$, $b_{1,1}^R=\frac{1}{2}b^R$, $b_{-1,2}^R=\frac{\mathrm{i}}{2}b^R$, $b_{-1,2}^R=\frac{\mathrm{i}}{2}b^R$ and $g\left(r\right)=H_1^{(2)}\left(kr\right)$. Substituting this into 7.47, the system of equations is

$$\frac{b^R}{2}\begin{bmatrix}-1 & \mathrm{i}\\ 1 & \mathrm{i}\end{bmatrix}\begin{bmatrix}\xi_1\\ \xi_2\end{bmatrix}=-\frac{\mathrm{i}a}{2}\begin{bmatrix}e^{\mathrm{i}\beta}\\ -e^{-\mathrm{i}\beta}\end{bmatrix} \tag{7.51}$$

which is solved to get:

$$\begin{bmatrix}\xi_1\\ \xi_2\end{bmatrix}=\frac{\mathrm{i}a}{b^R}\begin{bmatrix}\cos\beta\\ \sin\beta\end{bmatrix} \tag{7.52}$$

The total radiated wave is then:

$$\xi_1\eta_1^R+\xi_2\eta_2^R=\mathrm{i}a\cos\left(\theta-\beta\right)H_1^{(2)}\left(kr\right) \tag{7.53}$$

The total outgoing portion of the incident wave at $m=-1,1$ is:

$$\begin{aligned}\eta^{I,out} &= \frac{1}{2}a_{-1}H_{-1}^{(2)}\left(kr\right)e^{-\mathrm{i}\theta}+\frac{1}{2}a_1 H_1^{(2)}\left(kr\right)e^{\mathrm{i}\theta}\\ &= -\mathrm{i}a\cos\left(\theta-\beta\right)H_1^{(2)}\left(kr\right)\end{aligned} \tag{7.54}$$

and the sum of the radiated wave and the outgoing portion of the incident wave is 0.

In this example, two DOF, surge and sway, were needed to absorb power from an incident plane wave with an incident angle β, because a plane wave has two DOF: amplitude and direction. Wypych *et al.* (2012) are able to find the same power absorption for only

the surging DOF, because they define surge always to be in the direction as the incident wave, i.e. by rotating the surging wave so that relative incident wave angle is 0, which effectively gives the radiated wave two DOFs. One can see that, here when $\beta = 0$ in Eq. 7.52, $\xi_1 = \frac{\mathrm{i}a}{b^R}$ and $\xi_2 = 0$, and only surge is needed.

A particular case to consider is the overdetermined system, where there is indeed only a single body DOF, surge, but the incident wave still has an angle of rotation (two DOFs). The overdetermined system of equations is:

$$\frac{b^R}{2}\begin{bmatrix} -1 \\ 1 \end{bmatrix}\xi_1 = -\frac{\mathrm{i}a}{2}\begin{bmatrix} e^{\mathrm{i}\beta} \\ -e^{-\mathrm{i}\beta} \end{bmatrix} \tag{7.55}$$

where the best fit is: $\xi_1 = \frac{\mathrm{i}a}{b^R}\cos\beta$, which is the same value as is given in Eq. 7.52. Substituting $\xi_1 b_{-1,1} = -\frac{\mathrm{i}a}{2}\cos\beta$ and $\xi_1 b_{1,1} = \frac{\mathrm{i}a}{2}\cos\beta$ back into equations 7.27 and 7.28, the power of the surging wave is: $P = \rho g \frac{c_g}{k}|a|^2\cos^2\beta$, and the capture width is

$$CW = \frac{\lambda}{\pi}\cos^2\beta \tag{7.56}$$

An example of an underdetermined system is a surging-swaying, pitching-rolling point absorber. This has four modes of motion, $N = 4$, but only interacts with two wave components, $L = 2$. For such a system, different combinations of motions could produce optimal power absorption. Alternatively, certain sets of motions could potentially produce no radiated wave, which may be referred to as a "wave free" modes (Pizer, 1993).

7.3.3 Surging, swaying and heaving point absorber

In the case of a surging, swaying and heaving point absorber, one gets the system of equations:

$$\begin{bmatrix} -\frac{1}{2}b_s^R & \frac{\mathrm{i}}{2}b_s^R & 0 \\ 0 & 0 & b_h^R \\ \frac{1}{2}b_s^R & \frac{\mathrm{i}}{2}b_s^R & 0 \end{bmatrix}\begin{bmatrix} \xi_1 \\ \xi_2 \\ \xi_3 \end{bmatrix} = -\frac{a}{2}\begin{bmatrix} \mathrm{i}e^{\mathrm{i}\beta} \\ 1 \\ -\mathrm{i}e^{-\mathrm{i}\beta} \end{bmatrix} \tag{7.57}$$

From which it is clear that the surge-sway solution is decoupled from the heave solution, and so they can be treated independently and solved separately as in Sections 7.3.1 and 7.3.2. The total capture width is the sum of the heaving and the surging/swaying capture widths:

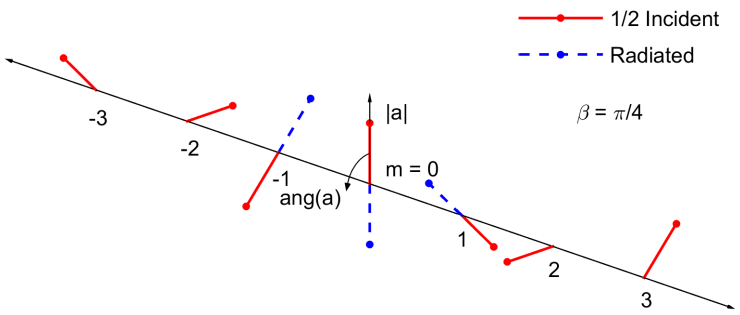

Figure 7.3: The figure shows a polar plot of the incident coefficients for a plane wave traveling in the direction, $\beta = \frac{\pi}{4}$, and the radiated coefficients due to optimal motions of a surging, swaying, heaving point-absorber.

$$\begin{aligned} CW &= \frac{\lambda}{2\pi} + \frac{\lambda}{\pi} \\ &= \frac{3\lambda}{2\pi} \end{aligned} \tag{7.58}$$

Figure 7.3 is a three-dimensional polar plot of the radiated wave coefficients ($\sum b_{m,i}\xi_i$) and half the incident coefficients ($\frac{1}{2}a_m$) as a function of m for an incident direction of $\beta = \pi/4$. One can clearly see that the radiated wave has an amplitude of $|a|/2$ and the opposite phase of the incident, but only exists for the wave components at $m = -1, 0, 1$.

In the absence of incident waves, the body's surge, sway and heave motions are decoupled. However, because a plane wave defines a relationship between the incident m coefficients, the resulting optimal motions are coupled. For a surge, sway, heave point absorber, because there are three body DOF and three incident wave coefficients of interest, optimal power can be absorbed for all coefficients. However, for a finite-sized body with, for example, two DOF, but body coefficients at $|m| > 1$, there will be an overdetermined system. The relationship between the different orders of radiated wave coefficients, $\xi_i b^R_{i,m}$ may not be the same as that of the diffracted coefficients, $\frac{1}{2}a_m + b^S_m$, which will result in inefficiencies. This shall be shown in the next example of a finite-sized 3D Bristol Cylinder.

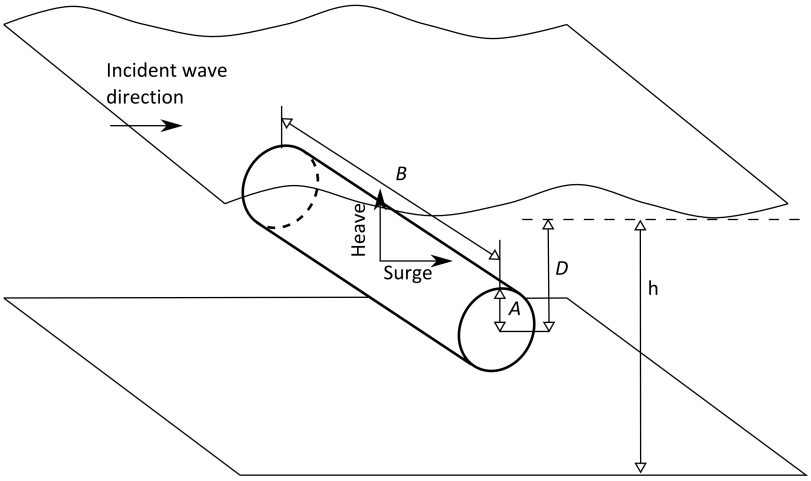

Figure 7.4: The diagram indicates the dimensions and modes of motion of a Bristol Cylinder.

7.3.4 Bristol cylinder

Ogilvie (1963) observes that a 2D cylinder moving in an orbital motion using surge and heave DOFs in otherwise calm water could produce a wave in only one direction. Evans (1976) (and Evans *et al.* (1979)) capitalize on this behavior to create a WEC known as the Bristol Cylinder, which can in 2D absorb 100% of the incident power by radiating a wave only in the direction of the incident wave, which destructively interfered with the incident wave to cancel it. In this section, the Bristol Cylinder is used as an example of the power computation with cylindrical coefficients of a finite sized body.

The Bristol Cylinder is defined by three properties: radius - A, beam (or width) - B, and depth of submergence, D. See Figure 7.4. The Cylinder is allowed to move in surge and heave but no other modes of motion. All dimensions are non-dimensionalized by the cylinder radius, A. The effect of varying the width of the cylinder shall be seen on its wave field coefficients. The parameters used in the study are shown in Table 7.1. Of particular note are the range of beams: $B/A = 1, 2, 5, 10, 20, 50$.

The core computation was conducted with the BEM solver WAMIT. Cylindrical coefficients for the scattered and the radiated waves were found using the cylindrical surface method developed in Chapter 4.

Figure 7.5 shows the results from the Bristol Cylinder simulations. Each row is a different nondimensional body beam. The figures on the left in column a) show the orbital motion of the optimal motions of the cylinder, and the arrows indicate the direction of motion. The dashed line shows the free-surface at time $t = 0$ to give a sense of the wavelength relative to the orbital motion. The figures in column b) show

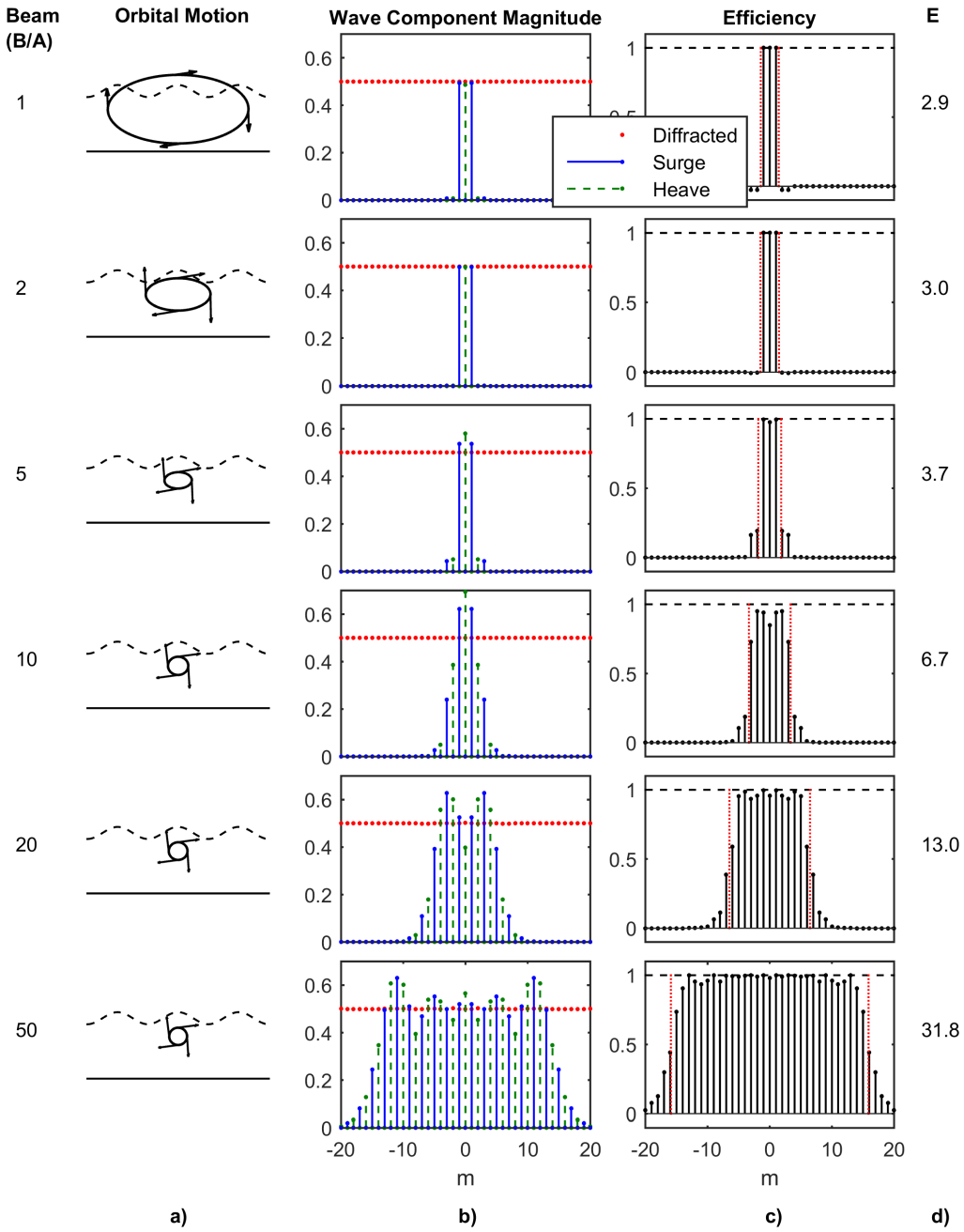

Figure 7.5: Each row of plots is for a different nondimensional beams of the Bristol Cylinder. Column a) shows the motions - the dashed line is the incident wave profile; column b) shows the magnitude of the wave coefficients - the red dots are the diffracted coefficients; the solid blue lines are the surge coefficients, and the green dashed lines are the heave coefficients; column c) shows the per wave component efficiencies; and in column d) the E value (Eq. 7.34) is given.

	Property	Parameter	Value
Wave	wavelength	λ/A	10
	water depth	h/A	10
	incident direction	β	0
	incident amplitude	a/A	1
Body	radius	A/A	1
	depth of submergence	D/A	3
	beam	B/A	1,2,5,10,20,50

Table 7.1: Table of the parameters used in the Bristol Cylinder study.

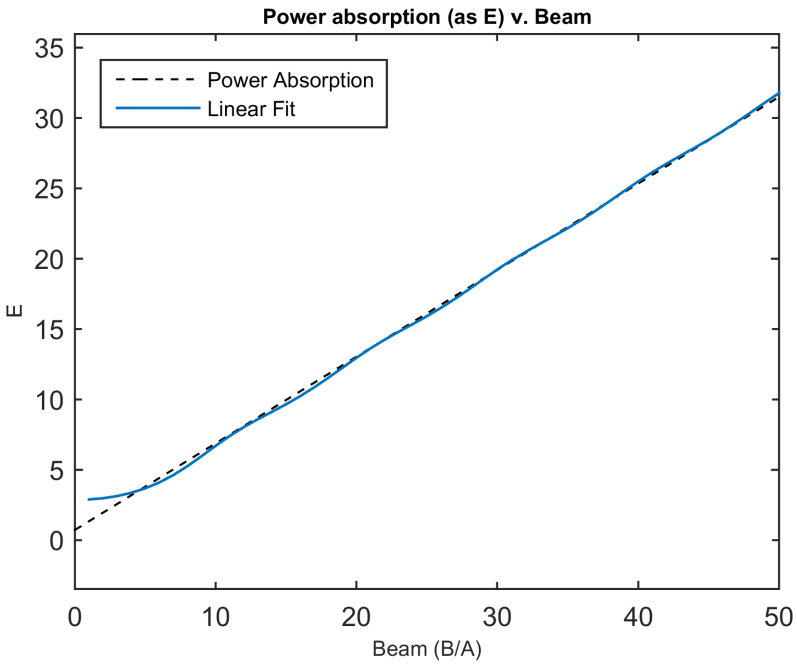

Figure 7.6: Plot of optimal power absorption of the Bristol Cylinder given as E (Eq. 7.34) as a function of the Cylinder's beam.

the magnitudes of the wave components: the diffracted components, $\frac{1}{2}a_m + b_m^S$ as the red dots, and the surge and heave radiated wave components due to optimal motions, $b_{m,1}^R\xi_1$ and $b_{m,2}^R\xi_2$ as the solid blue and green dashed lines respectively. Column c) plots show the wave component efficiency given by Eq. 7.32. Finally, along the right, the value of E (Eq. 7.34.) is given in column d).

For a the Bristol Cylinder at the depth, $D/A = 3$, scattering is negligible, and the diffracted wave components are almost equal to the incident value of $\frac{1}{2}a_m$ for all m and at all widths.

The first case, $B/A = 1$, is a very small cylinder, which generates small waves per amplitude motion. In order to generate a wave large enough for optimal power absorption, the cylinder must make very large motions. One can see that its orbital motions are unrealistic (it would emerge above the free surface) and violate the premises of linearity by passing across multiple waves in a single cycle. Like in the case of a surging-heaving cylinder, the heave motion only produces a wave component at $m = 0$, and the surge motion only produces components at $|m| = 1$. Neglecting this impossible behavior, one can see that it does *nearly* achieve the optimal power absorption for a surging-heaving point absorber, for which $E = 3$. As the Bristol Cylinder is not axisymmetric, it does not produce a perfect heave or surge wave. There is a significant amount of power at the $|m| = 0, 1$ components, but there is also power at components at $|m| = 2, 3$. In optimal motions, the components at $|m| = 2, 3$ radiate energy, which is shown as a negative efficiency in column c). The resulting value of E is very close to, but not quite 3. Besides being physically impossible to move as it would need to, the very thin Bristol Cylinder is not as effective as a surging and heaving point absorber.

At $B/A = 2$, shown in the second row, the motions still violate the limits of linearity. Nonlinearities, i.e. changes in the relative position of the body, will likely have an effect. However, it does reach (or at least very close to it) the optimal power absorption of a surging-heaving point absorber. And there is very little inefficiency in the active components. The $|m| = 0, 1$ components absorb nearly 100% of the energy and all other components absorb none.

In the next case, $B/A = 5$, one sees that there is noticeably more energy at $|m| = 2, 3$. In optimal motions, the Bristol Cylinder absorbs power at these components, but in doing so generates radiated waves at $|m| = 0, 1$ that are not perfectly tuned in amplitude and phase to the diffracted, lowering slightly the efficiency of these components. As compared to the $B/A = 2$ case, the power absorption is only increased by 23%, despite a 2.5 times increase in the beam. However, the amplitudes of the body motions are significantly reduced.

At $B/A = 10$, there are noticeable components up to $|m| = 5$, and like the $B/A = 5$

case, the higher order components contribute to the total power absorption, but at lower order components the radiated waves again are not perfectly tuned to the diffracted, bringing down their efficiency.

The pattern is continued at $B/A = 20$ and $B/A = 50$. Multiple peaks form in the cylindrical coefficients, where some coefficients are greater than the optimal magnitude and some are smaller. There are two peaks for $B/A = 20$, and five for $B/A = 50$.

As the beam gets larger, although the high order wave components are inefficient, the efficiencies of the lower order components approach 100%. The middle of a long cylinder, would resemble a 2D case, for which the Bristol Cylinder is known to have 100% energy absorption. This suggests that there is some sort of end effect occurring, which may reduce the overall performance of the cylinder. The multiple peak behaviour of the coefficients results in some inefficiencies of the lower order components as well.

Included in the plots of efficiency are two vertical red dashed lines at $\pm E/2$. Considering E to represent the number of components that are effectively absorbed completely, the region inside these lines is that where the fictitious components that are 100% absorbed. As the cylinder gets larger, it impacts more partial wave components, although, the components of the highest orders absorb less power than those of lower orders. Perhaps a more effective design would have less end effects, by having higher efficiencies at components inside the red lines and little impact on components outside them. This would mean that the fictitious components that are 100% absorbed are in fact real components that are 100% absorbed.

In a similar way to a heaving and surging point absorber, the heave motion only produces waves at even components (even m), and the surging motion only produces waves at odd components (odd m). Heave is an even wave mode of motion; it produces symmetric waves on each side of the body, and surge is an odd mode of motion - it produces a waves that are 180° out of phase on each side of the body. If the Bristol Cylinder only moved in surge, it would fail to absorb the even incident wave modes. The opposite would be true if it only absorbed in heave.

Figure 7.6 shows a plot of E as a function of the nondimensional beam, B/A, for a range of cylinders as well as a linear fit. Except for very small beams, the relationship between the beam and power absorption is close to linear. For $B/A < 4$, one can get more power than would be expected by the linear fit. This could be considered the point-absorber region, and the device is in a sense all ends. That is, it obtains a significant amount of power from its highest order components, which are only $|m| = 0, 1$. To compensate for its small size, it moves in a large amplitude of motion. Perhaps if the motions are physically realizable, the point absorber functionality offers an advantage.

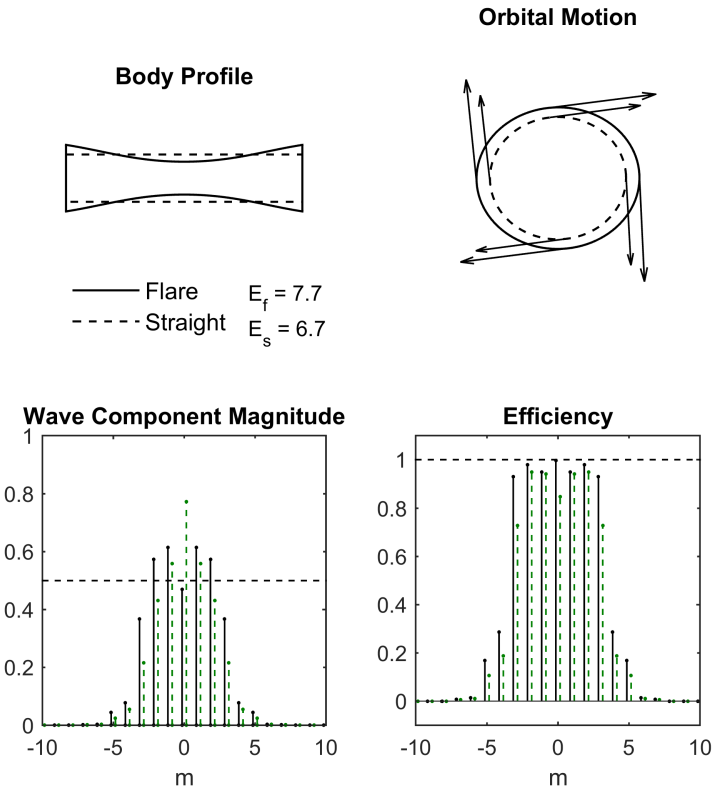

Figure 7.7: The figure gives results for the flare-end Bristol Cylinder compared to those of the straight Bristol Cylinder. In the top left plot are the body profiles, and in the top right are the orbital motions. The bottom left plot shows the magnitude of the coefficients; the flare-end coefficients are given by the solid black lines and the straight Cylinder coefficients are the green dashed lines; the black dashed line indicates the magnitude of $\frac{1}{2}|a_m|$, which is used rather than the diffracted coefficients as in Figure 7.5, because each cylinder would have different (although very slightly) diffracted coefficients. The figure in the bottom right shows the per wave component efficiencies. Finally, values of E (Eq. 7.34) are given for each body.

7.3.5 Bristol cylinder with flared ends

In the previous section, it was suggested that the straight Bristol Cylinder has a sort of end effect that reduces the overall performance. As was discussed in Section 7.2.1, the magnitude of a coefficient m is proportional to the magnitude of J_m integrated over the body's surface, and the body size limits the order of m that is obtainable. However, it seems that even in regions of m where there are non-zero values, there are still inefficiencies, because the relationship in amplitude and phase of the radiated components is not the same as that of the diffracted components.

Consider the results for the Bristol Cylinder with $B/A = 10$, the waves at $|m| = 0, 1$ are larger than they should be for optimal motions (i.e. $\left|\xi b_m^R\right| > \left|\frac{1}{2}a_m\right|$), while the waves at $|m| = 2-5$ are not large enough ($\left|\xi b_m^R\right| < \left|\frac{1}{2}a_m\right|$). This raises the question: can (or how

can) the geometry of the cylinder be modified so as to increase optimal performance?

In an attempt to do so, make the radius of the cylinder a function of y, where y is the position in direction along the beam. Intuitively, it seems that because the lowest order components are too large, and the highest are too small, one would want the radius to be smaller in the middle and larger near the ends. Bessel functions of the appropriate order have this behaviour, and since the cylindrical coefficients are proportional to the integral of Bessel functions, it seems not unreasonable to use them in a function for the cylinder radius. Take the function for the radius along the beam to be:

$$A(y) = \frac{1}{A'}\left(1 + \sum_{m=2}^{5} J_m(k|y|)\right) \tag{7.59}$$

where A' is a constant used to normalize the volume of the Cylinder with the modified profile so that it has the same volume as the straight Bristol Cylinder. Equation 7.59 gives a Bristol Cylinder with flared ends, which shall be referred to as the flare-end Cylinder. The total volume is kept constant because it makes it a more suitable comparison and because the cost of a WEC is proportional to the volume, and one would like to know if the WEC performance can be improved without increasing the cost.

The results of the flare-end Bristol Cylinder are shown alongside the results of the straight Bristol Cylinder in Figure 7.7. The body profiles are shown in the upper left. The figure in the upper-right is of the optimal orbital motions, where one can see that those of the flare-end Cylinder are slightly larger than the straight Cylinder. Considering the plot at the lower left, the coefficients of the flare-end Cylinder are closer in magnitude to $\frac{1}{2}|a_m|$ than are those of the straight Cylinder, which leads to improvements in the efficiencies, shown at the right, at all values of m. Finally, for the flare-end Cylinder, $E = 7.7$, compared to $E = 6.7$ for the straight Cylinder, which is a power performance improvement of 15%.

Equation 7.59 was chosen through a trial-and-error process and was only applied the the Bristol Cylinder of beam, $B/A = 10$. Other geometries were considered including a linearly increasing radius and rounded ends. Equation 7.59 likely does not define the optimal shape for longer beams. An useful investigation would be to evaluate other shapes, including non-cylindrical profiles, particularly at longer beams where multiple peaks in the coefficient magnitudes are seen.

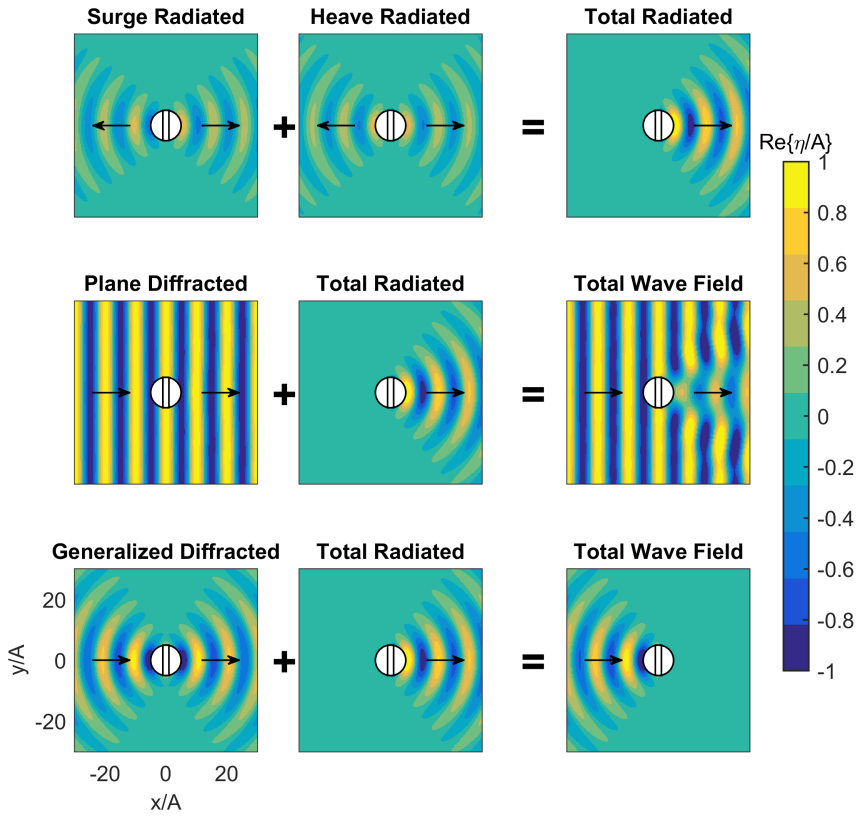

Figure 7.8: The figures show the superposition of various wave fields to demonstrate wave cancellation processes. The cylinder and the cylindrical region surrounding it are in white with black outlines. In the top row, the surge and heave radiated waves are added to produce a total wave that only travels to the right. In the middle row, the radiated wave is added to an incident plane diffracted wave field to show wave power absorption. And in the bottom row the total radiated wave is added to the "perfect" generalized diffracted wave. In the figure in the bottom right, all incident wave power is completely absorbed by the body.

7.3.6 Bristol cylinder wave field

Figure 7.8 shows plots of the wave field of the straight Bristol Cylinder with a beam, $B/A = 10$. The wave field is plotted as $\mathrm{Re}\{\eta\}$, which shows the wave elevation at time $t = 0$, in order to display the magnitude and phase of the wave. The body and cylindrical region circumscribing it are represented as a black outline about a white region. Arrows on either side of the body indicate the primary direction of the wave.

The plots are designed to show how various wave fields are superimposed to absorb wave energy by wave cancellation. The top row shows the superposition of the surging and the heaving radiated waves. Both motions emit waves that propagate away from the origin. On the left-hand side of the body, the surging and heaving waves have the same magnitude and shape but opposite phase, and on the right-hand side, they

have the same magnitude and shape and the same phase. When the waves are added together, the waves that propagate to the left cancel one another, while the waves that propagate to the right reinforce one another, and the resulting total radiated wave only propagates to the right.

The next row shows the superposition of the plane-wave diffracted wave field and the radiated wave to create a total wave field. As mentioned, the scattering is very low for the Cylinder at a depth of $D/A = 3$, so the diffracted wave field looks like a plane wave. The radiated wave propagates only to the right, and the total wave field shows a plane wave on the left-hand side of the body and a modified wave field, in which power is absorbed, on the right. Because the plane wave has straight crests, while the radiated wave has curved crests, the resulting total wave field has points where the waves destructively interfere to reduce local energy and points where they constructively interfere to increase the local energy. For a plane wave, this is the wave field of maximum power absorption.

The bottom row shows a generalized incident wave that can be perfectly absorbed by this particular Bristol Cylinder. The incident coefficients a_m are computed using Eq. 7.41, and the diffraction transfer matrix for the Cylinder is computed following Chapter 6. Again, the scattering is minimal, so the diffracted wave field looks like the incident wave field. The incident wave is a wave traveling primarily right to left, but converging towards the origin from the left and then diverging from the origin on the right. The diverging pattern has the same shape and magnitude, but opposite phase of the diverging pattern of the total radiated wave. When the generalized diffracted wave field and the total radiated wave field are added together, the radiated wave field completely cancels the diverging or outgoing portion of the diffracted wave field, and the incoming energy is 100% absorbed. The total wave field is then completely represented by energy sinks. This is a real efficiency of 100% in three-dimensions.

7.4 Discussion

The motivation for the analysis of the floating body wave field using cylindrical waves was 1) because such waves are very good at representing the wave field of floating bodies, and their use can reduce complex problems to linear algebra, and 2) in search of a measure of hydrodynamic efficiency. The cylindrical representation of the floating body wave field makes it clear that interactions with respect to power absorption occur independently on each partial cylindrical wave when the outgoing radiated wave destructively interferes with the outgoing portion of the diffracted wave. From this, a per wave component efficiency can be formulated.

A small body in 3D will only interact with a few wave components at the lowest orders, e.g. heaving and surging point absorbers have components at $|m| = 0, 1$. As a body becomes larger, it affects, and thus can absorb energy from, more wave components at higher orders of m, increasing the total energy absorption. The body must have two DOF, one that produces a symmetric wave to absorb power from the even modes, and one that produces an anti-symmetric wave to absorb power from the odd modes. Or it can have a single DOF that produces an asymmetric wave. For a heaving-surging point absorber, it is fairly easy to absorb 100% of the energy of the $|m| = 0, 1$ modes, but as the body gets larger, optimal efficiencies at each wave mode are sacrificed in favor of a better overall power absorption. The efficiencies are particularly poor at the highest m modes. A sort of 3D or end effect is observed, which was mitigatable by adjusting the shape of a body to increase performance.

The sum of the per wave component efficiencies forms a non-dimensional quantity, referred to here as E, which represents the number of fictitious wave components that are completely absorbed. E is equal to $k \cdot CW$ as well as the gain or wave focusing ability of the device. A value of $E > 1$ means that a WEC performs better than an optimal heaving point absorber, and $E < 1$ means that it performs worse. Although E is not an efficiency, it is a very meaningful quantity for assessing the hydrodynamic performance of a device.

Regarding the interaction of a body with an incident long-crested plane wave, it has been suggested that any portion of the radiated wave that does not propagate in the direction of the incident wave constitutes wasted energy, such that a heaving wave alone would be the most "inefficient" wave. It is true that the addition of more wave components to create a more focused radiated wave would in fact absorb more power, however, each radiated component only interacts with the same order component of the diffracted wave field. One still needs to absorb the $m = 0$ wave; a completely focused wave is not possible without it. A body that surges and does not heave misses this wave and generates a bidirectionally focused wave. The heaving wave does not represent inefficiency, but is a necessary low order wave that needs to be generated/absorbed. Furthermore, the $m = 0$ heave wave, being the lowest order, seems the easiest to absorb, and for long waves it contains a significant amount of power - a $1\,m$ amplitude, $8\,s$, $100\,m$ long wave in deep water has $500\,kW$ of power in the heave mode alone! So a WEC should strive to absorb this wave first, before trying to absorb waves of higher orders - i.e. heave before surge.

The standard definition of a point absorber is a body where the scattered wave is zero. Since such bodies must be small compared to the wavelength, it seems reasonable to presume that they could only produce $|m| = 0, 1$ heaving and surging waves. However, if one were to take a different definition of a point absorber to be a body that is

infinitesimally small, $kr_0 \approx 0$, as discussed in Section 7.2.1, only the $m = 0$ component could be non-zero. A point-absorber that is truly a point could only produce a heaving wave as a finite body size is required for a surging wave.

Also, here it is interesting to address the difference between the formulations for power absorption through the wave field discussed in Section 2.5 as that of Farley and Newman. Farley's formulation indicated that the total scattered and radiated waves traveling in the direction of the incident should be made to cancel the incident, while Newman's showed that the complex amplitude of the radiated wave traveling in the opposite direction from the incident needed to be optimized. The difference can be explained due to the fact that Newman's formula uses the complex conjugate of the radiated wave Kochin function. In a sense, the complex conjugate is the wave that represents a time reversal: $\mathrm{Re}\left\{\xi_i \mathcal{F}_i^{R*}(\beta - \pi)\, e^{\mathrm{i}\omega t}\right\} = \mathrm{Re}\left\{\xi_i^* \mathcal{F}_i^{R}(\beta - \pi)\, e^{-\mathrm{i}\omega t}\right\}$. Newman's formula says that to optimize the power absorption, the radiated waves that would be produced by a body moving in reverse, $\xi_i^* e^{-\mathrm{i}\omega t}$, must be as close as possible to the reversed incident wave. Consider the last row of Figure 7.8 showing complete absorption of a generalized incident wave. The final figure on the right is of the total wave field, where the incident wave travels to the right and is completely absorbed by the Cylinder. If one reverses time, this wave looks like a radiated wave due to the Bristol Cylinder moving in the opposite direction - i.e. flip the direction of the arrow.

For the example of 100% power absorption, a generalized incident wave was needed. Because the body is finite-sized, the wave that can be completely absorbed by it must have a finite amount of incoming power. This is in contrast to a long-crested incident plane wave, which has an infinite amount of incoming power and is the basis for the concepts of capture width and relative capture width. Efficiency is a difficult concept to apply to a system where the incoming power is infinite, but can readily be applied for finite incoming power.

The generalized incident wave is clearly not a real wave that one would find in the ocean. However, neither are harmonic plane waves; their utility arises because they can give a reasonable representation of the sea by the superposition of many plane waves traveling in different directions with random amplitudes and phases. This raises the question, is there a physical meaning to such a generalized incident wave as the one considered here? Does the curved generalized wave relate to random short-crested seas? And if so, can it be used to design WECs or define a WEC efficiency? It seems that future work is needed to improve the understanding of the cylindrical incident wave field.

Any incident wave has net zero power through a closed control surface. Infinite power arises in long-crested plane waves when considering either the flux through an infinitely long open surface or when considering just the *incoming* portion of the cylindrical form.

The incoming cylindrical wave is made up of Hankel functions of the first kind; for any partial wave, m, the flux through a cylindrical control surface of any radius is constant. This is implied by the conservation of energy, but mathematically it arises because for large radii, the magnitude of the wave decays as $1/\sqrt{kr}$, and for small radii, when $J_m \to 0$, $Y_m \to \infty$. For small radii, the *incoming* wave has Bessel functions of the second kind that go to infinity. However, the *incident* wave is made up solely of Bessel functions of the first kind, which go to zero at small kr. Like for a body of finite size, which has a finite number of coefficients, for a given finite region of the wave field, the incident wave should only have a finite number of coefficients that have an impact. This suggests that there exists a more general definition of efficiency that could be applied even to waves with non-decaying coefficients.

7.5 Summary

Expressions for water wave power absorption and optimal body motion using cylindrical partial waves have been developed. For a wave energy absorbing body, the efficiency of each wave component was defined as the ratio of the power absorbed at that component to the outgoing power in the diffracted wave at that component. Using the cylindrical coefficient power absorption, well-known results for heaving and surging point absorbers were readily obtained. An example of a computation of a finite-sized 3D body, the Bristol Cylinder, was given. Because the body's radiated coefficients were not aligned to the diffracted coefficients at all m, wave component inefficiencies resulted. As the cylinder got longer, the efficiencies for low order components, representing the middle of the cylinder, went to 100%, which connected the 3D body to 2D theory where a Bristol Cylinder is known to be 100% efficient. However, near the ends of the cylinder the efficiencies tended to be worse representing a sort of end effect. Optimal performance of the Bristol Cylinder was improved by 15% by modifying its shape to flare its ends but keeping its volume constant. A 3D wave body system was shown where all of the incident power was absorbed, representing a 100% efficiency. This required a non-standard generalized incident wave, which suggests the need for future work on incident cylindrical waves, particularly in relation to short-crested seas.

Chapter 8

Conclusion

The thesis presented fundamental and application-oriented developments for the cylindrical solutions to the linear wave boundary-value problem (BVP). New methods were developed for finding the cylindrical coefficients of floating bodies, where the coefficients were used to compute multi-body wave interactions and wave energy absorption. Throughout, examples have been given using wave energy converters (WECs), because both the wave farm problem and the wave energy absorption problem are compelling applications. However, the methods for finding the cylindrical coefficients are general and can be applied to floating bodies of any shape and mode of motion.

8.1 Cylindrical surface method

A new method, called the cylindrical surface method, was described in Chapter 4, in which numerical or physical measurements of the wave field over a circular-cylindrical surface that circumscribes a floating body are used to find the body's cylindrical scattered and radiated coefficients. The results showed that cylindrical wave representations are valid for an arbitrary geometry. For example, although the terminator and attenuator geometries used therein were not circular in shape, their wave fields were well represented by the summation of cylindrical waves. Due to the interaction of the cylindrical radiated and scattered waves with the planar incident wave, the wave field patterns for all geometries, circular or not, showed mostly parabolic standing waves and a wave shadow. In general, for any geometry or wave condition, linear WEC wave fields can be computed using the cylindrical surface method and represented as a summation of partial cylindrical waves.

8.2 Cylindrical surface method experiments

In Chapter 5, the cylindrical surface method was applied to results from experiments on two bodies at three frequencies. Cylindrical coefficients were computed from measurements around a circle of wave gauges, and the wave field predicted by cylindrical wave theory showed good agreement with measurements at other field points. The results served to validate the cylindrical surface method and the cylindrical representation of the wave field. The biggest problems with the accuracy of the results were due to tank reflections of the scattered and radiated waves. With only a single circle of wave gauges, the incoming reflected waves could not be isolated from the outgoing scattered and radiated waves.

8.3 Diffraction and force transfer matrices and interaction theory

The cylindrical surface method was extended to a new method for computing the diffraction transfer matrix in Chapter 6. The diffraction transfer matrix is a quantity necessary for solving the array interaction problem. Another linear operator useful in the interaction problem, the force transfer matrix, was introduced. The method for finding the diffraction transfer matrix theoretically requires the same number of problems to be solved as the method of Goo and Yoshida (1990). However, in practice, the method presented herein is computationally less efficient than that of Goo and Yoshida (1990), but it is more general and can be applied experimentally.

The method was applied to solve various interaction problems, and where possible, results were validated against outputs computed completely with WAMIT. The interaction theory and WAMIT results showed excellent agreement, except for small errors due to evanescent waves. Because the interaction theory computation represents each floating body in the array with 10s of coefficients, rather than 100s to $1,000$s of panels, solutions with interaction theory are on the order of $10,000$ times $((1,000/10)^2)$ faster than the direct method (i.e. solving for all bodies directly in WAMIT). For real array problems, like wave farms, interaction theory is the only practical approach possible.

8.4 Cylindrical wave power absorption

Motivated by a search for a physical definition of hydrodynamic efficiency, and the need for a better understanding of the process of wave energy absorption, in Chapter 7, a new expression for wave energy absorption based on the general cylindrical form of progressive waves was developed. This was applied to the wave field of floating bodies, and a new expression for energy absorption efficiency on a per wave component basis

was presented. The classical problem of optimal motions was solved with the cylindrical power formulations, and an expression for a incident wave that can be completely absorbed by a given body was found. The absorption of this wave by the body represents 100% efficiency.

The cylindrical power expressions were applied to the heaving and surging point absorber problems and well-know results were easily found. Then the three-dimensional (3D) case of a Bristol Cylinder with various beams was considered. A very narrow Bristol Cylinder was shown to act as a point absorber. Wider Bristol Cylinders exhibited 3D effects: the efficiencies of the lowest components, which represented the middle of the cylinder, went towards 100%, while the efficiencies of the higher-order components, which represented the cylinder ends, were low. The middle of the cylinder behaved like the two-dimensional case, where 100% energy absorption is possible, while near the ends, there was a sort of end-effect. The end-effect was shown to be mitigatable by flaring the tips of the cylinder, which improved the WEC's maximum power absorption by 15%. Also shown was an example of a wave that was 100% absorbed by a finite-sized Bristol Cylinder.

8.5 Future work

The results presented in this thesis, particularly from Chapter 7, suggest that more work on the cylindrical form of incident waves could advance engineering applications and fundamental understanding. The general cylindrical form of incident waves (Eq. 3.87) has been explored very little. However, to some degree, the author has conducted some preliminary numerical and experimental research. The experiments conducted for the thesis included tests on generalized incident waves.

In the interaction problem, the waves incident to a body that were the scattered or radiated waves of another body are given as the general cylindrical form of the incident waves. A general harmonic curved incident wave can be created computationally or experimentally, but it seems challenging to imagine its real-world physical significance.

Real ocean waves are short-crested and random. A useful further development of the cylindrical solutions would be to extend the general form of the incident cylindrical waves to that of a stochastic wave field represented by a variance density spectrum. This could improve the efficiency of the computation of wave-body and multi-body interaction problems for short-crested seas. For example, for axisymmetric bodies, only the lowest two cylindrical waves ($|m| = 0, 1$) are needed to compute the body forces. In a short-crested sea, the standard means of computing the wave effects is to dissect the directional dependence into an arbitrary number of incident plane waves at different

directions and solve the problem for each one. The number of waves directions is usually based on the shape of the directional variance density spectrum and personal judgment. However, if stochastic incident waves can be defined with cylindrical waves, only 3 incident waves ($m = -1, 0, 1$) would be needed to solve the problem for any directional spreading. That is, the body would define the number of problems that need to be solved. Because arbitrary finite-sized geometries can be described by a finite number of cylindrical coefficients, the same would be true for any body.

Efficiency on a per cylindrical wave component basis was shown in Chapter 7. As a body wave field can be represented with a finite number of coefficients, there is a limit to the amount of power that a body defined by a finite size (e.g. the radius of the circumscribing circle) can absorb. However, only fuzzy relationships between the cylindrical coefficients and the relative size of the body were developed (see Section 7.2.1). It is shown that an incident long-crested plane wave contains an infinite amount of power in an infinite wave field. However, reason states that a finite sized body does not have an infinite amount of power available to it. Here, it seems that the cylindrical solutions could be useful in developing a more complete theory of the efficiency of wave energy absorption, which would be of great academic and practical interest.

Appendix A

OpenORE

The scholarships that funded my PhD were the University of Edinburgh Principal's Career Development and the Edinburgh Global Research Scholarships. For which, I needed to engage in a career development activity. I chose to look at the importance of open-source practices in scientific research and in the field of offshore renewable energy. I found this activity extremely interesting and it took me down pathways that I would not have been exposed to otherwise, including: open-source practices, web development, project development, international networking, and fund raising. Some of the resulting research in open-source practices can be found in McNatt *et al.* (2014).

Specifically, I developed a website called OpenORE, which stands for open source offshore renewable energy:

`http://openore.org/`

The goal was to create a place where researchers and businesses could share and find free software tools and data. I presented the idea at the 2013 INORE Symposium in Wales, where it received tremendous support from the INORE community. The International Network on Offshore Renewable Energy (INORE) (`http://inore.org/`) is a network of early-stage researchers working in offshore renewable energy. INORE wanted to help move the idea forward and I was elected to the INORE steering committee.

Over the course of the two years that I served on the INORE steering committee, I searched for funding to build the website that I envisioned. However, I was never able to raise adequate funding, and I came to realize that the project was perhaps too big for the voluntary INORE steering committee to handle perpetually.

I have personally maintained the OpenORE site, posting about open source developments in the offshore renewable energy, of which there have been many. Even though

the website that I originally envisioned did not come to fruition, I feel the project was a success. I learned a tremendous amount, I had the priviledge of serving with amazing people on the INORE committee, and I created a website that contains useful information. My decision to share the code and experimental data developed during my PhD (see Appendix B) came from my experience working on OpenORE.

Appendix B

Code and Data Repositories

In order to increase the impact of my work and in an effort to see that the code and experimental data I created over the course of my PhD was not lost, I have made the code and data available for free online. The impetus to do so arose out of my work on OpenORE (see Appendix A)

B.1 Mwave

Mwave is a Matlab package that contains the methods to perform all the computations presented in this thesis. It began as a pre- and post-processor for WAMIT, particularly for computing body motions, power absorption and wave fields. It can perform the interaction theory computation which makes it useful for wave farms. Also, some hooks have been writen for integrating it with Nemoh.

I did my best to include comments and some unit tests for the code, but of course as time pressures developed these were the first to go. There are some examples, which is a good place to start with the code. If users have questions, I shall be happy to help. The code can be found on my Github page:

`https://github.com/cmcnatt/mwave`

B.2 Cylindrical wave field experiments

Experiments can be costly and time consuming. So it is best to make the most of any experimental data available. As I was planning my experiments, I kept in mind that I wanted to release them publicly, and I think this helped me tremendously to stay organized.

The experimental data is hosted on Figshare.com, but it is accessed most easily by following the links on my Github page, which also contains the code I wrote to analyze the data:

`https://github.com/cmcnatt/cyl_wfe`

B.3 Thesis results

The Matlab code I wrote to create the results presented in this thesis is also available online. It is dependent on both the mwave and the cyl_wfe packages and having the experimental data. But if you get all three and the thesis code, you should be able to reproduce every figure in this thesis.

`https://github.com/cmcnatt/mcnatt_thesis`

Appendix C

Experimental Results

This appendix contains the complete set of radiated and scattered wave field results from the cylindrical wave field experiments discussed in Chapter 5.

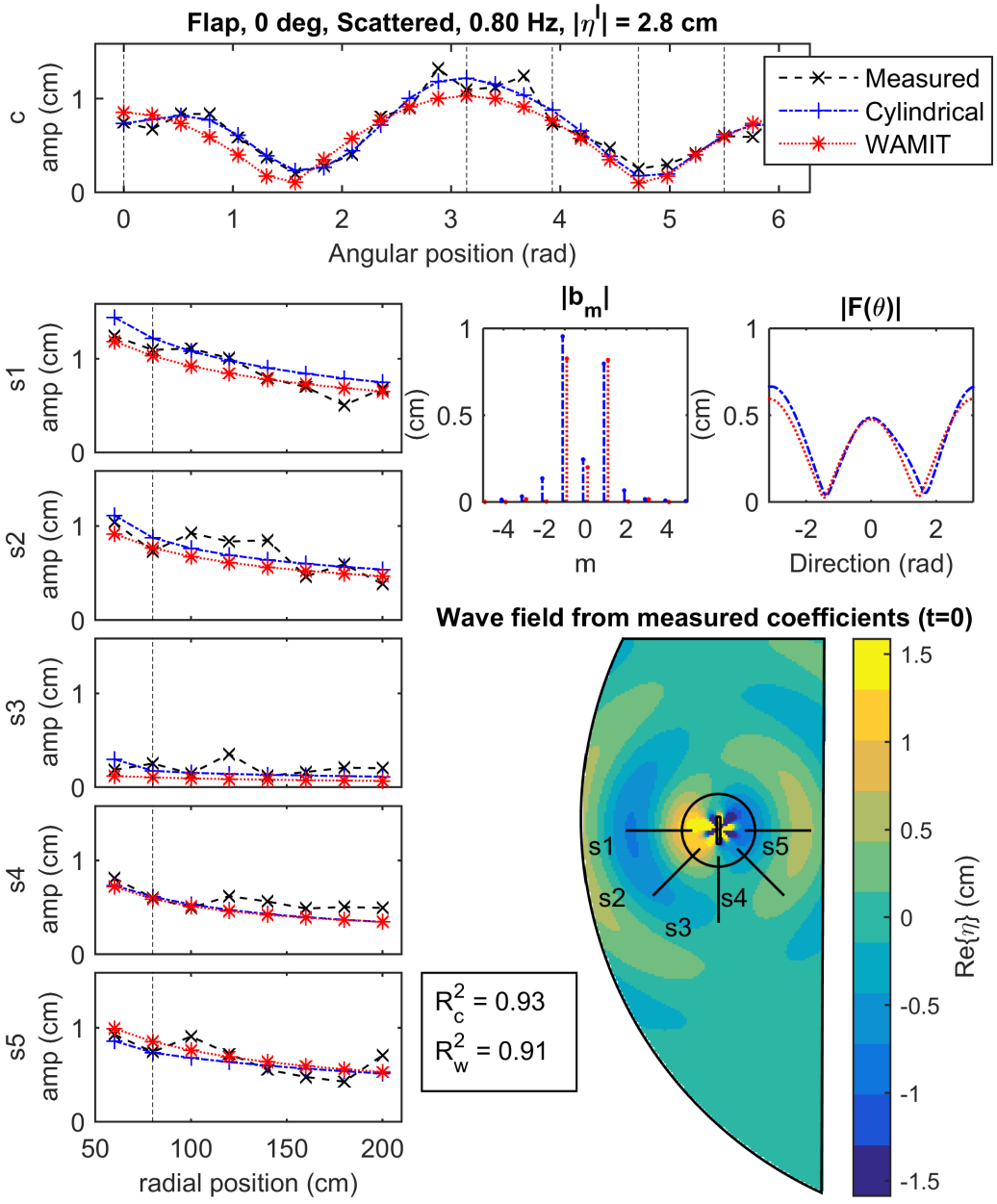

Figure C.1: Flap, 0° orientation, scattered wave field, 0.8 Hz

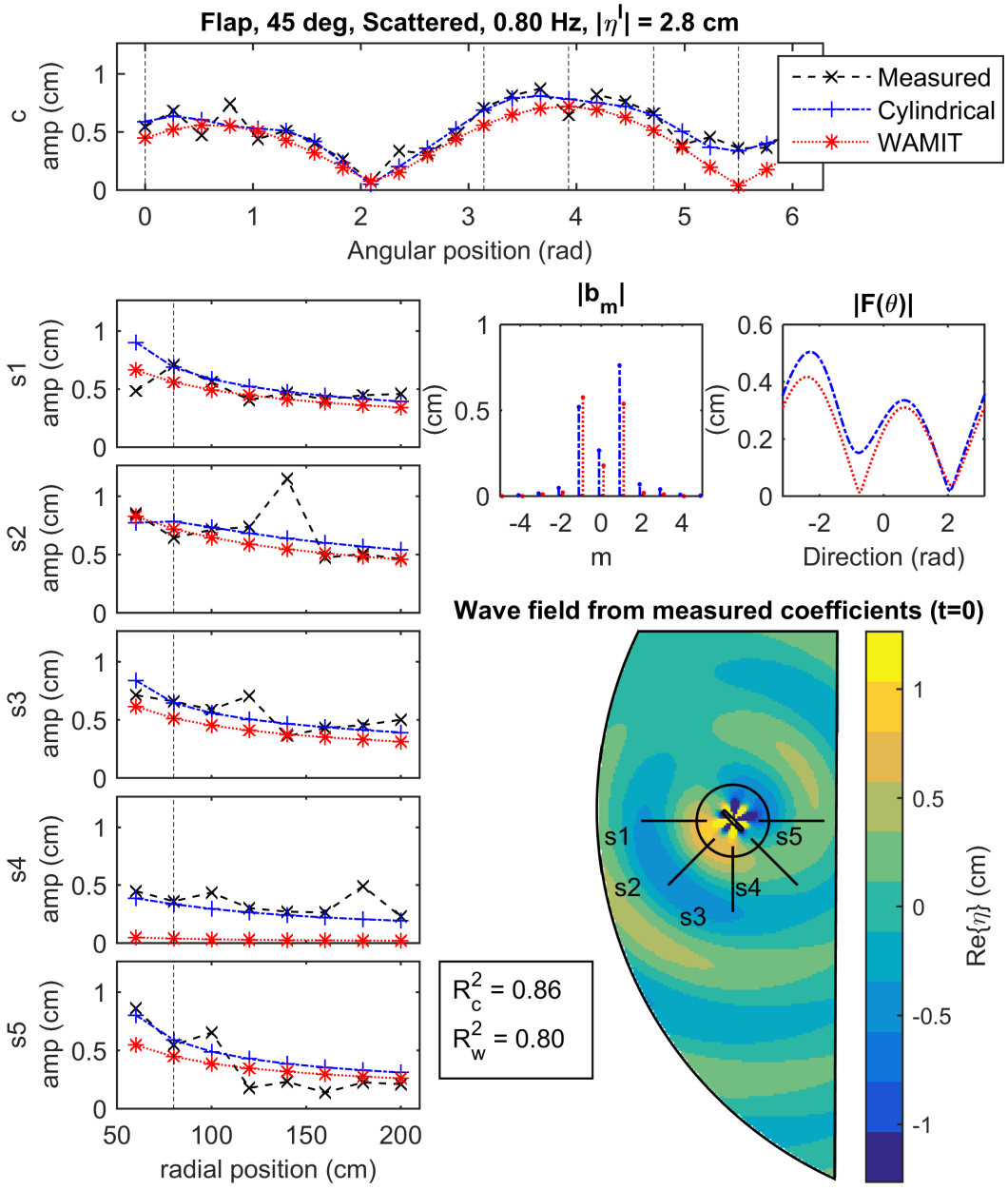

Figure C.2: Flap, 45° orientation, scattered wave field, 0.8 Hz

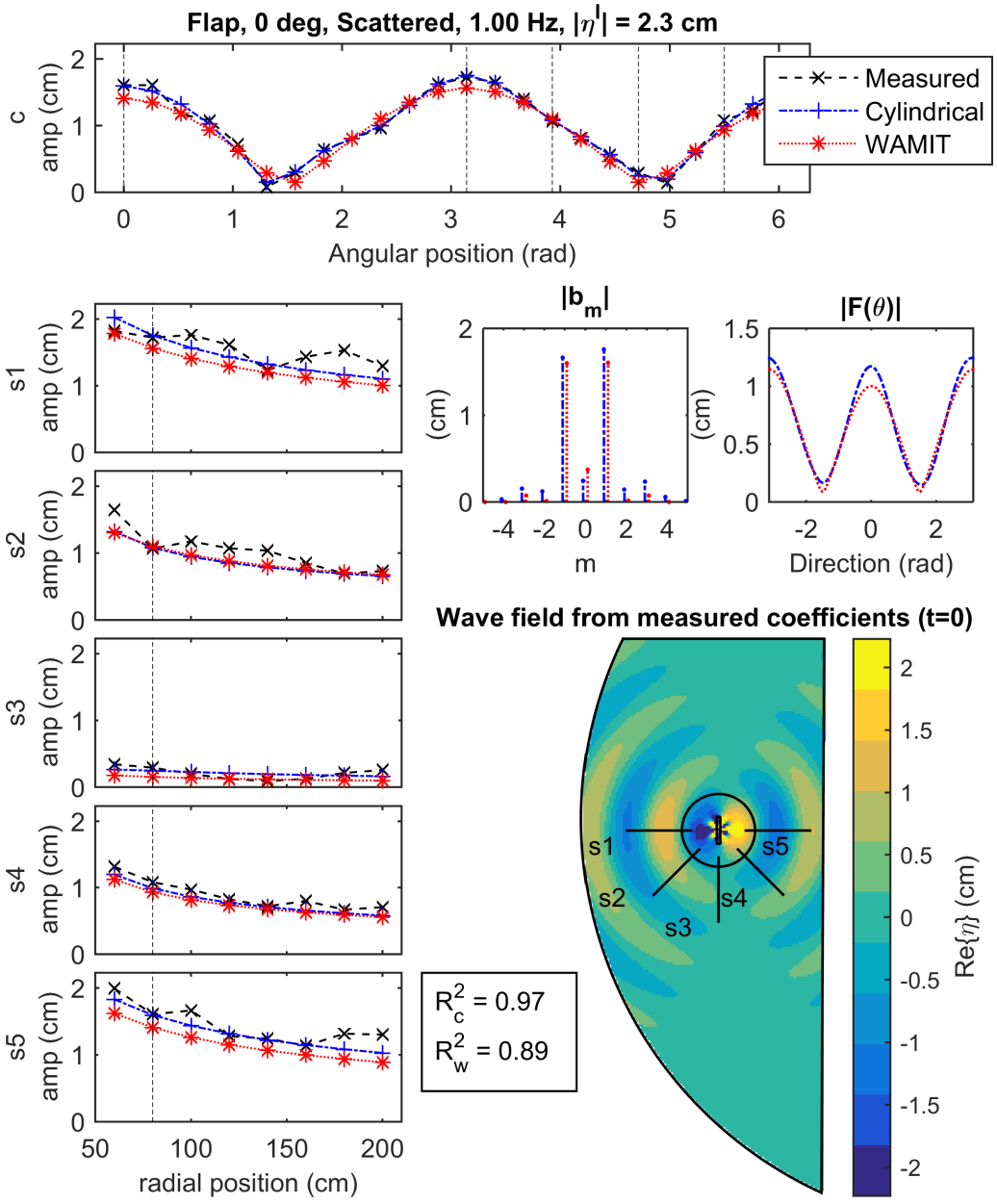

Figure C.3: Flap, 0° orientation, scattered wave field, 1 Hz

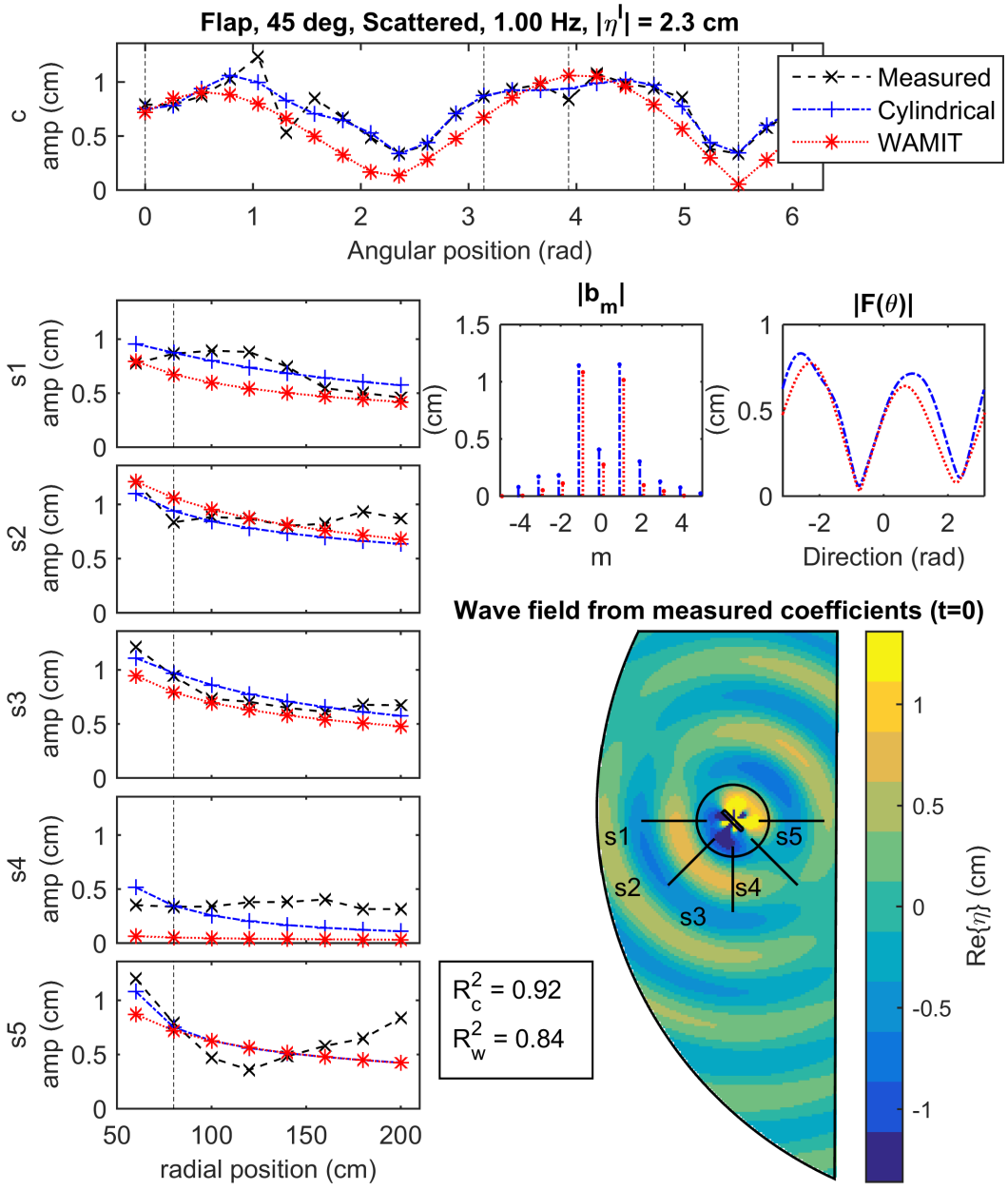

Figure C.4: Flap, 45° orientation, scattered wave field, 1 Hz

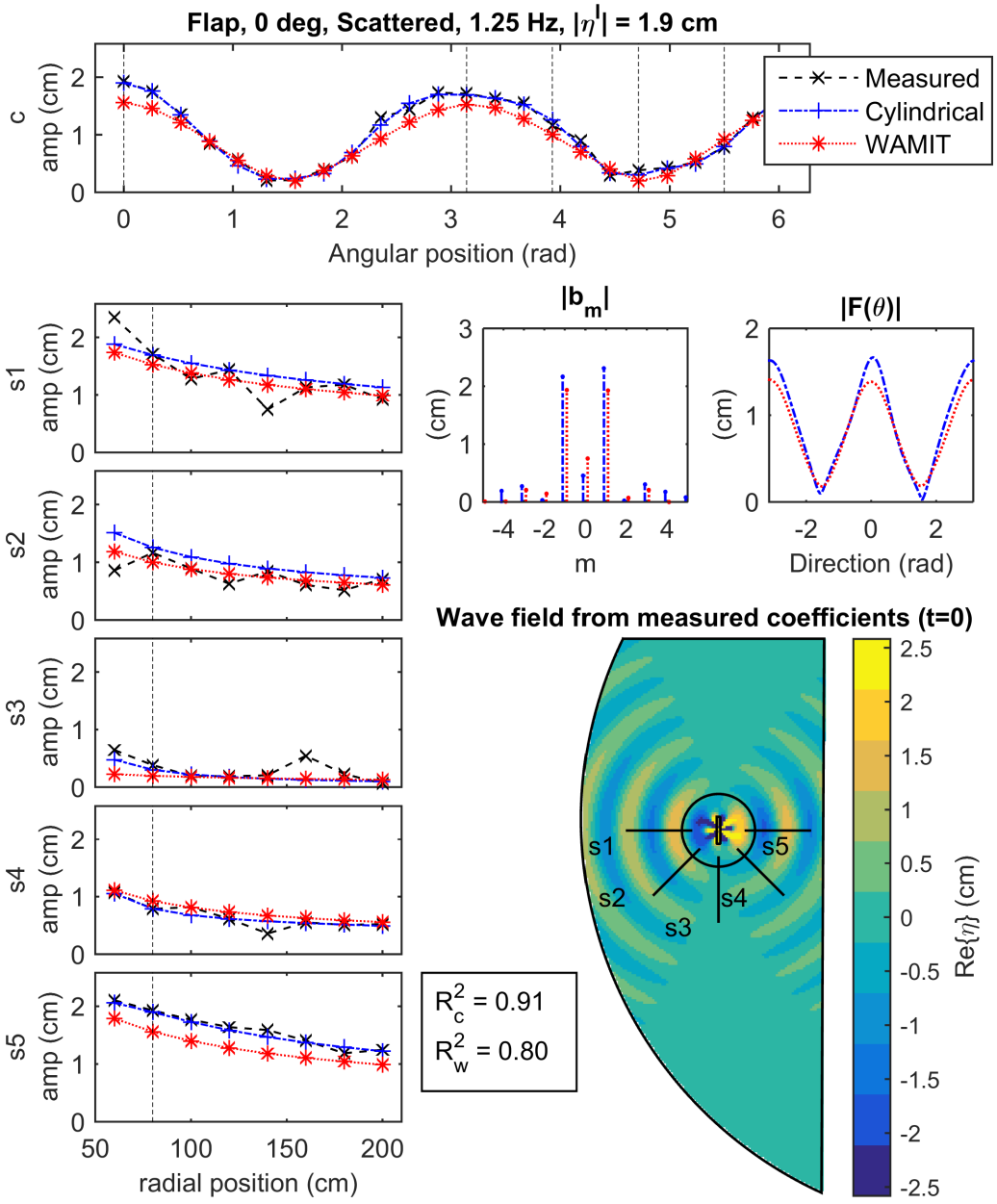

Figure C.5: Flap, 0° orientation, scattered wave field, 1.25 Hz

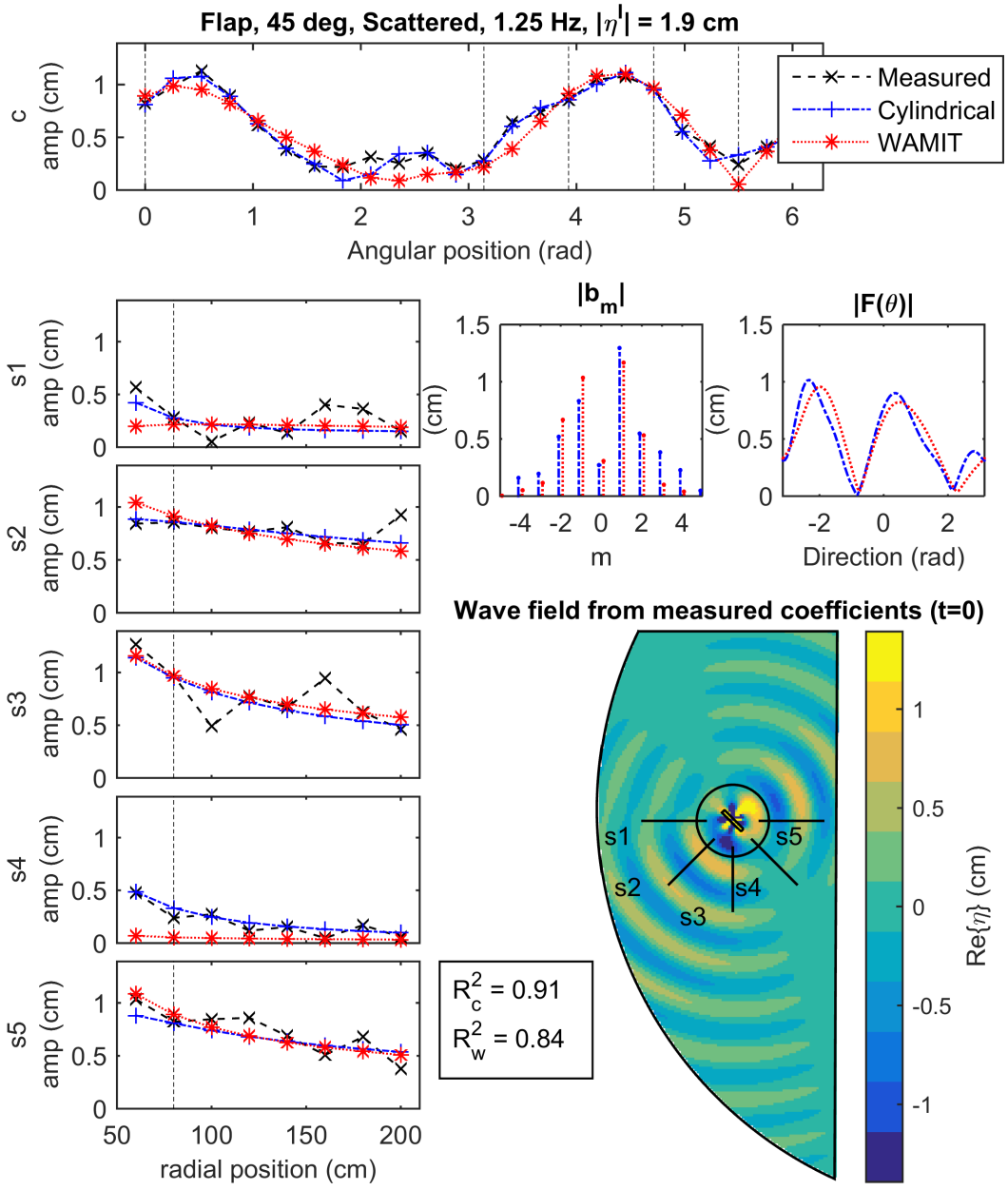

Figure C.6: Flap, 45° orientation, scattered wave field, 1.25 Hz

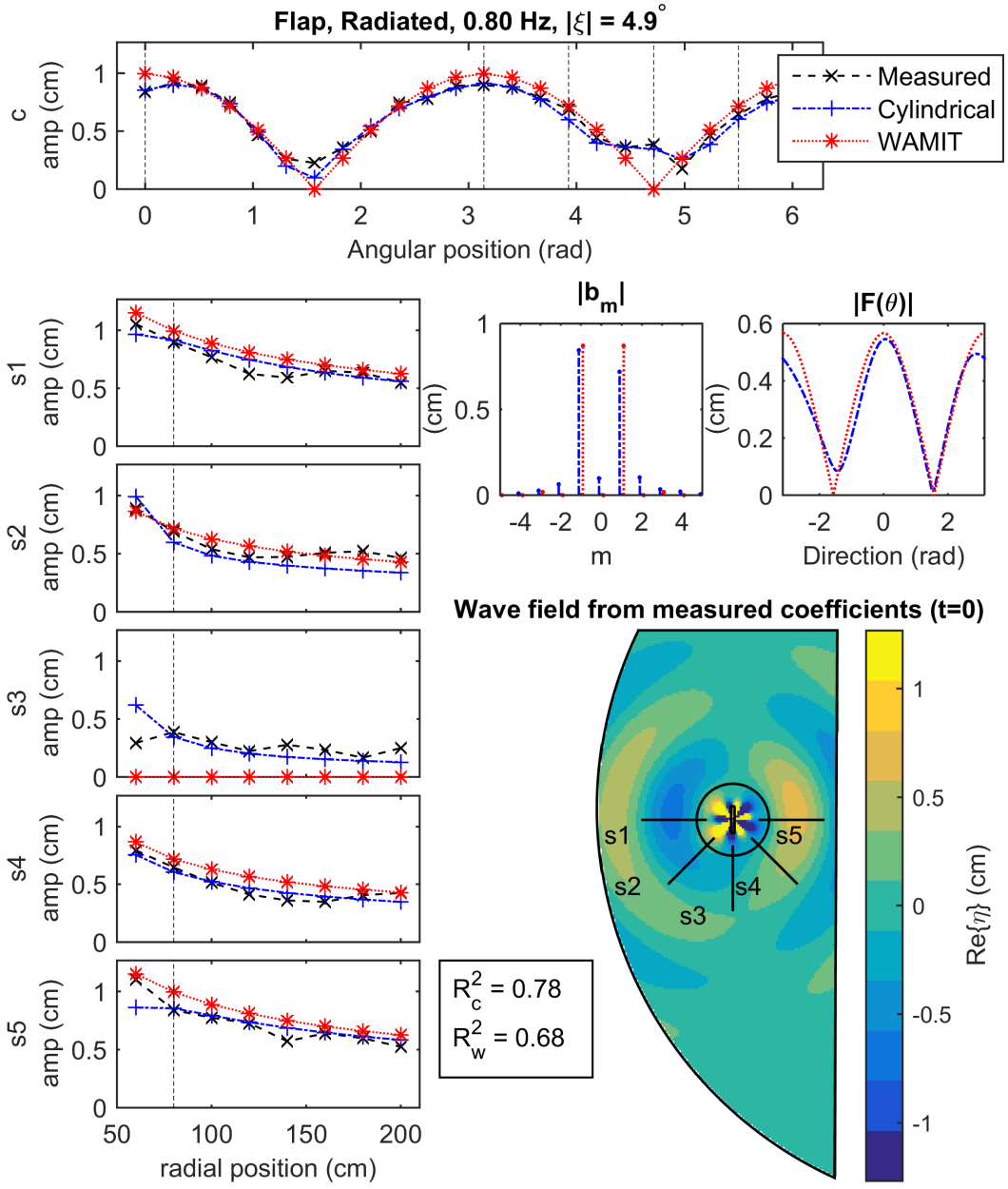

Figure C.7: Flap, radiated wave field, 0.8 Hz

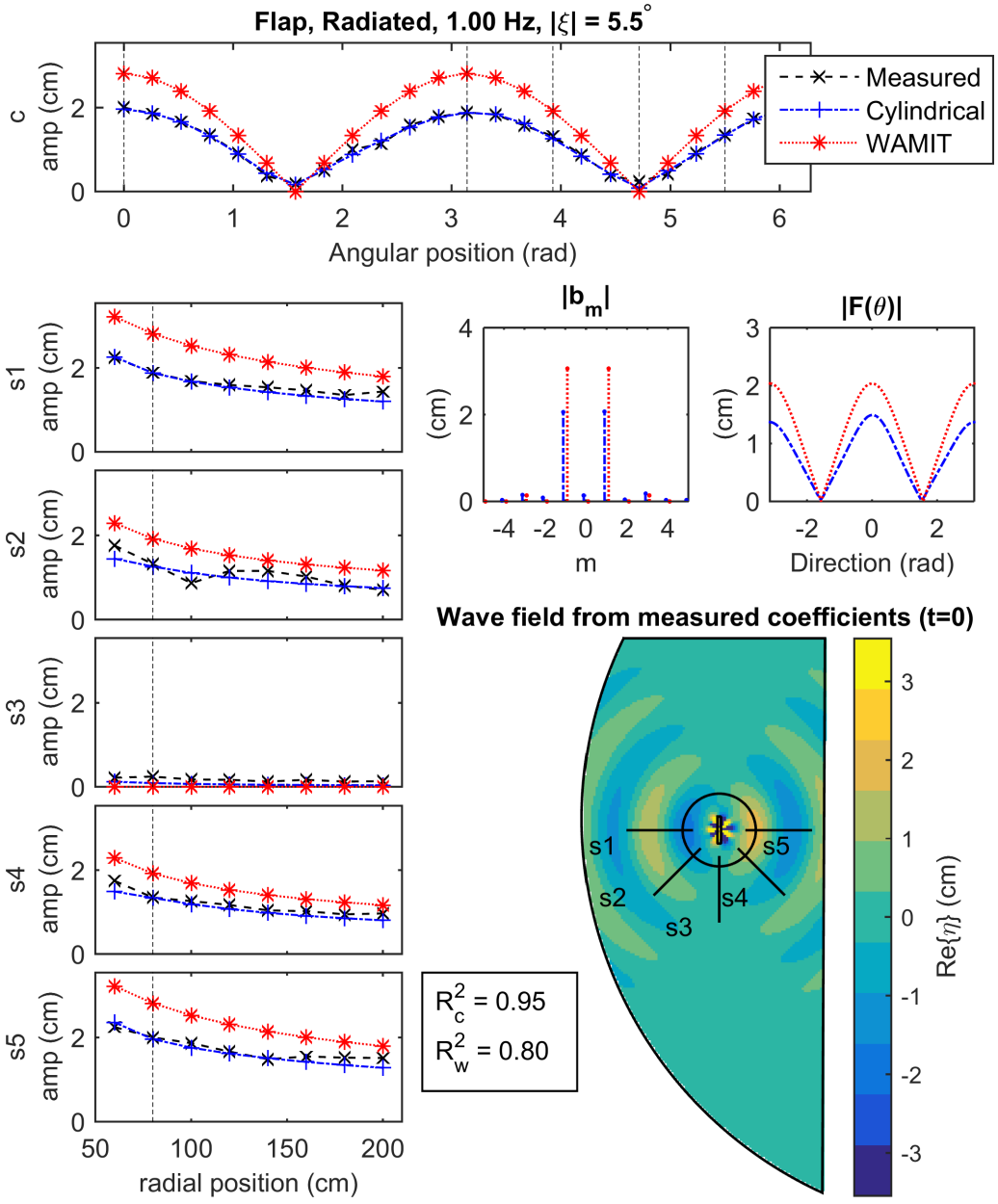

Figure C.8: Flap, radiated wave field, 1 Hz

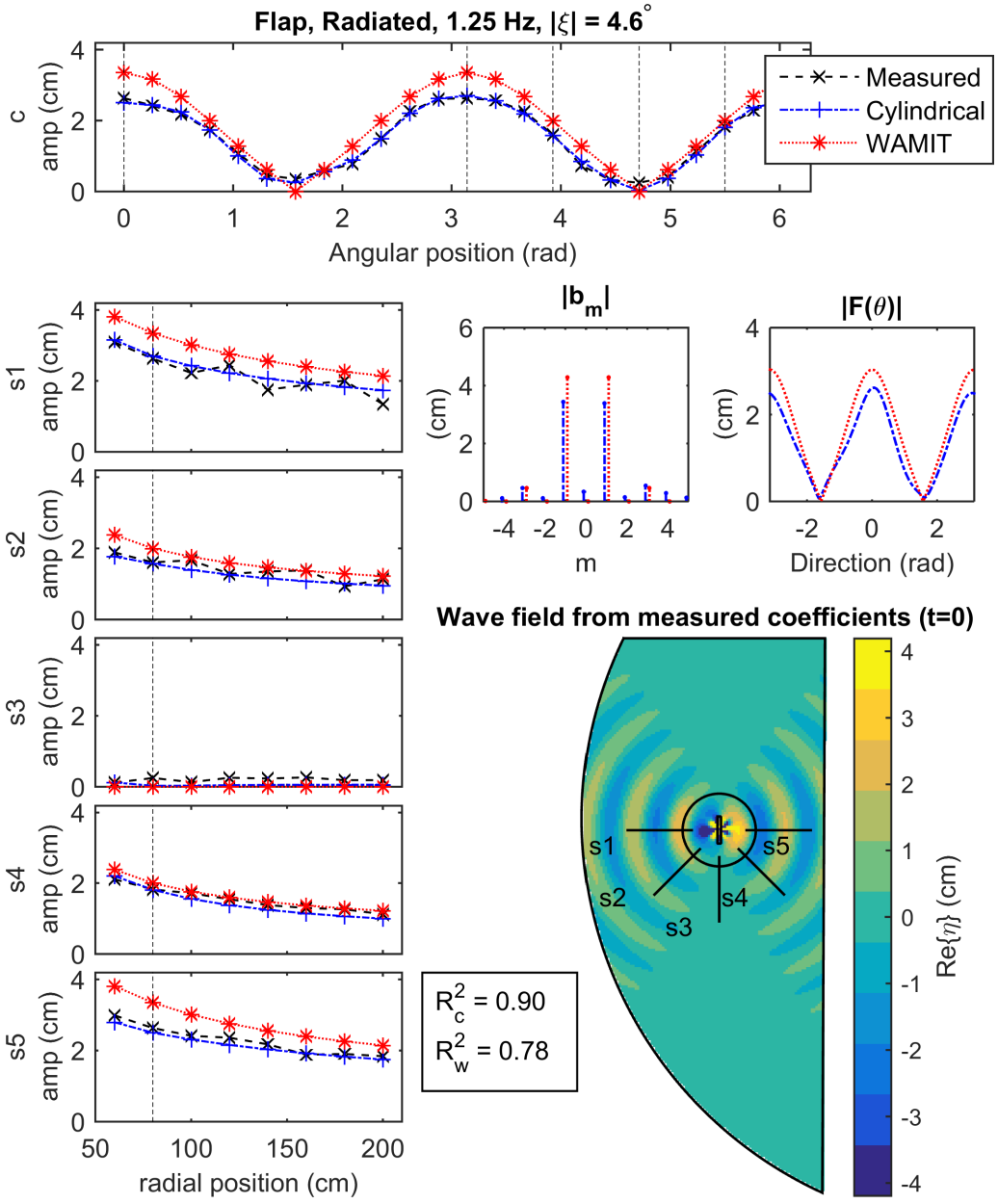

Figure C.9: Flap, radiated wave field, 1.25 Hz

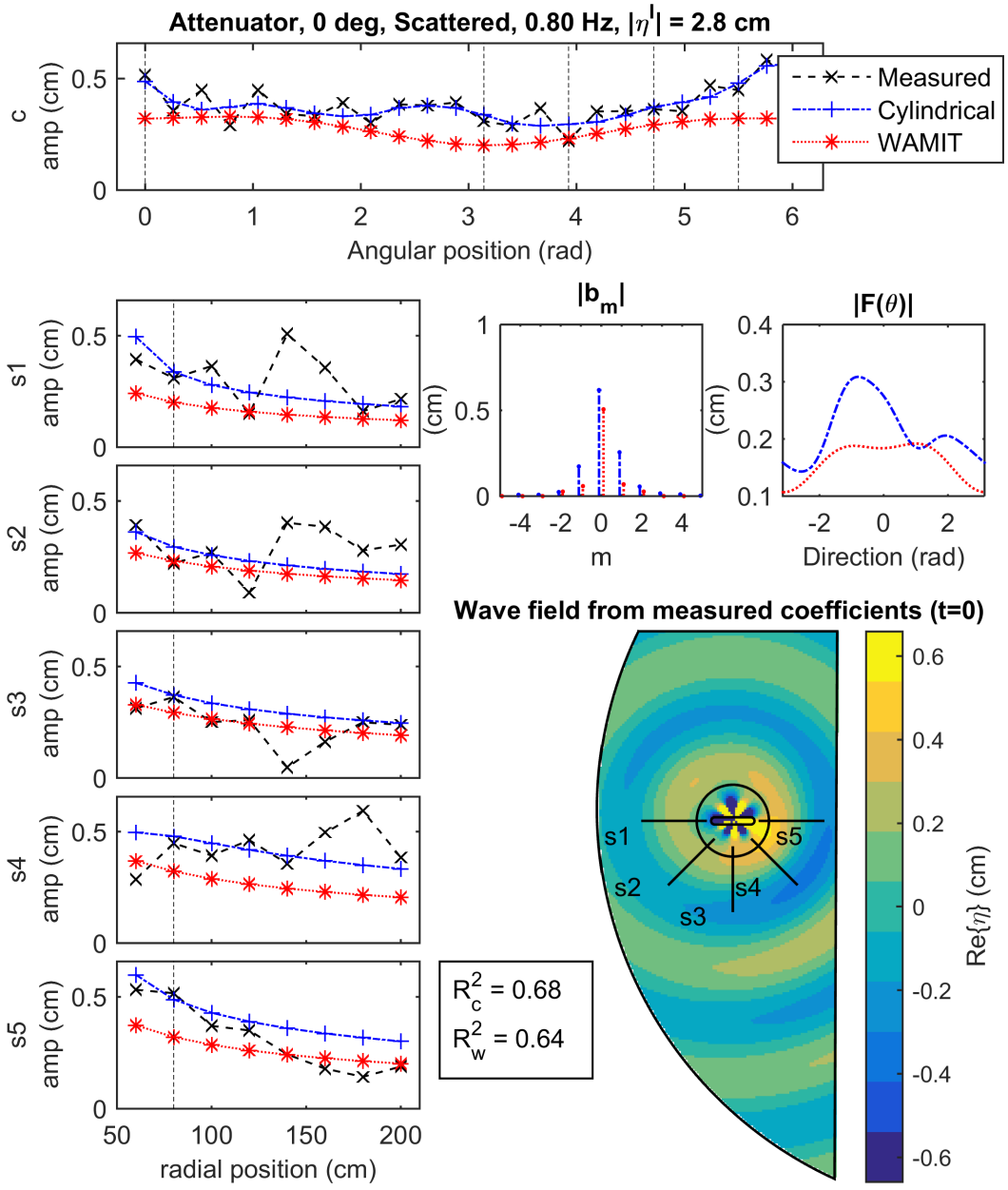

Figure C.10: Attenuator, 0° orientation, scattered wave field, 0.8 Hz

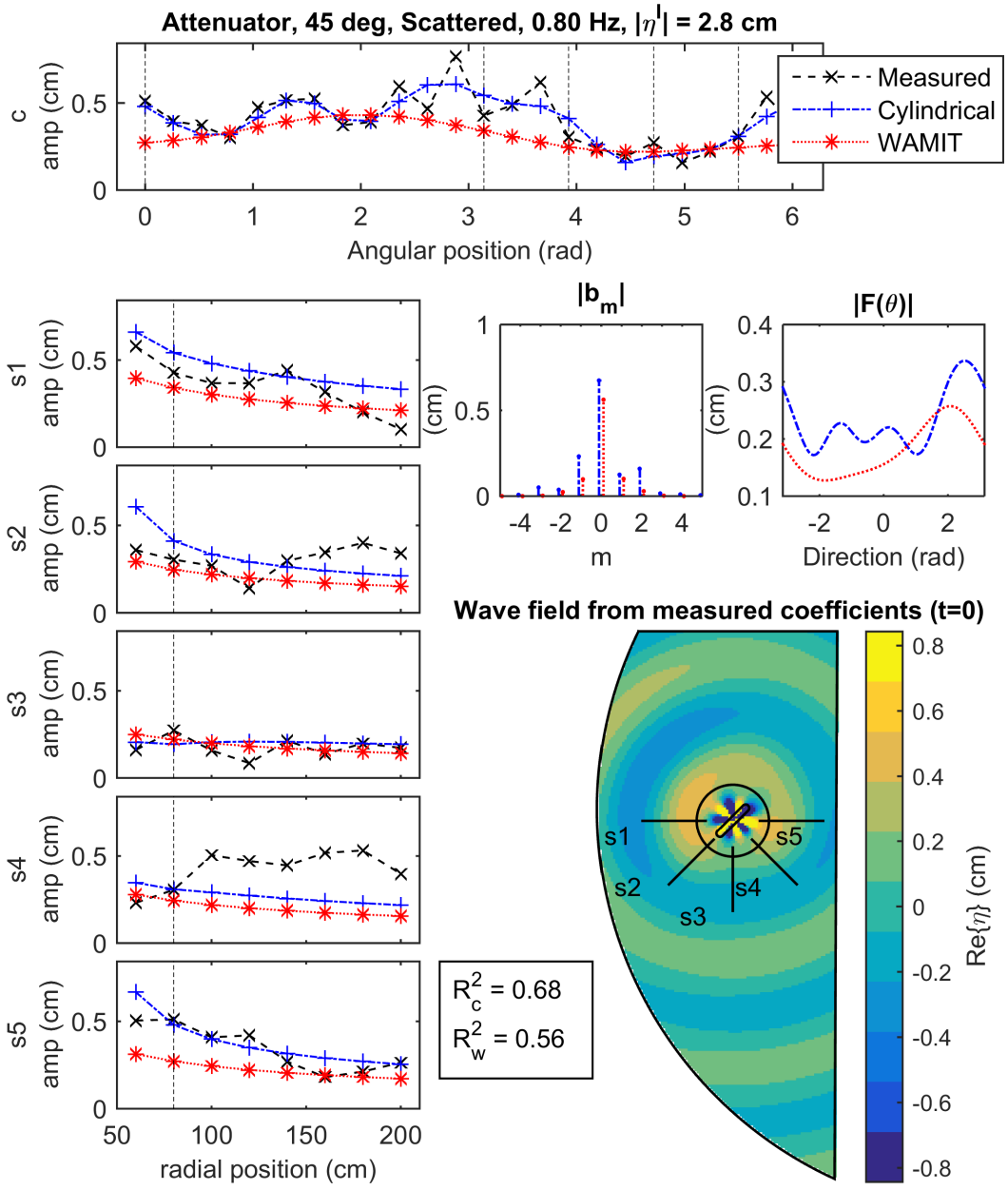

Figure C.11: Attenuator, 45° orientation, scattered wave field, 0.8 Hz

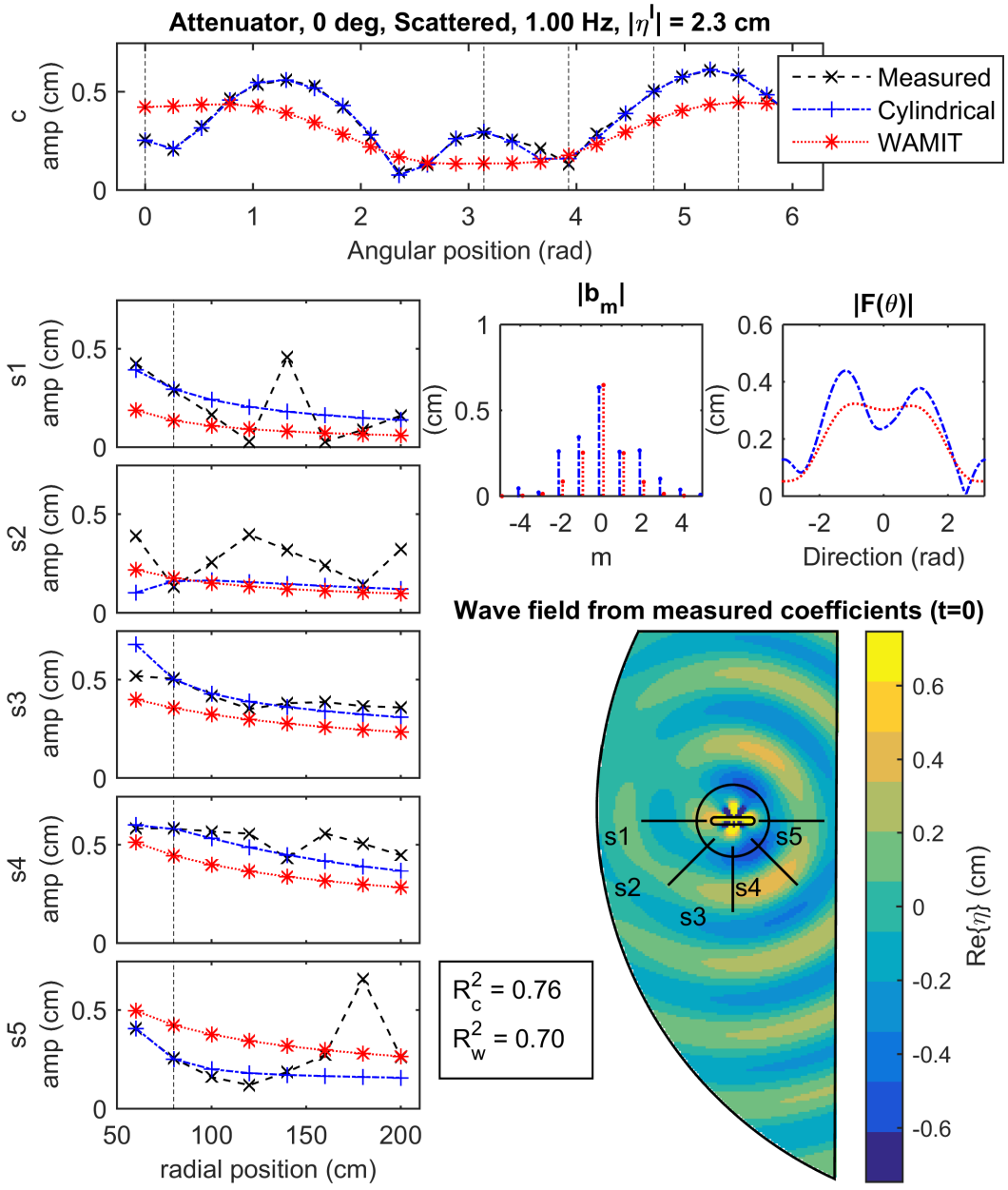

Figure C.12: Attenuator, 0° orientation, scattered wave field, 1 Hz

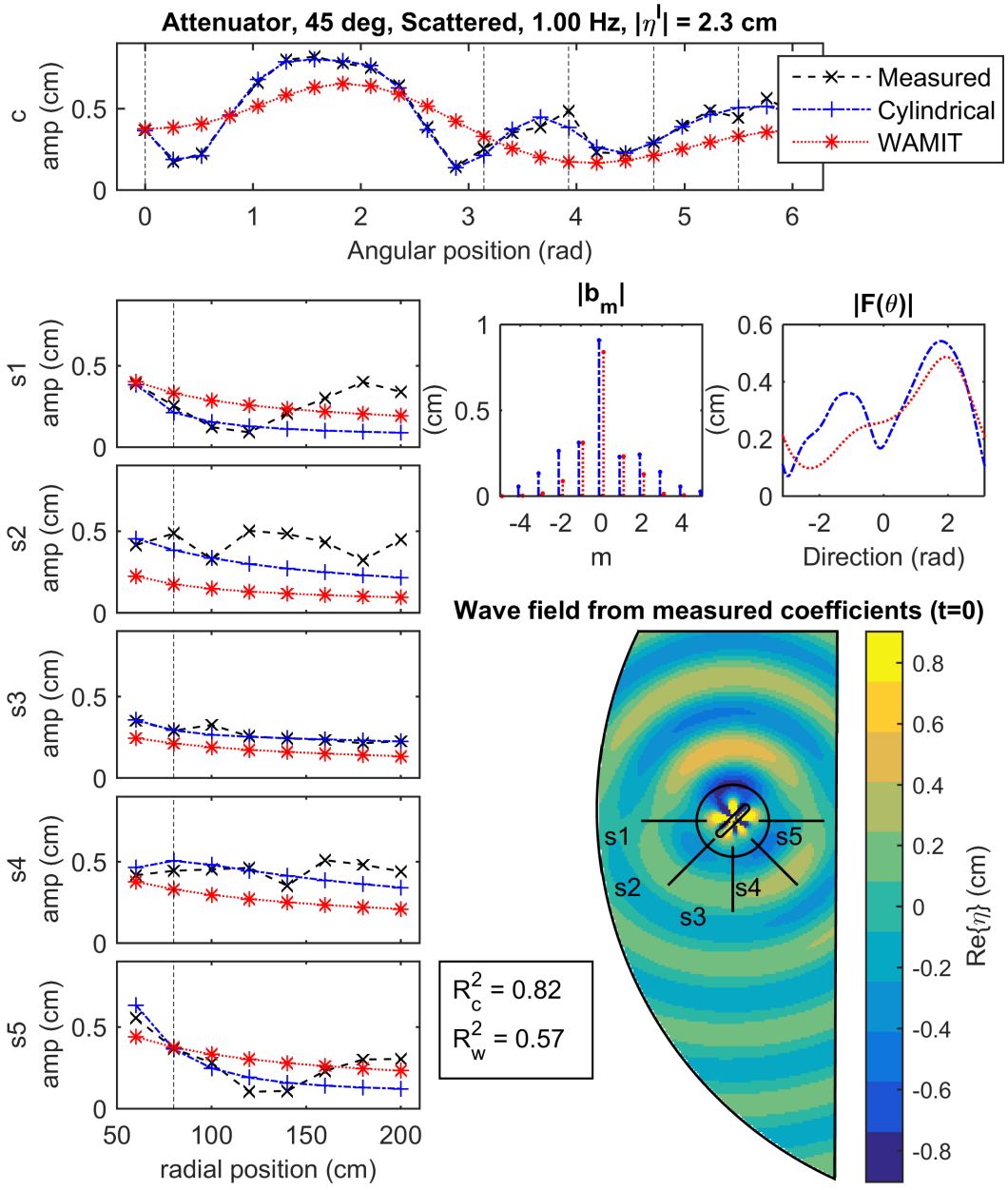

Figure C.13: Attenuator, $45°$ orientation, scattered wave field, 1 Hz

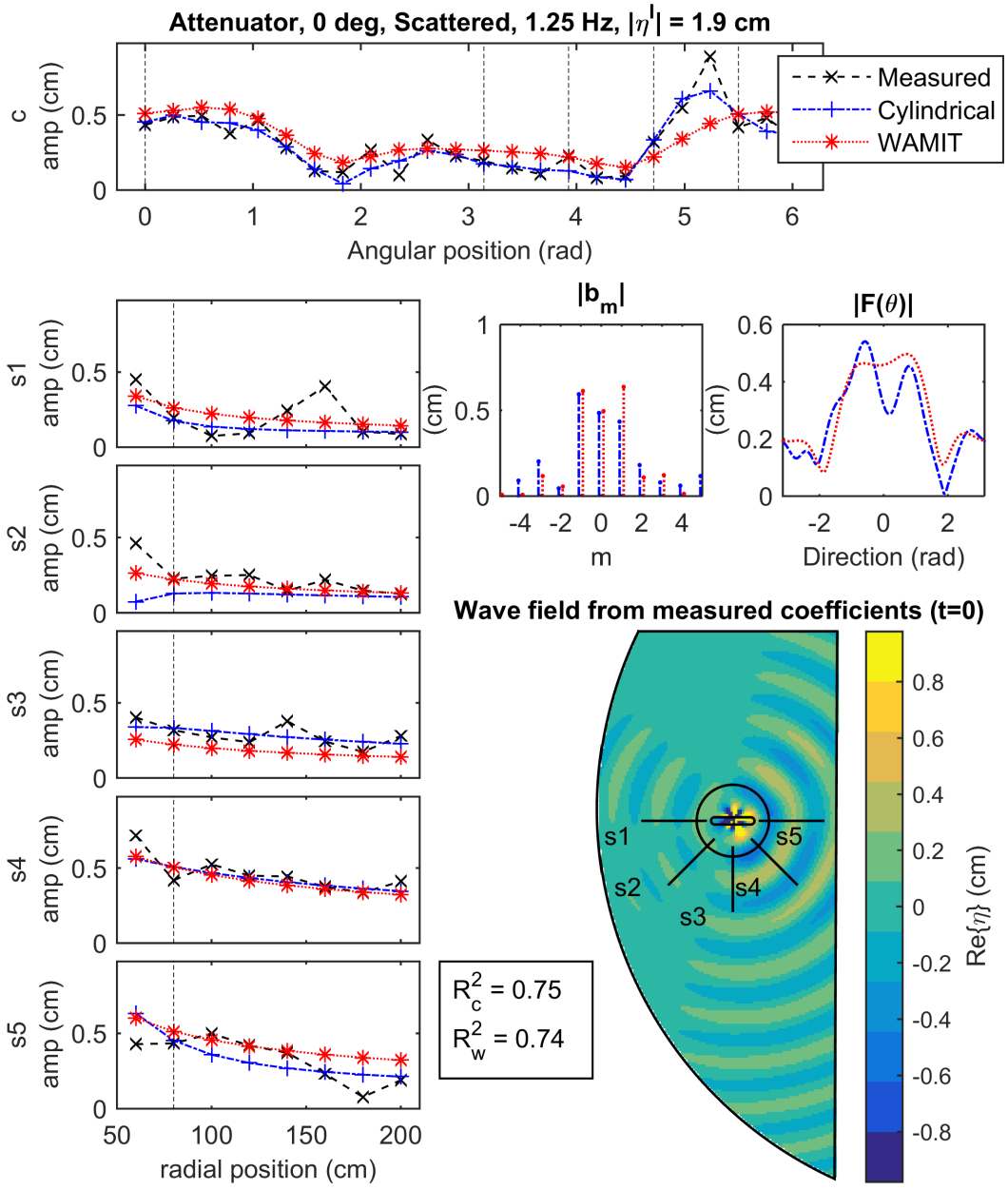

Figure C.14: Attenuator, 0° orientation, scattered wave field, 1.25 Hz

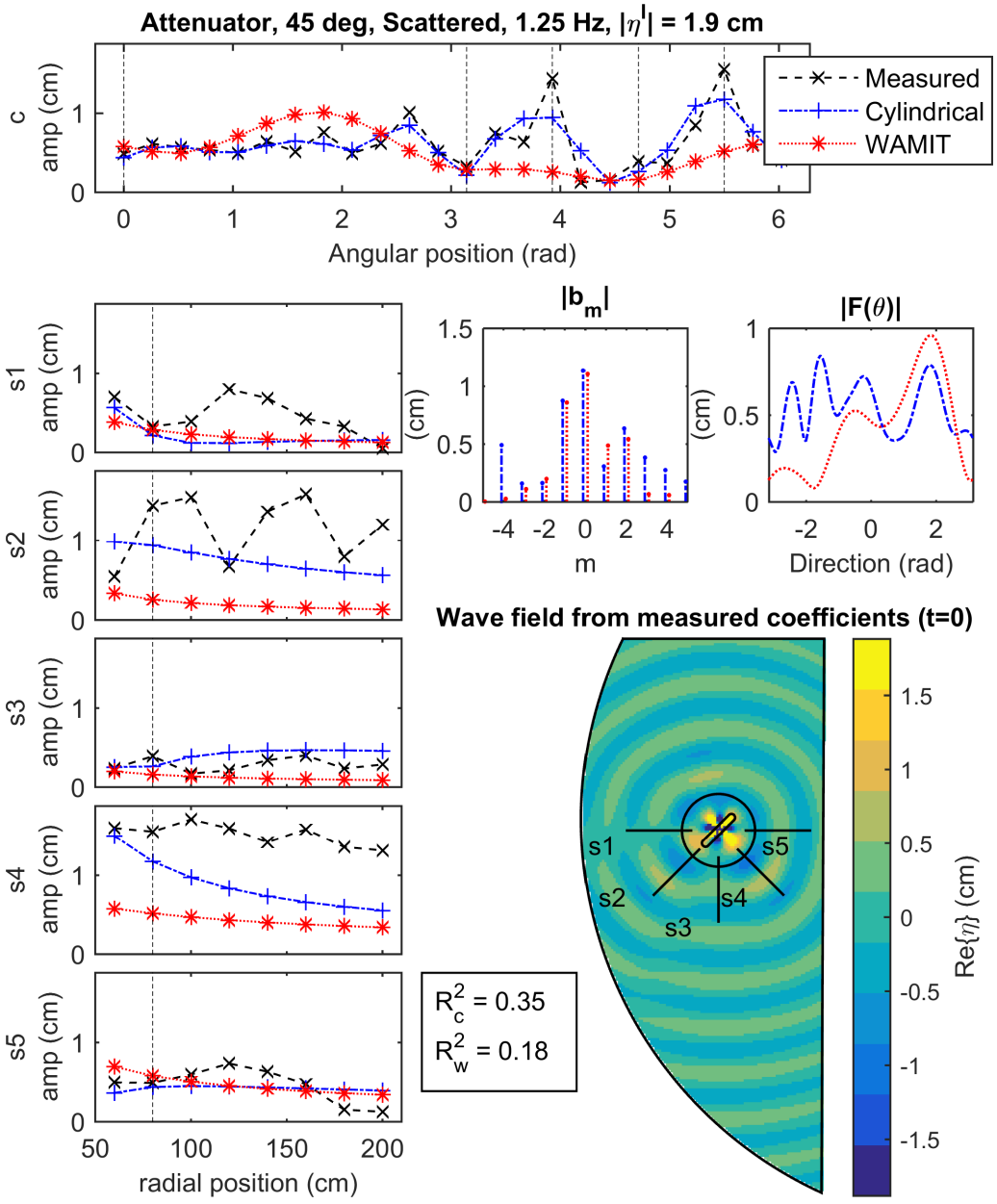

Figure C.15: Attenuator, 45° orientation, scattered wave field, 1.25 Hz

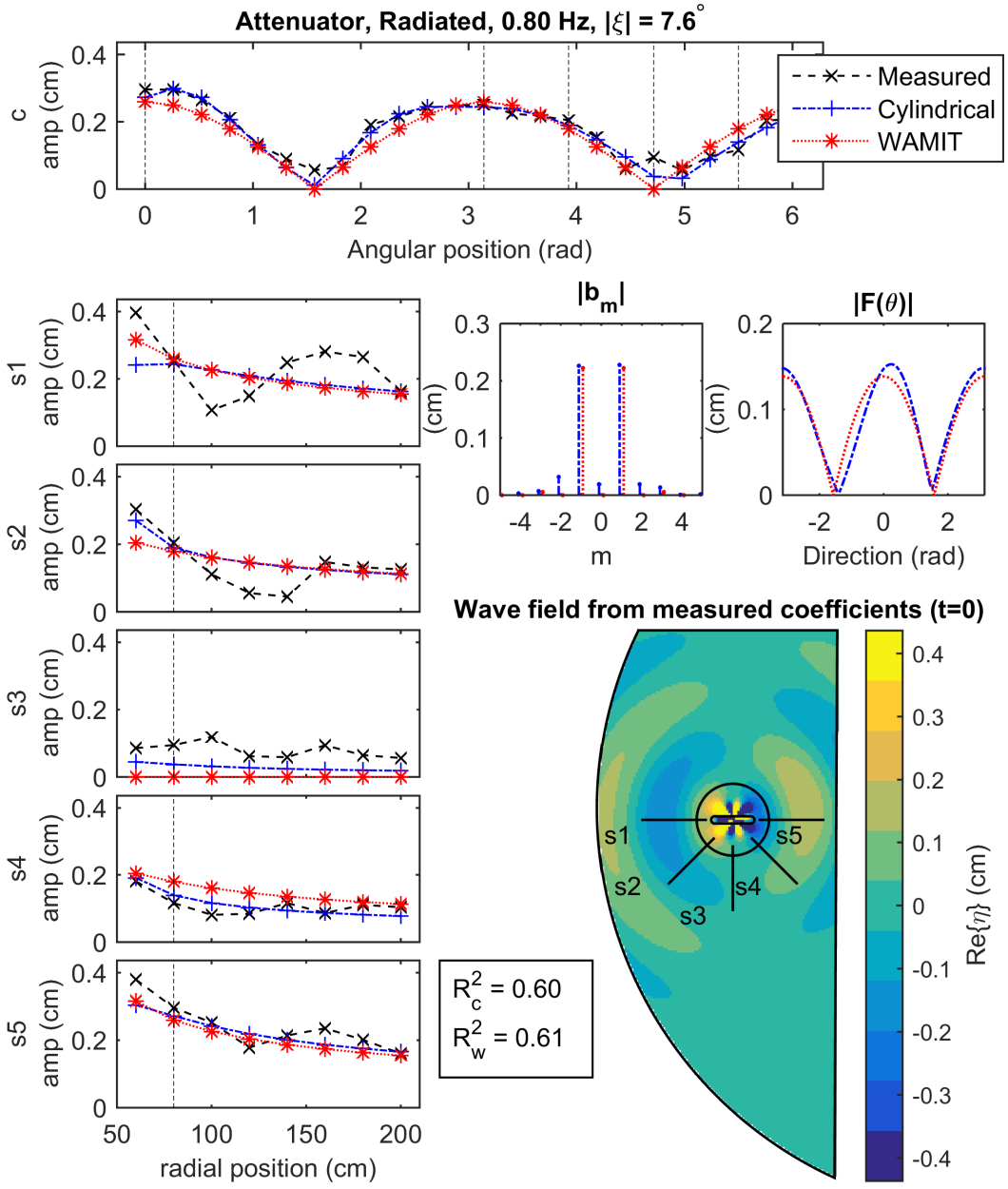

Figure C.16: Attenuator, radiated wave field, 0.8 Hz

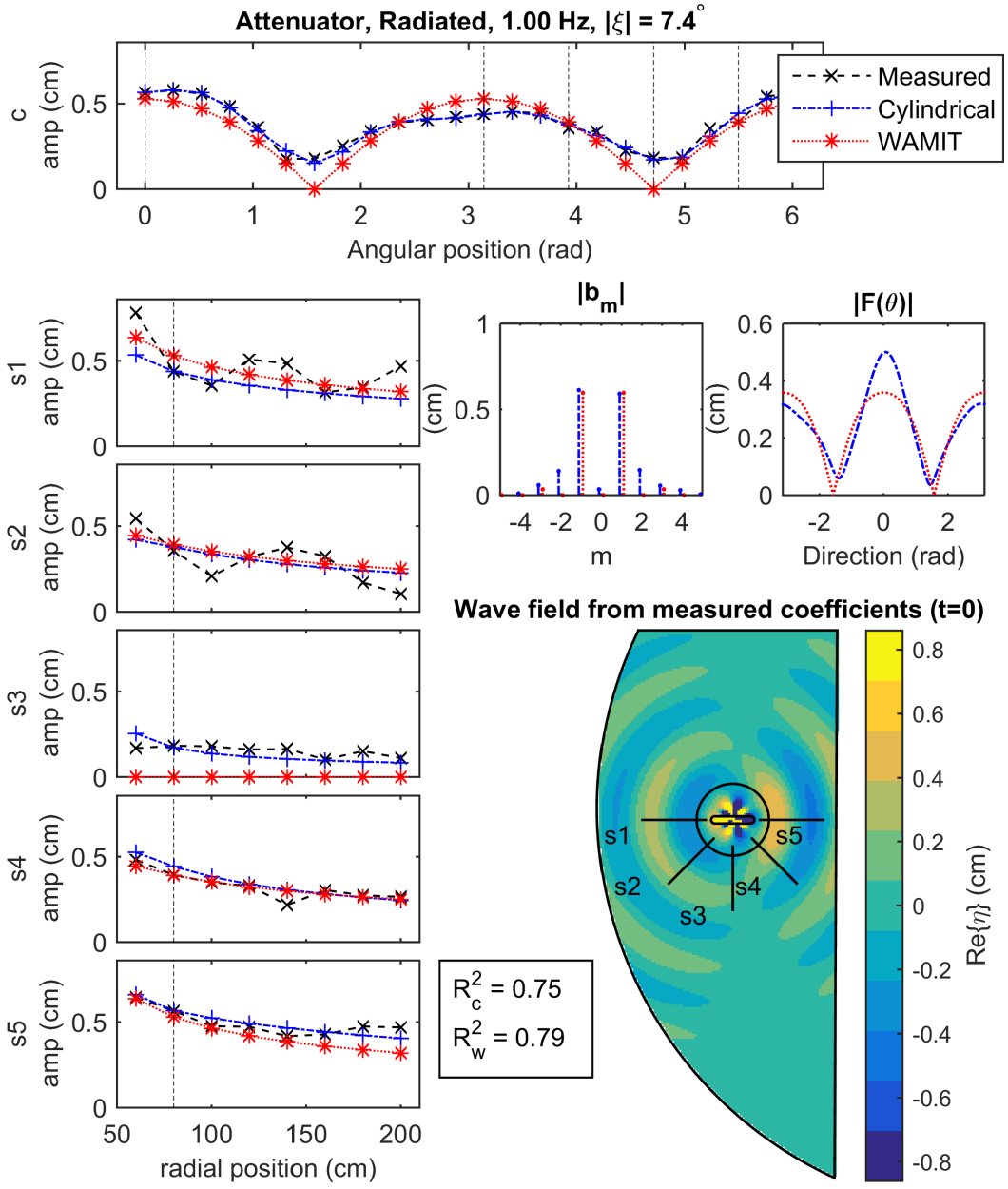

Figure C.17: Attenuator, radiated wave field, 1 Hz

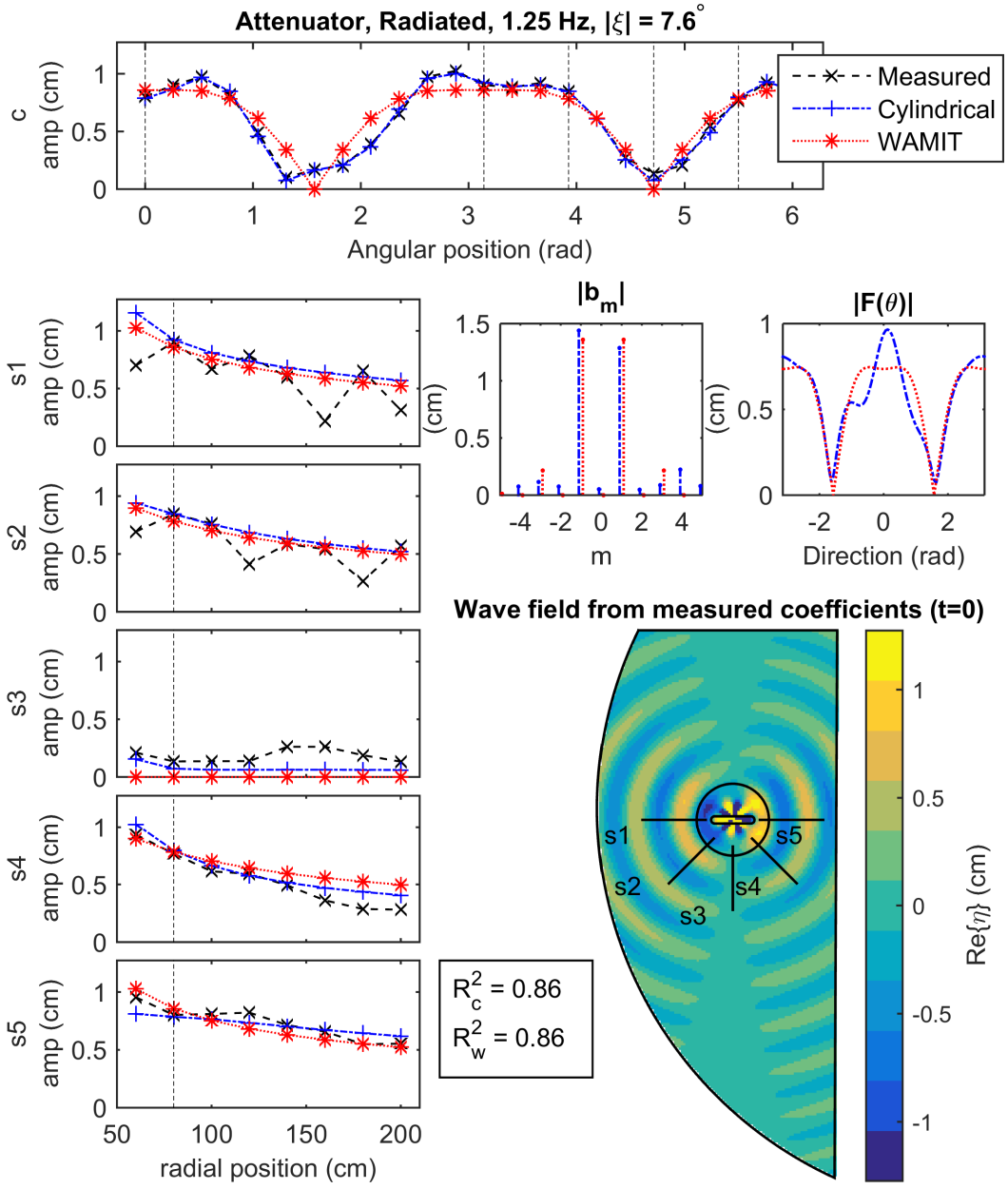

Figure C.18: Attenuator, radiated wave field, 1.25 Hz

References

M. Abramowitz and I. Stegun. *Handbook of Mathematical Functions with Formulas, Graphs, and Mathematical Tables*. National Bureau of Standards, Washington DC, 1964.

A. Babarit. On the park effect in arrays of oscillating wave energy converters. *Renewable Energy*, 58:68–78, October 2013.

A. Babarit, M. Folley, F. Charrayre, C. Peyrard, and M. Benoit. On the modelling of WECs in wave models using far field coefficients. In *Proc. of the 10th European Wave and Tidal Energy Conf., Aalborg, Denmark*, Aalborg, Denmark, 2013.

J. L. Black. Wave forces on vertical axisymmetric bodies. *Journal of Fluid Mechanics*, 67(02):369, 1975.

B. Borgarino, A. Babarit, and P. Ferrant. Impact of wave interactions effects on energy absorption in large arrays of wave energy converters. *Ocean Engineering*, 41:79–88, February 2012a.

B. Borgarino, A. Babarit, and P. Ferrant. An implementation of the fast multipole algorithm for wave interaction problems on sparse arrays of floating bodies. *Journal of Engineering Mathematics*, 77(1):51–68, June 2012b.

B. Buchner. An Evaluation and Extension of the Shallow Draft Diffraction Theory. In *Proc. of the 3rd International Offshore and Polar Engineering Conference*, volume 2, pages 6–11, 1993.

K. Budal and J. Falnes. A resonant point absorber of ocean-wave power. *Nature*, 256: 478–479, 1975.

K. Budal. Theory for absorption of wave power by a system of interacting bodies. *Journal of Ship Research*, 21(4):248–253, 1977.

Bykst. waves-circles-285359, 2015. URL `https://pixabay.com/en/waves-circles-drop-of-water-wave-285359/`.

S. Chakrabarti. Hydrodynamic interaction forces on multi-moduled structures. *Ocean Engineering*, 27(10):1037–1063, October 2000.

B. F. M. Child. *On the configuration of arrays of floating wave energy converters*. PhD thesis, The Univeristy of Edinburgh, 2011.

B. Child and V. Venugopal. Optimal configurations of wave energy device arrays. *Ocean Engineering*, 37:1402–1417, 2010.

J. Cruz. *Ocean Wave Energy: Current Status and Future Prespectives (Green Energy and Technology)*. Springer, 2008.

A. M. J. Davis. A relation between the radiation and scattering of surface waves by axisymmetric bodies. *Journal of Fluid Mechanics*, 76(1):85–88, 1976.

R. B. Dean and R. A. Dalrymple. *Water Wave Mechanics for Engineers and Scientists: v. 2 (Advanced Series on Ocean Engineering)*. World Scientific Publishing Co Pte Ltd, 1991.

G. Delhommeau. *Les problèmes de diffraction-radiation et de résistance de vagues: étude théorique et résolution numérique par la méthode des singularités*. PhD thesis, Ecole Nationale Supérieure de Mécanique, 1987.

D. Evans. A theory for wave-power absorption by oscillating bodies. *Journal of Fluid Mechanics*, 77(1):1–25, 1976.

D. Evans. Some analytic results for two and three dimensional wave-energy absorbers. *Power from sea waves*, 1980.

D. Evans and R. Porter. Trapped modes about multiple cylinders in a channel. *Journal of Fluid Mechanics*, 339:331–356, 1997a.

D. Evans and R. Porter. Near-trapping of waves by circular arrays of vertical cylinders. *Applied Ocean Research*, 19(2):83–99, April 1997b.

D. Evans, D. C. Jeffrey, S. H. Salter, and J. R. M. Taylor. Submerged cylinder wave energy device: theory and experiment. *Applied Ocean Research*, 1(1):3–12, 1979.

J. Falnes. A review of wave-energy extraction. *Marine Structures*, 20:185–201, 2007.

F. J. M. Farley. Far-field theory of wave power capture by oscillating systems. *Transactions of the Royal Society A: Mathematical, Physical & Engineering Sciences*, 370:278–287, 2012.

J. D. Fenton. Wave forces on vertical bodies of revolution. *Journal of Engineering Mathematics*, 85(2):241–255, 1978.

FloWave TT Limited. FloWave Ocean Energy Research Facility, 2015. URL `http://www.flowavett.co.uk/`.

M. Folley and T. Whittaker. The effect of sub-optimal control and the spectral wave climate on the performance of wave energy converter arrays. *Applied Ocean Research*, 31(4):260–266, October 2009.

M. Folley, B. Child, D. Forehand, L. O. Boyle, K. Silverthorne, J. Spinneken, and P. Troch. A review of numerical modelling of wave energy converter arrays. In *Proc. of the ASME 2012 31th International Conference on Ocean, Offshore and Arctic Engineering*, 2012.

X. Garnaud and C. C. Mei. Bragg scattering and wave-power extraction by an array of small buoys. *Proceedings of the Royal Society A: Mathematical, Physical and Engineering Sciences*, 466(2113):79–106, 2010.

C. J. R. Garrett. Wave forces on a circular dock. *Journal of Fluid Mechanics*, 46(1): 129–139, 1971.

J.-S. Goo and K. Yoshida. A numerical method for huge semisubmersible responses in waves. *Transactions of the Society of Naval Architects and Marine Engineers*, 98: 365–387, 1990.

I. Gyongy, J.-B. Richon, T. Bruce, and I. Bryden. Validation of a hydrodynamic model for a curved, multi-paddle wave tank. *Applied Ocean Research*, 44:39–52, January 2014.

T. H. Havelock. The pressure of water wave upon a fixed obstacle. *Transactions of the Royal Society A: Mathematical, Physical & Engineering Sciences*, 175(A):409–421, 1940.

L. H. Holthuijsen. *Waves in Oceanic and Coastal Waters*. Cambridge University Press, Cambridge, 2007.

J. N. Hunt and R. E. Baddour. The diffraction of nonlinear progressive waves by a vertical cylinder. *Quarterly Journal of Mechanics and Applied Mathematics*, 34(1): 69–87, 1981.

F. John. On the motion of floating bodies II. *Communications on Pure and Applied Mathematics*, 3:45–101, 1950.

H. Kagemoto. Minimization of wave forces on an array of floating bodies - The inverse hydrodynamic interaction theory. *Applied ocean research*, 14:83–92, 1992.

H. Kagemoto and D. Yue. Hydrodynamic interaction analyses of very large floating structures. *Marine structures*, 6:295–322, 1993.

H. Kagemoto, M. Murai, M. Saito, B. Molin, and v. Malenica. Experimental and theoretical analysis of the wave decay along a long array of vertical cylinders. *Journal of Fluid Mechanics*, 456(2002), April 2002.

H. Kagemoto, M. Murai, and M. Kashiwagi. Can a single floating body be expressed as the sum of two bodies? *Journal of Engineering Mathematics*, 68(2):153–164, July 2010.

H. Kagemoto and D. K.-P. Yue. Interactions among multiple three-dimensional bodies in water waves: an exact algebraic method. *Journal of Fluid Mechanics*, 166:189–209, 1986.

H. Kagemoto, M. Fujino, and M. Murai. Theoretical and experimental predictions of the hydroelastic response of a very large floating structure in waves. *Applied Ocean Research*, 20(3):135–144, 1998.

M. Kashiwagi. Hydrodynamic interactions among a great number of columns supporting a very large flexible structure. *Journal of fluids and structures*, 14:1013–1034, 2000a.

M. Kashiwagi. 3-D calculation for multiple floating bodies in proximity using wave interaction theory. *International Journal of Offshore and Polar Engineering*, 18(1): 14–20, 2008.

M. Kashiwagi. Research on hydroelastic responses of VLFS: Recent progress and future work. *International Journal of Offshore and Polar Engineering*, 10(2):81–90, 2000b.

M. Kashiwagi and Y. Ohwatari. Spatial distribution of the wave around multiple floating bodies. *Proc. of the 12th Int. Offshore and Polar Engineering Conference, Kitakyushu, Japan*, 3:479–486, 2002.

H. Lamb. On water waves due to disturbance beneath the surface. *Proc. of the London Mathematical Society*, 21(1):359–372, 1923.

H. Lamb. *Hydrodynamics*. Cambridge University Press, Cambridge, UK, 6 edition, 1932.

U. Leonhardt. Optical conformal mapping. *Science*, 313:1777–1780, 2006.

C. M. Linton and D. V. Evans. The Radiation and Scattering of Surface Waves by a Vertical Circular Cylinder in a Channel. *Philosophical Transactions of the Royal Society A: Mathematical, Physical and Engineering Sciences*, 338(1650):325–357, 1992.

C. M. Linton and P. McIver. The scattering of water waves by an array of circular cylinders in a channel. *Journal of Engineering Mathematics*, 30:661–682, 1996.

C. Linton and D. Evans. The interaction of waves with arrays of vertical circular cylinders. *J. Fluid Mech*, 215:549–569, 1990.

R. C. MacCamy and R. A. Fuchs. Wave forces on piles: a diffraction theory. *Technical Memorandum No. 69, U. S. Army Corps of Engineers*, 1954.

S. Malenica. Second-order water wave diffraction by an array of vertical cylinders. *Journal of Fluid Mechanics*, 390:349–373, 1999.

P. A. Martin. *Multiple Scattering: Interaction of Time-Harmonic Waves with N Obstacles*. Cambridge University Press, Cambridge, UK, 2006.

D. Masson and P. H. Leblond. Spectral evolution of wind-generated surface gravity waves in a dispersed ice field. *Journal of Fluid Mechanics*, 202(-1):43, 1989.

S. Mavrakos and P. McIver. Comparison of methods for computing hydrodynamic characteristics of arrays of wave power devices. *Applied Ocean Research*, 19:283–291, 1997.

M. McIver. The scattering properties of a system of structures in water waves. *The Quarterly Journal of Mechanics and Applied Mathematics*, 0(0), 2014.

P. McIver. Wave interaction with arrays of structures. *Applied Ocean Research*, 24(3): 121–126, June 2002.

P. McIver. Complex resonances in the water-wave problem for a floating structure. *Journal of Fluid Mechanics*, 536:423–443, July 2005.

P. McIver and D. Evans. Approximation of wave forces on cylinder arrays. *Applied Ocean Research*, 6(2):101–107, 1984.

P. McIver and J. N. Newman. Trapping structures in the three-dimensional water-wave problem. *Journal of Fluid Mechanics*, 484:283–301, 2003.

J. C. McNatt, M. Hall, J. Davidson, A. de Andres, and S. Hamawi. Innovation in Offshore Renewable Energy: International Collaboration and INORE. In *Proc. of the 5th International Conf. on Ocean Energy*, Halifax, Canada, 2014.

J. C. McNatt, V. Venugopal, and D. Forehand. The cylindrical wave field of wave energy converters. *International Journal of Marine Energy*, 3-4:e26–e39, December 2013a.

J. C. McNatt, V. Venugopal, and D. Forehand. The Cylindrical Wave Field of Wave Energy Converters. In *Proc. of the 10th European Wave and Tidal Energy Conf., Aalborg, Denmark*, Aalborg, Denmark, 2013b.

J. C. McNatt, V. Venugopal, and D. Forehand. A novel method for deriving the diffraction transfer matrix and its application to multi-body interactions in water waves. *Ocean Engineering*, 94:173–185, January 2015a.

J. C. McNatt, V. Venugopal, D. Forehand, and G. S. Payne. Experimental Analysis of Cylindrical Wave Fields. In *Proc. of the 11th European Wave and Tidal Energy Conf., Nantes, France*, 2015b.

J. C. McNatt. *Wave field patterns generated by wave energy converters*. Masters thesis, Oregon State University, 2012.

C. Mei. Power extraction from water waves. *Journal of Ship Research*, 20(2):62–66, 1976.

C. C. Mei, M. Stiassnie, and D. K.-P. Yue. *Theory and Applications of Ocean Surface Waves: Pt. 1: Linear Aspects*. World Scientific Publishing Co Pte Ltd, 2005.

M. H. Meylan. Wave response of an ice floe of arbitrary geometry. *Journal of Geophysical Research*, 107(C1), 2002.

M. H. Meylan and V. A. Squire. Response of a circular ice floe to ocean waves. *Journal of Geophysical Research*, 101(C4):8869, 1996.

J. Miles and F. Gilbert. Scattering of gravity waves by a circular dock. *Journal of Fluid Mechanics*, 34(4):783–793, 1968.

P. M. Morse and H. Feshbach. *Methods of Theoretica Physics: Parts I & II*. McGraw-Hill Book Company, Inc., New York, 1953.

B. R. Munson, D. F. Young, T. H. Okiishi, and W. W. Huebsch. *Fundamentals of Fluid Mechanics*. John Wiley & Sons, Inc., Jefferson City, sixth edit edition, 2009.

M. Murai, H. Kagemoto, and M. Fujino. On the hydroelastic responses of a very large floating structure in waves. *Journal of Marine Science and Technology*, 4(3):0123–0153, December 1999.

J. N. Newman. The second-order wave force on a vertical cylinder. *Journal of Fluid Mechanics*, 320(-1):417, 1996.

J. N. Newman. Cloaking a circular cylinder in water waves. *European Journal of Mechanics, B/Fluids*, 47:145–150, 2014.

J. N. Newman and C.-H. Lee. Boundary-Element Methods In Offshore Structure Analysis. *Journal of Offshore Mechanics and Arctic Engineering*, 124(2):81, 2002.

J. Newman. Wave effects on deformable bodies. *Applied Ocean Research*, 16:47–59, 1994.

J. N. Newman. The exciting forces on fixed bodies in waves. *Journal of Ship Research*, 6(3):10–17, 1962.

J. N. Newman. Interaction of waves with two-dimensional obstacles : a relation between the radiation and scattering problems. *Journal of Fluid Mechanics*, 71(2):273–282, 1975.

J. N. Newman. The Interaction of Stationary Vessels with Regular Waves. In *Proc. 11th Symposium on Naval Hydrodynamics*, pages 491–501, London, UK, 1976.

J. N. Newman. *Marine Hydrodynamics*. MIT Press, 1977.

J. N. Newman. Absorption of wave energy by elongated bodies. *Applied Ocean Research*, 1(4):189–196, 1979.

J. N. Newman. Wave effects on hinged bodies Part I body motions. *Self-published at www.wamit.com/Publications*, 1997.

J. N. Newman and C.-H. Lee. Sensitivity of wave loads to the discrectization of bodies. In *BOSS 92: 6th International Conference on the Behaviour of Offshore Structures*, 1992.

F. Noblesse and C. Yang. Elementary water waves. *Journal of Engineering Mathematics*, 59(3):277–299, 2007.

T. F. Ogilvie. First- and second-order forces on a cylinder submerged under a free surface. *Journal of Fluid Mechanics*, 16(3):451–472, 1963.

M. Ohkusu. Hydrodynamic forces on multiple cylinders in waves. *Proc. of the Int. Symp. on Dynamics of Marine Vehicles and Structures in Waves, London*, pages 107–112, 1974.

G. S. Payne, J. R. Taylor, T. Bruce, and P. Parkin. Assessment of boundary-element method for modelling a free-floating sloped wave energy device. Part 1: Numerical modelling. *Ocean Engineering*, 35(3-4):333–341, March 2008.

M. A. Peter and M. H. Meylan. Infinite-depth interaction theory for arbitrary floating bodies applied to wave forcing of ice floes. *Journal of Fluid Mechanics*, 500(2004): 145–167, January 2004a.

M. A. Peter and M. H. Meylan. The eigenfunction expansion of the infinite depth free surface Green function in three dimensions. *Wave Motion*, 40(1):1–11, June 2004b.

M. A. Peter, M. H. Meylan, and C. M. Linton. Water-wave scattering by a periodic array of arbitrary bodies. *Journal of Fluid Mechanics*, 548:237–256, February 2006.

D. Pizer. Maximum wave-power absorption of point absorbers under motion constraints. *Applied Ocean Research*, 15(4):227–234, 1993.

R. Porter and J. N. Newman. Cloaking of a vertical cylinder in waves using variable bathymetry. *Journal of Fluid Mechanics*, 750:124–143, 2014.

S. Salter. Wave power. *Nature*, 249:720–724, 1974.

P. Siddorn and R. Eatock Taylor. Diffraction and independent radiation by an array of floating cylinders. *Ocean Engineering*, 35(13):1289–1303, September 2008.

M. Simon. Multiple scattering in arrays of axisymmetric wave-energy devices. Pt. 1: a matrix method using a plane-wave approximation. *Journal of Fluid Mechanics*, 120: 1–25, 1982.

J. Singh and A. Babarit. A fast approach coupling Boundary Element Method and plane wave approximation for wave interaction analysis in sparse arrays of wave energy converters. *Ocean Engineering*, 85:12–20, July 2014.

A. Sommerfeld. *Partial Differential Equations in Physics (Pure and Applied Mathematics: A Series of Monographs and Textbooks, Vol. 1)*. Academic Press Inc., New York, 1949.

B. H. Spring and P. L. Monkmeyer. Interaction of plane waves with vertical cylinders. In *Proc. of the 14th Int. Conf. on Coastal Engineering*, pages 1828–1847, 1974.

V. A. Squire. Of ocean waves and sea-ice revisited. *Cold Regions Science and Technology*, 49(2):110–133, 2007.

V. A. Squire, J. P. Dugan, P. Wadhams, P. J. Rottier, and A. K. Liu. Of Ocean Waves and Sea Ice. *Annual Review of Fluid Mechanics*, 27(1):115–168, 1995.

P. Stansell and D. J. Pizer. Maximum wave-power absorption by attenuating line absorbers under volume constraints. *Applied Ocean Research*, 40:83–93, March 2013.

W. L. Stutzman and G. A. Thiele. *Antenna Theory and Design*. John Wiley & Sons, Inc., New York, 2nd edition, 1998.

K.-T. Tang. *Mathematical Methods of Engineerings and Scientists 3*. Springer, New York, 2007.

The Mathematical Tables Project and The MIT Underwater Sound Laboratory. Scattering and Radiation from Circular Cylinders and Spheres. Technical report, 1946.

V. Twersky. Multiple scattering of radiation by an arbitrary configuration of parallel cylinders. *The Journal of the Acoustical Society of America*, 24:42–46, 1952.

Unsplash. water-802050, 2015. URL https://pixabay.com/en/water-surface-ripples-liquid-blue-802050/.

F. Ursell. Trapping modes in the theory of surface waves. *Mathematical Proceedings of the Cambridge Philosophical Society*, 47(02):347, 1951.

F. Ursell. Mathematical aspects of trapping modes in the theory of surface waves. *Journal of Fluid Mechanics*, 183(-1):421, 1987.

WAMIT Inc. *WAMIT User Manual, Version 7.0*. 2012.

C. M. Wang and Z. Y. Tay. Very large floating structures: Applications, research and development. *Procedia Engineering*, 14:62–72, 2011.

E. Watanabe, T. Utsunomiya, and C. M. Wang. Hydroelastic analysis of pontoon-type VLFS: A literature survey. *Engineering Structures*, 26(2):245–256, 2004.

J. Wehausen. The motion of floating bodies. *Annual Review of Fluid Mechanics*, 3: 237–268, 1971.

M. Wypych. *A study of radiated surface waves in the context of the capture of ocean wave energy*. Phd thesis, University of Canterbury, 2012.

M. Wypych, L. Le-Ngoc, K. Alexander, and A. Gardner. On the application of circular-cylindrical waves to ocean wave power absorption. *Ocean Engineering*, 40:69–75, February 2012.

R. Yemm, D. Pizer, C. Retzler, and R. Henderson. Pelamis: experience from concept to connection. *Philosophical Transactions of the Royal Society. Series A, Mathematical, Physical, and Engineering Sciences*, 370(1959):365–80, January 2012.

R. W. Yeung. Added mass and damping of a vertical cylinder in finite-depth waters. *Applied Ocean Research*, 3(3):119–133, 1981.

O. Yilmaz and A. Incecik. Analytical solutions of the diffraction problem of a group of truncated vertical cylinders. *Ocean engineering*, 25(6):385–394, 1998.

O. Yilmaz. Hydrodynamic interactions of waves with group of truncated vertical cylinders. *Journal of Waterway, Port, Coastal, and Ocean Engineering*, 124(5):272–279, 1998.

O. Yilmaz, A. Incecik, and N. Barltrop. Wave enhancement due to blockage in semi-submersible and TLP structures. *Ocean Engineering*, 28(5):471–490, May 2001.